

MASTER

Preload loss of stainless (steel) bolts in aluminium / steel joints

den Otter, C.L.J.

Award date:
2019

[Link to publication](#)

Disclaimer

This document contains a student thesis (bachelor's or master's), as authored by a student at Eindhoven University of Technology. Student theses are made available in the TU/e repository upon obtaining the required degree. The grade received is not published on the document as presented in the repository. The required complexity or quality of research of student theses may vary by program, and the required minimum study period may vary in duration.

General rights

Copyright and moral rights for the publications made accessible in the public portal are retained by the authors and/or other copyright owners and it is a condition of accessing publications that users recognise and abide by the legal requirements associated with these rights.

- Users may download and print one copy of any publication from the public portal for the purpose of private study or research.
- You may not further distribute the material or use it for any profit-making activity or commercial gain

Eindhoven University of Technology & Bayards

Preload loss of stainless (steel) bolts in aluminium / steel joints

Student: C.L.J. (Christiaan) den Otter
Student- / ID-number: s090603 / 0720625
Faculty: Department of the Built Environment
Unit: Structural Design

Graduation committee: Prof. Dr. Ir. J. (Johan) Maljaars
Ir. B.W.E.M. (Dianne) van Hove
Ing. J.M. (Johan) van Loon

Graduation date: May 16th 2019
Graduation number: A-2019.271
Publication date: May 16th 2020

Summary

Bolted joints are common in the world of structural engineering to create adjustable and cost effective connections, but are also sensitive to fatigue, loosening and stress concentrations. A possible solution for the disadvantages can be found in the application of preloaded bolts. Current legislation allows 8.8 and 10.9 (carbon) steel bolts to be preloaded. However, the application of stainless steel bolts is not allowed unless otherwise specified. The preload force in a bolt can fluctuate due to several phenomena subdivided in time-dependent and time-independent effects. This research focuses on distinguishing the major topics via qualification and quantification of the preload behaviour of preloaded (stainless) steel bolts in aluminium/steel joints. In order of importance, the major topics are: Poisson effect, bolt relaxation, plate creep, embedment creep and temperature variations. The topics are considered with a combination of research conducted in the past, calculations, and/or experiments.

The calculations are based on an analytical spring model described in VDI 2230. The spring model transforms the bolt and joint into linear springs with specific stiffness characteristics. Preload variation is implemented in the model by estimating the deformations introduced by the time-dependent and time-independent effects. Contraction or extension due to the aforementioned effects will affect the spring equilibrium and will subsequently result in preload variation. Guide values regarding embedment creep are used to model embedment creep. Creep data of stainless steel and aluminium is used to estimate bolt relaxation and plate creep. A creep parameter function is used to relate the expected creep strain to stress to be able to account for varying stress levels in a bolted joint. Thermal variations are included by considering the various coefficients of thermal expansion of bolt and plate material resulting in uneven deformations. The Poisson effect describes that a tensile force in a plate will result in lateral contraction. Lateral contractions in bolted joints are amplified by occurring stress concentrations around a bolt hole resulting in preload losses. The lateral contractions are modeled and used to predict the preload behaviour prior to slip.

The model is validated using experiments with lubricated A4 80 bolts combined with as-delivered and grit-blasted 5083 O/H111 plates considering embedment creep, bolt relaxation, plate creep and Poisson effect. Various joint types and initial preload levels are regarded to be able to compare the model in practical situations. The preload force is monitored by either a Load Cell or a Strain Gauge installed in the shank of the bolt or a combination of both load measuring systems. A combination of both the Load Cell Method and the Strain Gauge method exhibit comparable preload loss behaviour indicating that both methods can be applied to monitor preload forces.

The model predicts the relaxation and creep losses accurately at high preload levels, but underestimates the preload losses at lower preload levels. The discrepancies can be explained with the occurrence of embedment creep at the start of the relaxation test and inaccuracies of the model. Experimental tensile testing of a double lap joint demonstrates that the Poisson model gives an accurate prediction of the results prior to slip and that the slip resistance described in NEN-EN-1999-1-1 can be used to minimize the preload losses and to preserve a sufficient preload level.

Using the spring model, parametric studies regarding the initial preload force, total plate thickness and bolt diameter are performed and demonstrate that a sufficient amount of preload force can be guaranteed during service life by application of a high initial preload force equal to the nominal preload force P_{nom} . Respecting a minimum plate thickness – bolt diameter ratio requirement ($\sum t / d > 3$) will minimize the preload losses in most of the considered cases. To be able to account for the unavoidable preload losses due to relaxation and creep, it is recommended to consider $P_{nom} = 0.59 f_{ub} A_t$ as the engineering preload level.

Symbols

A_G	bearing area engaged threads
A_{LC}	effective bearing area interface Load Cell – Adapter ring
A_M	bearing area nut
$A_{SK,b}$	bearing interface bolt head - washer
A_d	nominal cross section unthreaded part
A_{dW}	critical bearing area interface washer-plate
A_{d_1}	cross section of threaded part at minor diameter
A_{d_3}	cross section of thread at minor diameter
A_g	Gross cross section plate
A_{net}	Netto cross section plate at bolt hole
A_t	reduced-shank cross section
$A(z)$	bearing surface area in z-direction
D_{1min}	minimum minor diameter nut
D_{1max}	maximum minor diameter nut
D_{1avg}	average minor diameter nut
E	Young's modulus of frustum material
E_b	Young's modulus of the bolt material
E_j	Young's modulus of plate material
E_w	Young's modulus of washer material
E_A	Young's modulus Adapter ring material
E_L	Young's modulus Load Cell material
F_p	proof load bolt
$F_{p,Cd}$	design preload force
$F_{s,Rd}$	design slip resistance
F_{slip}	theoretical slip load
K	Ramberg-Osgood constant
K_t	stress concentration ratio between peak stress and remote stress
$K_{t,byp}$	stress concentration factor in the case of bypass loading
$K_{t,pin}$	stress concentration factor in the case of pin loading
M	applied torque
N	strain-hardening exponent Kossakowski
P	preload force
P_i	preload force at thread number i
P_{ini}	initial preload force
P_{nom}	nominal minimum preload force
P_s	theoretical preload force at slip
$\Delta P_{cr,b}$	loss of preload due to relaxation

$\Delta P_{cr,j}$:	loss of preload due to plate creep
ΔP_{em} :	loss of preload due to embedment effects
$\Delta P_{poisson}$:	loss of preload due to poisson's effect
$\Delta P_{poisson,s}$:	preload loss due to poisson's effect at $\sigma_{//} = \sigma_s$
ΔP_{th} :	preload variation due to thermal effects
T :	temperature in Kelvin
$T_{assembly}$:	initial temperature during assembly
ΔT :	temperature variation with respect to assembly temperature
U_0 :	activation energy constant
V :	activation volume
W :	plate width
d :	bolt diameter
d_0 :	diameter bolt hole
d_1 :	basic minor diameter bolt
d_3 :	minor diameter of the bolt thread
d_{avg} :	average major diameter bolt
d_{max} :	maximum major diameter bolt
d_{min} :	minimum major diameter bolt
d_h :	diameter hole
dt :	time increment in seconds
d_{w1} :	inner diameter washer
d_w :	bearing surface outside diameter
e_1 :	edge distance bolt hole parallel with loading direction
e_2 :	edge distance bolt hole perpendicular to loading direction
$f_{0.2}$:	0.2% proof strength material
$f_1(\sigma)$:	creep parameter with function of applied stress
f_o :	proof strength plate material
f_u :	tensile strength plate material
f_{ub} :	tensile strength bolt material
f_y :	yield strength
h :	coefficient of work hardening
h_A :	effective height Adapter ring
h_L :	effective height Load Cell
k :	height bolt head or Boltzmann's constant
k_A :	elastic stiffness Adapter ring
k_L :	elastic stiffness Load Cell
k_{LC} :	elastic stiffness Load Cell - Adapter ring combination
k_G :	stiffness of the engaged thread

k_{GM}	stiffness of the engaged thread and of the nut
k_M	stiffness of the nut
k_{SK}	stiffness of the bolt head
k_{avg}	average coefficient of friction
k_b	elastic bolt stiffness (bolt head, unthreaded shaft, threaded shaft, nut)
k_d	stiffness of the unthreaded part
k_j	elastic joint stiffness (washers and plates)
k_t	stiffness of the threaded part located in the grip
k_{t_i}	stiffness plate i
$k_{\sum t}$	combined plate stiffness
l_d	length of the unthreaded part
l_g	grip length
l_t	length of the threaded part located in the grip
l_G	substitutional extension length for the deformation of the engaged thread
l_M	substitutional extension length for the deformation of the nut
l_{SK}	substitutional extension length for the deformation of the bolt head
n	interval number
n	number of friction surfaces
n	Ramberg-Osgood parameter
p	pitch height
t	time in seconds
t_0	time translation parameter
t	frustum height
t	thickness plate
t_i	thickness plate i
t_w	washer thickness
$\sum t$	total thickness of plates
$\sum t_w$	total thickness of washers
z	depth in z-direction
α	frustum angle
α_T	coefficient of linear thermal expansion
γ_{Ms}	partial safety factor for a slip resistant bolt
β	bearing ratio
δ_b	deformation bolt
$\delta_{cr,G,b,1...6}$	creep in threads, bearing, cumulative 1-7
$\delta_{cr,G,t}$	creep in threaded length located in the nut, tension
$\delta_{cr,M,b,1...7}$	creep in nut flank, bearing, cumulative 1-7
$\delta_{cr,SK,b}$	creep bolt head, bearing

$\delta_{cr,b}$:	total amount of bolt creep
$\delta_{cr,j}$:	total amount of plate creep
$\delta_{cr,ld,t}$:	creep in unthreaded length, tension
$\delta_{cr,lt,t}$:	creep in threaded length located in grip length, tension
δ_{em}	:	total amount of embedment creep
δ_j	:	deformation joint
$\delta_{poisson}$:	deformation due to poisson's effect
\mathcal{E}	:	strain
\mathcal{E}_0	:	yield strain
\mathcal{E}_1	:	initial hardening strain
\mathcal{E}'_0	:	constant related to the initial plastic strain rate
$\mathcal{E}_{cr,G,b,i}$:	creep strain in thread, bearing, thread i
$\mathcal{E}_{cr,G,t,i}$:	creep strain in threaded length located in the nut, thread number i, tension
$\mathcal{E}_{cr,M,b,i}$:	creep strain in nut flank, bearing, thread i
$\mathcal{E}_{cr,SK,b}$:	creep strain bolt, bearing
$\mathcal{E}_{cr,ld,t}$:	creep strain unthreaded length, tension
$\mathcal{E}_{cr,lt,t}$:	creep strain threaded length located in grip length, tension
$\mathcal{E}'_{cr}(t)$:	creep strain rate
$\mathcal{E}_{\perp,i}$:	perpendicular strain in plate i
$\mathcal{E}_{\parallel,i}$:	parallel strain in plate i
μ	:	slip factor
ν	:	Poisson's ratio
ν_{el}	:	elastic Poisson's ratio
ν_{pl}	:	plastic Poisson's ratio
σ	:	applied stress
σ_0	:	yield stress
σ_{01}	:	initial stress at the start of the nonlinear part of the approximation curve
σ_1	:	initial hardening stress
$\sigma_{G,b,i}$:	bearing stress threads at thread number i
$\sigma_{G,t,i}$:	tension stress threaded length located in nut at thread number i
$\sigma_{SK,b}$:	bearing stress at interface bolt head
σ_{max}	:	peak stress at edge hole
$\sigma_{ld,t}$:	tension stress unthreaded length
$\sigma_{lt,t}$:	tension stress unthreaded length
σ_z	:	bearing stress in z-direction
$\sigma_{\parallel,i}$:	remote stress in plate i
σ_{∞}	:	unaffected stress

Table of Contents

SUMMARY	1
SYMBOLS.....	2
1 INTRODUCTION	8
2 LITERATURE REVIEW	9
2.1 INTRODUCTION	9
2.2 EMBEDMENT CREEP	10
2.2.1 Construction errors	10
2.2.2 Positive design choices.....	11
2.3 STRESS RELAXATION STAINLESS STEEL.....	12
2.3.1 Time-independent properties stainless steel.....	12
2.3.2 Time-dependent properties stainless steel	14
2.3.3 Relaxation experiments Krapf.....	14
2.3.4 Relaxation experiments Hradil.....	15
2.3.5 Relaxation experiments Afzali.....	17
2.4 PLATE CREEP.....	19
2.5 THERMAL EFFECTS	21
2.6 ELASTIC INTERACTIONS	22
2.7 POISSON'S EFFECT.....	24
2.8 SUMMARY AND CONCLUSIONS LITERATURE REVIEW	26
3 ANALYTICAL MODELLING	27
3.1 INTRODUCTION	27
3.2 BACKGROUND AND APPLICATION VDI-MODEL	28
3.2.1 Bolt stiffness.....	29
3.2.2 Joint stiffness.....	30
3.3 DIMENSIONAL DATA AND MATERIAL PROPERTIES.....	33
3.3.1 Dimensional data	33
3.3.2 Material properties	34
3.4 EMBEDMENT EFFECTS.....	35
3.4.1 Theory	35
3.4.2 Parametric study.....	36
3.5 BOLT RELAXATION.....	39
3.5.1 Theory	39
3.5.2 Creep properties stainless steel bolt material.....	39
3.5.3 Subdivision bolt	46
3.5.4 Parametric study.....	54
3.6 PLATE CREEP.....	57
3.6.1 Theory	57
3.6.2 Creep properties plate material	57
3.6.3 Model stress distribution	60
3.6.4 Parametric study.....	62
3.7 THERMAL EFFECTS	65
3.7.1 Theory	65
3.7.2 Verification model with data Ydstebo.....	66
3.7.3 8.8 steel bolt + 50830/6082T6 plates	67
3.7.4 A4 80 stainless steel bolt + S235 plates	69
3.7.5 A4 80 stainless steel bolt + 50830/6082T6 plates	71
3.7.6 Comparison material combinations.....	73

3.8	POISSON'S EFFECT.....	74
3.8.1	<i>Theory</i>	74
3.8.2	<i>Stress concentration at holes</i>	77
3.8.3	<i>Verification with data Chakherlou</i>	80
3.8.4	<i>Poisson's effect 8.8 steel bolt + S235 plates</i>	85
3.8.5	<i>Poisson's effect A4 80 stainless steel bolt + S235 plates</i>	88
3.8.6	<i>Poisson's effect A4 80 stainless steel bolt + 5083 O plates</i>	90
3.8.7	<i>Poisson's effect A4 80 stainless steel bolt + 6082T6 plates</i>	92
3.8.8	<i>Comparison material combinations</i>	94
3.9	CASE STUDY	96
3.9.1	<i>Bolt and joint characteristics</i>	96
3.9.2	<i>5083O + M16 A4 80 bolt</i>	98
3.9.3	<i>6082T6 + M16 A4 80 bolt</i>	100
3.10	SUMMARY AND CONCLUSIONS ANALYTICAL MODELLING	102
4	EXPERIMENTAL VERIFICATION	104
4.1	INTRODUCTION	104
4.2	LOAD CELL APPLICATION AND PROPERTIES	105
4.2.1	<i>Load Cell dimensions and properties</i>	106
4.2.2	<i>Comparison Load Cell output and calibrated Instron system</i>	108
4.3	PLATE SURFACE CONDITIONS.....	110
4.4	RELATIONSHIP TORQUE – BOLT FORCE.....	111
4.4.1	<i>Relationship A4 80 M16x110</i>	112
4.4.2	<i>Relationship A4 80 M20x100</i>	114
4.5	CREEP EXPERIMENT ALUMINIUM.....	116
4.6	RELAXATION EXPERIMENTS WITH LOAD CELL METHOD.....	120
4.6.1	<i>Load Cell relaxation experiment 1 (P = 63 kN = 0.7F_p)</i>	120
4.6.2	<i>Load Cell relaxation experiment 2 (P = 82 kN = 0.9F_p)</i>	125
4.6.3	<i>Load Cell relaxation experiment 3 (P ≈ 32 kN = 0.34F_p)</i>	127
4.6.4	<i>Load Cell relaxation experiment 4 (P ≈ 85 kN = 0.9F_p)</i>	129
4.7	RELAXATION EXPERIMENTS WITH STRAIN GAUGE METHOD.....	131
4.7.1	<i>Stress – strain behaviour 316 (A4) bolt material</i>	131
4.7.2	<i>Calibration of bolts equipped with strain gauge</i>	135
4.7.3	<i>Strain gauge relaxation experiment 5 (P ≈ 32 kN = 0.34F_p)</i>	139
4.7.4	<i>Comparison Load Cell method with Strain Gauge method</i>	141
4.8	TENSILE TEST INTRODUCING POISSON'S EFFECT	142
4.8.1	<i>Tensile test M16x75 monitored with Load Cell</i>	145
4.8.2	<i>Tensile test M16x110 monitored with Load Cell</i>	146
4.8.3	<i>Tensile test M16x75 monitored with Strain Gauge</i>	147
4.8.4	<i>Tensile test M16x110 monitored with Strain Gauge</i>	149
4.9	SUMMARY AND CONCLUSIONS EXPERIMENTAL VERIFICATION	152
5	CONCLUSIONS AND RECOMMENDATIONS	153
5.1	MAJOR CONCLUSIONS	153
5.2	DESIGN AND SERVICE RECOMMENDATIONS	154
5.3	FUTURE RESEARCH RECOMMENDATIONS	155
6	BIBLIOGRAPHY	156
ANNEX A.1	LITERATURE REVIEW GASKET CREEP	158
ANNEX B.1	SPECIFICATIONS BOLTSAFE LOAD CELL	160
ANNEX B.2	TABLE OF DIMENSIONS BOLTSAFE LOAD CELL	161

1 Introduction

Preloaded bolts are used in joints where the load is reversal, high stress ranges will develop or if slip of the adjacent members needs to be prevented. The preload force in a bolt can be defined as a tension load introduced during the tightening process of a bolt set. Several advantages of using preloaded bolts are (Steel Industry 2010):

- rigidity of joints and (often) higher static resistance
- reduction or nullify loosening of bolts due to vibrations
- better fatigue performance

However, the preload force has to be sufficient to guarantee above mentioned aspects during service life, but also has to be low enough to guarantee that overloading during tightening and service life will not be a problem. Overloading during tightening is a well-known phenomenon and occurs due to the application of torque when turning the nut. Theoretically, overloading in service life can also occur due to thermal expansion of the plate material and due to the Poisson's effect behavior. Overall, the preload level will fluctuate due to the following time-dependent and time-independent effects (Kassner, Smith, and Campbell 2015; Nijgh 2016):

Time-dependent effects:

- embedment creep
- gasket creep
- plate creep
- stress relaxation

Time-independent effects:

- thermal effects
- elastic interactions
- poisson's effect

EN 1993-1-1, EN 1999-1-1 and NEN-EN 1090-2 allow 8.8 and 10.9 (carbon) steel bolts to be preloaded. However, the application of stainless steel bolts is not allowed unless otherwise specified (NEN-EN 1090-2 2018). In a collaboration between the Eindhoven University of Technology and Bayards, this research will qualify and quantify the above mentioned topics with research conducted in the past, calculations, and tests to be able to predict the fluctuating preload level of preloaded (stainless) steel bolts in aluminium/steel joints.

The master thesis will focus on answering the following questions: **what are the main short- and long term (qualitative and quantitative) consequences of the time-dependent and independent effects on the preload force in aluminium/steel joints combined with preloaded (stainless) steel bolts and what is the impact of the initial preload force, the total thickness of the joint, and the bolt diameter (i.e. considering joint design) on the remaining preload force if the bolted joint is subjected to time-dependent and time-independent influences?**

2 Literature review

2.1 Introduction

Research conducted in the past can be used to gain insight in the importance of the topics listed in the introduction. The topics regarded during the literature review include:

- embedment creep
- plate creep
- stress relaxation
- thermal effects
- elastic interactions
- poisson's effect

As mentioned in the introduction in section 1, creep and relaxation are time-dependent effects. Creep can be explained as an increasing deformation under constant loading which can be observed in plates and surfaces. Relaxation is related to creep and can be defined as a decreasing stress under a constant deformation or strain which can be discovered in the bolts.

Embedment creep of stainless steel bolted assemblies will be reviewed in section 2.2. The quantitative impact of embedment creep in aluminium joints has not been reported in literature. However, this type of creep will occur in any material combination as will be exemplified in section 2.2. Plate creep can lead to preload losses if the plate material is susceptible to creep. Under specific circumstances, creep deformation can be introduced in aluminium plates. Section 2.3 will summarize the completed research regarding aluminium creep. Plate creep in carbon and stainless steel joints is reported to be negligible (Afzali et al. 2017) and is therefore not regarded in this literature review. Stress relaxation of stainless steel has received more attention in literature compared to the other topics. Next to an introduction regarding the chemical composition and mechanical behaviour of stainless steel, three completed studies are reviewed in section 2.4.

The time-independent effects include thermal effects, elastic interactions and poisson's effect. Thermal variations can be observed in connections with hybrid material combinations. A FEM-research regarding a joint with an aluminium plate and a steel plate connected by a carbon steel bolt is added in section 2.5. During the tightening process of a bolted assembly, adjacent bolts can be affected by the induced preload force of the bolted assembly. An elaborate study reviewing the impact of bolt spacing, thickness of the joint material, the type of joint material, diameter of the bolt hole, and outer diameter of the washer is added in section 2.6. A research regarding the impact of poisson's effect is reviewed in section 2.7. The research includes a FEM-analysis and test results of an aluminium joint with a preloaded stainless steel bolt subjected to a tensile longitudinal loading.

Insulation or gaskets are mainly used at the transition of a steel to aluminium to avoid galvanic corrosion. Gasket creep, or creep of the insulation, can have a negative effect on the preload level depending on the material type of the gasket. However, the majority of aluminium/steel joints combined with (stainless steel) bolts are applied without a gasket or isolation. Therefore, gasket creep is excluded as a main topic of this research. Literature studying gasket creep is added in Annex A.1. The literature review is completed with a summary and conclusions which can be found in section 2.8.

2.2 Embedment creep

Threads of bolts, nuts and surfaces of washers and plates, even with a high rate of finish, are never perfectly flat. Under a microscope a rough surface with hills and valleys can be distinguished instead of a smooth surface. When load is introduced in a joint, these high spots will be the first locations where load is transferred and since this initial contact is relatively small, plastic deformation occurs until a more or less stable situation is obtained when enough surface is used to prevent further plastic deformation. The process of settling of imperfections is called embedment creep or embedment relaxation (Brown et al. 2008). Embedment creep occurs at adjacent surfaces (illustrated in figure 2.2.1) between:

- Nut/bolt head – Washer
- Washer – Plate
- Plate – Plate
- Nut thread – bolt thread

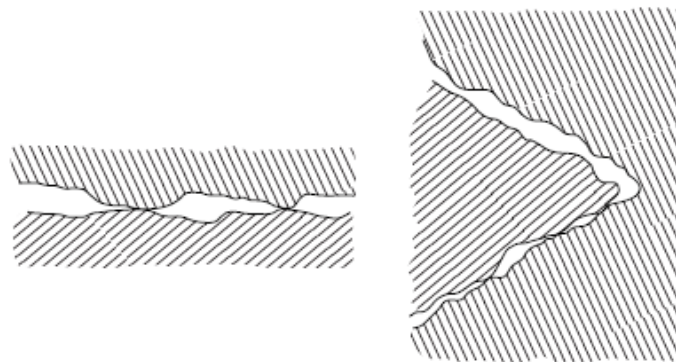


Figure 2.2.1: Imperfections on threads and other contact surfaces (Blatt 2003)

Embedment relaxation is a short term relaxation (Jaglinski et al. 2007) and is defined as localized plastic deformation due to small material imperfections on thread contact surfaces. A great variation of relaxation is experienced, depending on the condition of the parts, finishes, initial and local tension levels and fit of parts. A study into the amount of embedment to be expected in a $\frac{3}{4}$ x 6 inch A325 bolt-heavy nut bolt assembly with two $\frac{3}{4}$ -inch A7 steel plates (Chesson 1964) reports a 2 – 11% loss of preload immediately after tightening. The quantity of embedment creep can be further influenced by construction errors and design choices. These aspects will be discussed in more detail.

2.2.1 Construction errors

The contact area between nut and bolt thread can be insufficient when a bolt is undersized or a nut is oversized which leads to plastic deformation / embedment creep, as shown in figure 2.2.2. This problem can be addressed by applying appropriate bolt-nut combinations.

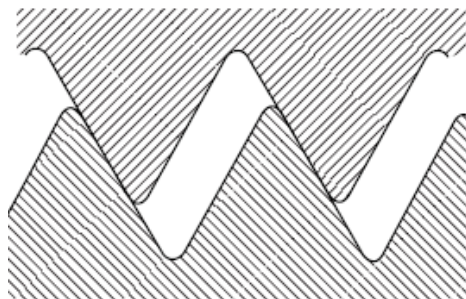


Figure 2.2.2: poor thread engagement (Blatt 2003)

Next to errors made during the selection of bolt- nut combinations, errors can be made during the preparation of the joint. A bolt can be bended when tightened, leading to peak stresses on one side of the plate exceeding the yield strength. This effect is also present when the bolt shaft is not placed perfectly straight in the bolt hole or when the bolt hole is under- or oversized, as shown in figure 2.2.3.

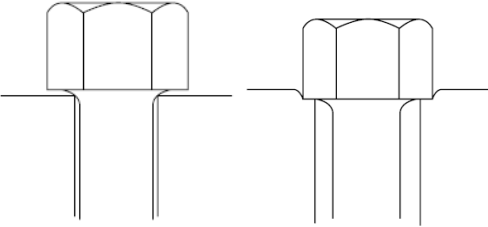


Figure 2.2.3: undersized hole (left) and oversized hole (right) (Blatt 2003)

2.2.2 Positive design choices

Adding bushings (figure 2.2.4) or using thicker plates can have a positive effect on the total loss of preload. Preload loss is proportional to the length of a bolt. Using a longer bolt and increasing the clamping length of a bolt in a joint will result in relatively less relaxation than by using the minimum required bolt length. The effects of embedment in adjacent surfaces discussed before will be equal. However, by using a longer bolt the total embedment deformation will be a smaller percentage of the clamping length resulting in less preload loss. On the other hand, increasing the number of surfaces by using extra plates (e.g. in double shear joints) can have a negative effect due to additional plate – plate embedment creep.

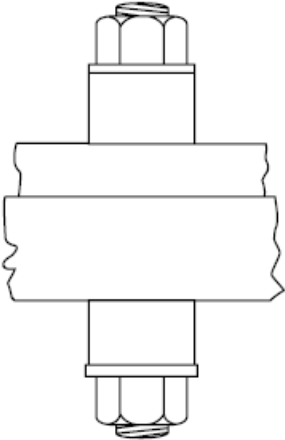


Figure 2.2.4: added bushings to increase clamping length (Blatt 2003)

2.3 Stress relaxation stainless steel

2.3.1 Time-independent properties stainless steel

Stainless steel distinguishes itself from carbon steel by its greatly increased corrosion resistance resulted by the addition of a minimum quantity of 10.5% chromium and limiting the content of carbon to a maximum of 1.2%. The differentiation of the chemical composition results in the formation of microstructures that do not usually occur in carbon steels and is the main influencing factor on the physical and mechanical properties of stainless steel (Tylek 2014). Structural stainless steel can be divided into 4 categories distinguished by the microstructure and chemical composition: austenitic, martensitic, ferritic, and austenitic-ferritic (or duplex) stainless steel (SSINA 2000).

Type of stainless steel	Chemical composition [wt%]			
	C (max)	Cr	Ni	Mo
Ferritic	0.03–0.08	10.50–18.00	0–1.00	–
Austenitic	0.02–0.08	16.50–21.00	6.00–26.00	0–7.00
Austenitic-ferritic	0.03	21.00–24.00	3.50–6.50	0.10–3.50

Table 2.3.1: Chemical composition ranges for structural stainless steels (Tylek and Krzysztof 2014)

Type of stainless steel	Grade of stainless steel	Hardness HB ¹⁾ max	0.2% proof strength $R_{p0.2}$ [MPa] min.	Tensile strength R_m [MPa]	Elongation after fracture A [%] (long.)
Ferritic	1.4003	100	260	450–600	20
	1.4016	100	240	400–630	20
Austenitic	1.4307	215 ²⁾	175	500–700 ²⁾	45
	1.4306	215 ²⁾	180	460–680 ²⁾	45
	1.4311	230 ²⁾	270	550–760 ²⁾	40
	1.4301	215 ²⁾	190	500–700 ²⁾	45
	1.4541	215 ²⁾	190	500–700 ²⁾	40
	1.4404	215 ²⁾	200	500–700 ²⁾	40
	1.4406	250 ²⁾	280	580–800 ²⁾	40
	1.4401	215 ²⁾	200	500–700 ²⁾	40
	1.4571	215 ²⁾	200	500–700 ²⁾	40
	1.4432	215 ²⁾	200	500–700 ²⁾	40
	1.4435	215 ²⁾	200	500–700 ²⁾	40
	1.4439	250 ²⁾	280	580–800 ²⁾	35
	1.4539	230 ²⁾	230	530–730 ²⁾	35
	1.4547	260 ²⁾	300	650–850 ²⁾	35
1.4529	250 ²⁾	300	650–850 ²⁾	40	
Austenitic-ferritic	1.4462	270	450	650–880	25
	1.4362	260	450	600–830	25

¹⁾ Only for guidance
²⁾ The maximum HB-values may be raised by 100 HB or the tensile strength value may be raised by 200 MPa and the minimum elongation value may be lowered to 20% for sections and bars of ≤ 35 mm thickness having a final cold deformation and for hot formed sections and bars of ≤ 8 mm thickness.

Table 2.3.2: Mechanical properties of stainless steel in the annealed condition at room temperature (Tylek and Krzysztof 2014)

The effect of cold work highly affects the properties of stainless steel, therefore different properties can be expected for stainless steel fasteners as compared to non-worked plates. Generally, work hardening of stainless steel results in higher proof and tensile strength. Next to that, elongation at fracture is decreased. The effects of cold work on austenitic stainless steel are shown in figure 2.3.1 and mechanical properties of stainless steel fasteners are presented in table 2.3.3.

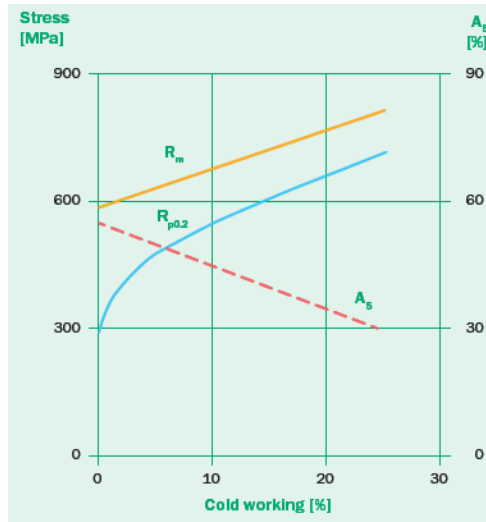


Figure 2.3.1: Effect of cold work on an austenitic stainless steel (Outokumpu 2013)

Table 3 MECHANICAL REQUIREMENTS FOR STAINLESS STEEL BOLTS, SCREWS, STUDS AND NUTS (ASTM F593-91)

GRADE ¹	GENERAL DESCRIPTION	MECHANICAL REQUIREMENTS							
		BOLTS, SCREWS AND STUDS					NUTS		
		FULL SIZE BOLTS, SCREWS, STUDS		MACHINED TEST SPECIMENS OF BOLTS, SCREWS, STUDS			HARDNESS ROCKWELL Min	PROOF LOAD STRESS ksi	HARDNESS ROCKWELL Min
		YIELD ² STRENGTH min ksi	TENSILE STRENGTH min ksi	YIELD ² STRENGTH min ksi	TENSILE STRENGTH min ksi	ELON-GATION ³ % Min			
303-A 304-A	Austenitic Stainless Steel-Sol. Annealed	30	75	30	75	20	B75	75	B75
304 305 316 384 XM7*	Austenitic Stainless Steel-Cold Worked	50	90	45	85	20	B85	90	B85
305-A 316-A 384-A XM7-A*	Austenitic Stainless Steel-Sol. Annealed	30	75	30	75	20	B70	75	B70
304-SH 305-SH 316-SH	Austenitic Stainless Steel-Strain Hardened	See Note 6	See Note 6	See Note 6	See Note 6	15	C25	See Note 6	C20
410-H 416-H	Martensitic Stainless Steel-Hardened and Tempered	95	125	95	125	20	C22	125	C22
410-HT 416-HT	Martensitic Stainless Steel-Hardened and Tempered	135	180	135	180	12	C36	180	C36
430	Ferritic Stainless Steel-	40	70	40	70	20	B75	70	B75

Table 2.3.3: mechanical properties of stainless steel in the annealed condition at room temperature (SSINA 2000)

The stress-strain behavior of stainless steel is different from carbon steel. Carbon steel has an elastic branch followed by a yield plateau with strain hardening. Stainless steel, however, behaves non-linear even with low stresses. The stress-strain relationship of non-linear materials can be described with the Ramberg-Osgood stress-strain relationship (NASA Scientific and Technical Information Facility 1965):

$$\varepsilon = \frac{\sigma}{E} + K \left(\frac{\sigma}{E} \right)^n$$

$$K = \frac{0.002}{\left(\frac{f_{0.2}}{E} \right)^n}$$

Nonlinearity of the stress-strain relationship is characterized by the coefficient n . The larger the coefficient n , the more nonlinearity of the stress strain relationship can be observed. This typical behaviour is shown in figure 2.3.2, where stainless steel is compared with carbon steel.

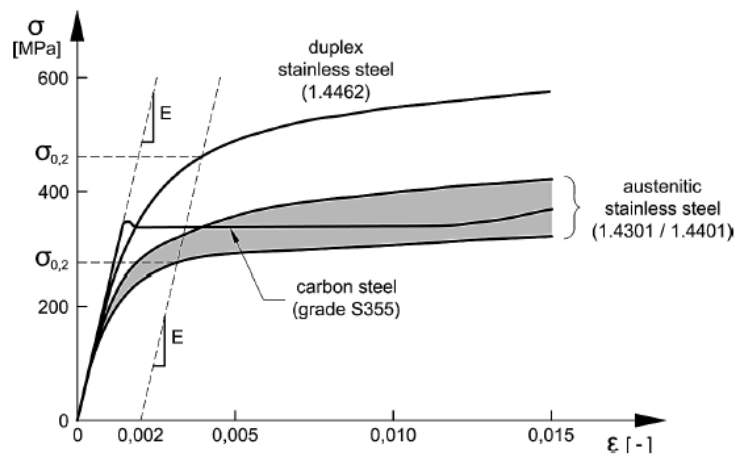


Figure 2.3.2: Typical experimental stress-strain curves of carbon and stainless steel (Tylek 2014)

2.3.2 Time-dependent properties stainless steel

Stainless steel is susceptible to stress relaxation and/or creep. According to C.N. Krapf (Krapf 2010), stress relaxation is a time-dependent phenomenon that occurs in viscoelastic and viscoplastic materials. When a material is subjected to a constant total strain (or deformation), stresses in the material gradually decreases (or relaxes) with time due to viscoplastic behaviour. This behaviour is illustrated in figure 2.3.3. The total strain ϵ_t can be divided into elastic strain ϵ_e and plastic strain ϵ_p . The decreasing stress can be explained with the appearance of plastic strain within the material. This plastic strain can be defined as creep and is equal to the loss of elastic strain and subsequently the loss of stress in the object.

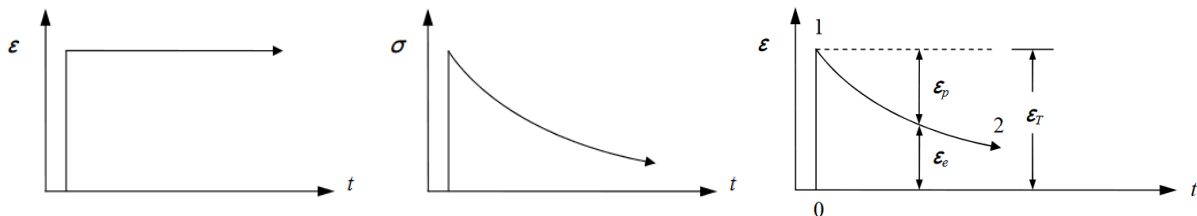


Figure 2.3.3: stress relaxation behaviour (left and middle); strain behaviour with time (right) (Krapf 2010)

2.3.3 Relaxation experiments Krapf

Krapf used an analytical model composed by Liu and Krempl to describe viscoplastic stress relaxation in stainless steel rods. The model could predict long-term stress relaxation behavior and creep behaviour for a given material at any arbitrary initial design strain based on short-term stress relaxation tests. Krapf validated the model with experiments containing 304/304L austenitic stainless steel rods. Smooth rods were used instead of threaded rods to be able to focus the research on the material behavior only instead of taking into account local stress concentrations at the grooves. The experimental results were compared with the analytical model and are plotted in figure 2.3.4.

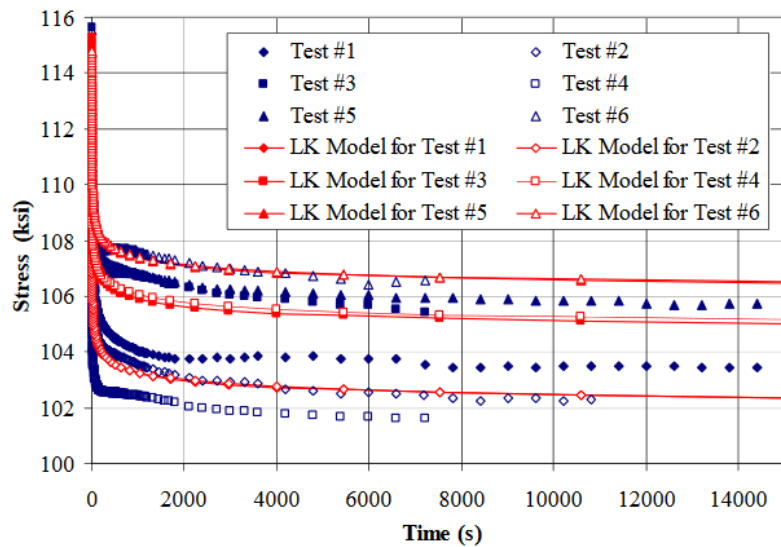


Figure 2.3.4: Comparison of the Liu and Krempl (LK) model predictions with experimental data (Krapf 2010)

The model predicts an approximate stress loss of 10 % in 50 years, with 80% of this stress loss occurring in the first hour of constant straining with initial stress values above $0.9f_u$. Krapf suggests a limiting design strength of $0.6f_u$ to ensure that relaxation will not be a problem for the intended purpose.

2.3.4 Relaxation experiments Hradil

Hradil presented a study titled: ‘Numerical modelling of stainless steel preloaded bolted connections’ (Hradil 2017). The focus was the development of material models and finite element models for bolt assemblies based on an extensive experimental study of creep relaxation and tension effects on austenitic, ferritic, duplex and lean duplex steel plates and bars for different loading rates . Hradil makes use of a material model (composed by Chaboche) within FEM software to predict the room temperature creep of stainless steel. The model and mesh are shown figure 2.3.5.

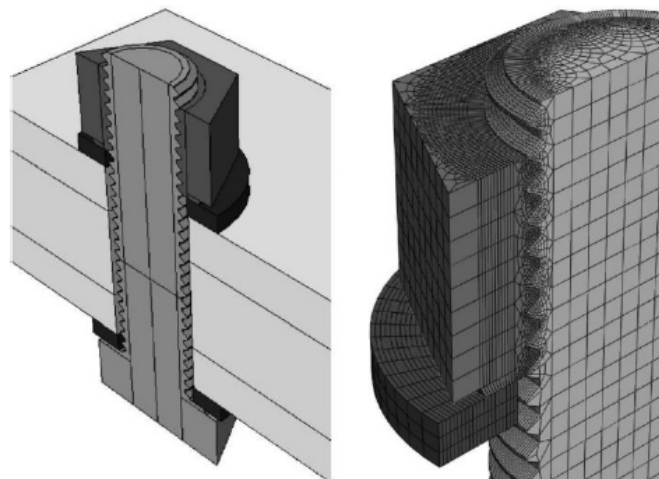


Figure 2.3.5: The 3D model of a M16 bolt assembly (left) and its mesh (right) (Hradil 2017)

The material parameters were identified with tensile tests with various constant loading rates ($1 \cdot 10^{-2} - 1 \cdot 10^{-7} \text{ s}^{-1}$) and creep tests with different stress levels (84 – 336 MPa). The material model was implemented in FEM-software and compared with relaxation tests containing various constant strains (0.09 - 2.17%). The material model was based on the viscoplastic behaviour of stainless steel, embedment effects were not regarded. The comparison of the material model within FEM-software and a relaxation test with a loading rate of $1 \cdot 10^{-4} \text{ s}^{-1}$ can be seen in figure 2.3.6. The impact of the

initial preload level on bolts composed of 1.4436 stainless steel can be found in figure 2.3.7 (right). It can be discovered that stainless steel bolt material is susceptible to relaxation at medium and high initial stress levels. According to figure 2.3.8, relaxation appears to reoccur after retightening the bolt. Therefore, retightening the bolt appears to have a minimal effect on the reduction of preload losses.

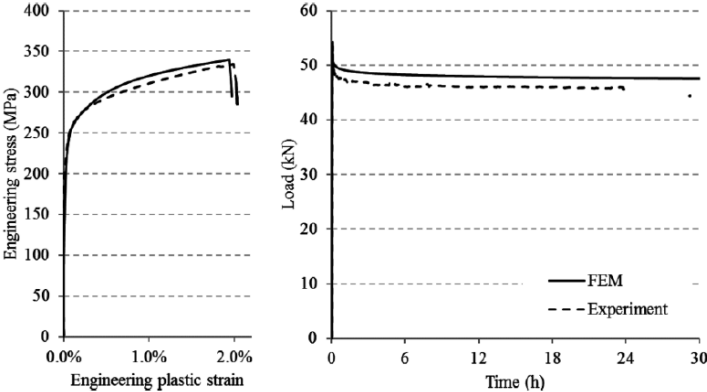


Figure 2.3.6 Example of validation of the material model against relaxation test (right) and its loading phase (left) for EN 1.4404 (316L) austenitic stainless steel at strain level of 2.17% (Hradil 2017)

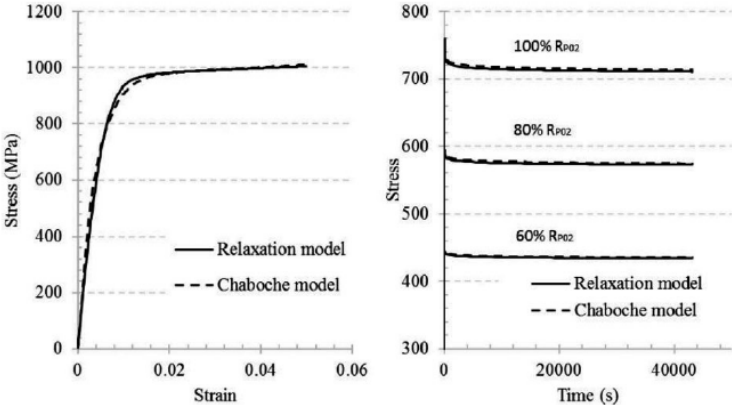


Figure 2.3.7: Comparison of Chaboche and strain hardening relaxation model for austenitic 1.4436 bolt material (Hradil 2017)

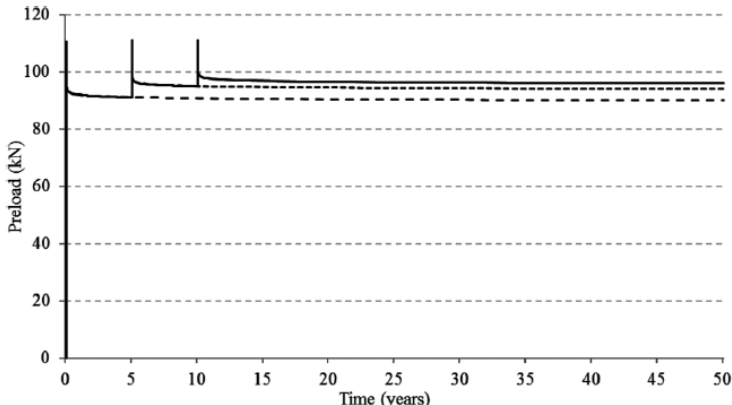


Figure 2.3.8: Loss of preload in models without retightening (dotted line) and models with retightening after 5 years (dashed line) and 5 and 10 years (solid line) (Hradil 2017)

Hradil performed experiments of austenitic stainless steel plates with grit-blasted surface finish jointed by stainless steel M16 bolts preloaded up to 110 kN used in slip resistant bolted joints. Preload losses up to 12% were observed. The duration length of the tests was not reported.

2.3.5 Relaxation experiments Afzali

Relaxation of stainless steel and carbon steel bolted joints was experimentally investigated by Afzali in the frame of the European RFCS-research project 'Execution and reliability of slip resistant connections for steel structures using CS and SS (SIROCO)'. The goal of the research was to find the effect of viscoplastic behaviour of stainless steel in bolted assemblies. Two types of test samples were developed, both containing M16 and M20 bolts. The samples are visualized in figure 2.3.9.

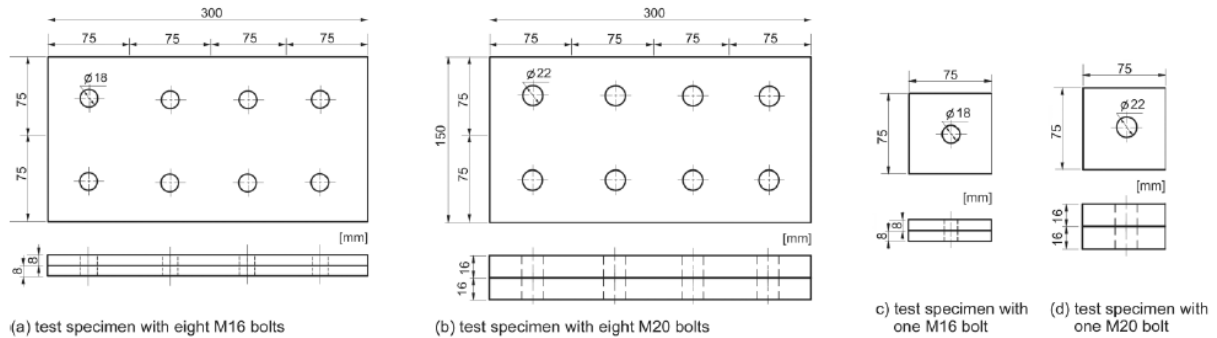


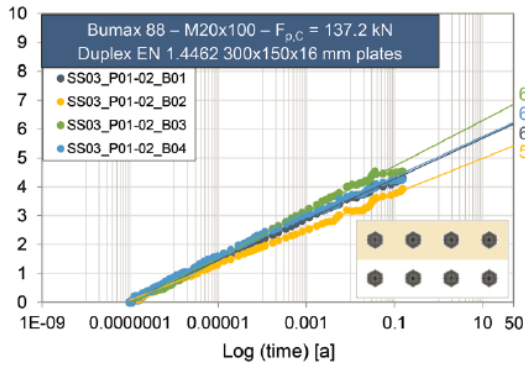
Figure 2.3.9: The test specimen geometry for relaxation test (Afzali et al. 2017)

The stainless steel bolts used during the tests were M20x75 HV 10.9, M16x100 A4 Bumax 88 / 109 and M20x100 A4 Bumax 88. The bolts were loaded up to 70% of the ultimate strength of the tensile stress area of the bolt. The selection of used stainless steel plates consists of austenitic, ferritic, duplex and lean-duplex with a 1D surface condition and did not gain surface treatment before practical use. To clean the carbon steel plates from any rust, the surfaces were shot blasted. The observed preload losses and a 50 year extrapolation assuming a logarithmic preload loss behaviour are presented in table 2.3.4 and figures 2.3.10 and 2.3.11.

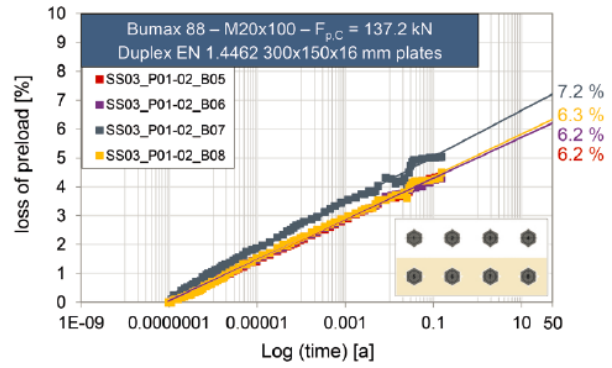
	Specimen ID ¹⁾	Number of tests	Σt^2 [mm]	$\Sigma t/d$ [-]	Bolt material	Clamped plates		Surface condition	Loss of preload		
						Type of material	Thickness [mm]		measured after	after 50 years (extrapolated)	
											days - min / max [%]
Carbon steel	HV-bolts - M20 x 75										
	CS	2	48	2.4	HV-bolt Class ³⁾ 10.9	Carbon steel	20	Shot blasted	68 - 5.2 / 8.1	7.8 / 10.5	
Stainless steel	Bumax 88 - M20 x 100										
	SS01	12	75	3.75	Bumax 88	Austenitic EN 1.4404	16	1D	14 - 3.7 / 6.0	6.0 / 8.7	
	SS02	12				Ferritic EN 1.4005			14 - 3.4 / 4.7	5.3 / 7.5	
	SS03	8				Duplex EN 1.4462			55 - 3.9 / 5.0	5.4 / 7.2	
	SS04	3				Lean Duplex EN 1.4162			14 - 4.0 / 4.5	6.4 / 7.1	
	Bumax 88 - M16 x 100										
	SS21	12	59	3.70	Bumax 88	Austenitic EN 1.4404	8	1D	14 - 3.9 / 5.5	6.1 / 8.5	
	SS22	12				Ferritic EN 1.4005			14 - 3.5 / 5.0	5.6 / 7.7	
	SS23	12				Duplex EN 1.4462			14 - 3.9 / 5.8	6.1 / 8.7	
	SS24	3				Lean Duplex EN 1.4162			14 - 4.9 / 5.5	7.3 / 8.5	
	SS26	2			Bumax 109	Austenitic EN 1.4404	14 - 5.7 / 6.6	9.2 / 10.3			
	SS27	2				Ferritic EN 1.4005	14 - 4.2 / 4.9	6.2 / 7.4			
SS28	12	Duplex EN 1.4462				55 - 4.2 / 5.6	6.4 / 8.6				

¹⁾ all bolts were preloaded to the $F_{p,C}$ level ²⁾ clamping length ³⁾ property class

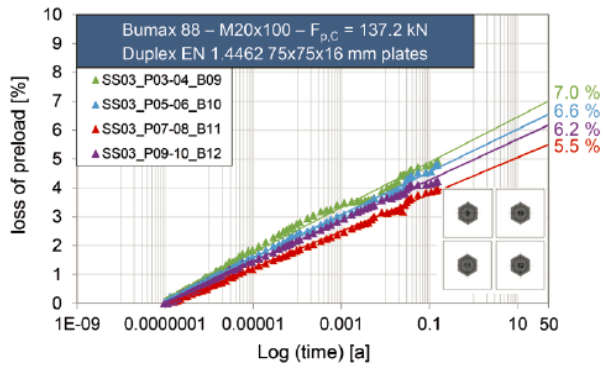
Table 2.3.4: Test matrix for the relaxation tests of bolted assemblies made of carbon and stainless steel (Afzali et al. 2017)



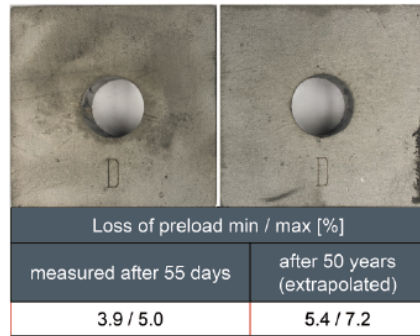
(a) preload losses-log (time) diagrams for eight-bolts specimens – first raw



(b) preload losses-log (time) diagrams for eight bolts specimens – second raw

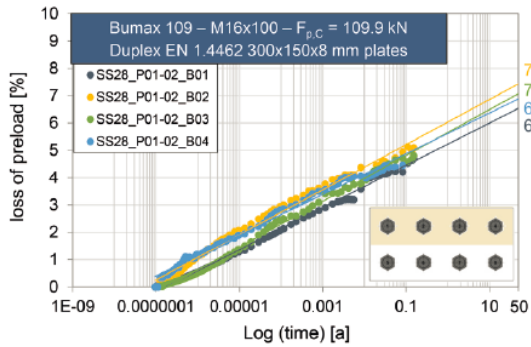


(c) preload losses-log (time) diagrams for four one-bolts specimens

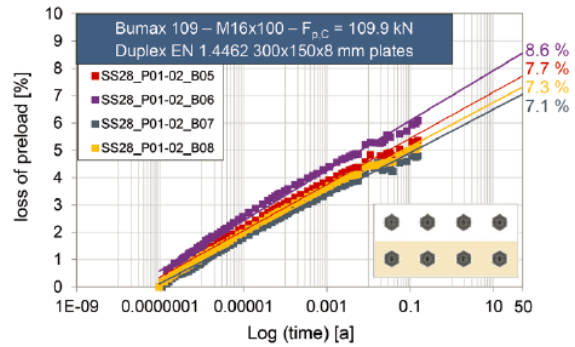


(d) loss of preload 55 days / 50 years

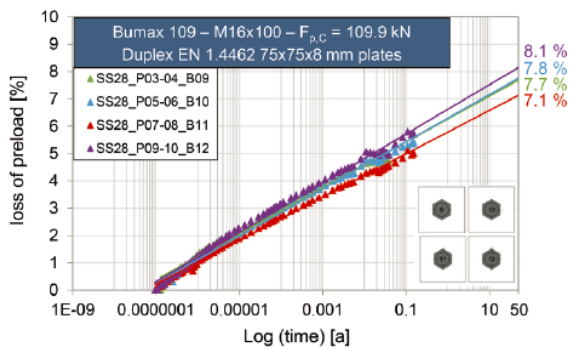
Figure 2.3.10: Preload loss exemplary for Bumax 88 – M20 bolts and Duplex EN 1.4462 plates (Afzali et al. 2017)



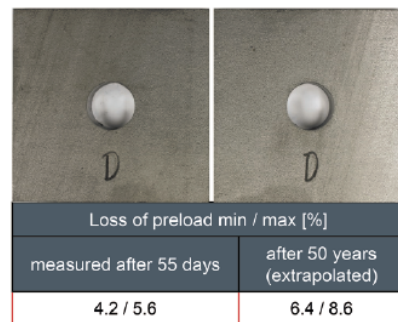
(a) preload losses-log (time) diagrams for eight-bolts specimens – first raw



(b) preload losses-log (time) diagrams for eight bolts specimens – second raw



(c) preload losses-log (time) diagrams for four one-bolts specimens



(d) loss of preload 55 days / 50 years

Figure 2.3.11: Preload loss exemplary for Bumax 109 – M16 bolts and Duplex EN 1.4462 plates (Afzali et al. 2017)

2.4 Plate creep

Joint or plate materials are subjected to a bearing load once a preload force has been introduced. Creep of the plates (or plate creep) occurs if the plate material is susceptible to creep. Comparable with embedment creep, the additional deformation could lead to preload losses. Creep in metals can be divided into three ranges considering the melting temperature of the material T_m (Kassner et al. 2015): high temperature creep acting at $T > 0.6T_m$, intermediate creep ($0.3T_m < T < 0.6T_m$) and low temperature creep ($T < 0.3T_m$). Creep at low temperature has received less attention compared to the other ranges, because materials generally don't fail when subjected to temperatures lower than $0.3T_m$.

Kassner studied short time creep behavior of high-purity aluminium with data provided by Wyatt and Sherby at a temperature of 77 K (-196°C). Logarithmic creep behavior was discovered for various stresses as shown in figure 2.4.1. The yield or proof stress and the type of alloy were not reported.

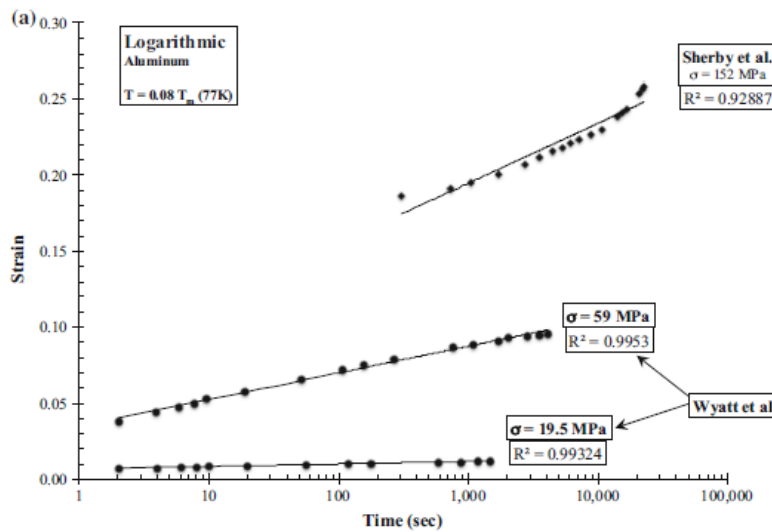


Figure 2.4.1: Low temperature creep behavior of pure aluminium (Kassner et al. 2015)

To give more insight into the effect of occurring stress versus yield stress, the experimental creep data of high purity aluminium (Matsunaga and Sato 2014) are presented in figure 2.4.2. The creep curves were obtained at 300K (27°C).

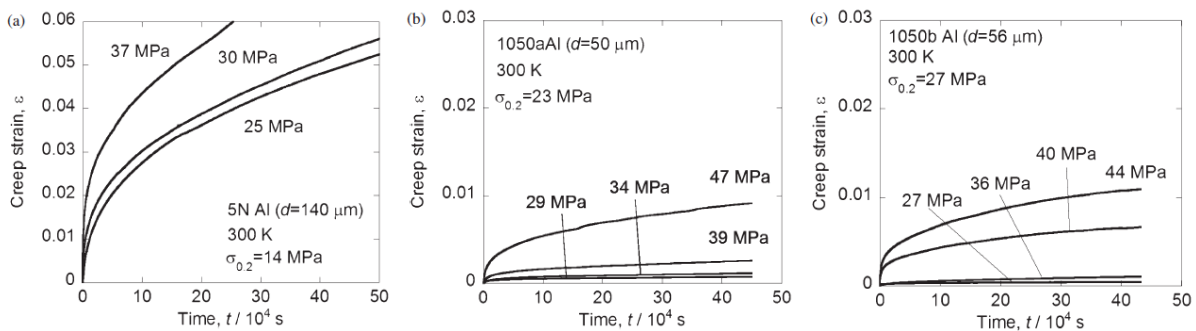


Figure 2.4.2: Examples of creep curves of (a) 5N Al, (b) 1050a Al and (c) 1050b Al at 300K (Matsunaga and Sato 2014)

It can be discovered that low temperature creep in pure aluminium will only be significant at stresses higher than the proof stress ($\sigma > f_0$). Below and at the proof stress, the strain increase at room temperature seems to be insignificant. Matsunaga also states that a larger creep rate is observed with increasing purity, alloying aluminium will therefore result in material less susceptible for low temperature creep at comparable stresses.

Creep behaviour at room temperature of 2024-T3 aluminium alloy was investigated by Deibler (Deibler 2014). A short term test of 10 minutes with three stress levels ($0.24f_y$, $1.20f_y$ and $1.29f_y$) was performed resulting in the creep behaviour presented in figure 2.4.3. The short term data is extrapolated assuming a logarithmic relationship. The approximated amount of creep strain after 10 hours, 1000 hours and 50 years is listed in table 2.4.1. The statement of Matsunaga that decreasing purity results in less significant creep effects seems to be valid since the creep strain of 2024-T3 aluminium does reach 0.01 mm/mm after 50 years where high-purity aluminium needs $40 \cdot 10^4$ seconds to reach 0.01 mm/mm creep strain.

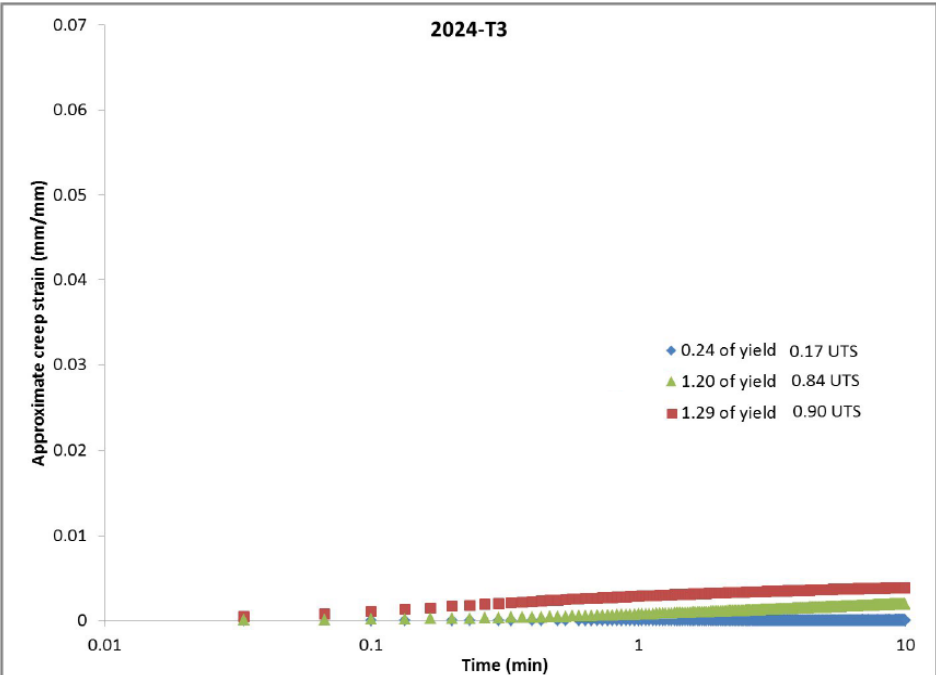


Figure 2.4.3: Creep curves from a 2024 Al sample (Deibler 2014)

Extrapolated creep strain Deibler					
	Stress	Creep strain 10 min	Creep strain 10 hours	Creep strain 1000 hours	Creep strain 50 years
	[MPa]	[-]	[-]	[-]	[-]
0.24 f_y	83	0.00013	0.00025	0.00029	0.00036
1.20 f_y	410	0.00203	0.00379	0.00379	0.00553
1.29 f_y	440	0.00385	0.00719	0.00719	0.01048

Table 2.4.1: Amount of approximated creep strain derived from experiments Deibler

Creep properties of aluminium alloys at various constant temperatures are published by The Aluminium Association and Kaufmann (J.G. Kaufmann 1999). The data is too extensive to be discussed in this literature review. The data corresponding to the alloys considered in the calculations will be discussed in detail in section 3.6.2.

2.5 Thermal effects

When a structure is subjected to temperature variations, the joint will expand or contract. If a joint with a hybrid material combination is used, the expansion or contraction of the parts will vary due to deviating coefficients of thermal expansion. If deformations within a joint are restricted, thermal stresses are introduced. In joints with preloaded bolts, deformations are prevented by the clamping of the preloaded bolt. This can lead to an increase of the bolt force or loss of preload. Subsequently, the friction resistance of the joint will be affected. During a FEM-analysis (Ydstebø 2017), the thermal response of a preloaded bolted connection was discovered. The joint contained M16 8.8 steel bolts and 6082 T6 aluminium / S355 steel plates as indicated in figure 2.5.1. The differences in the coefficients of thermal expansion α_T can be observed in table 2.5.1.

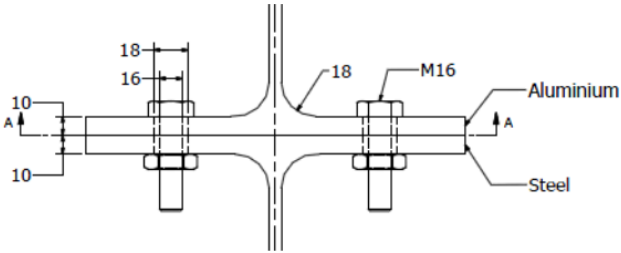


Figure 2.5.1: Aluminium – steel connection (Ydstebø 2017)

Coefficients of thermal expansion steel vs. aluminium				
		S355	6082T6	8.8 bolt
α_T	[mm/mm/°C]	0.0000111	0.000023	0.0000111

Table 2.5.1: Coefficients of thermal expansion steel vs. aluminium (Ydstebø 2017)

At a temperature of -20°C, the joint was preloaded up to 89.3 kN. The temperature was gradually increased and the preload force in the bolt was monitored (figure 2.5.2). The deviations appear to be relatively small; at a temperature of 200 °C ($\Delta T=220^\circ\text{C}$), the preload level was increased by 4.16% compared to the original preload stress.

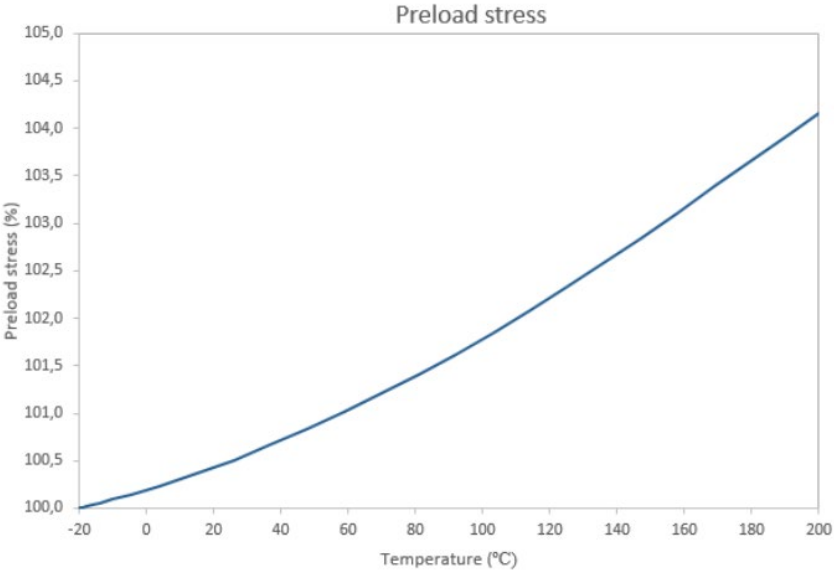


Figure 2.5.2: Percent preload stress vs temperature aluminium – steel connection (Ydstebø 2017)

A FEM analysis is not required for consideration of the thermal variations within a joint. Section 3.7 will demonstrate that a simple calculation model can be used to analyze this topic.

2.6 Elastic interactions

When a bolt is tightened, elastic deformation of the plate material under the bolt head and nut can be expected as shown in figure 2.6.1. The amount of deformation depends on the stiffness of the plate material defined as compression stiffness K_{ii} . (Wang et al. 2017)

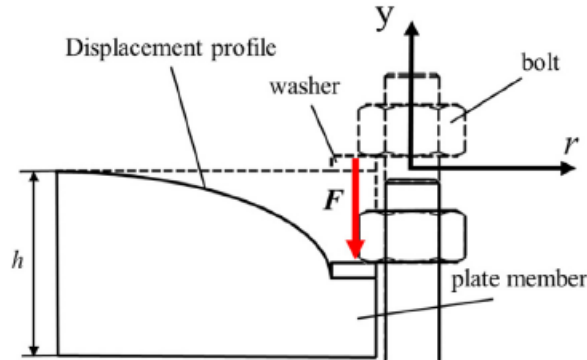


Figure 2.6.1: deformation of plate material (Wang et al. 2017)

When a joint with multiple bolts is used, variation in preloading force will occur due to elastic interaction. Tightening a bolt will affect the preloading force in the neighboring bolts due to the elastic response of the assembled part. The stiffer the joint member, the less variation in preload can be expected. The stiffness is independent of the preloading and is affected only by the structural properties of the joint member and is defined as *elastic interaction stiffness* K_{ij} . The principle of elastic interaction is shown in figure 2.6.2.

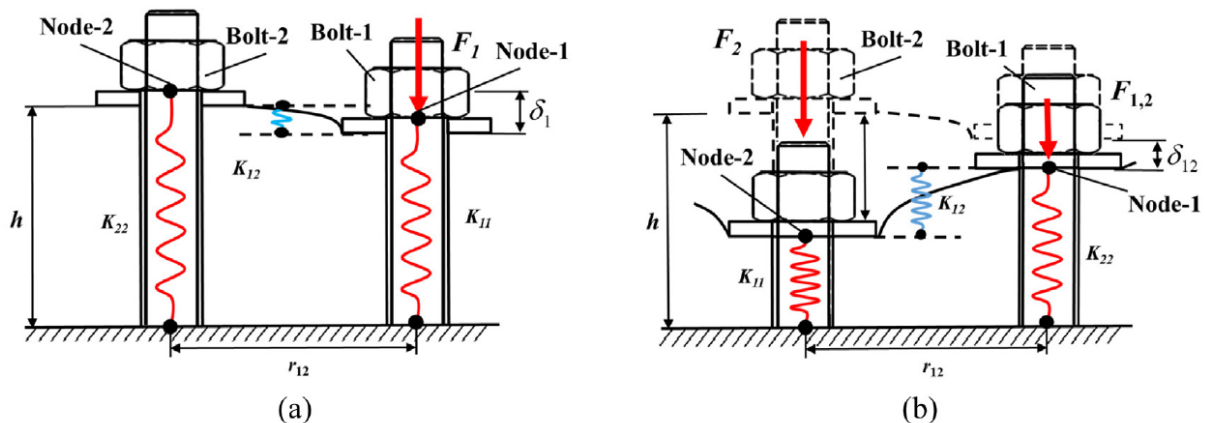


Figure 2.6.2: schematization of elastic interaction between 2 bolts; (a) only tightening bolt-1, (b) tightening bolt -2 sequentially. (Wang et al. 2017)

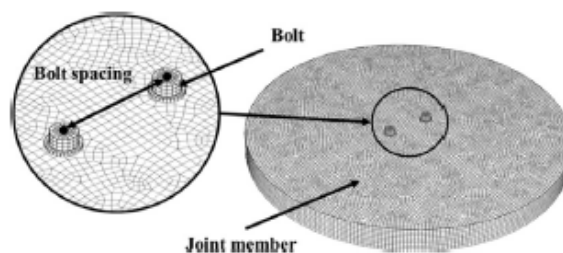


Figure 2.6.3: 3D model of investigated joint (Wang et al. 2017)

Wang conducted an analytical and FE research (visualized in figure 2.6.3) varying bolt spacing, thickness of the joint member, Young's modulus, diameter of the bolt hole and outer diameter of the

washer. The aim of this research was to discover the relationship between the change rate of initial preload in bolt 1 due to tightening of bolt 2. The results of this research are given in figure 2.6.4.

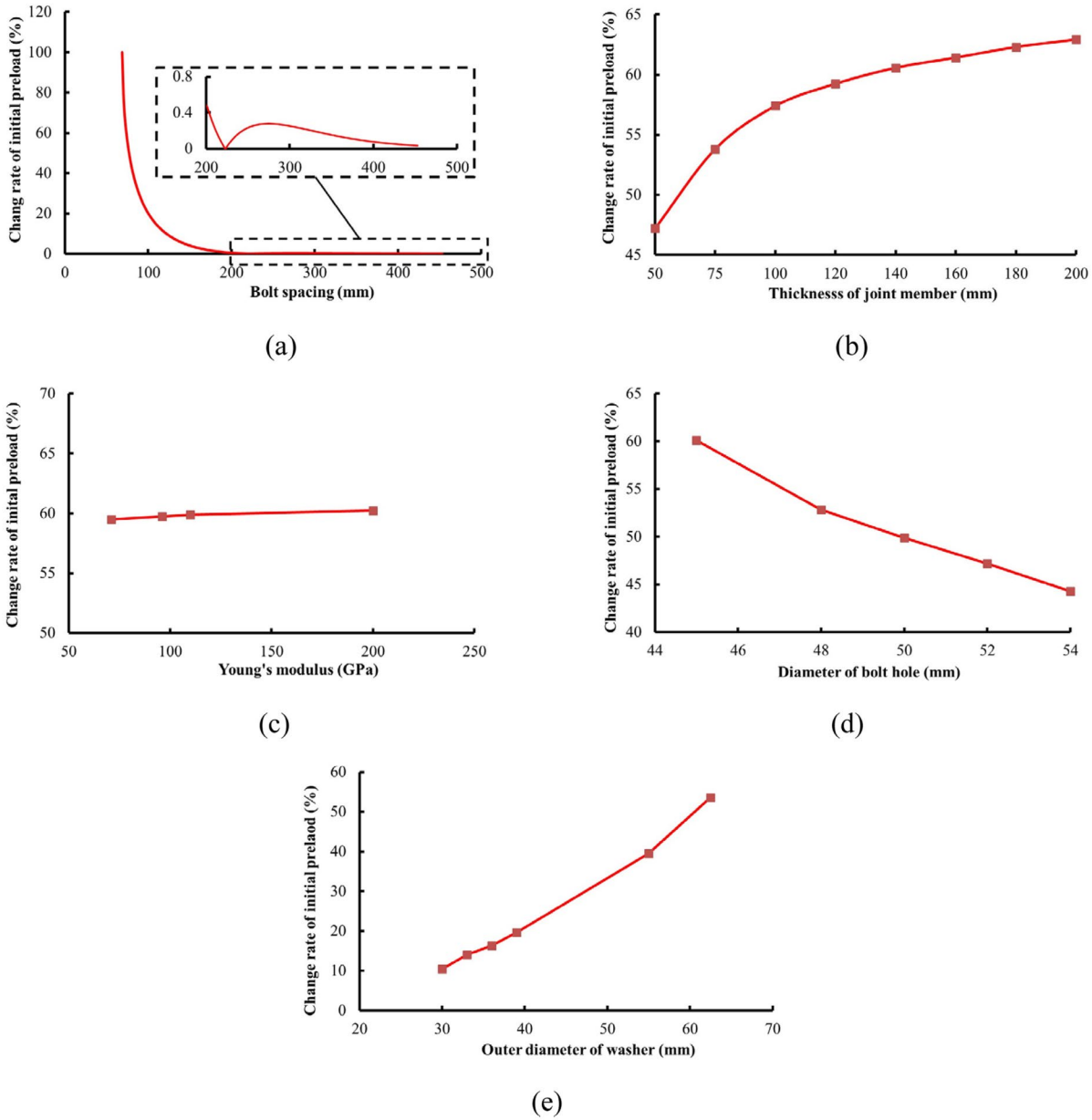


Figure 2.6.4: influence of different factors on preloading force; (a) bolt spacing, (b) thickness of joint member, (c) material of joint member, (d) diameter of bolt hole, (e) outer diameter of washer (Wang et al. 2017)

Bolt spacing, thickness of the joint member, diameter of the bolt hole and diameter of the washer have a significant effect on the elastic interaction, as can be concluded from figure 2.6.4. The plate material, however, has no effect on the preload variation.

2.7 Poisson's effect

Loss of preload force due to contraction of the clamped package occurs in lap joints subjected to longitudinal loading. Tensile force in a member leads to elongation of the member and contraction of the member thickness caused by the Poisson's effect behaviour shown in figure 2.7.1. Compressive force on the other hand lead to shortening and expansion of the material thickness.

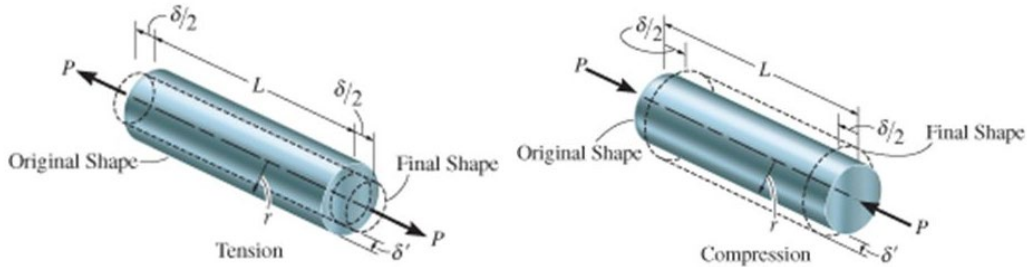


Figure 2.7.1: Poisson's effect (Chaudhari 2015)

T.N. Chakherlou conducted an experimental and numerical research (Chakherlou et al. 2012) to discover the variation of clamping force in lap-joints subjected to tensile longitudinal loading. Tests were carried out on an aluminium 2042-T3 double lap shear joint with 2 stainless steel bolts M6, indicated in figures 2.7.2 and 2.7.3.

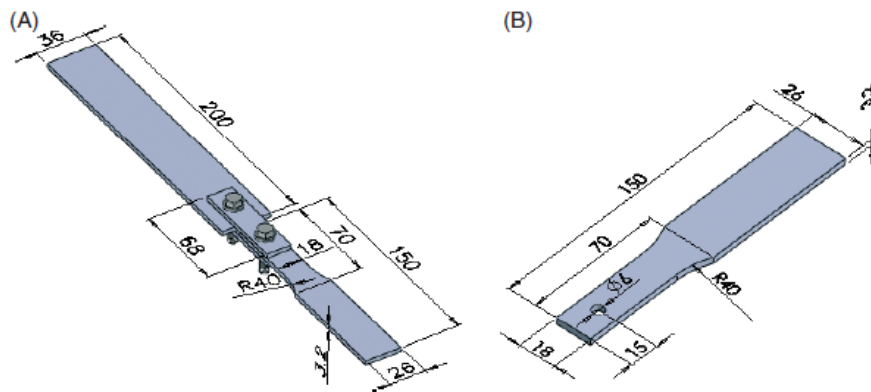


Figure 2.7.2: Dimensions of the joint used for tests in [mm] (Chakherlou et al. 2012)

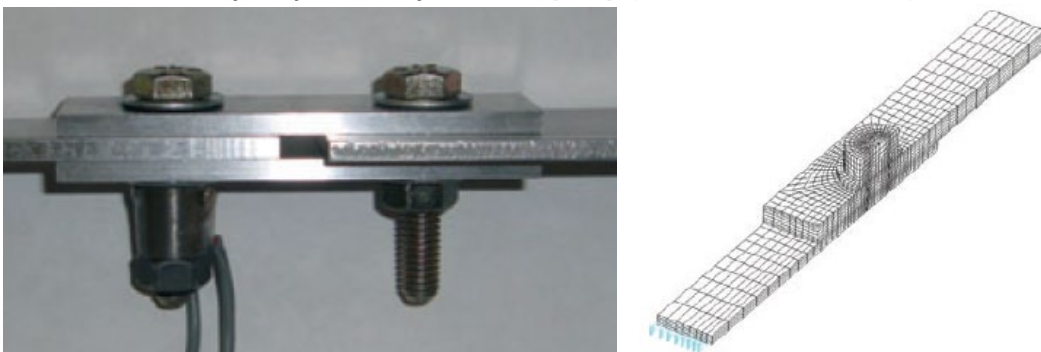


Figure 2.7.3: Test setup joint with load cell (left) and numerical research (right) (Chakherlou et al. 2012)

The tensile longitudinal force was gradually increased and the tensile force in one bolt was monitored with a load cell. Two levels of tightening torques, 2 Nm and 4 Nm, were applied to represent two levels of preload force ($\pm 1.3 \text{ kN}$ ($\approx 0.06 \cdot f_u$) and $\pm 2.7 \text{ kN}$ ($\approx 0.13 \cdot f_u$) respectively). The low initial preload level is not comparable to the required preload levels in friction-resistant joints, where bolts are preloaded up to 70% of the ultimate strength. However, since no additional research is available regarding this topic, this research is added to be able to gain insight in the preload behaviour if Poisson's effect is present. The results of the experimental test and numerical simulation are plotted in figures 2.7.4 and 2.7.5.

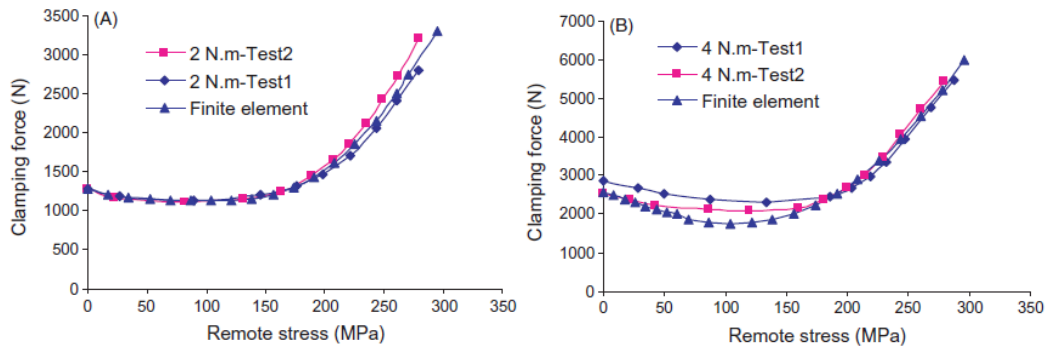


Figure 2.7.4: Variation of clamping force versus remote stress obtained from finite element modelling and experiments (A) for 2 Nm (B) for 4 Nm tightening torques (Chakherlou et al. 2012)

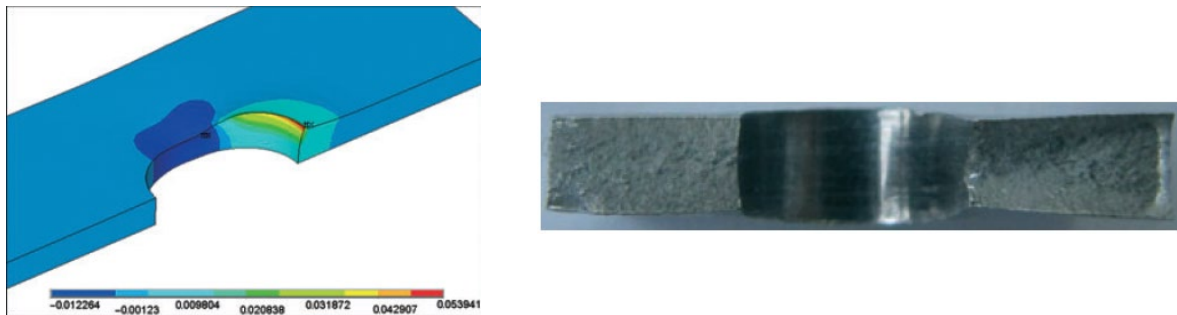


Figure 2.7.5: Plastic strain contours in direction of plate thickness for the initial tightening torque of 4 Nm and tensile remote load of 17 kN (left) and Fractures section of the main plate demonstrating large plastic deformation at the hole edge (right) (Chakherlou et al. 2012)

As can be observed, longitudinal tensile force will indeed lead to preload loss due to poisson’s effect. However, the clamping force will increase rapidly when the tensile force in longitudinal direction is increased. This effect is caused by plastic deformation at the end of the bolt hole caused by bolt bending and will result in expansion of the plate thickness due to Poisson’s effect. This phenomena is present when slip is occurring in the clamped part. The slip that could occur was rather small due to the use of an almost perfect-fit joint (bolt diameter: 5.9 mm; bolt hole diameter 6.0 mm). Chakherlou also investigated the ratio of the longitudinal force between friction and bearing, shown in figure 2.7.6. It can be concluded that even when protrusions on the bolt hole edge lead to extra preloading force and therefore extra friction force, the ratio between friction force and bearing will gradually decrease and bearing will be dominant.

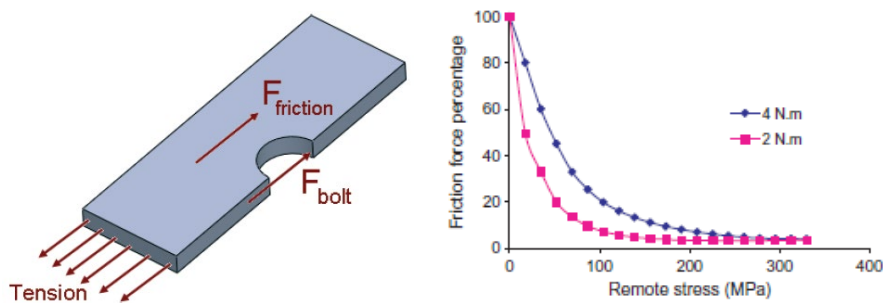


Figure 2.7.6: Division of longitudinally applied load between the bolt and plates (left); normalized friction force versus longitudinally applied remote stress (Chakherlou et al. 2012)

2.8 Summary and conclusions literature review

Embedment creep is an inevitable effect which occurs at all material and joint types since imperfections at the surfaces can not be prevented. This type of creep is defined as a short term creep effect and will lead to a preload loss of 2 – 11 %. If construction errors are present, the relative preload loss can exceed 11%. Experiments can be used to predict the occurring embedment creep.

Relaxation of stainless steel has been widely investigated and does occur at medium stresses and stresses approaching the proof stress of the material. A preload loss of 10% can be expected according to multiple sources. Retightening does not have a significant impact on the preload force after 50 years.

Creep in aluminium is present at room temperature and stresses near and above the proof stress. Alloying the aluminium will result in a material type exhibiting less dominant viscoplastic behaviour compared to pure aluminium. Examining a creep test of 2024 T6 aluminium, stresses approaching the ultimate tensile stress of the material will lead to a creep strain of approximately 1% after 50 years.

Preload variation due to thermal fluctuations is present in aluminium joints combined with a steel bolt. A preload loss of 4.16 % was discovered with a temperature change of 220 °C. This temperature range should not be considered in normal operating conditions. Therefore, the deviations within normal conditions will be minimal if sufficient preload force is applied.

Elastic interactions can lead up to 100% preload loss due to the effect of minimal bolt spacing. Thickness of the joint member, diameter of the bolt hole and diameter of the washer are less important factors, but can lead to high preload losses. Although being the most dominant factor regarding preload variation, the effects of elastic interactions are limited due to the use of retightening procedures of bolted joints. Retightening the bolts repeatedly with the initial torque will minimize the effects of elastic interaction. Minimal variation can be expected, elastic interaction is therefore not considered as a main cause of long-term preload loss.

Poisson's effect due to longitudinal tensile force in a shear joint can lead to preload losses up to 29% of the initial preload force. However, the clamping force can increase when plastic deformation at the end of the bolt hole caused by bolt bending will result in expansion of the plate thickness counterbalancing the earlier experienced preload loss. The reviewed literature considers a joint with low initial preload forces and a small clearance between bolt and bolt hole. Therefore, deviations can be expected if standard joints with high preload forces are considered.

3 Analytical modelling

3.1 Introduction

To be able to predict preload losses in practical cases, a computational efficient analytical model should be constructed. The background of this model is based on a spring model defined in VDI 2230. However, the model does not consider creep and relaxation effects. If these effects could be implemented into the model, a simple model is created which gives a designer a tool to perform simple calculations and study the preload variation with respect to time. To gain insight into the behavior of the combination of different materials, 4 material combinations are suggested. By considering four types of joints, it is possible to distinguish the impact of the different parts in the connections if the required data is available. The 4 material combinations involve:

- Steel joint with carbon steel bolt (8.8)
- Steel joint with stainless steel bolt (A4 80)
- Aluminium joint with carbon steel bolt (8.8)
- Aluminium joint with stainless steel bolt (A4 80)

The input needed in the model will be based on data provided in literature and if possible compared with results of previous research regarding the important topics:

- embedment creep (3.4)
- stress relaxation (3.5)
- plate creep (3.6)
- thermal effects (3.7)
- poisson's effect (3.8)

The background of the VDI- model is described in 3.2. The material properties and dimensional data used in the model are summarized in 3.3. A study regarding a case where all topics are included is analyzed in 3.9.

3.2 Background and application VDI-model

The principle of load spreading in a bolted joint is illustrated in figure 3.2.1 (left). The area in the joint affected by compression widens from the bolt head and nut toward the interface of the plates and has a parabolic shape. Therefore, the axial compressive stress in the cross section decreases radially outward. VDI 2230 (Blatt 2003) suggests a simplification of the parabolic shape into a deformation cone. The stress distribution is simplified into a linear distribution by using the angle of the substitutional deformation cone for bolted joints φ_D , shown in figure 3.2.1 (right).

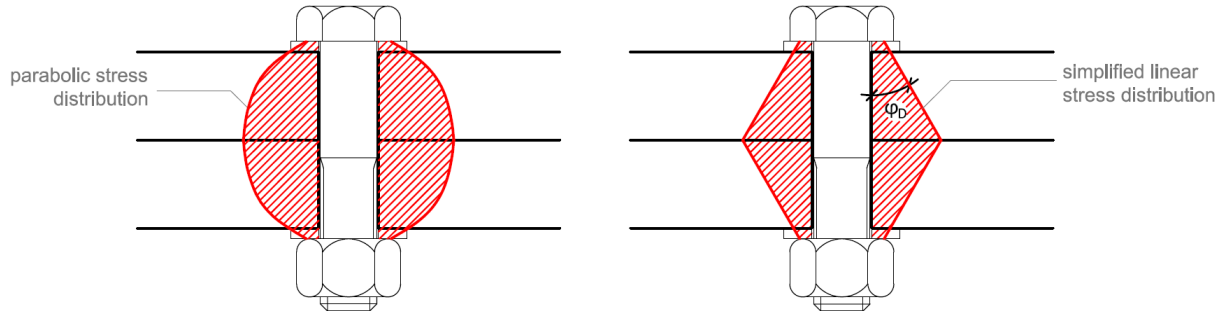


Figure 3.2.1: Realistic parabolic stress distribution (left) vs. simplified linear stress distribution (right)

The cone angle can vary between approximately 20° and 35° and is influenced by the clamping length, bolt diameter and edge distances (Blatt 2003). If a washer is used, a general cone angle of 30° is recommended (Brown et al. 2008). The joints considered in this master thesis will include washers, therefore a cone angle of 30° will be adopted during future calculations. The schematization of a bolted joint containing two plates, two washers, and a bolt is shown in figure 3.2.2.

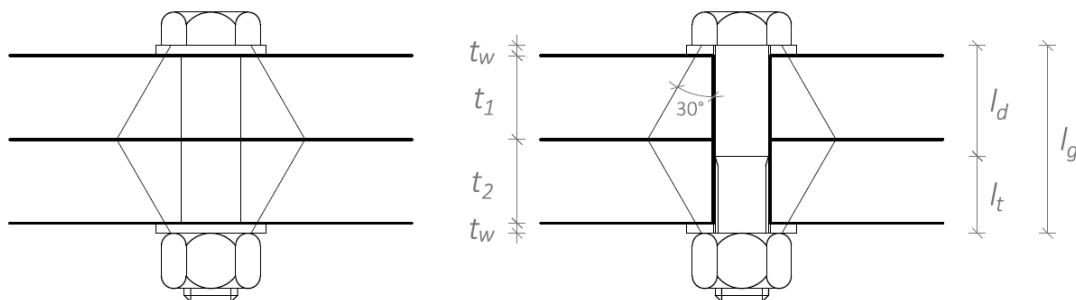


Figure 3.2.2 Simplification bolted joint

With:

- l_d : length of the unthreaded part of the bolt
- l_g : grip length
- l_t : length of the threaded part of the bolt located in the grip
- t_w : washer thickness
- t_1 : thickness plate 1
- t_2 : thickness plate 2

Using the simplification of the bolted connection, it can be subdivided into several parts representing bolt, washers and plates. Following the procedure described in VDI 2230, these parts will be transformed into linear-elastic springs as indicated in figure 3.2.3.

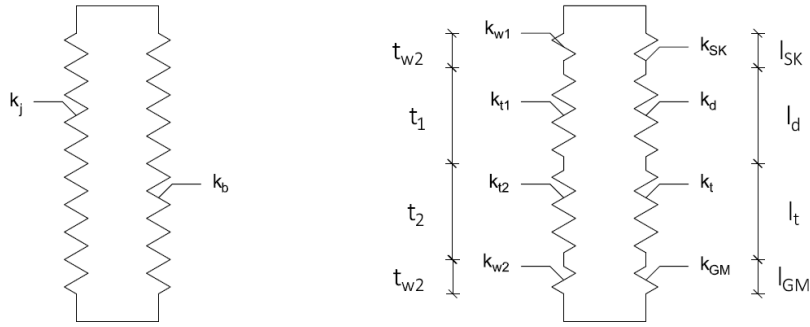


Figure 3.2.3: Spring model VDI 2230

The elastic stiffness of the total connection can be calculated with:

$$k = \frac{1}{\frac{1}{k_b} + \frac{1}{k_j}} \quad (3.1)$$

With:

- k_b : elastic bolt stiffness including bolt head, unthreaded shaft, threaded shaft, nut
- k_j : elastic joint stiffness including washers and plates

The bolt stiffness can be subdivided into separate stiffnesses representing bolt head k_{SK} , unthreaded shaft k_d , threaded part located in the grip length k_t and the threaded part in the nut k_{GM} . The joint stiffness is subdivided into stiffnesses representing washers k_w and plates represented by k_{ti} .

3.2.1 Bolt stiffness

The total stiffness of the bolt, subdivided into 4 parts, can be expressed with:

$$k_b = \frac{1}{\frac{1}{k_{SK}} + \frac{1}{k_d} + \frac{1}{k_t} + \frac{1}{k_{GM}}} \quad (3.2)$$

Where:

- k_{SK} : stiffness of the bolt head
- k_d : stiffness of the unthreaded part
- k_t : stiffness of the threaded part located in the grip
- k_{GM} : stiffness of the engaged thread and of the nut

The elastic stiffness of the subdivided parts is defined as:

$$\frac{1}{k_{SK}} = \frac{l_{SK}}{E_b A_d} = \frac{0.5d}{E_b A_d} \quad (3.3)$$

$$\frac{1}{k_d} = \frac{l_d}{E_b A_d} \quad (3.4)$$

$$\frac{1}{k_t} = \frac{l_t}{E_b A_t} \quad (3.5)$$

$$\frac{1}{k_{GM}} = \frac{1}{k_G} + \frac{1}{k_M} = \frac{l_G}{E_b A_{d_3}} + \frac{l_M}{E_b A_d} = \frac{0.5d}{E_b \frac{\pi}{4} d_3^2} + \frac{0.4d}{E_b A_d} \quad (3.6)$$

Where:

- A_d : nominal cross section unthreaded part
- A_{d_3} : cross section of thread at minor diameter
- A_t : reduced-shank cross section
- E_b : Young's modulus of the bolt material
- d : bolt diameter
- d_3 : minor diameter of the bolt thread
- k_G : stiffness of the engaged thread
- k_M : stiffness of the nut
- l_{SK} : substitutional extension length for the deformation of the bolt head
- l_d : length of the unthreaded part
- l_t : length of the threaded part located in the grip
- l_G : substitutional extension length for the deformation of the engaged thread
- l_M : substitutional extension length for the deformation of the nut

3.2.2 Joint stiffness

A joint with a fixed cone angle can be subdivided into several conical frusta equipped with a hole representing washers and plates as shown in figure 3.2.4.

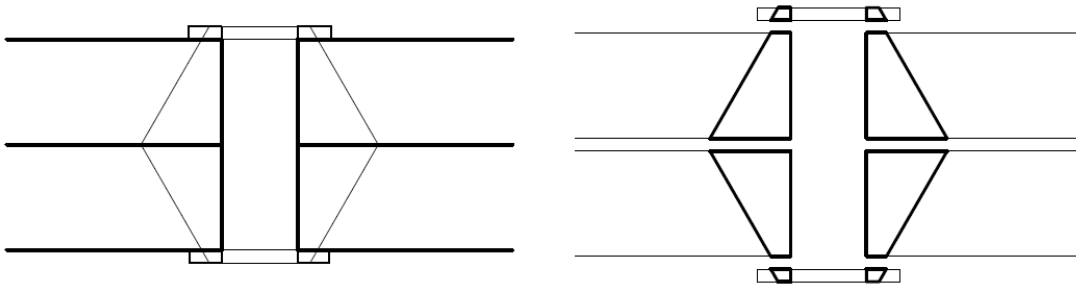


Figure 3.2.4: Schematization of subdivision joint into frusta

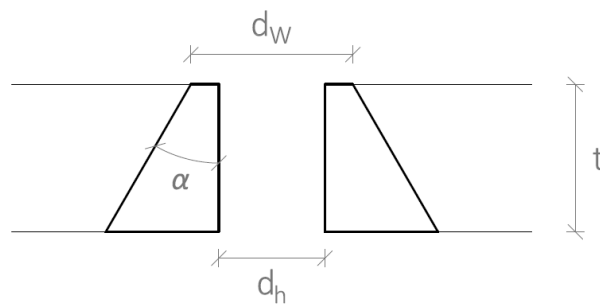


Figure 3.2.5: Dimensional properties single frustum

The dimensional properties of a single frustum with angle α are shown in figure 3.2.5. VDI 2230 provides a general stiffness equation for this type of frustum:

$$k = \frac{\pi E d_h \tan \alpha}{\ln \left(\frac{(2t \tan \alpha + d_w - d_h)(d_w + d_h)}{(2t \tan \alpha + d_w + d_h)(d_w - d_h)} \right)} \quad (3.7)$$

Where:

- E : Young's modulus of frustum material
- d_h : diameter hole
- d_w : bearing surface outside diameter
- t : frustum height
- α : frustum angle

The washer stiffness k_w can be determined using the frustum stiffness equation with modified dimensional data. A schematization of the washer frustum is shown in figure 3.2.6.

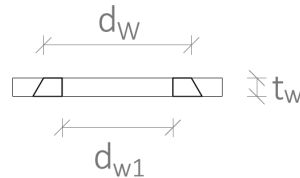


Figure 3.2.6: Dimensional properties washer frustum

The outside diameter of the plane head bearing surface under the bolt head d_w can be calculated using the rule of thumb that the bearing surface is equal to 1.5 times the bolt diameter d (Staab n.d.). The frustum angle is equal to the angle of the substitutional deformation cone for bolted joints φ_D . Therefore:

$$d_w = 1.5d \quad (3.8)$$

$$\alpha = \varphi_D = 30^\circ \quad (3.9)$$

Using the simplifications regarding the bearing surface diameter d_w and frustum angle α the washer stiffness is defined as:

$$k_w = \frac{\pi E_w d_{w1} \tan 30}{\ln \left(\frac{(2t_w \tan 30 + 1.5d - d_{w1}) \cdot (1.5d + d_{w1})}{(2t_w \tan 30 + 1.5d + d_{w1}) \cdot (1.5d - d_{w1})} \right)} \quad (3.10)$$

Where:

- E_w : Young's modulus of washer material
- d : bolt diameter
- d_{w1} : inner diameter washer
- t_w : washer thickness

The plate stiffness of the upper plate k_{t1} can be determined using the modified frustum stiffness regarding the plate dimensions. A schematization of the plate frustum is shown in figure 3.2.7.

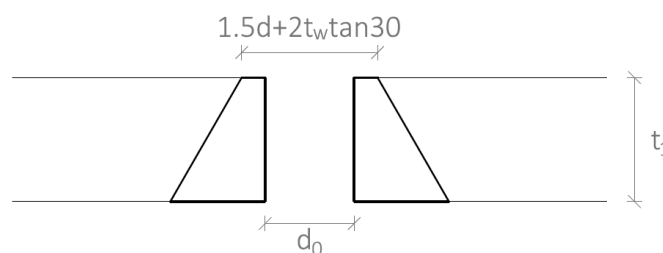


Figure 3.2.7: Dimensional properties plate frustum

As can be observed in figure 3.2.7, the bearing surface outside diameter at the top of the plate frustum is increased compared to the bearing surface diameter under the bolt head due to load spreading in the washer height under an angle of 30°. The bearing surface outside diameter in the interface between washer and nut is therefore equal to:

$$d_w = 1.5d + 2t_w \tan 30 \quad (3.11)$$

The stiffness of plate 1 can be expressed as:

$$k_{t1} = \frac{\pi E_j d_0 \tan 30}{\ln \left(\frac{(2t_1 \tan 30 + (1.5d + 2t_w \tan 30) - d_0) \cdot ((1.5d + 2t_w \tan 30) + d_0)}{(2t_1 \tan 30 + (1.5d + 2t_w \tan 30) + d_0) \cdot ((1.5d + 2t_w \tan 30) - d_0)} \right)} \quad (3.12)$$

Where:

- E_j : Young's modulus of plate material
- d : bolt diameter
- d_0 : diameter bolt hole
- k_{t1} : stiffness plate 1
- t_w : washer thickness
- t_1 : thickness plate 1

With the procedure defining frustum dimensions, all frustum stiffnesses in the joint can be determined. The combined plate stiffness can be expressed as:

$$\frac{1}{k_{\sum t}} = \frac{1}{k_{t1}} + \frac{1}{k_{t2}} + \dots + \frac{1}{k_{ti}} \quad (3.13)$$

Where:

- $k_{\sum t}$: combined plate stiffness
- k_{t1} : stiffness plate 1
- k_{t2} : stiffness plate 2
- k_{ti} : stiffness plate i

The total joint stiffness, represented by k_j , is determined by combining the washer stiffnesses with the combined plate stiffness:

$$k_j = \frac{1}{\frac{1}{k_w} + \frac{1}{k_{\sum t}} + \frac{1}{k_w}} \quad (3.14)$$

3.3 Dimensional data and material properties

To be able to use the VDI-model described in 3.2, the dimensional data and material properties are summarized. The material properties of 8.8 and A4 80 bolt material and S235/50830/6082T6 plate material and dimensional data corresponding to the bolts, washers and plates are presented in the tables of this section. The data in the tables are found in codes and literature. The nominal cross section of the unthreaded part A_d is calculated with:

$$A_d = \frac{\pi}{4} d^2 \quad (3.15)$$

3.3.1 Dimensional data

The dimensional data needed in the calculation of bolt and joint stiffness can be found in table 3.3.1. The bolt and nut data are in accordance with ISO 724 and tolerance class 6g/6H.

Dimensional data per diameter						
d	[mm]	12	16	20	24	
Bolt						
A_t	[mm ²]	84.3	157	245	353	¹
A_d	[mm ²]	113	201	314	452	
k	[mm]	7.5	10	12.5	15	⁴
p	[mm]	1.75	2	2.5	3	⁴
d_{min}	[mm]	11.732	15.682	19.623	23.577	⁴
d_{max}	[mm]	11.968	15.962	19.958	23.952	⁴
d_{avg}	[mm]	11.850	15.822	19.791	23.765	
d_1	[mm]	10.106	13.835	17.294	20.752	⁴
d_3	[mm]	9.853	13.546	16.933	20.319	¹
Nut						
D_{1min}	[mm]	10.376	13.835	17.294	20.752	⁴
D_{1max}	[mm]	10.676	14.210	17.744	21.252	⁴
D_{1avg}	[mm]	10.526	14.023	17.519	21.002	
Washer						
t_w	[mm]	2.5	3	3	4	²
d_{w1}	[mm]	13	17	21	25	²
Plates						
d_0	[mm]	13	18	22	26	³

Table 3.3.1: Dimensional data (¹ Blatt 2003) (² Fastenal 2017) (³ NEN-EN 1090-2 2018) (⁴ ISO 724)

As can be observed in table 3.3.1, next to the required parameters used in the stiffness calculations, the dimensional data needed in following calculations is added. These parameters are listed below:

- k : height bolt head
- p : pitch height
- d_{min} : minimum major diameter bolt
- d_{max} : maximum major diameter bolt
- d_{avg} : average major diameter bolt
- d_1 : basic minor diameter bolt
- D_{1min} : minimum minor diameter nut
- D_{1max} : maximum minor diameter nut
- D_{1avg} : average minor diameter nut

The average values for the major bolt diameter and the minor nut diameter are determined with:

$$d_{avg} = \frac{d_{min} + d_{max}}{2} \quad (3.16)$$

$$D_{1avg} = \frac{D_{1min} + D_{1max}}{2} \quad (3.17)$$

3.3.2 Material properties

The material properties needed for the VDI-model contains the Young's modulus of the bolt, washer and plates. The washer and nut material properties are assumed to be equal to the bolt material properties. The bolt, washer and nut material properties can be found in table 3.3.2, the plate material properties can be found in table 3.3.3.

Material properties bolt/nut/washer					
		A4 80		8.8	
E_w or E_b	[N/mm ²]	193000	^{1,3}	200000	⁴
α_T	[mm/mm/°C]	0.000016	^{1,3}	0.000012	^{4,5}
$f_{0.2}$	[N/mm ²]	600	²	640	^{1,6}
f_u	[N/mm ²]	800	²	800	^{1,6}

Table 3.3.2: Material properties bolt/nut/washer (¹ Bossard 2005) (² NEN-EN 1993-1-4 2006) (³ Atlas Specialty Metals 2006) (⁴ Elgin Fastener Group 2019) (⁵ Ydstebø 2017) (⁶ NEN-EN 1993-1-1 2010)

Material properties plate				
		S235 ¹	50830 ²	6082T6 ²
E_j	[N/mm ²]	210000	70000	70000
α_T	[mm/mm/°C]	0.000012	0.000023	0.000023
ν	[-]	0.3	0.3	0.3
$f_{0.2}$ or f_y	[N/mm ²]	235	125	260
f_u	[N/mm ²]	360	275	310
n	[-]	-	6	25

Table 3.3.3: Material properties plate (¹ NEN-EN 1993-1-1 2010) (² NEN-EN 1999-1-1 2013)

Next to the required value for the Young's modulus, the material properties needed in following calculations are added in tables 3.3.2 and 3.3.3. These parameters involve:

- α_T : coefficient of linear thermal expansion
- $f_{0.2}$: 0.2% proof strength
- f_y : yield strength
- n : Ramberg-Osgood parameter
- ν : Poisson's ratio

3.4 Embedment effects

3.4.1 Theory

Embedment effects due to plastic deformation of the imperfections on the surface will lead to a decrease in the clamping length and a corresponding decrease in preload force. VDI 2230 provides a table with guide values for the expected amount of creep in (carbon) steel connections, presented in table 3.4.1. A comparable table with guide values for embedment creep of aluminium and stainless steel is not given in literature and can therefore only be examined with experiments. The amount of embedment creep in the case of aluminium is more dominant than in the case of steel (Blatt 2003).

Average roughness height	Loading	Guide values for amounts of embedding in μm		
		in the thread	per head or nut bearing area	per inner interface
R_z according to DIN 4768				
< 10 μm	tension/compression shear	3 3	2,5 3	1,5 2
10 μm up to < 40 μm	tension/compression shear	3 3	3 4,5	2 2,5
40 μm up to < 160 μm	tension/compression shear	3 3	4 6,5	3 3,5

Table 3.4.1: Guide values for amounts of embedding of bolts, nuts and compact clamped parts made of (carbon) steel (Blatt 2003)

The total amount of embedment creep is defined as δ_{em} and is equal to the sum of creep in the threads, head/nut bearing area and interfaces as quantified in table 3.4.1. As discussed before, the clamping length of the joint will reduce due to embedment creep. The total reduction of the clamping length is influenced by the loss of preload since the elastic contraction of the plates will reduce as a result of the reducing preload level. This counterbalancing effect is visualized in figure 3.4.1 and formulated in equation 3.19. The preload change due to embedment creep is defined as ΔP_{em} . If joint separation does not occur, i.e. a preload force remains present, the deformations in bolt and plate should be equal. The effect of embedment creep can be visualized as shown in figure 3.4.1.

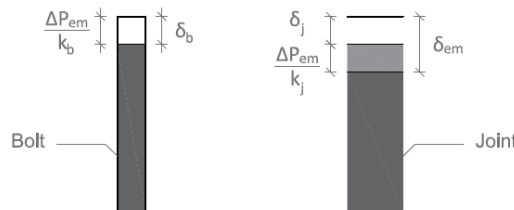


Figure 3.4.1: Visualization of equal deformations during embedment creep

The deformation of the bolt is affected by the loss of preload due to embedment effects ΔP_{em} . The deformation of the joint is affected by ΔP_{em} and the occurring embedment creep. If joint separation does not occur, the deformations of bolt and joint should be equal:

$$\delta_b = \frac{\Delta P_{em}}{k_b} \quad (3.18)$$

$$\delta_j = \delta_{em} - \frac{\Delta P_{em}}{k_j} \quad (3.19)$$

$$\delta_b = \delta_j \rightarrow \frac{\Delta P_{em}}{k_b} = \delta_{em} - \frac{\Delta P_{em}}{k_j} \rightarrow \Delta P_{em} = \delta_{em} \left(\frac{k_b k_j}{k_b + k_j} \right) \quad (3.20)$$

With:

ΔP_{em} : loss of preload due to embedment effects

k_b : elastic bolt stiffness

k_j : elastic joint stiffness

δ_b : deformation bolt

δ_{em} : total amount of embedment creep

δ_j : deformation joint

3.4.2 Parametric study

An estimation regarding the variation of preload can be made for a double lap joint containing three S235 steel plates connected with a 8.8 steel bolt loaded in tension and shear. A schematization of the joint is presented in figure 3.4.2.

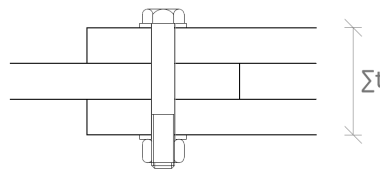


Figure 3.4.2: Double lap joint used in parametric study

Using the guide values of table 3.4.1 with maximum roughness will result in:

- Embedment in the threads: $3 \mu m$
- Embedment under the head/nut area: $2 \cdot 6.5 = 13 \mu m$
- Embedment in the interface of the plates: $2 \cdot 3.5 = 7 \mu m$

A total embedment creep of $23.0 \mu m$ is expected to occur. Therefore:

$$\Delta P_{em} = 0.0230 \left(\frac{k_b k_j}{k_b + k_j} \right) \quad (3.21)$$

During the parametric study the total thickness of the plates, indicated with Σt , and the bolt diameter are varied. The results are presented in figure 3.4.3.

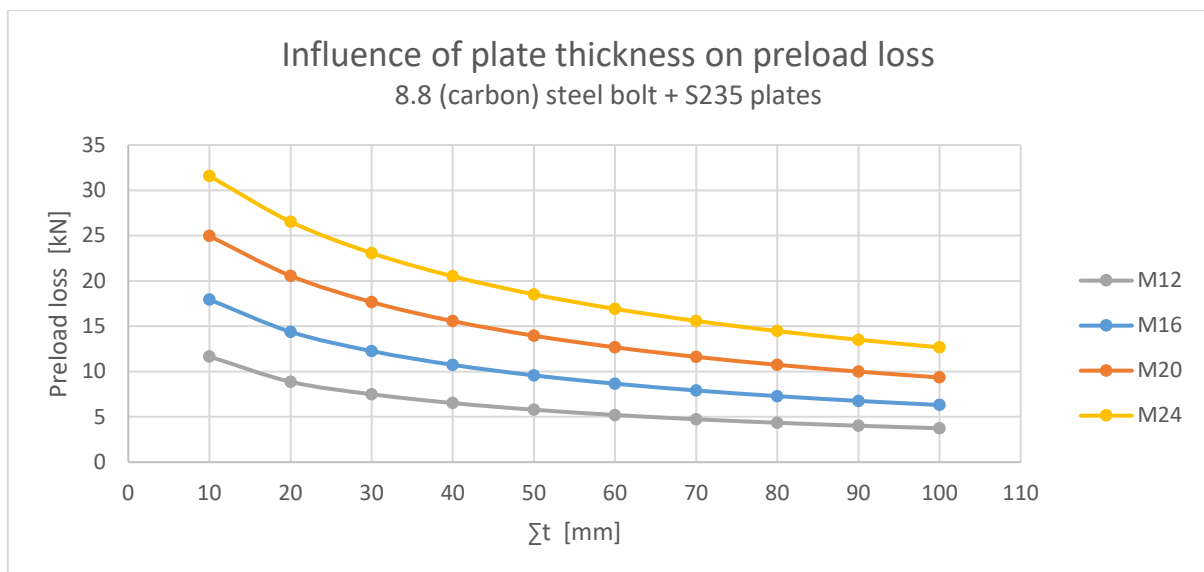


Figure 3.4.3: Influence of plate thickness vs. preload loss due to embedment creep

Following NEN-EN 1090, a slip resistant joint requires a nominal minimum preload force of 70% of the tensile strength of the bolt:

$$P_{nom} = 0.7 f_{ub} A_t \tag{3.22}$$

With:

- A_t : reduced-shank cross section
- P_{nom} : nominal minimum preload force
- f_{ub} : tensile strength bolt

The values for f_{ub} and A_t can be found in 3.3, the results are presented in table 3.4.2.

Nominal preload force		
	A_t	P_{nom}
	mm^2	kN
M12	84.3	47.2
M16	157	87.9
M20	245	137.2
M24	353	197.7

Table 3.4.2: Nominal minimum preload force vs. bolt diameter according to NEN-EN 1090

Using the nominal minimum preload forces listed in table 3.4.2, a relative preload loss can be determined. The results are presented in figure 3.4.4.

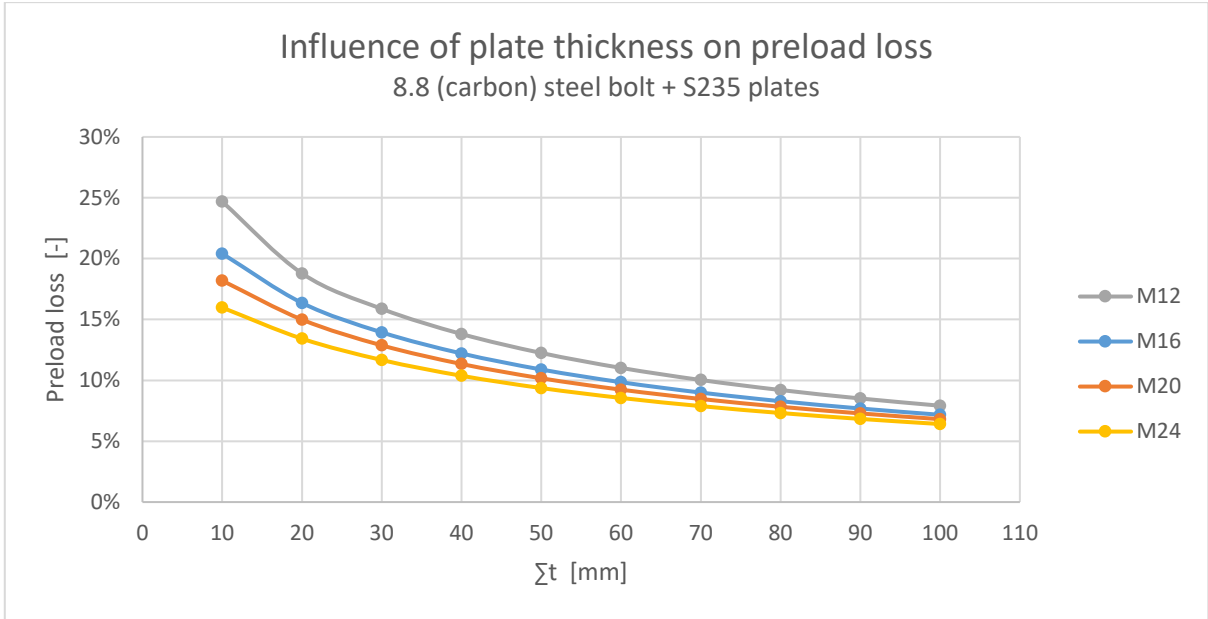


Figure 3.4.4: Influence of plate thickness vs. relative preload loss due to embedment creep

As can be observed in figure 3.4.3, preload loss becomes less dominant with increasing joint thickness and increasing bolt diameter. However, when the relative preload loss is examined, increasing the bolt diameter will lead to lower relative preload loss. As mentioned in 2.2, preload losses up to 11% could be expected, which is comparable with the results of figure 3.4.4 if $\Sigma t > 50$ mm.

The impact of the initial preload force in a carbon steel joint with a total plate thickness $\Sigma t = 50$ mm is presented in figure 3.4.5. No literature was found regarding the relationship between the amount of embedment creep and the initial preload force. Therefore, the expected amount of embedment creep in equation 3.21 derived from table 3.4.1 is applied. The initial preload force P is presented proportional with the proof load of the bolt. The ratio between the nominal minimum preload force P_{nom} and the proof load F_p is equal to:

$$\frac{P_{nom}}{F_p} = \frac{0.7 f_{ub} A_t}{f_{0.2} A_t} = \frac{0.7 \cdot 800}{640} = 0.875 \rightarrow P_{nom} = 0.875 F_p \tag{3.23}$$

With:

- A_t : reduced-shank cross section
- F_p : proof load bolt
- $f_{0.2}$: 0.2% proof strength bolt material
- f_{ub} : ultimate strength bolt material

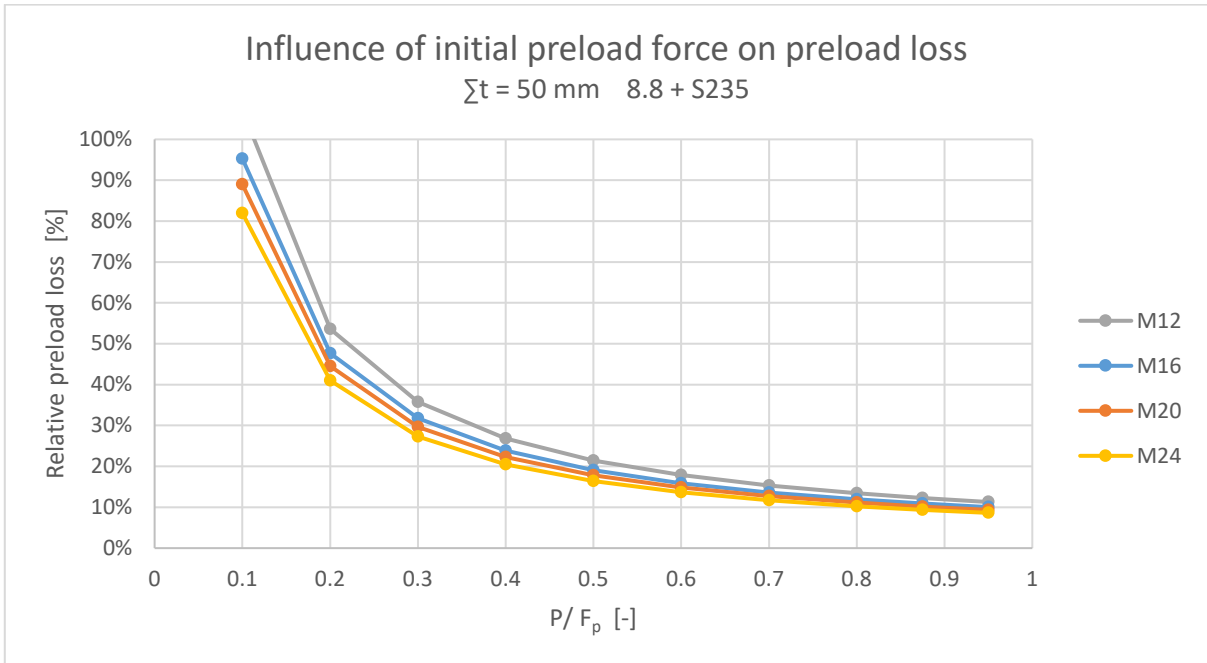


Figure 3.4.5: Influence of initial preload force vs. relative preload loss due to embedment creep

As can be observed in figure 3.4.5, the initial preload level has a significant impact on the relative preload loss. Increasing the preload force will lead to decreasing preload losses. Therefore, it can be concluded that the initial preload force should be maximal to be able to reach minimal preload losses. Theoretically, the application of retightening should neutralize embedment creep, since leveling of the surfaces is accomplished after embedment creep has occurred. Therefore, it is advised to retighten the bolt to neutralize the effects of embedment creep.

3.5 Bolt relaxation

3.5.1 Theory

The principle of relaxation behaviour is discussed in section 2.3.2. The decreasing stress in a material can be explained with the appearance of plastic strain. This plastic strain can be defined as bolt creep and is equal to the loss of elastic strain and subsequently the loss of stress in the object. Comparable with the preload loss behaviour of embedment and plate creep, the variation of clamping length is affected by the occurring bolt creep and the variation of preload force. The preload change due to bolt creep can be defined as $\Delta P_{cr,b}$. The effect of relaxation can be visualized as shown in figure 3.5.1.

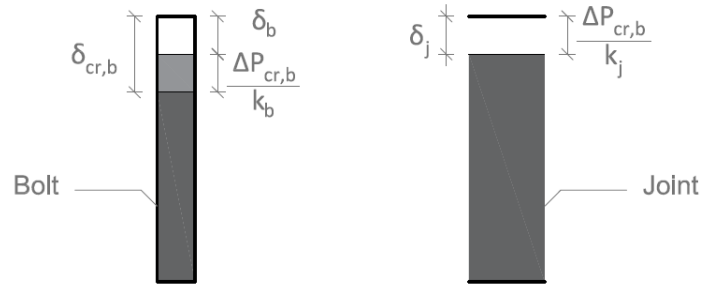


Figure 3.5.1: Visualization of equal deformations during relaxation

Following the analysis of embedment creep, preload loss due to bolt creep can be expressed as:

$$\delta_b = \delta_j \rightarrow \delta_{cr,b} - \frac{\Delta P_{cr,b}}{k_b} = \frac{\Delta P_{cr,b}}{k_j} \rightarrow \Delta P_{cr,b} = \delta_{cr,b} \left(\frac{k_b k_j}{k_b + k_j} \right) \quad (3.24)$$

With:

$\Delta P_{cr,b}$: loss of preload due to relaxation

$\delta_{cr,b}$: total amount of bolt creep

3.5.2 Creep properties stainless steel bolt material

No literature is found regarding relaxation of 8.8 steel bolts, therefore the analysis is limited to austenitic stainless steel bolts. Due to insufficient creep data at room temperature for 316 (A4-80) stainless steel, creep data for 304L austenitic stainless steel wire obtained by Deibler (Deibler 2014) will be used. Both materials show more or less comparable proof and tensile properties after cold work as indicated in table 3.5.1. The properties of 304L were found during experiments, the properties of 316 (A4-80) are design values. Therefore, in reality the physical properties of 316 (A4-80) should be more in accordance with 304L (wire) than table 3.5.1 is suggesting.

Physical properties stainless steel			
		316 (A4-80)	304L (wire) ¹
$f_{0.2}$	[N/mm ²]	600	684
f_u	[N/mm ²]	800	914

Table 3.5.1: Proof and tensile properties 316 (A4-80) vs. 304L (wire) (¹Deibler 2014)

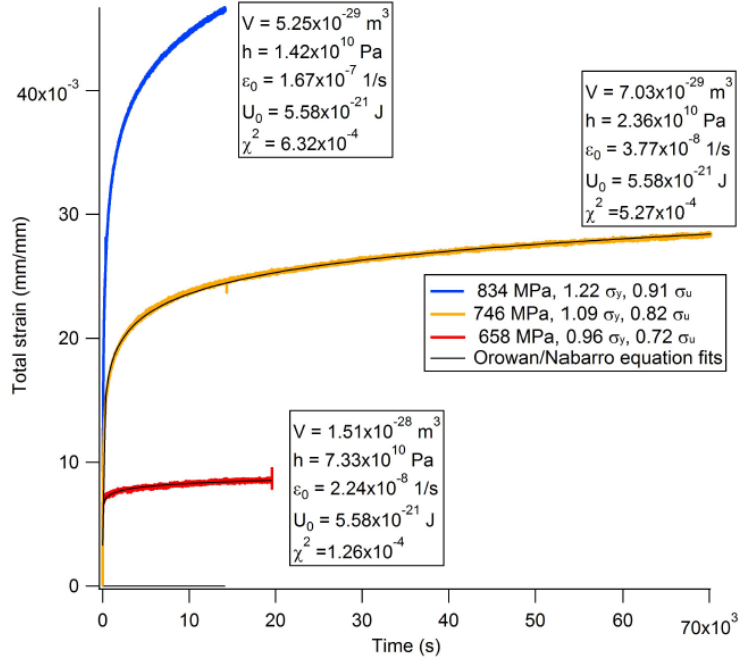


Figure 3.5.2: The Orowan/Nabarro equation fit to data from 304L dead-weight creep experiments. Coefficients are reported in the text boxes (Deibler 2014)

The creep data for 304L derived by Deibler contains total strain behaviour at stress levels of 0.96, 1.09 and 1.22 $f_{0.2}$ derived from 5-20 hour creep tests. The results are presented in figure 3.5.2. The creep data was evaluated using Orowan/Nabarro's strain equation, where creep strain is related to stress using coefficients with physical measurable values. The total strain equation holds:

$$\varepsilon(t) = \frac{kT}{Vh} \left(\ln \left(\frac{Vh\varepsilon'_0(t+t_0)}{kT} \right) - \frac{U_0 - V\sigma}{kT} \right) \quad (3.25)$$

$$t_0 = \frac{kT}{Vh\varepsilon'_0} e^{\left(\frac{U_0 - V\sigma}{kT} \right)} \quad (3.26)$$

With:

- T : temperature in Kelvin
- U_0 : activation energy constant
- V : activation volume
- h : coefficient of work hardening
- k : Boltzmann's constant
- t : time in seconds
- t_0 : time translation parameter
- ε'_0 : constant related to the initial plastic strain rate
- σ : applied stress

Boltzmann's constant, temperature and applied stress are known parameters. Deibler determined the remaining parameters experimentally by curve fitting the creep data. The creep strain rate can be formulated by determining the first derivative of the total strain:

$$\varepsilon'_{cr}(t) = \frac{kT}{Vh} \frac{1}{(t+t_0)} \quad (3.27)$$

A comparable creep strain rate equation of austenitic steel grades at room temperature was found in literature (Afzali et al. 2017):

$$\dot{\varepsilon}_{cr}(t) = f_1(\sigma)t^{-1} \quad (3.28)$$

With:

- $f_1(\sigma)$: creep parameter with function of applied stress
- t : time in seconds
- $\dot{\varepsilon}_{cr}(t)$: creep strain rate

The creep strain rate equation of Afzali is comparable with the derived creep strain rate equation from Orowan/Nabarro's total strain relationship with the exception of leaving out the time translation parameter t_0 . The values corresponding to the creep parameter function $f_1(\sigma)$ are related to the Orowan/Nabarro parameters k , T , V and h :

$$f_1(\sigma) = \frac{kT}{Vh} \quad (3.29)$$

The values for the activation volume V and the coefficient of work hardening h are stress dependent and can be found in figure 3.5.2. The values for the Boltzmann's constant k and the temperature T are stress independent and can be found in table 3.5.2.

Stress independent parameters	
k	$1.38064852 \cdot 10^{-23} \text{ J K}^{-1}$
T	293.15 K

Table 3.5.2: Stress independent parameters used in Orowan/Nabarro's equation

The creep parameters corresponding to the tested stress levels, derived by taking into account the Orowan/Nabarro parameters, are listed in table 3.5.3.

Creep parameter f_1 vs. applied stress 304L				
		658 MPa	746 MPa	834 MPa
f_1	[-]	$3.6567 \cdot 10^{-4}$	$2.4395 \cdot 10^{-3}$	$5.4291 \cdot 10^{-3}$

Table 3.5.3: Creep parameter f_1 vs. applied stress 304L wire

A power law function can be used to describe the creep parameter function at low stresses; at high stresses, the creep parameter function behaves exponentially (Rieth et al. 2004). The data points of Deibler described in table 3.5.3 are plotted in figure 3.5.3. Both a power law trendline and an exponential trendline are added to be able to distinguish the transition point between the low stress range and high stress range.

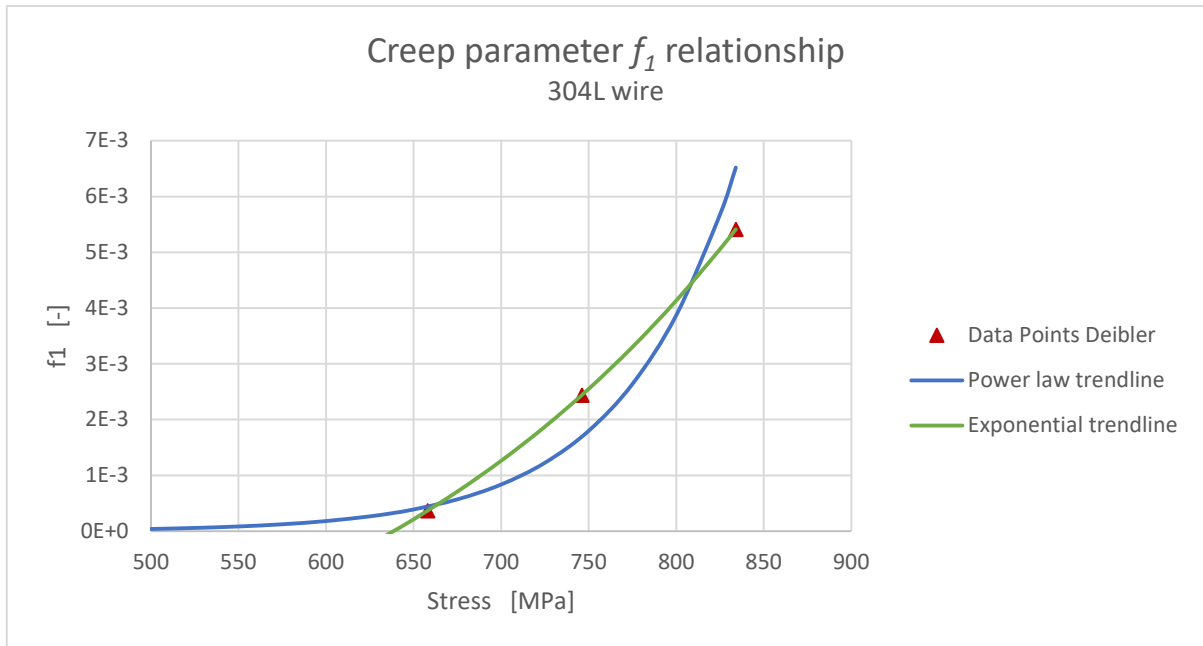


Figure 3.5.3: Creep parameter f_1 vs. applied stress with possible trendlines

As expected, the trendline with an exponential relationship is more accurate in the high stress range, where the power law trendline is more accurate in a lower stress range. The transition point can be found at a stress of 663 MPa. A combination of the two trendlines is presented in figure 3.5.4. The creep parameter functions $f_1(\sigma)$ corresponding to the combined trendline of figure 3.5.4 within specific intervals are listed in table 3.5.4.

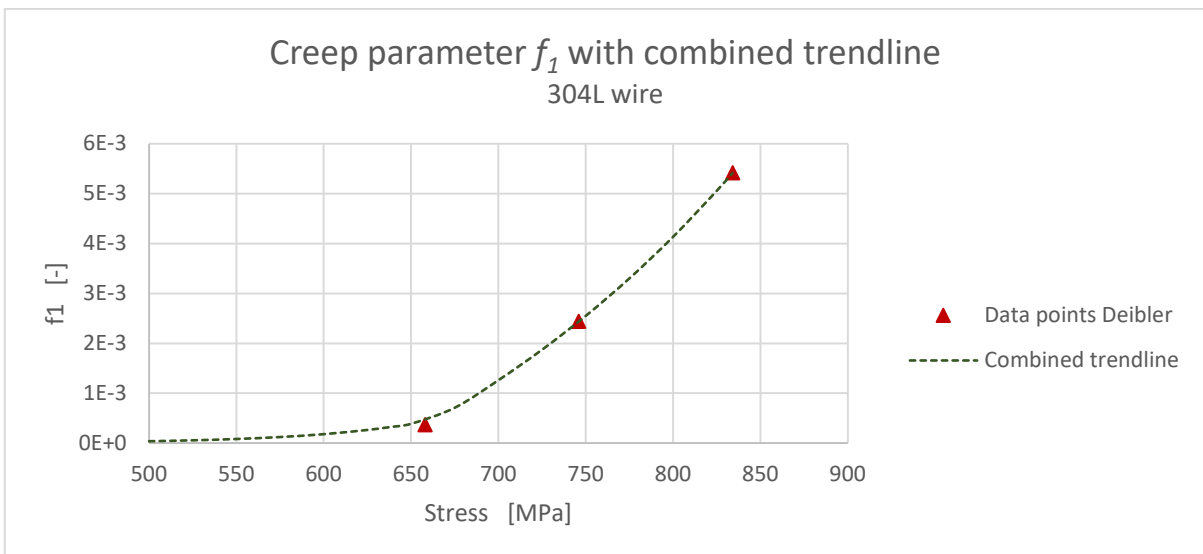


Figure 3.5.4: Creep parameter f_1 vs. applied stress with combined trendline

Creep parameter function $f_1(\sigma)$			
		[0,663 MPa]	[663,834 MPa]
$f_1(\sigma)$	[-]	$2.32082E-36 \cdot \sigma^{(11.4474)}$	$-4.3886E-03 + 3.17923E-04 \cdot e^{(4.11093E-03\sigma)}$

Table 3.5.4: Creep parameter functions $f_1(\sigma)$ applied in combined trendline

During stress relaxation, the stress is fluctuating. Therefore, the formulated creep strain rate equation should be adjusted continuously over time to be able to model stress relaxation. To increase computational efficiency, a discrete model with an increasing time interval is adopted. As illustrated in

figure 3.5.5, a discrete model is created by subdividing the creep time into time increments dt with constant strain rate within the interval $[t, t+dt]$. Creep strain in an interval $[t, t+dt]$ can be approximated by multiplying the creep strain rate with a time increment dt . The upper red line represents an overestimation with the application of the creep strain rate at the start of the time increment:

$$\varepsilon_{cr,[t,t+dt]} = \varepsilon'_{cr}(t) dt \quad (3.30)$$

$$\varepsilon_{cr,1} = \varepsilon'_{cr,0} dt(1) \quad (3.31)$$

The lower red line represents an underestimation of the real creep behaviour by considering the creep strain rate at the end of the time increment:

$$\varepsilon_{cr,[t,t+dt]} = \varepsilon'_{cr}(t + dt) dt \quad (3.32)$$

$$\varepsilon_{cr,1} = \varepsilon'_{cr,1} dt(1) \quad (3.33)$$

An average approximation of the creep strain can be obtained by taking into account the average creep strain rate of the time increment:

$$\varepsilon_{cr,[t,t+dt]} = \frac{\varepsilon'_{cr}(t) + \varepsilon'_{cr}(t + dt)}{2} dt \quad (3.34)$$

$$\varepsilon_{cr,1} = \frac{\varepsilon'_{cr,0} + \varepsilon'_{cr,1}}{2} dt(1) \quad (3.35)$$

The discrete model is illustrated in figure 3.5.6. The curved black line represents the real creep response. The overestimating discrete model is represented by the upper red line, the lower red line represents an underestimation.

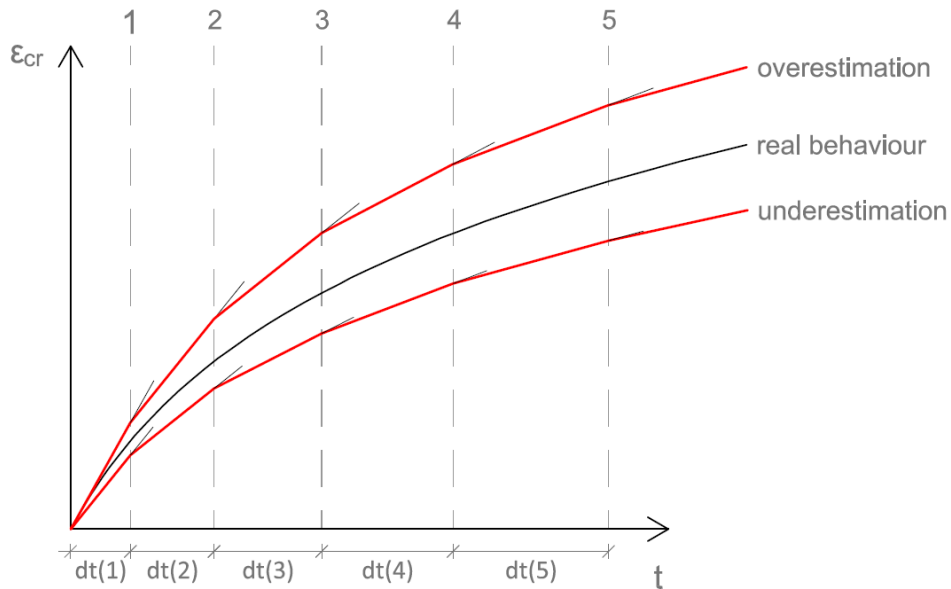


Figure 3.5.5: Discrete model with increasing time interval

The total amount of creep can be derived with the summation of the creep of the subdivided intervals:

$$\varepsilon_{cr} = \sum \left(\varepsilon_{cr,[t_i,t_i+dt]} + \dots + \varepsilon_{cr,[t_j,t_j+dt]} \right) \quad (3.36)$$

The accuracy of the discrete model can be assured by the application of sufficient small time increments. The increase of creep strain becomes less dominant over time, the time increment dt could

therefore be raised gradually with respect to time. To exclude elastic and initial plastic strain during assembly, the discrete model and comparison with real creep behaviour starts at $t=3s$ (Afzali et al. 2017). A time increment function is formulated:

$$dt(n) = 0.03 \cdot 1.01^n \quad (3.37)$$

With:

dt : time increment in seconds
 n : interval number

The time function corresponding with the interval numbers can be formulated as:

$$t(n) = 3 \cdot 1.01^n \quad (3.38)$$

The average discrete model of equation 3.34 combined with the time increment function described in equation 3.37 and the creep parameter function of table 3.5.4 is compared with the creep data containing stresses applied in Deiblers experiments: 658, 746 and 834 MPa. Figure 3.5.6 represents the relative difference between the discrete model and the real creep behaviour. The relative difference is defined as:

$$\frac{\varepsilon_{cr,model} - \varepsilon_{cr,Deibler}}{\varepsilon_{cr,Deibler}} \quad (3.39)$$

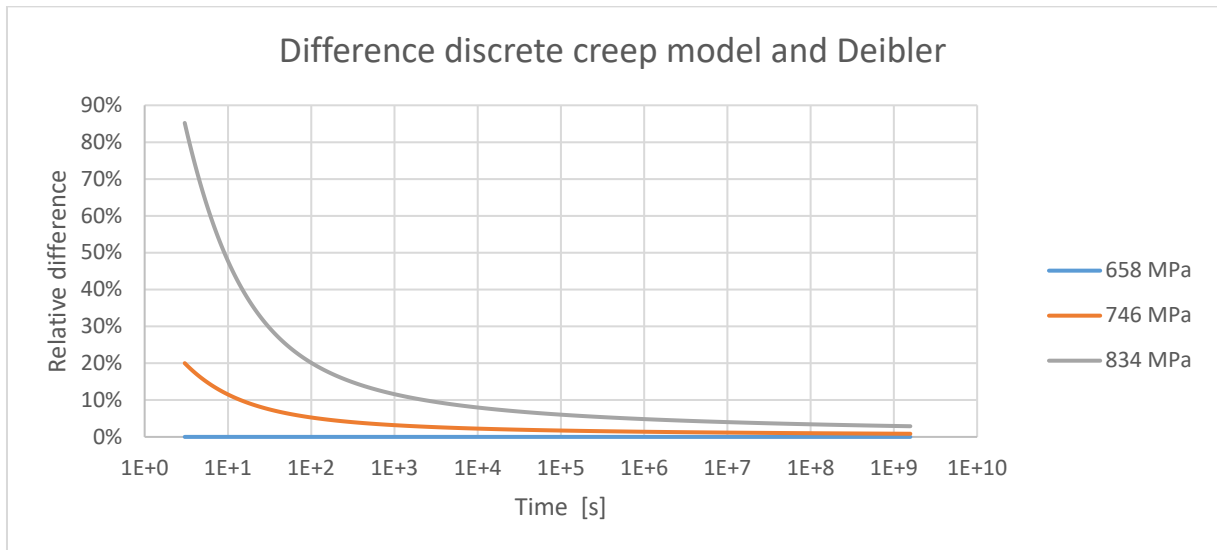


Figure 3.5.6: Relative difference between discrete model and creep data Deibler

As can be observed, the average discrete model will lead to an overestimation of the occurring creep in higher stress ranges. The model seems to be accurate for the lowest stress, but inaccurate for the medium and higher stress. Deviations occur due to the missing time translation parameter t_0 defined in equation 3.26. Application of the time translation parameter will lead to a shift of the point in time where the approximate creep strain is determined within a time increment:

$$\varepsilon_{cr,[t,t+dt]} = \frac{\varepsilon'_{cr}(t+t_0) + \varepsilon'_{cr}(t+t_0+dt)}{2} dt \quad (3.40)$$

According to equation 3.26, the time translation parameter is stress-dependent. Using the constants given in figure 3.5.3 and table 3.5.2, the values of t_0 can be determined. Table 3.5.5 and figure 3.5.7 give an overview of the given time translation parameters.

Time translation parameter t_0 vs. applied stress				
		658 MPa	746 MPa	834 MPa
t_0	[s]	$1.4132 \cdot 10^{-6}$	0.6058	2.5853

Table 3.5.5: Time translation parameter t_0 vs. applied stress 304L wire

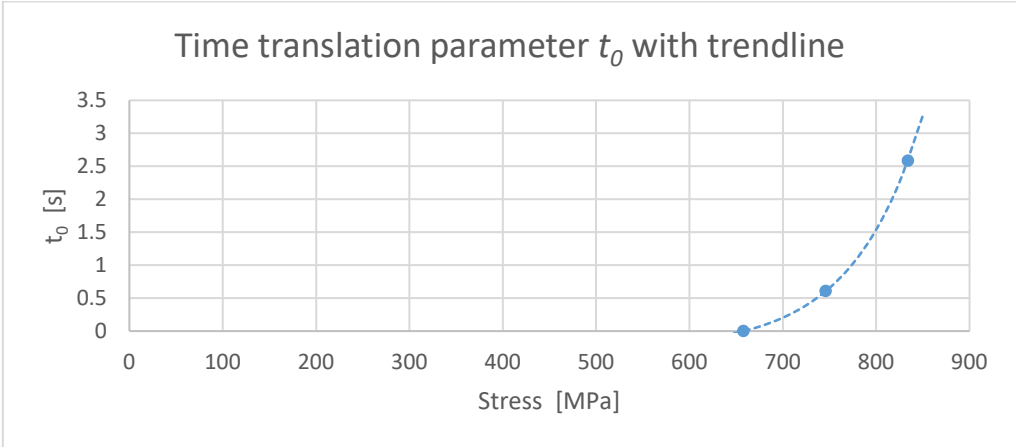


Figure 3.5.7: Creep parameter t_0 vs. applied stress with exponential trendline

An exponential trendline is added to estimate the time translation parameter at various stresses. Since a negative translation will lead to extra deviations, only positive translation parameters have to be taken into account. The relationship fitting the exponential trend line is defined as:

$$t_0(\sigma) = 3.044 \cdot 10^{-7} e^{1.507 \cdot 10^{-2} \sigma} \geq 0 \tag{3.41}$$

The discrete model with application of the time translation parameter t_0 is compared with the creep data containing stresses applied in Deiblers tests: 658, 746 and 834 MPa. Figure 3.5.8 represents the relative difference between the adjusted discrete model and the real creep behaviour.

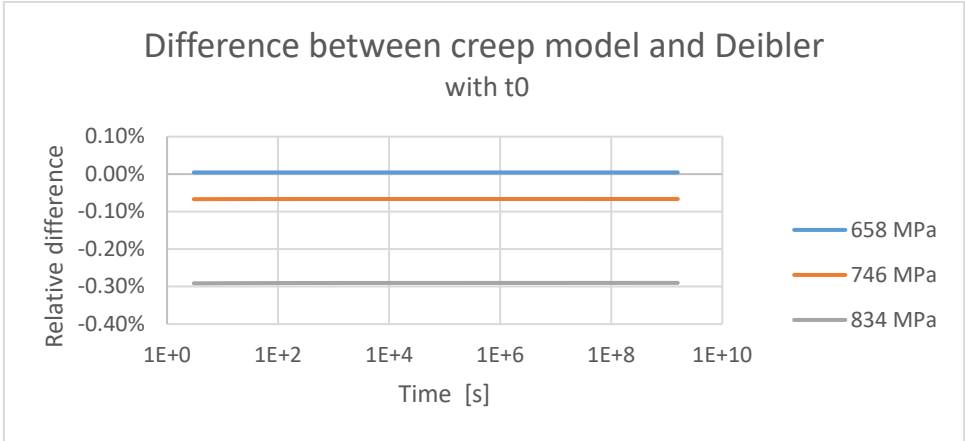


Figure 3.5.8: Relative difference between discrete model with t_0 and creep data Deibler

The model exhibit differences with a maximum absolute relative difference of 0.30%. It can be concluded that the discrete creep strain rate model with increasing time increments dt and a time translation parameter t_0 predicts the creep behaviour accurately with a minimal underestimation of higher stress creep behaviour.

3.5.3 Subdivision bolt

To be able to simulate the stress distribution within a bolt, the bolt will be subdivided into 6 parts, respecting bearing and tension and the varying stresses in the bolt. The transfer of tension into bearing and vice versa is assumed to be performed via shear as indicated in figure 3.5.9. The 6 parts include:

- Part 1: Flank bolt head (bearing)
- Part 2: Unthreaded shaft (tension)
- Part 3: Threaded part located in grip (tension)
- Part 4: Threaded part located in nut (tension)
- Part 5: Threads (bearing)
- Part 6: Flank nut (bearing)

The total expected bolt creep $\delta_{cr,b}$ is equal to the summation of the occurring creep in the separate parts and can be expressed with:

$$\delta_{cr,b} = \delta_{cr,SK,b} + \delta_{cr,ld,t} + \delta_{cr,lt,t} + \delta_{cr,G,t} + \delta_{cr,G,b,1...6} + \delta_{cr,M,b,1...6} \quad (3.42)$$

With:

- $\delta_{cr,SK,b}$: creep in bolt head, bearing
- $\delta_{cr,ld,t}$: creep in unthreaded length, tension
- $\delta_{cr,lt,t}$: creep in threaded length located in grip length, tension
- $\delta_{cr,G,t}$: creep in threaded length located in the nut, tension
- $\delta_{cr,G,b,1...6}$: creep in threads, bearing, 1-6
- $\delta_{cr,M,b,1...6}$: creep in flank nut, bearing, 1-6

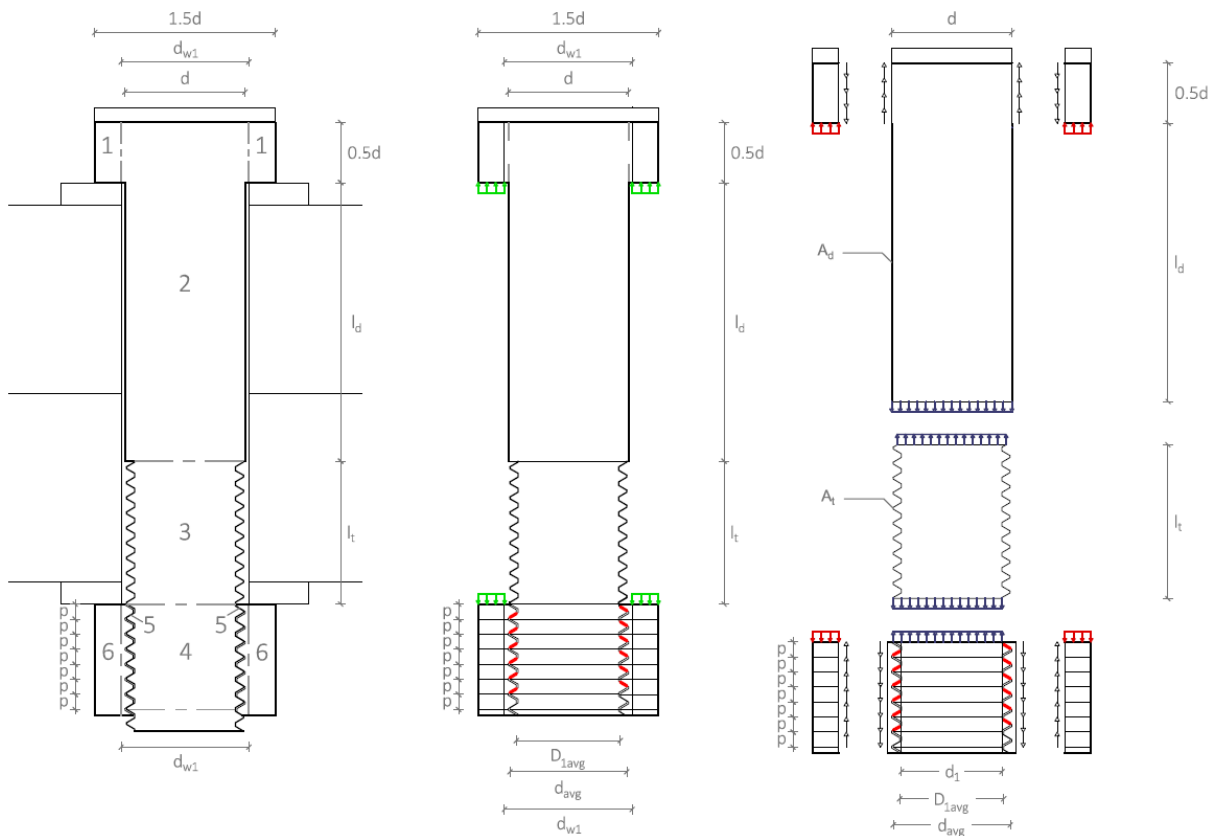


Figure 3.5.9: Subdivision of bolt

3.5.3.1 Creep bolt head interface (bearing)

A preload force in the bolt will result in a bearing stress between washer and bolt head as indicated in figure 3.5.10, the corresponding dataset is presented in table 3.5.6. The effective area is affected by the bearing surface outside diameter ($d_w = 1.5d$) as discussed in equation 3.8 and the inner diameter of the washer d_{w1} .

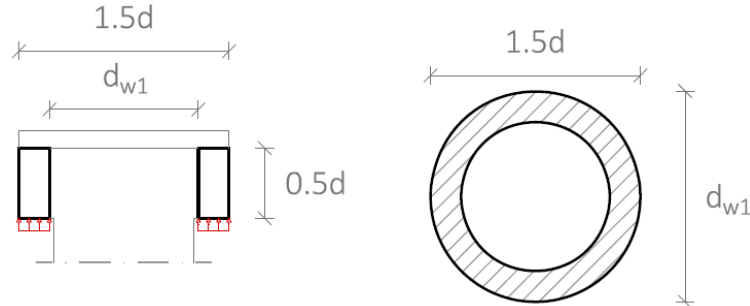


Figure 3.5.10: Effective area bolt head

		Dataset bolt head interface			
		M12	M16	M20	M24
d	[mm]	12	16	20	24
d_{w1}	[mm]	13	17	21	25

Table 3.5.6: Dataset bolt head interface used in calculation

The effective area can be calculated with the difference between the bolt head diameter and the inner diameter of the washer. The area and corresponding stress can be expressed with:

$$\sigma_{SK,b} = \frac{P}{A_{SK,b}} = \frac{P}{\frac{\pi}{4} \left((1.5d)^2 - d_{w1}^2 \right)} \quad (3.43)$$

With:

- $A_{SK,b}$: bearing interface bolt head - washer
- P : Preload force
- d : bolt diameter
- d_{w1} : inner diameter washer
- $\sigma_{SK,b}$: bearing stress at interface bolt head

As described in section 3.2 and equation 3.3, the substitutional extension length for the deformation of the bolt head l_{SK} can be approximated with $0.5d$ (Blatt 2003). Following the substitutional extension length, bearing creep is calculated over a height of $0.5d$. Since creep strain is related to stress as described in section 3.5.2, bearing creep can be calculated by multiplying the creep strain with the substitutional extension length:

$$\delta_{cr,SK,b} = \varepsilon_{cr,SK,b} \cdot 0.5d \quad (3.44)$$

With:

- d : bolt diameter
- $\delta_{cr,SK,b}$: creep bolt head, bearing
- $\varepsilon_{cr,SK,b}$: creep strain bolt, bearing

3.5.3.2 Creep unthreaded part (tension)

A preload force in the bolt will result in a tensile stress in the center of the bolt head and unthreaded part of the bolt as indicated in figure 3.5.11.

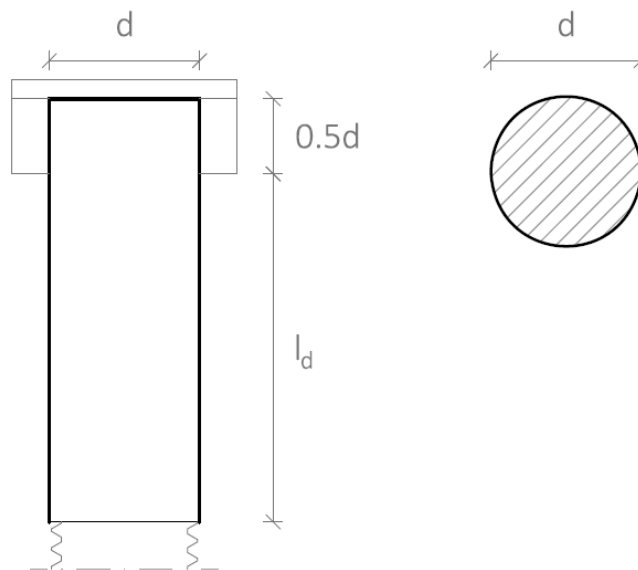


Figure 3.5.11: Effective area unthreaded part

The effective area and corresponding stress can be expressed with:

$$\sigma_{ld,t} = \frac{P}{A_d} = \frac{P}{\frac{\pi}{4}d^2} \quad (3.45)$$

With:

- A_d : nominal cross section unthreaded part
- P : preload force
- d : bolt diameter
- $\sigma_{ld,t}$: tension stress unthreaded length

Tension creep is calculated by multiplying the creep strain with the summation of the unthreaded length of the bolt and the substitutional extension length of the bolt head $0.5d$ since the center of the bolt head is assumed to be loaded in tension as indicated in figure 3.5.9 (right). Creep deformation of the unthreaded length can therefore be approximated by:

$$\delta_{cr,ld,t} = \varepsilon_{cr,ld,t} (0.5d + l_d) \quad (3.46)$$

With:

- d : bolt diameter
- l_d : length of the unthreaded part
- $\delta_{cr,ld,t}$: creep in unthreaded length, tension
- $\varepsilon_{cr,ld,t}$: creep strain unthreaded length, tension

3.5.3.3 Creep unengaged threaded part located in grip (tension)

A preload force in the bolt will result in a tensile stress in the threaded part of the bolt as indicated in figure 3.5.12, the corresponding dataset is presented in table 3.5.7.

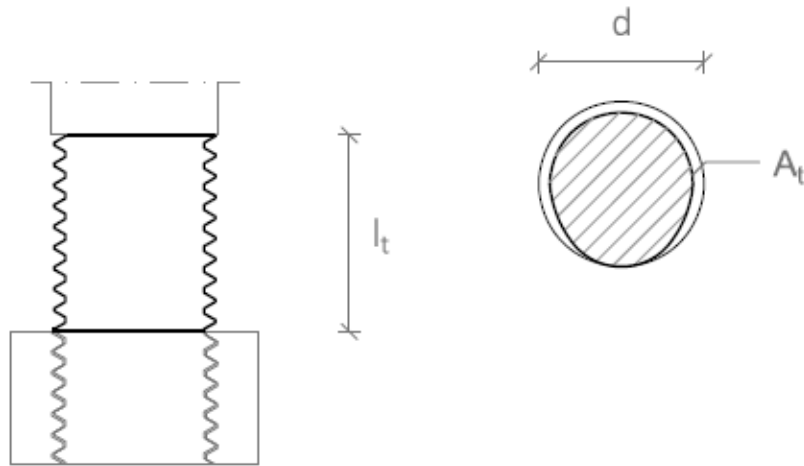


Figure 3.5.12: Effective area threaded part

Dataset bolt head interface					
		M12	M16	M20	M24
A_t	[mm ²]	84.3	157	245	353

Table 3.5.7: Dataset used in calculation

The effective area and corresponding stress can be expressed with:

$$\sigma_{lt,t} = \frac{P}{A_t} \quad (3.47)$$

With:

- A_t : reduced-shank cross section
- P : preload force
- $\sigma_{lt,t}$: tension stress threaded length

Comparable with the determination of tension creep in the unthreaded part and the bolt head, tension creep is calculated by multiplying the creep strain with the threaded length located in the grip:

$$\delta_{cr,lt,t} = \varepsilon_{cr,lt,t} l_t \quad (3.48)$$

With:

- l_t : length of the threaded part located in grip length
- $\delta_{cr,lt,t}$: creep in threaded length located in grip length, tension
- $\varepsilon_{cr,lt,t}$: creep strain threaded length located in grip length, tension

3.5.3.4 Creep engaged threaded part center bolt located in nut (tension)

The tensile force in the threaded part of the bolt located in the nut is decreasing due the connection with the threads. The stress distribution in the threads is known to be maximum at the first engaged thread and minimum at the free threads at the end of the bolt (Brien 2009). The elastic distribution is illustrated and given in figure 3.5.13.

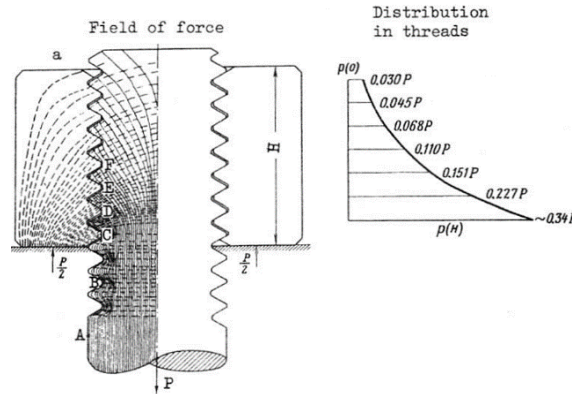


Figure 3.5.13: Elastic load distribution threaded joint (Brien 2009)

The load distribution will deviate if the preload force results in yielding of one of the threads. Once a thread yields the remaining threads take most of the increasing load (Moeller 2016). Moeller determined the force distribution with respect to the preload force. The load distribution is simplified in a specific percentage of the load per thread. The results are presented in figure 3.5.14.

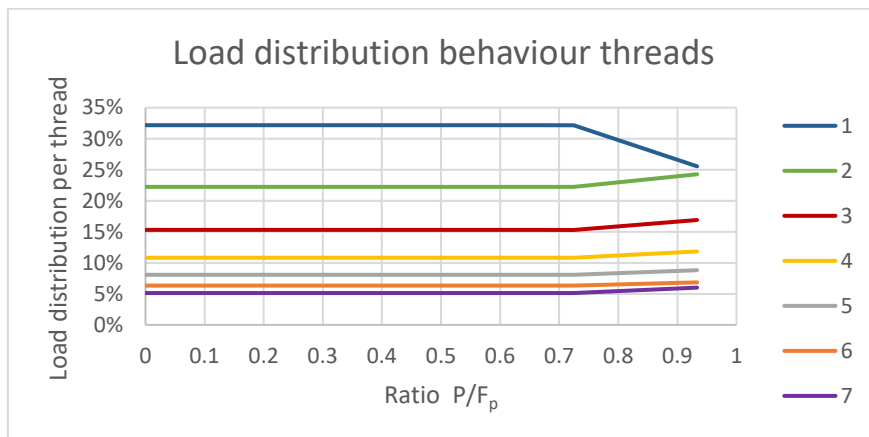


Figure 3.5.14: Load distribution threaded joint accounting for yielding

The elastic load distribution in the threaded area up to yielding (using the distribution found by Moeller) can be calculated by subtracting the load per thread from the applied preload force. The distribution is presented in table 3.5.8.

Cumulative load distribution		
Thread number	$\Delta P/P$	P_i
1	32%	P
2	22%	$0.68P$
3	16%	$0.46P$
4	11%	$0.30P$
5	8%	$0.19P$
6	6%	$0.11P$
7	5%	$0.05P$

Table 3.5.8: Cumulative load distribution threaded joint

The effective area and part numbers are indicated in figure 3.5.15. The effective diameter is considered to be the minor diameter of the bolt using tolerance class 6g. The dataset presented in table 3.5.9 contains the pitch height and minor diameter versus bolt diameter.

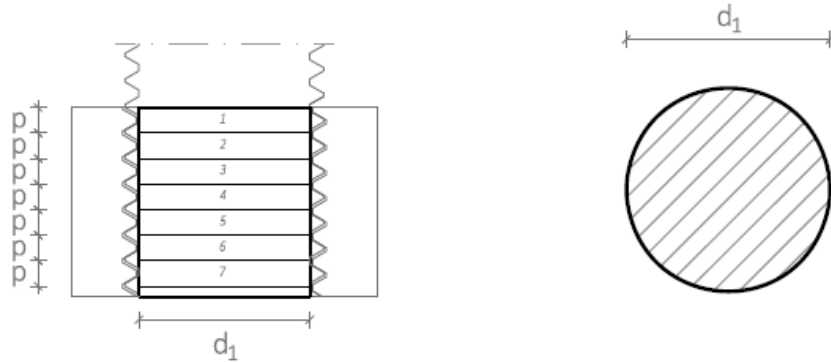


Figure 3.5.15: Effective area and distribution threaded part located in nut

Dataset threaded length (located in nut)					
		M12	M16	M20	M24
d_1	[mm]	10.106	13.835	17.294	20.752
p	[mm]	1.75	2.0	2.5	3.0

Table 3.5.9: Dataset threaded length (located in nut) used in calculation

The effective area and stress in the different parts of the center of the bolt can be expressed with:

$$\sigma_{G,t,i} = \frac{P_i}{A_{d_1}} = \frac{P_i}{\frac{\pi}{4}d_1^2} \quad (3.49)$$

With:

- A_{d_1} : cross section of threaded part at minor diameter
- d_1 : basic minor diameter bolt
- P_i : preload force at thread number i
- $\sigma_{G,t,i}$: tension stress threaded length located in nut at thread number i

The total tensile creep of the threaded part of the center of the bolt located in the nut is calculated with the summation of the different parts taking into account the deviating load distribution in the threads. Tension creep of one part is calculated by multiplying the creep strain with the pitch height:

$$\delta_{cr,G,t} = \varepsilon_{cr,G,t,1}P + \varepsilon_{cr,G,t,2}P + \varepsilon_{cr,G,t,3}P + \varepsilon_{cr,G,t,4}P + \varepsilon_{cr,G,t,5}P + \varepsilon_{cr,G,t,6}P + \varepsilon_{cr,G,t,7}P \quad (3.50)$$

With:

- p : pitch height
- $\delta_{cr,G,t}$: creep in threaded length located in the nut, tension
- $\varepsilon_{cr,G,t,i}$: creep strain in threaded length located in the nut, thread number i, tension

3.5.3.5 Creep engaged thread interface bolt-nut (bearing)

The stresses in the threads can be calculated using the load distribution presented in figure 3.5.14 and table 3.5.8. The effective area per pitch height is calculated with the difference between the average major diameter of the bolt and average major diameter of the nut as indicated in figure 3.5.16. Tolerance class 6h is used together with the basic profile of a thread described in ISO 68-1 (figure 3.5.17). The corresponding dataset is presented in table 3.5.10.

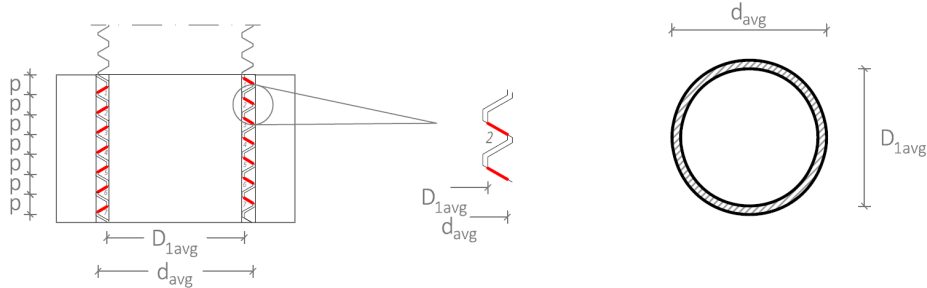


Figure 3.5.16: Effective area threaded part

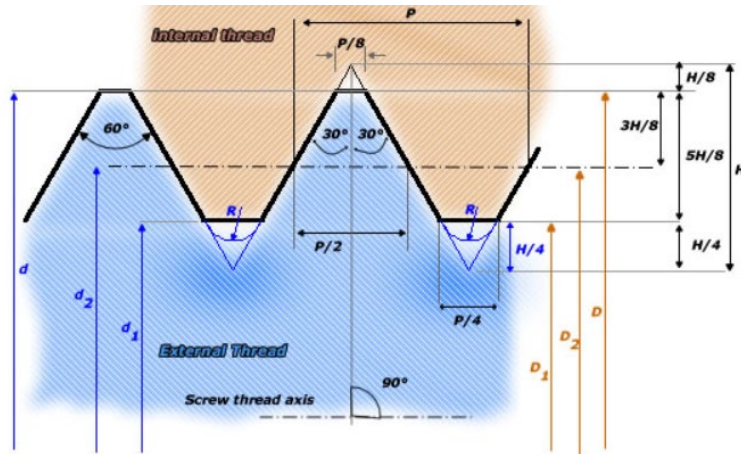


Figure 3.5.17: ISO metric screw thread basic profile according to ISO 68-1 (amesweb.info)

Dataset thread interface		M12	M16	M20	M24
d_{avg}	[mm]	11.850	15.822	19.791	23.765
D_{1avg}	[mm]	10.526	14.023	17.519	21.002

Table 3.5.10: Dataset thread interface used in calculation

The effective area and corresponding stress per thread can be expressed with:

$$\sigma_{G,b,i} = \frac{P_i}{A_G} = \frac{P_i}{\frac{\pi}{4} (d_{min}^2 - D_{1max}^2)} \quad (3.51)$$

With:

- A_G : bearing area engaged threads
- D_{1max} : maximum minor diameter nut
- P_i : preload force at thread number i
- d_{min} : minimum major diameter bolt
- $\sigma_{G,b,i}$: bearing stress threads at thread number i

Bearing creep of one thread is calculated by multiplying the creep strain with the pitch height. The cumulative bearing creep of the threads is calculated with the summation of the separate parts corresponding with the load distribution in the threads:

$$\delta_{cr,G,b,1...6} = \varepsilon_{cr,G,b,1}p + \varepsilon_{cr,G,b,2}p + \dots \varepsilon_{cr,G,b,7}p \quad (3.52)$$

With:

- p : pitch height
- $\delta_{cr,G,b,1...6}$: creep in threads, bearing, cumulative 1-7
- $\varepsilon_{cr,G,b,1}p$: creep strain in thread, bearing, thread i

3.5.3.6 Creep interface nut - washer (bearing)

The bearing stress in the interface between the washer and the flanks of the nut as indicated in figure 3.5.18 is decreasing towards the free end of the bolt due the connection with the threads. The used load distribution is identical to table 3.5.8, the corresponding dataset is identical to table 3.5.6. Comparable with the derivation of creep of the bolt head, the effective area is affected by the bearing surface outside diameter ($d_w = 1.5d$) as discussed in equation 3.8.

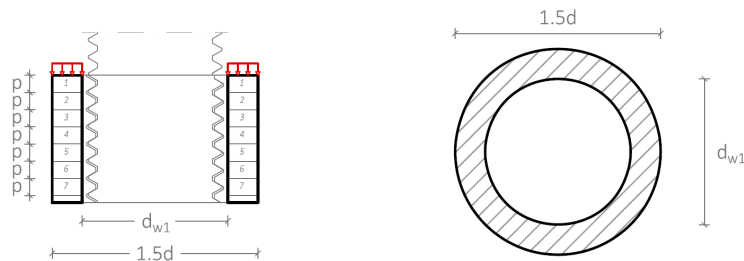


Figure 3.5.18: Effective area flank nut

The effective area can be calculated with the difference between the nut diameter and the inner diameter of the washer. The area and corresponding stress can be expressed as:

$$\sigma_{M,b,i} = \frac{P_i}{A_M} = \frac{P_i}{\frac{\pi}{4} \left((1.5d)^2 - d_{w1}^2 \right)} \quad (3.53)$$

With:

- A_M : bearing area nut
- P_i : preload force at thread number i
- d : bolt diameter
- d_{w1} : inner diameter washer
- $\sigma_{M,b,i}$: bearing stress threads at thread number i

Bearing creep of one part is calculated by multiplying the creep strain with the pitch height. The cumulative bearing creep in the threads is calculated with the summation of the creep in the 7 parts:

$$\delta_{cr,M,b,1...7} = \varepsilon_{cr,M,b,1}p + \varepsilon_{cr,M,b,2}p + \dots \varepsilon_{cr,M,b,7}p \quad (3.54)$$

With:

- p : pitch height
- $\delta_{cr,M,b,1...7}$: creep in nut flank, bearing, cumulative 1-7
- $\varepsilon_{cr,M,b,i}$: creep strain in nut flank, bearing, thread i

3.5.4 Parametric study

The preload variation due to relaxation in a joint with A4 80 stainless steel bolts and aluminium plates is examined with varying preload levels. As can be observed in equation 3.24, the joint stiffness k_j and subsequently the joint material are affecting the preload loss. Plate creep is not considered, section 3.6 will focus on this subject. Furthermore, embedment effects are not taken into account to distinguish the impact of relaxation separately. The preload losses are determined with equations 3.24 and 3.42 in combination with tables 3.3.1, 3.3.2 and 3.3.3. The relative preload losses, defined as preload loss versus initial preload force, after 50 years are presented in figure 3.5.19. The effect of the total plate thickness on the relative preload loss for P_{nom} is shown in figure 3.5.20. The initial preload force is presented proportional with the proof load of the bolt. The ratio between the nominal minimum preload force P_{nom} and the proof load F_p is equal to:

$$\frac{P_{nom}}{F_p} = \frac{0.7 f_{ub} A_t}{f_{0.2} A_t} = \frac{0.7 \cdot 800}{600} \approx 0.93 \quad \rightarrow \quad P_{nom} \approx 0.93 F_p \quad (3.55)$$

With:

- A_t : reduced-shank cross section
- F_p : proof load bolt
- $f_{0.2}$: 0.2% proof strength bolt material
- f_{ub} : ultimate strength bolt material

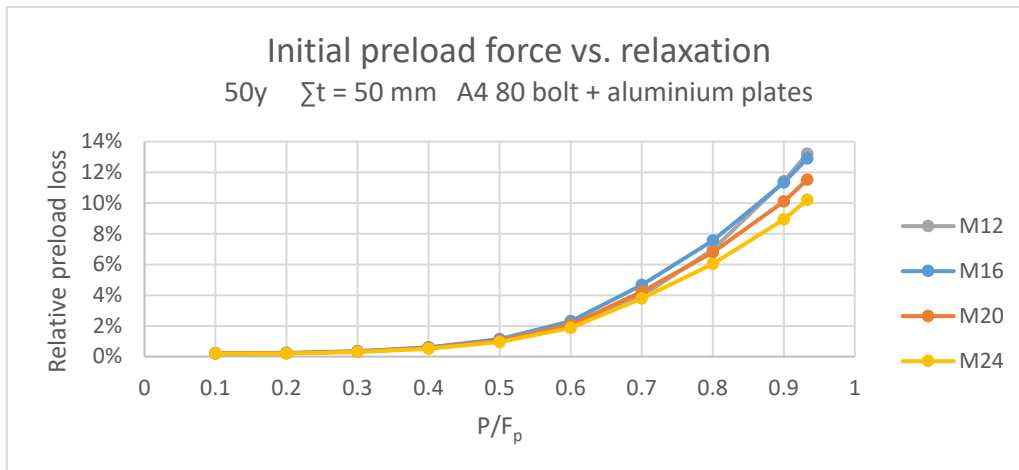


Figure 3.5.19: Preload loss due to relaxation after 50 years versus initial preload force

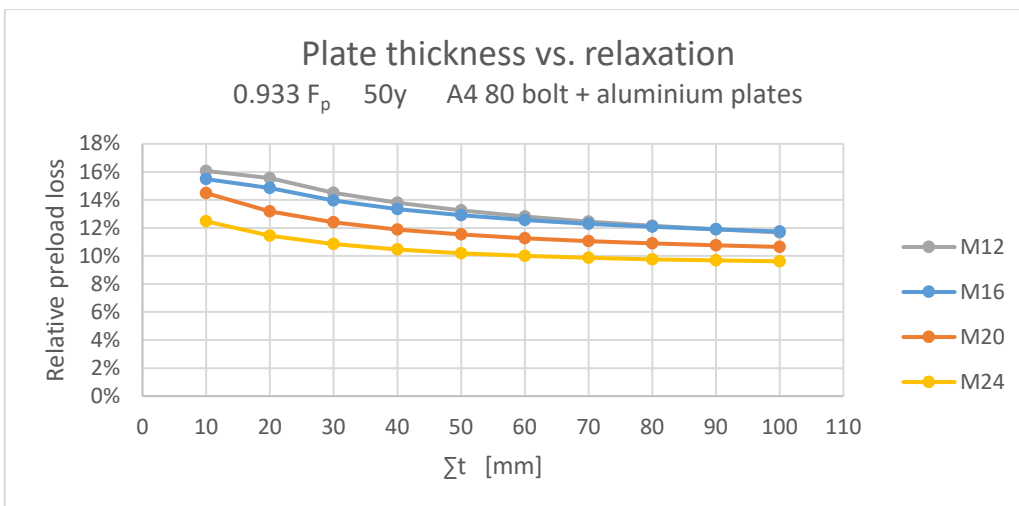


Figure 3.5.20: Preload loss due to relaxation after 50 years vs. total thickness plates at $0.93F_p$

The preload behaviour of a joint containing an M16 bolt and a total plate thickness $\sum t = 50$ mm at $0.933F_p$ is examined for 10 hours, 42 days (= 1000 hours) and 50 years. The results are presented in figures 3.5.21, 3.5.22 and 3.5.23.

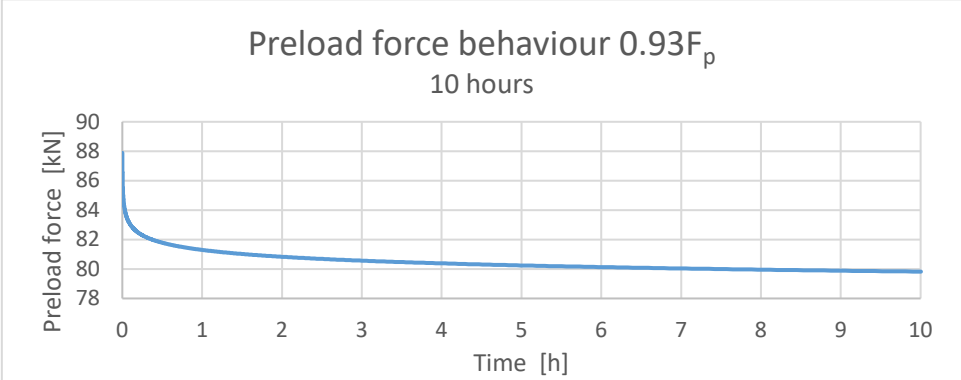


Figure 3.5.21: Preload behaviour 10 hours

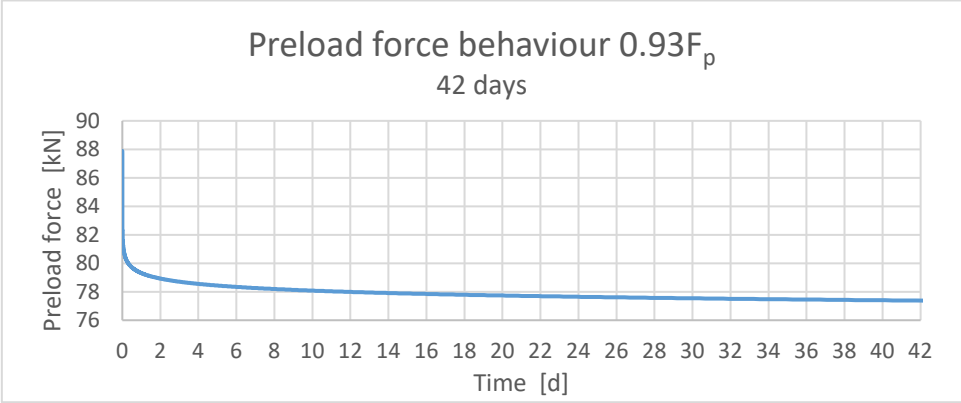


Figure 3.5.22: Preload behaviour 42 days

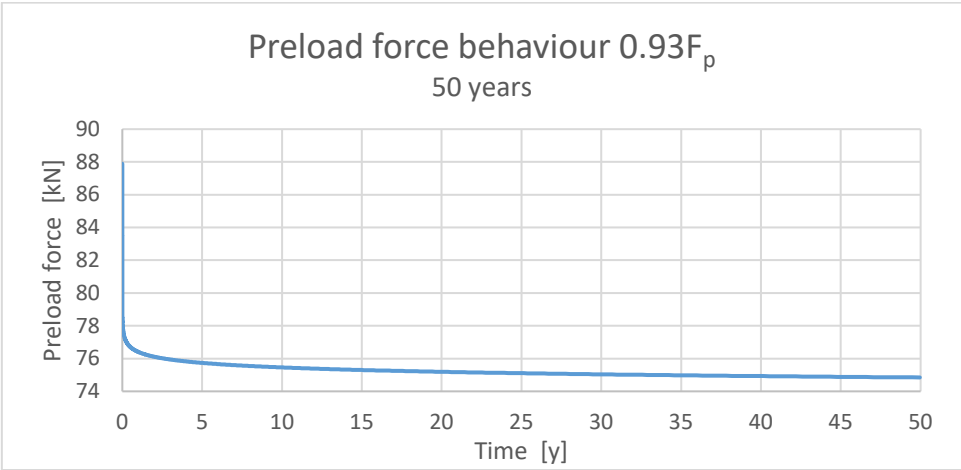


Figure 3.5.23: Preload behaviour 50 years

The model seems to be in agreement with the observations obtained in section 2.3 regarding the amount of expected preload losses. It can be concluded that relaxation can lead to preload losses up to 16% in the case of a short plate packages and small bolt diameters. Furthermore, the majority of the preload losses occur in a relatively short time after application of the preload force. To gain insight in the preload behaviour just after application of the preload force. The preload behaviour of the first minute after tightening is presented in figure 3.5.24.

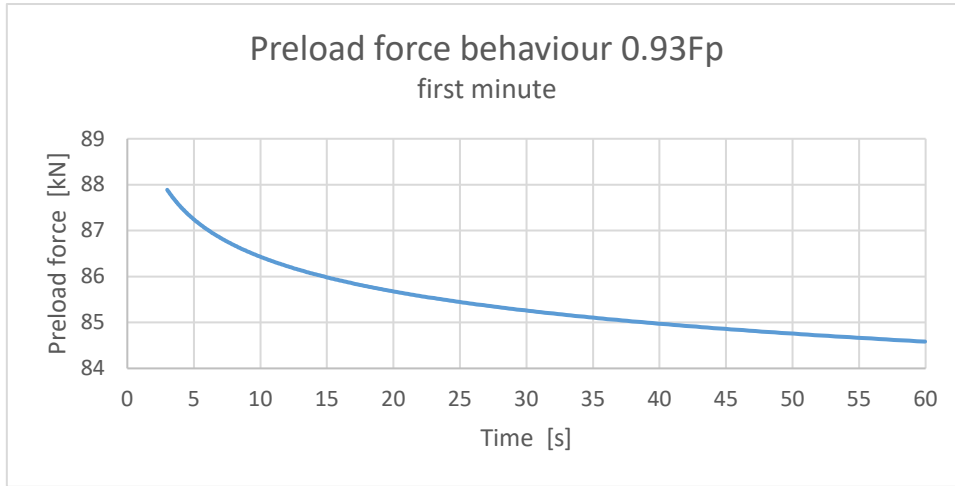


Figure 3.5.24: Preload behaviour 1 minute

It can be observed that substantial preload losses occur in the first minute after tightening. The time needed for application of the preload force $t_{assembly}$ and, subsequently, the assumption to exclude the first 3 seconds after tightening to exclude elastic and initial plastic strain during assembly (Afzali et al. 2017) will have a significant impact on the preload level after 50 years. The impact of the assembly time can be analyzed by replacing the fixed value $t_{assembly} = 3s$ used in equation 3.38 with a variable value for $t_{assembly}$:

$$t(n) = t_{assembly} \cdot 1.01^n \quad (3.56)$$

Using equation 3.56, the impact of the assembly time on the preload force after 50 years is analyzed for an aluminium joint with a total plate thickness $\sum t = 50$ mm combined with an A4 80 M16 bolt preloaded up to $0.933F_p$. The results are presented in figure 3.5.25.

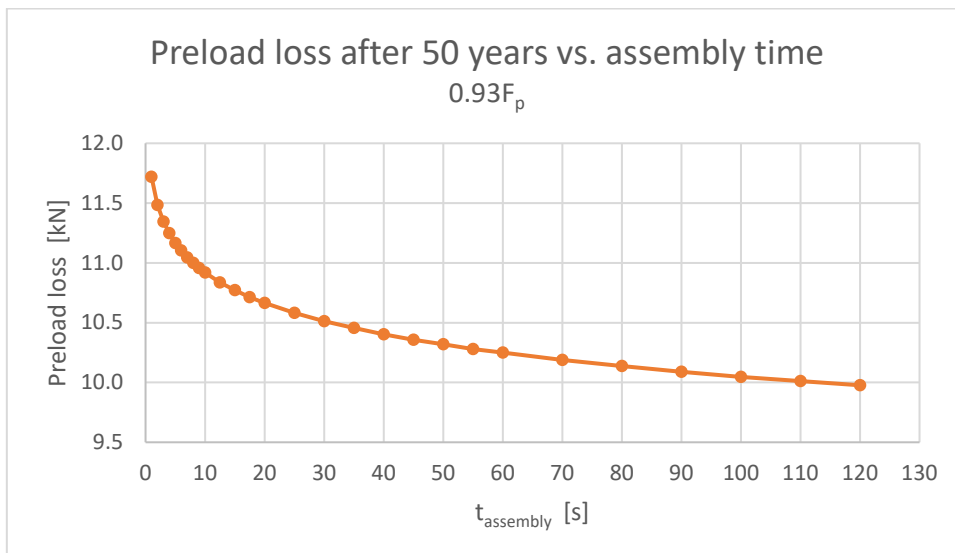


Figure 3.5.25: Influence of the time needed for assembly on the preload loss after 50 years

It can be concluded that rapid tightening will lead to increased preload losses compared to slow tightening. As can be observed in figure 3.5.25, the assembly time has a significant impact on the preload loss. The relationship between preload losses and assembly time appears to be logarithmic:

$$\Delta P_{cr,b} = 11.755 - 0.368 \ln(t_{assembly}) \quad (3.57)$$

3.6 Plate creep

3.6.1 Theory

Comparable with embedment creep, plate creep due to bearing stresses caused by a preload force will result in loss of preload force due to unimpeded reduction of the thickness of the clamped part of the bolted joint. This principle is visualized in figure 3.6.1.

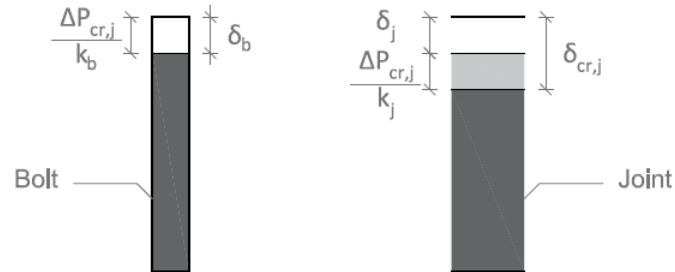


Figure 3.6.1: Visualization of equal deformations during plate creep

The formulae regarding embedment creep are adjusted to estimate the impact of plate creep:

$$\delta_b = \delta_j \rightarrow \frac{\Delta P_{cr,j}}{k_b} = \delta_{cr,j} - \frac{\Delta P_{cr,j}}{k_j} \rightarrow \Delta P_{cr,j} = \delta_{cr,j} \left(\frac{k_b k_j}{k_b + k_j} \right) \quad (3.58)$$

With:

$\Delta P_{cr,j}$: loss of preload due to plate creep

$\delta_{cr,j}$: total amount of plate creep

3.6.2 Creep properties plate material

Plate creep in carbon steel and stainless steel is negligible (Afzali et al. 2017), therefore the analysis is limited to aluminium joints combined with a stainless steel bolt. As mentioned in 2.4, the amount of creep is related to the occurring stress; higher stresses will result in more creep. Creep properties of aluminium alloys at constant various temperatures are published by The Aluminium Association and Kaufmann (J.G. Kaufmann 1999). Creep data regarding 5083O/H111 and 6082T6 is not available or insufficient, therefore the calculations will include alloys 5454O and 6061T6. Both alloys exhibit more or less comparable proof and ultimate strength values at room temperature as the aforementioned alloys, as can be observed in table 3.6.1.

Physical properties aluminium alloys					
		5083O ¹	5454O ¹	6082T6 ²	6061T6 ²
f_o	[N/mm ²]	145	115	240	240
f_u	[N/mm ²]	290	250	290	290

Table 3.6.1: Proof and tensile properties (¹J.G. Kaufmann 1999; ²NEN-EN 1999-1-1 2013)

Kaufmann presented the amount of expected creep at room temperature versus time for various stresses. The available data for 5454O and 6061T6 are presented in figure 3.6.2 and figure 3.6.3. The creep strain behaviour will evolve logarithmic in time as discussed in 2.4, therefore logarithmic trendlines are added between the data points of Kaufmann and an origin with coordinate (1, 0).

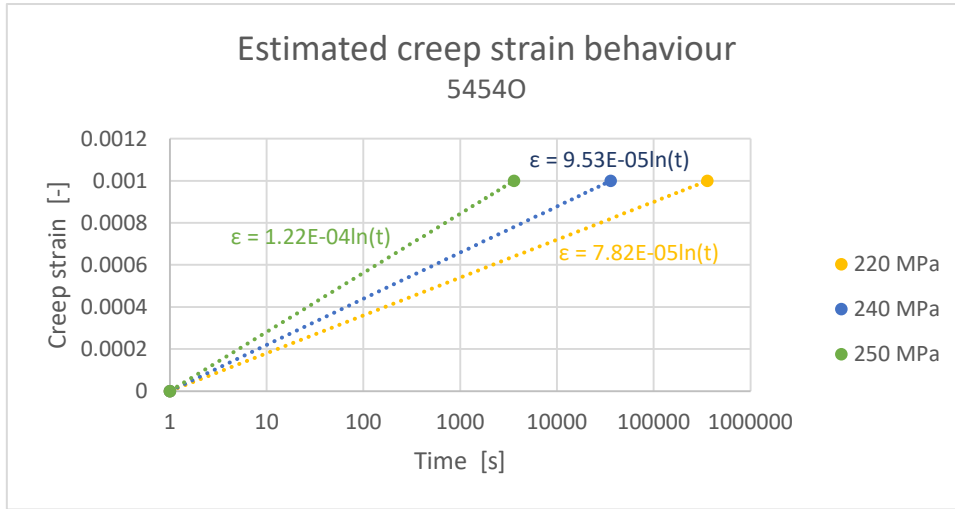


Figure 3.6.2: Estimated logarithmic creep strain rate behaviour 5454 O using data Kaufmann

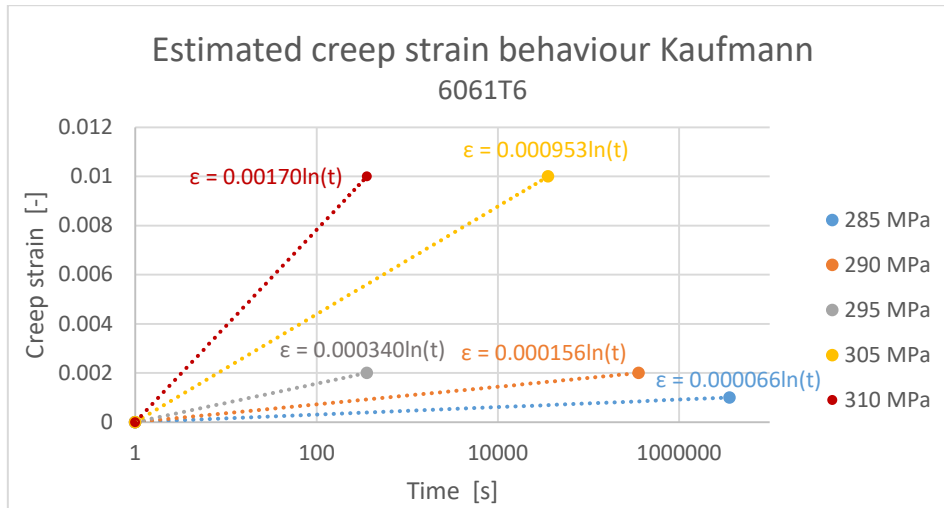


Figure 3.6.3: Estimated logarithmic creep strain rate behaviour 6061T6 using data Kaufmann

Using the logarithmic creep strain relationship, a creep strain rate behaviour can be estimated by taking the first derivative of the logarithmic creep strain behaviour. The creep strain rate behaviour has the following basic relationship:

$$\varepsilon'_{cr}(t) = a \cdot t^{-1} \quad (3.59)$$

The basic relationship of the creep strain rate behaviour is a reciprocal function of t multiplied with a scaling factor a . The scaling factor a depends on the applied stress. The creep strain rate relationship is identical to the creep strain rate behaviour of austenitic stainless steel with a deviating creep parameter function $f_1(\sigma)$:

$$\varepsilon'_{cr}(t) = f_1(\sigma) t^{-1} \quad (3.60)$$

If the scaling factor $f_1(\sigma)$ is plotted versus stress, a creep parameter function can be formulated that enables estimation of the creep strain rate at various stresses. The creep parameter function $f_1(\sigma)$ is reported to have a power law relationship (Ahmad et al. 2017). Figures 3.6.4 and 3.6.5 evaluate the behaviour of 5454O and 6061T6 derived from the slope of the creep strain rate behaviour (first derivative of the logarithmic creep strain) of the various stress levels and accompanying trend lines considered in figure 3.6.2 and figure 3.6.3. The creep parameter functions $f_1(\sigma)$ corresponding to the trendlines are listed in table 3.6.2.

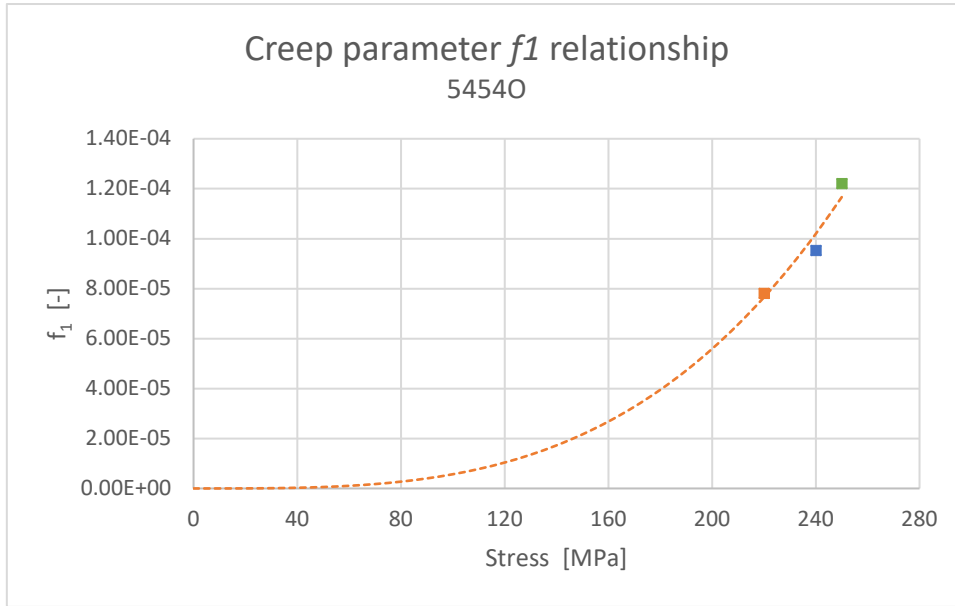


Figure 3.6.4: Creep parameter f_1 vs. applied stress 5454 O with trendline

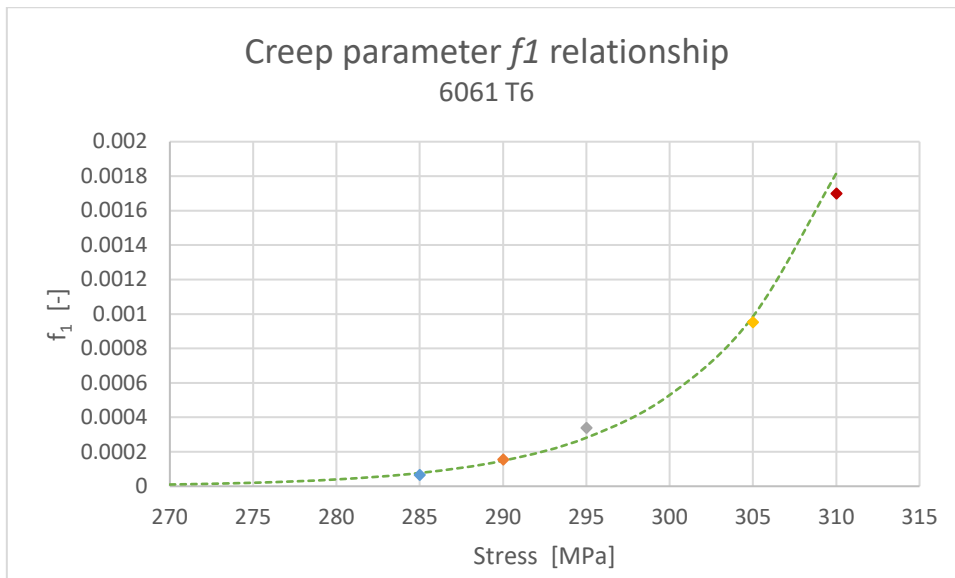


Figure 3.6.5: Creep parameter f_1 vs. applied stress 6061T6 with trendline

Creep parameter function $f_1(\sigma)$			
		5454O	6061T6
$f_1(\sigma)$	[-]	$1.4530E-12 \cdot \sigma^{3.2964}$	$4.6338E-97 \cdot \sigma^{37.567}$

Table 3.6.2: Creep parameter function $f_1(\sigma)$ derived from trendlines

The creep parameter functions listed in table 3.6.2 can be used in combination with the proposed discrete time model discussed in 3.5.2. To exclude initial creep strain during assembly, the start of the discrete model is again set at $t=3s$. The time increment function and time function corresponding with the interval numbers are therefore identical to the discrete time model used during the analysis of relaxation of stainless steel:

$$dt(n) = 0.03 \cdot 1.01^n \quad (3.61)$$

$$t(n) = 3 \cdot 1.01^n \quad (3.62)$$

3.6.3 Model stress distribution

As discussed in section 3.2, the area in the joint affected by compression widens from the bolt head and nut toward the interface of the plates and will create a frustum. The compressive stress is decreasing with respect to the height of the clamped area as visualized in figure 3.6.6. The creep parameter function, determined in 3.6.2, can be used to calculate creep strain behaviour at any stress.

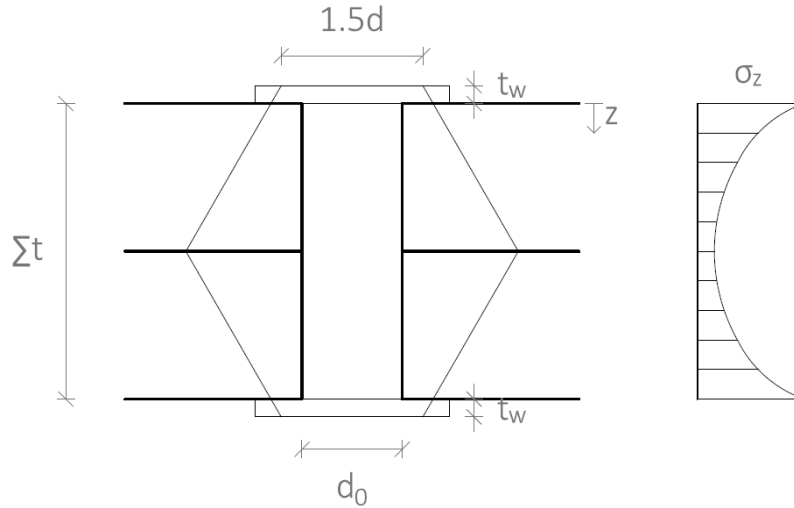


Figure 3.6.6: Load distribution (left) and stress distribution (right) bolted joint

The decreasing stress with respect to the height of the clamped area is visualized in figure 3.6.6. The relationship corresponding the stress with the height of the joint is equal to:

$$\sigma_z = \frac{P}{A(z)} \quad \rightarrow \quad \sigma_z = \frac{P}{\frac{\pi}{4} \left((1.5d + 2t_w \tan 30 + 2z \tan 30)^2 - d_0^2 \right)} \quad (3.63)$$

With:

- $A(z)$: bearing surface area in z-direction
- P : initial preload force
- d : bolt diameter
- d_0 : diameter bolt hole
- t_w : washer thickness
- Z : depth in z-direction
- σ_z : bearing stress in z-direction

The amount of plate creep in a frustum can be calculated by taking the integral of the creep strain over the height of the frustum. Since a symmetrical joint contains two identical frusta, the total amount of plate creep is equal to:

$$\delta_{cr,j} = 2 \cdot \int_0^{\Sigma t/2} \varepsilon_{cr,j} dz \quad (3.64)$$

The integral describing the plate creep can be simplified by dividing the height of the clamped area into cylinders with a height of dz as illustrated in figure 3.6.7. The stress corresponding to the effective area is assumed to be equal over the full height of the cylinders. The effective area is calculated at the top height of the cylinders. Therefore, this model will give an overestimation of the expected creep.

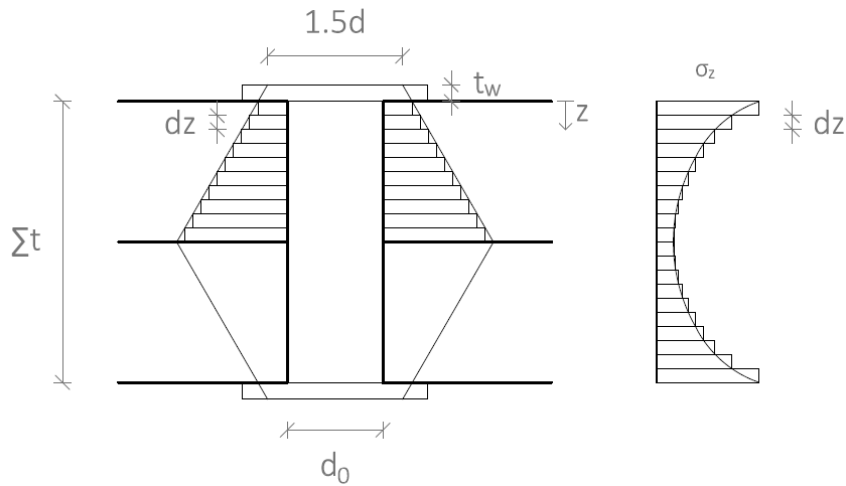


Figure 3.6.7: Simplified load and stress distribution joint

The total amount plate creep and corresponding preload loss behaviour, calculated with the model shown in figure 3.6.7, can be determined with the summation of the plate creep of the separate cylinders. The accuracy of the model improves when dz approaches zero. To determine a suitable value of dz , the preload loss after 50 years is calculated with a varying dz for two variations of aluminium alloy combined with an M16-bolt preloaded up to P_{nom} . Since the most dominant region regarding plate creep is located near the interface of the plate and the washer, the analysis is performed with a short plate package thickness of $\Sigma t = 10$ mm. The results can be found in figures 3.6.8 and 3.6.9.

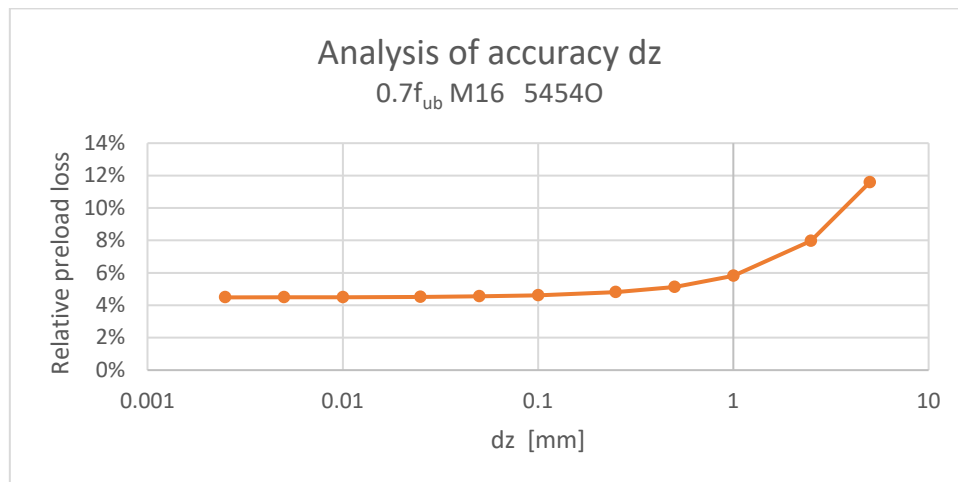


Figure 3.6.8: Analysis of accuracy dz with 54540

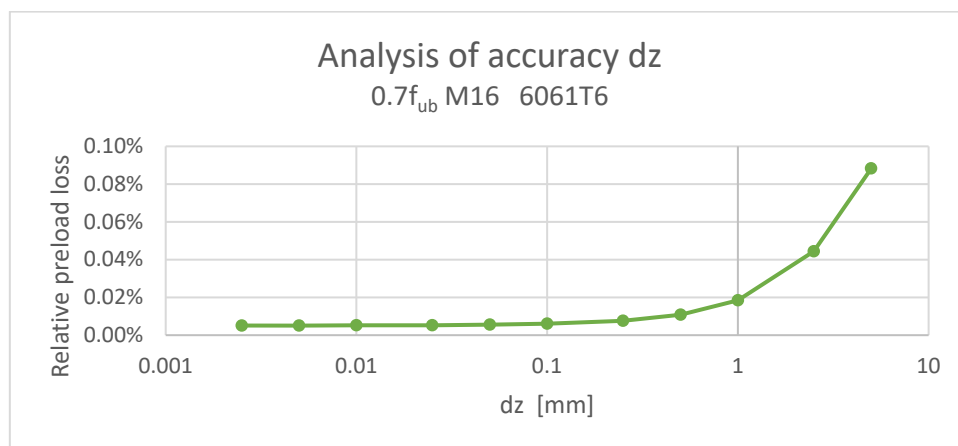


Figure 3.6.9: Analysis of accuracy dz with 6061T6

It can be concluded that convergence is reached at a dz of 0.1 mm for both alloys. Further improvement of dz will lead to more accurate results, but will lead to a less computational efficient model. Since the model will lead to an overestimation of the plate creep, the results will be conservative.

The effect of the variation of the initial preload force on plate creep is tested with a stainless steel M16 bolt combined with $\Sigma t = 50$ mm. The results are presented in figure 3.6.10. The initial preload force is presented proportional with the proof load of the bolt F_p .

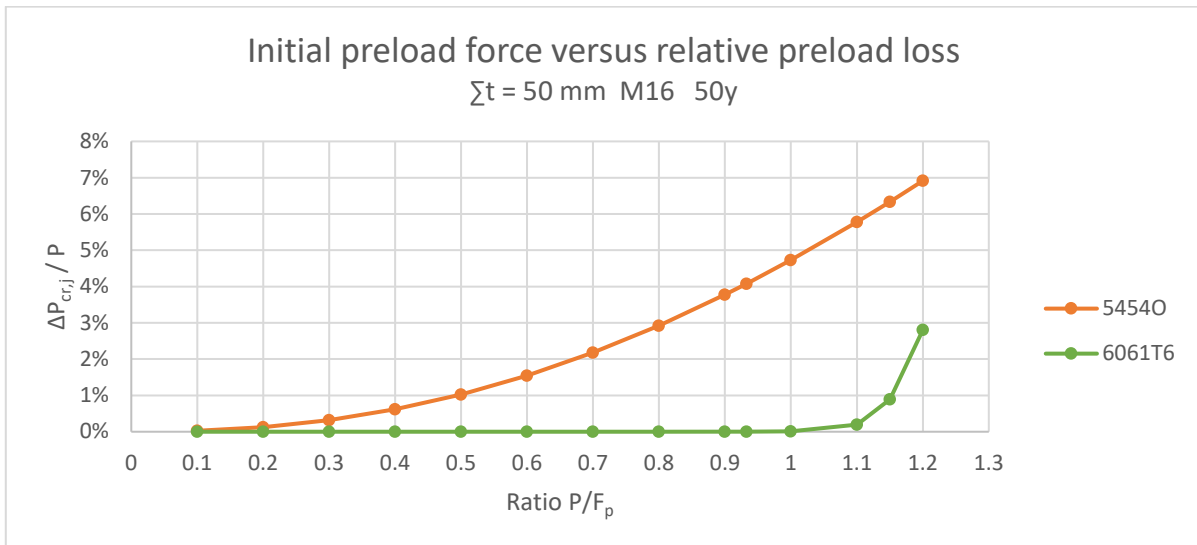


Figure 3.6.10: Effect of variation preload force versus relative preload loss

It can be discovered that preload loss due to aluminium creep gradually increases with increasing initial preload forces. Creep in 6061T6 only exists at preload forces above the proof load of the bolt. Therefore, 6061T6 will be excluded in the parametric study and the analysis is limited to 5454O.

3.6.4 Parametric study

Following the analysis regarding the variation of preload force shown in figure 3.6.10, the analysis is extended with a parametric study containing a variation of bolt diameter. The relative preload losses are presented in figure 3.6.11.

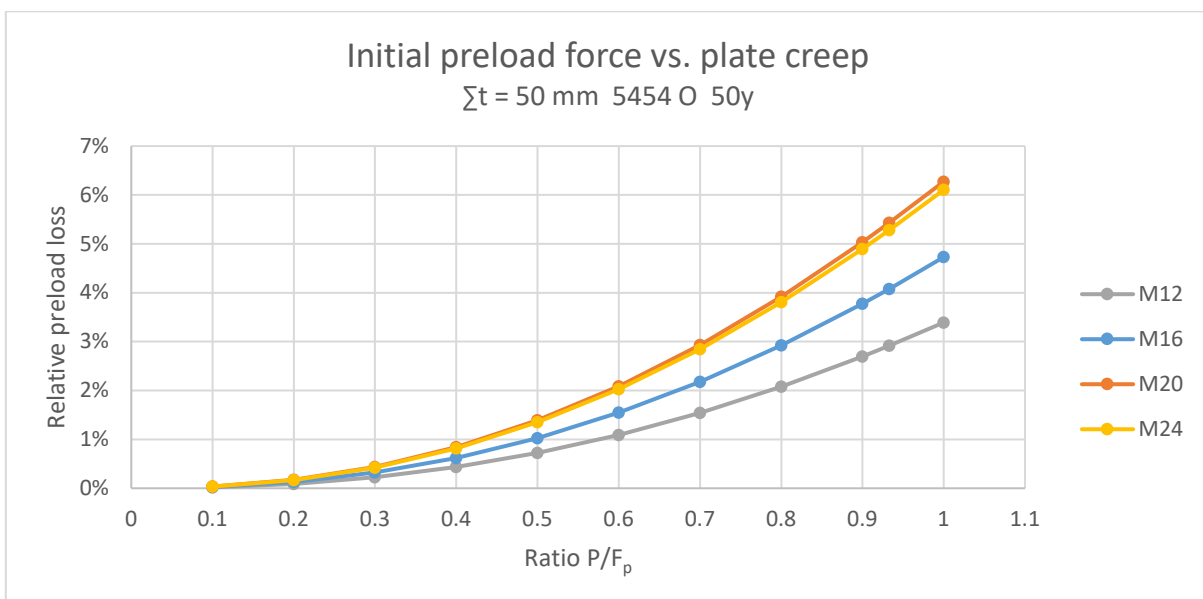


Figure 3.6.11: Relative preload loss due to aluminium creep of 5454O after 50 years

A deviation in preload loss behaviour can be observed with the application of M20 bolts. This bolt diameter is more susceptible for plate creep due to the use of a relatively thin washer compared with other bolt diameters. A lower washer thickness will result in a decreased bearing surface area in the interface between washer and plate and subsequently higher bearing stresses.

The effect of a variation of the total plate thickness is analyzed with an initial preload force of $0.93F_p$ ($=P_{nom}$). The relative preload losses are presented in figures 3.6.12.

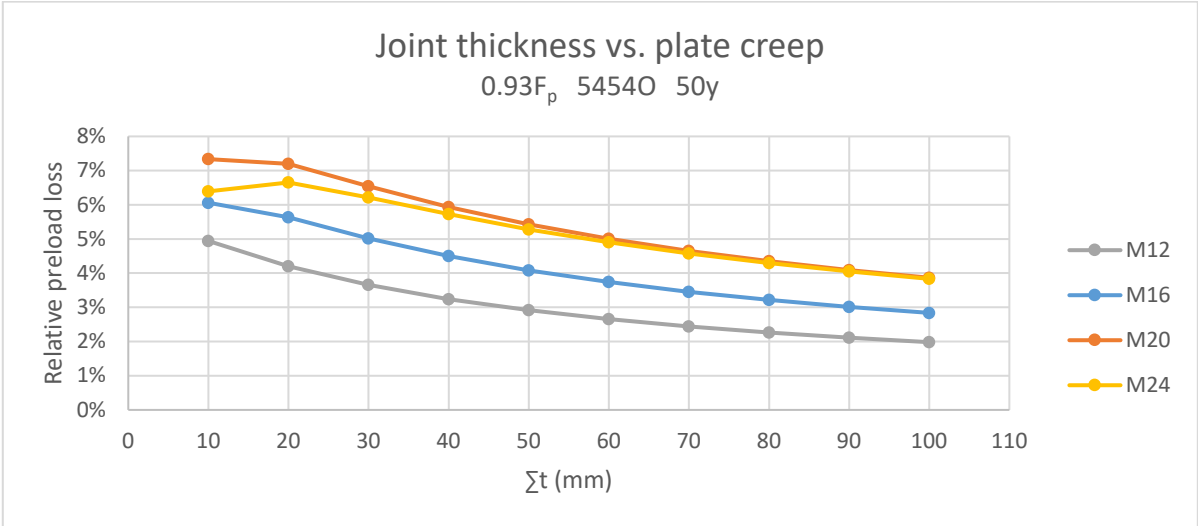


Figure 3.6.12: Preload loss due to creep of 54540 after 1000h vs. total thickness plates with $P = P_{nom}$

Comparable with the preload loss behaviour experienced with embedment creep, preload losses due to plate creep become less dominant with increasing joint thickness with the exception of $d = M24$. A maximum preload loss is observed with $\Sigma t = 20$ mm indicating that the majority of plate creep occurs in the top 10 mm of the plate. A maximum preload loss of 7.3% was experienced with $d = M20$ combined with $\Sigma t = 10$ mm. The application of a more common thickness of $\Sigma t = 50$ mm combined with an initial preload force of P_{nom} will lead to preload losses of 2.9% – 5.4%.

The preload behaviour of a joint containing an M16 bolt and a total plate thickness $\Sigma t = 50$ mm at $0.93F_p$ is examined for 10 hours, 42 days (=1000 hours) and 50 years. The results are presented in figures 3.6.13, 3.6.14 and 3.6.15.

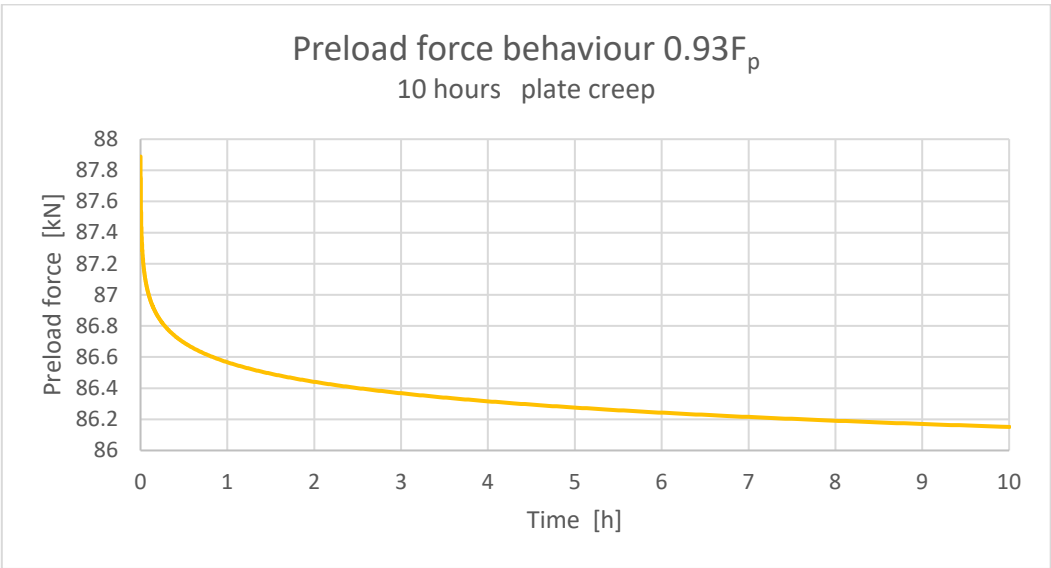


Figure 3.6.13: Preload behaviour plate creep 10 hours

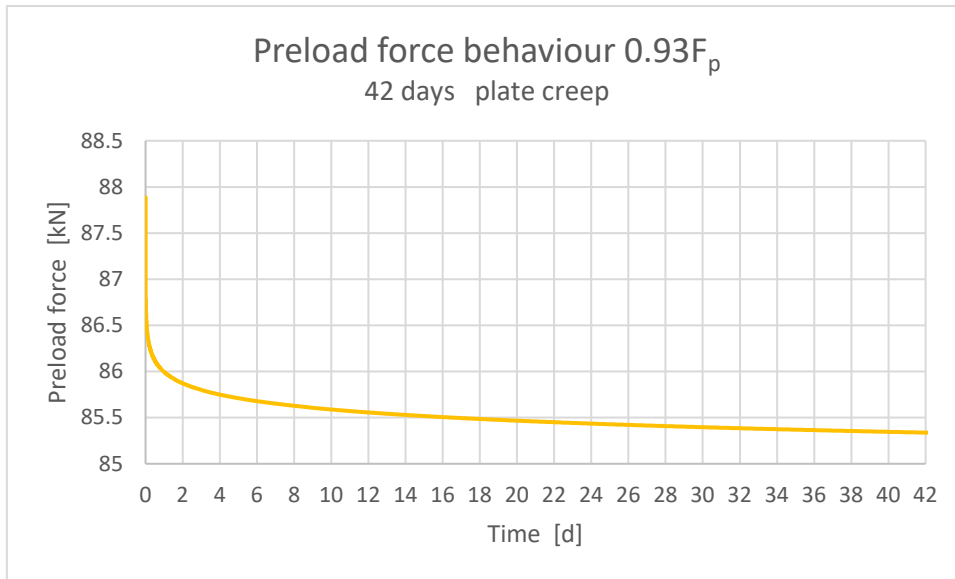


Figure 3.6.14: Preload behaviour plate creep 42 days

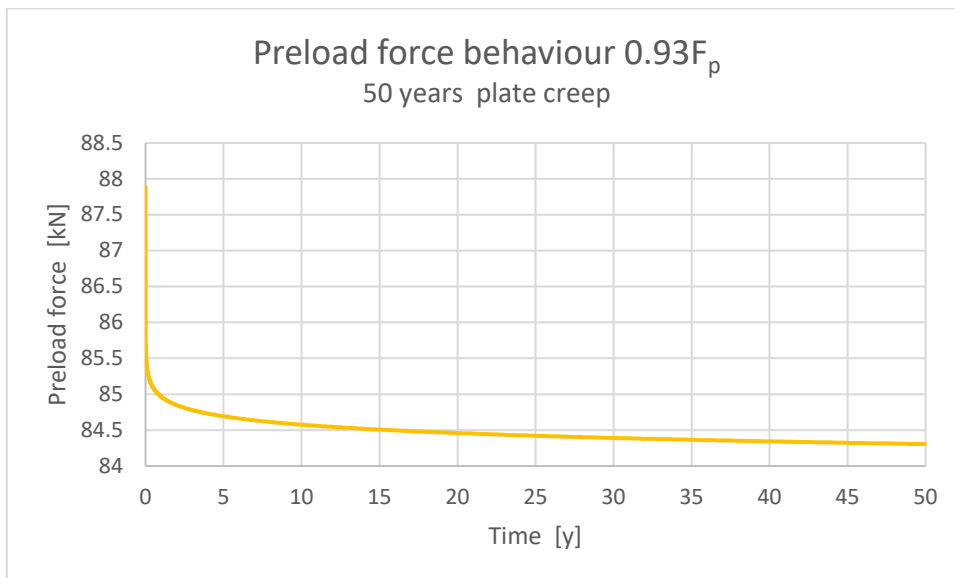


Figure 3.6.15: Preload behaviour plate creep 50 years

Comparable with bolt relaxation, the majority of the preload losses occur in a relatively short time after application of the preload force. It can be concluded that plate creep in aluminium has a smaller impact on the preload loss behaviour of bolted joints compared to the relaxation behaviour of stainless steel. Furthermore, if the plate material will include 6061T6 or 6082T6, the creep effects will be minimal up to a preload level of $P=F_p$.

3.7 Thermal effects

3.7.1 Theory

When a structure is subjected to temperature variations, expansion or contraction of the several components of the bolted joint will occur. If a hybrid joint with different material types is used, the linear expansion will vary due to deviating coefficients of linear expansion. When expansion or contraction is restricted, thermal stresses will occur. Deformations in connections with preloaded bolts are restricted due to clamping of the preloaded bolt.

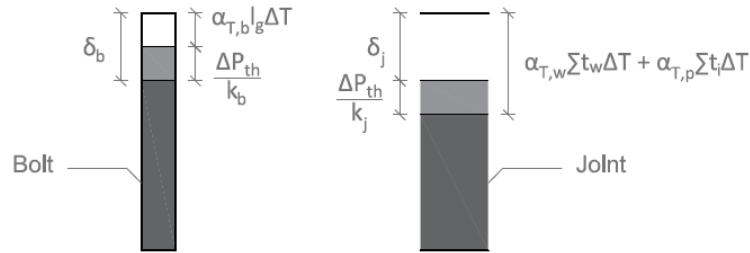


Figure 3.7.1: Visualization of equal deformations during thermal variations

The deformation of the bolt δ_b is affected by the variation of preload due to thermal effects ΔP_{th} and the linear expansion/contraction of the bolt. The deformation of the joint δ_j is affected by ΔP_{th} and the linear expansion/contraction of the washers and plates. This principle is visualized in figure 3.7.1. If joint separation will not occur, the variation of preload can be determined by using the bolt and joint stiffnesses calculated with VDI 2230:

$$\delta_b = \delta_j \quad \rightarrow \quad \frac{\Delta P_{th}}{k_b} + \alpha_{T,b} l_g \Delta T = (\alpha_{T,w} \sum t_w + \alpha_{T,p} \sum t) (T - T_{ini}) - \frac{\Delta P_{th}}{k_j} \quad (3.65)$$

$$\Delta P_{th} = \left(\frac{k_b k_j}{k_b + k_j} \right) \left((\alpha_{T,w} \sum t_w + \alpha_{T,p} \sum t) - \alpha_{T,b} l_g \right) \Delta T \quad (3.66)$$

With:

ΔP_{th} : preload variation due to thermal effects

T : considered temperature

ΔT : temperature variation with respect to assembly temperature

T_{ini} : initial temperature during assembly

l_g : grip length

$\sum t$: total thickness of plates

$\sum t_w$: total thickness of washers

$\alpha_{T,b}$: coefficient of linear thermal expansion bolt material

$\alpha_{T,p}$: coefficient of linear thermal expansion plate material

$\alpha_{T,w}$: coefficient of linear thermal expansion washer material

Where:

$$l_g = \sum t_w + \sum t \quad (3.67)$$

$$\Delta T = (T - T_{ini}) \quad (3.68)$$

3.7.2 Verification model with data Ydstebo

The validity of the thermal model can be verified by applying the VDI thermal model on the test sample tested by Ydstebo illustrated in figure 3.7.2. The material properties are presented in table 3.7.1.

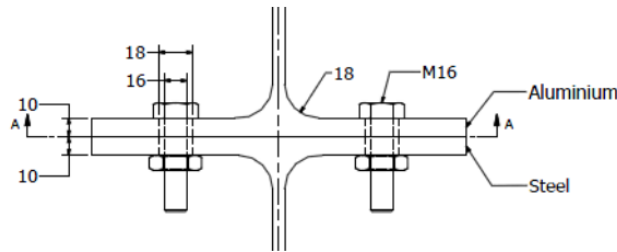


Figure 3.7.2: Test sample aluminium – steel connection (Ydstebo 2017)

Material properties				
		S355	6082T6	8.8 bolt
E	[N/mm ²]	210000	70000	205000
α_T	[mm/mm/°C]	0.0000111	0.000013	0.0000111

Figure 3.7.3: Material properties used by Ydstebo

The coefficient of thermal expansion of 6082 T6 used by Ydstebo is not in accordance with data found in Eurocode 9. NEN-EN 1999-1-1 determines $\alpha_T = 0.000023$ mm/mm/°C. Next to a verification with the coefficients used by Ydstebo, a comparison with a correct coefficient of thermal expansion for 6082 T6 is added in figure 3.7.3.

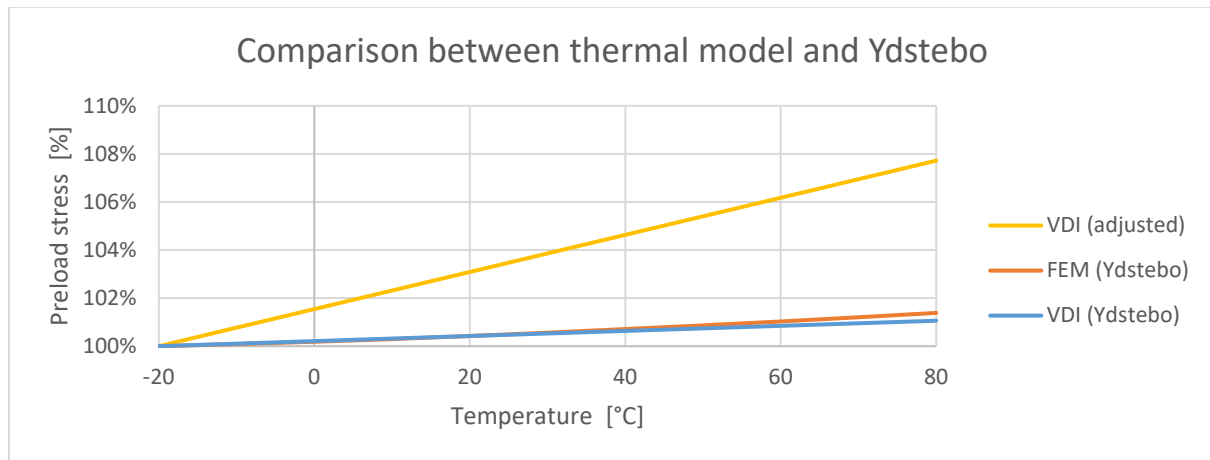


Figure 3.7.3: Thermal model vs. FEM-model Ydstebo

It can be concluded that the thermal model constructed with VDI 2230 including the incorrect coefficient of thermal expansion appears to be in good agreement with the FEM model of Ydstebo. Ydstebo modeled the joint without any clearance between the bolt and the plates ($d = d_0$). Therefore, horizontal displacements due to thermal expansion were able to introduce additional stresses resulting in non-linear preload behaviour. Consequently, the thermal model described in equation 3.66 does underestimate the variation of preload force after a temperature difference of $\Delta T = 60^\circ\text{C}$ is reached. Under normal circumstances, this temperature variation will not be reached. Furthermore, under normal circumstances, sufficient clearance between the bolts and the plates will be present. The comparison with realistic values for α_T show a 4.6% increase in preload force for $\Delta T = 60^\circ\text{C}$.

The dimensional data and material properties of tables 3.2.2 and 3.2.3 are applied in a parametric study. Since 8.8 bolt material and S235 plate material show similar coefficients of thermal expansion,

no thermal stresses will be introduced in the bolt if sufficient clearance between bolt and plate is guaranteed. The analysis is therefore continued containing the following three material combinations:

- 8.8 steel bolt + 5083O/6082T6 plates
- A4 80 stainless steel bolt + S235 plates
- A4 80 stainless steel bolt + 5083O/6082T6 plates

3.7.3 8.8 steel bolt + 5083O/6082T6 plates

The data presented in table 3.2.2 and 3.2.3 are used in combination with the joint showed in figure 3.4.2 to analyze a combination of a joint with an 8.8 steel bolt and aluminium plates. The coefficient of thermal expansion of 5083O is identical to the coefficient of 6082T6, the data found in this analysis is therefore applicable for both alloys. The effect of the plate thickness on the absolute preload variation is presented in figure 3.7.4. The preload variation is defined with $\Delta T = 1^\circ\text{C}$.

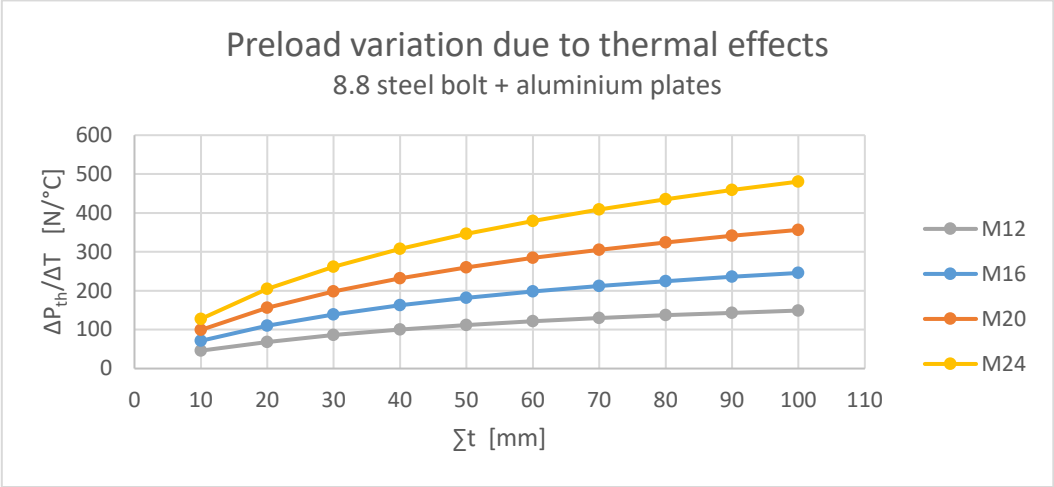


Figure 3.7.4: Influence of plate thickness vs. thermal effects (8.8 bolt + aluminium)

An increasing plate thickness results in increasing preload variation. Once the temperature at assembly is known, a plot of the preload variation versus temperature can be made. An initial assembly temperature $T_{assembly} = 15^\circ\text{C}$ and a total plate thickness $\Sigma t = 50\text{ mm}$ is assumed, figure 3.7.5 represents the preload variation determined with the thermal VDI-model.

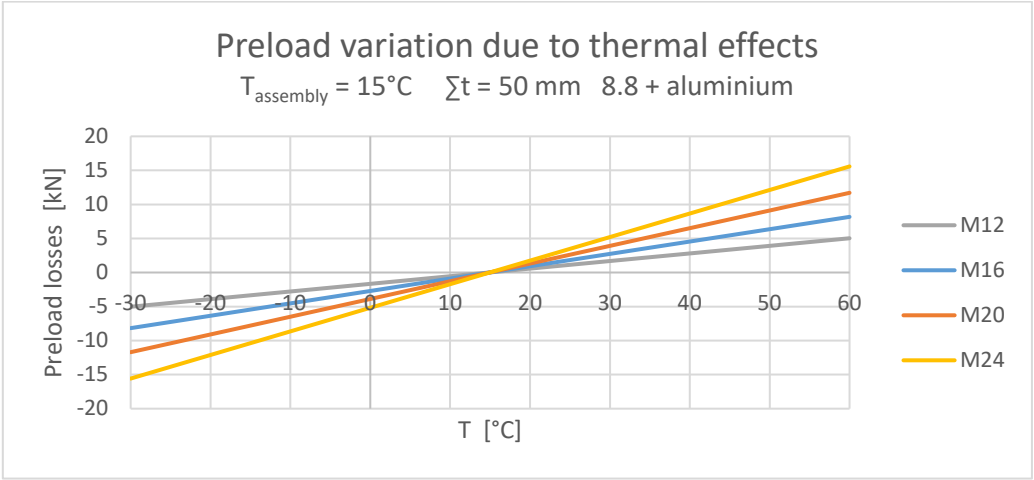


Figure 3.7.5: Preload variation of reviewed connection (8.8 bolt + aluminium)

A decreasing temperature with respect to the initial assembly temperature will result in significant preload losses at a temperature of -30°C . A decreasing bolt diameter has a positive effect on the preload variation.

Assuming an initial preload force of P_{nom} , the relative preload losses of the reviewed connection can be calculated. The results are presented in figure 3.7.6. A decreasing bolt diameter has a decreasing effect on the absolute preload variation, but a negative effect on the relative preload variation (e.g. relative preload losses with M12 bolts are higher than relative preload losses with M16 bolts).

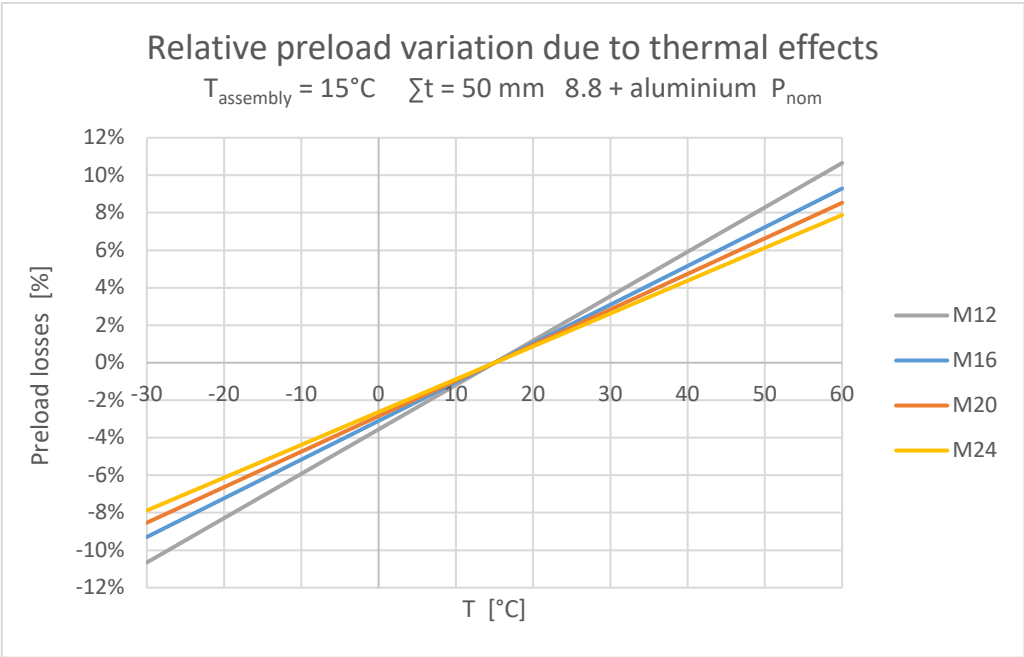


Figure 3.7.6: Relative preload variation of reviewed connection (8.8 bolt + aluminium)

The impact of the initial preload force on the relative preload losses is analyzed in figure 3.7.7. The preload losses are determined at a maximum temperature of $T=60^{\circ}\text{C}$ ($\Delta T=+45^{\circ}\text{C}$). It can be concluded that the initial preload force has a major impact on the relative preload losses. Since the absolute preload loss is not affected by the initial preload force, the application of a low preload force will lead to loosening of the bolt if no initial preload force is applied.

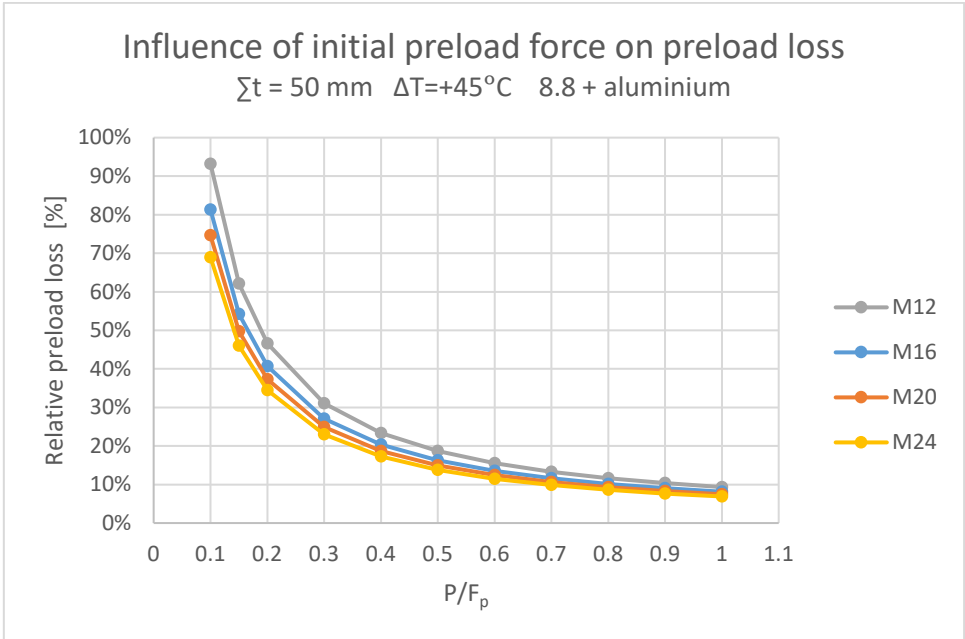


Figure 3.7.7: Influence of initial preload force vs. preload loss due to thermal effects (8.8 + aluminium)

3.7.4 A4 80 stainless steel bolt + S235 plates

The effect of the plate thickness on the absolute preload variation of a connection with an A4 80 bolt combined with S235 plates is presented in figure 3.7.8. The preload variation is defined with $\Delta T = 1^\circ\text{C}$. An increasing plate thickness results in increasing preload variation.

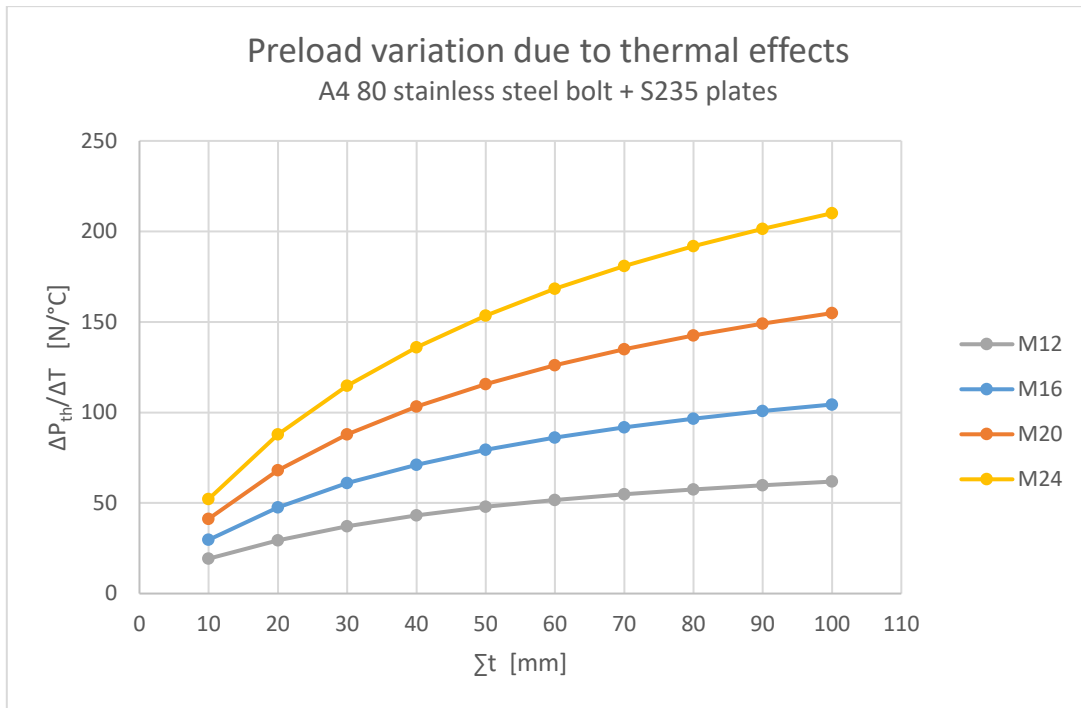


Figure 3.7.8: Influence of plate thickness vs. thermal effects A4 80 bolt + S235

An initial assembly temperature $T_{\text{ini}} = 15^\circ\text{C}$ and a total plate thickness $\Sigma t = 50 \text{ mm}$ is applied, figure 3.7.9 represents the preload variation determined with the thermal VDI-model. The preload loss behaviour is inversely proportional to the preload loss behaviour of 8.8 steel combined with A4 80, since the coefficient of thermal expansion of A4 80 bolt material is larger than the coefficient of thermal expansion of S235 plate material, resulting in a decreasing preload force with increasing temperature.

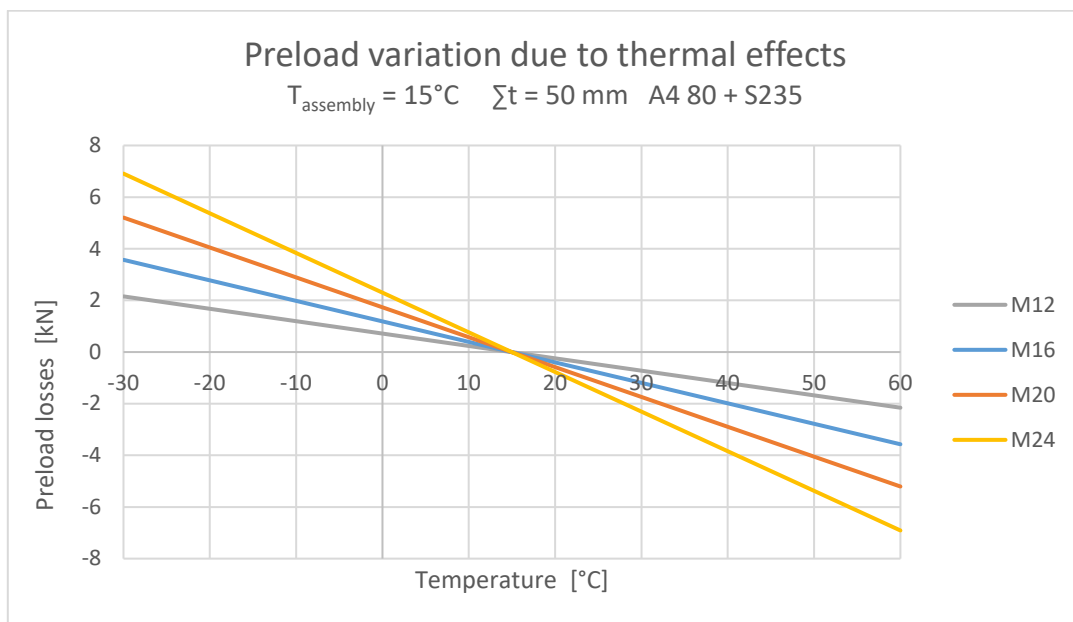


Figure 3.7.9: Preload variation of reviewed connection (A4 80 bolt + S235)

Assuming an initial preload force of P_{nom} , the relative preload losses of the reviewed connection are determined. The results are presented in figure 3.7.10.

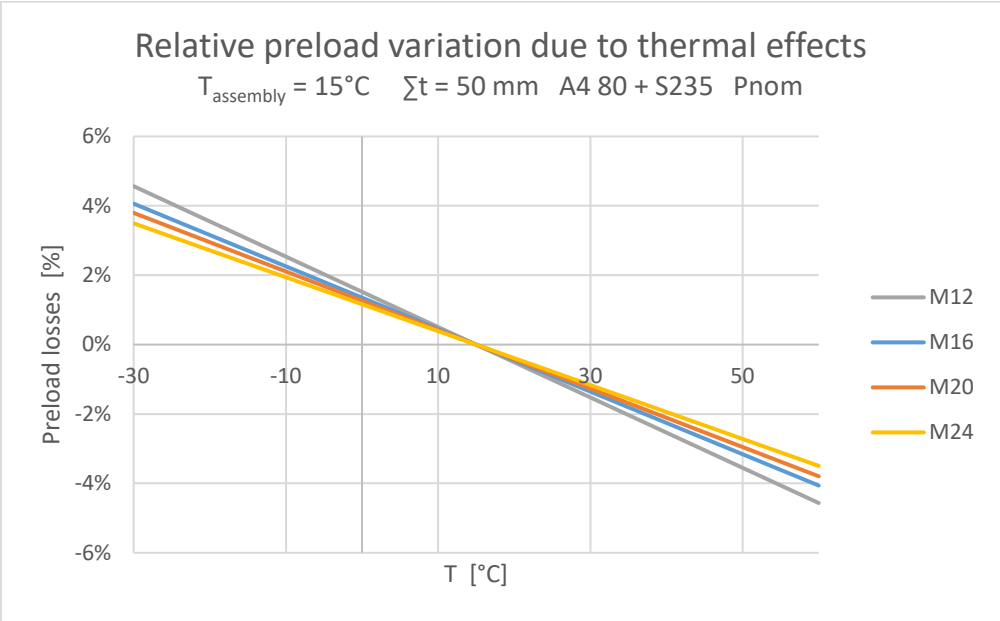


Figure 3.7.10: Relative preload variation of reviewed connection (A4 80 + S235)

The impact of the initial preload force on the relative preload losses is analyzed in figure 3.7.11. The preload losses are determined at a minimum temperature of $T=-30^{\circ}C$ ($\Delta T = -45^{\circ}C$). The level of initial preload force is less dominant compared to the material combination 8.8 + aluminium, since the absolute preload losses are smaller resulting in lower relative preload variations.

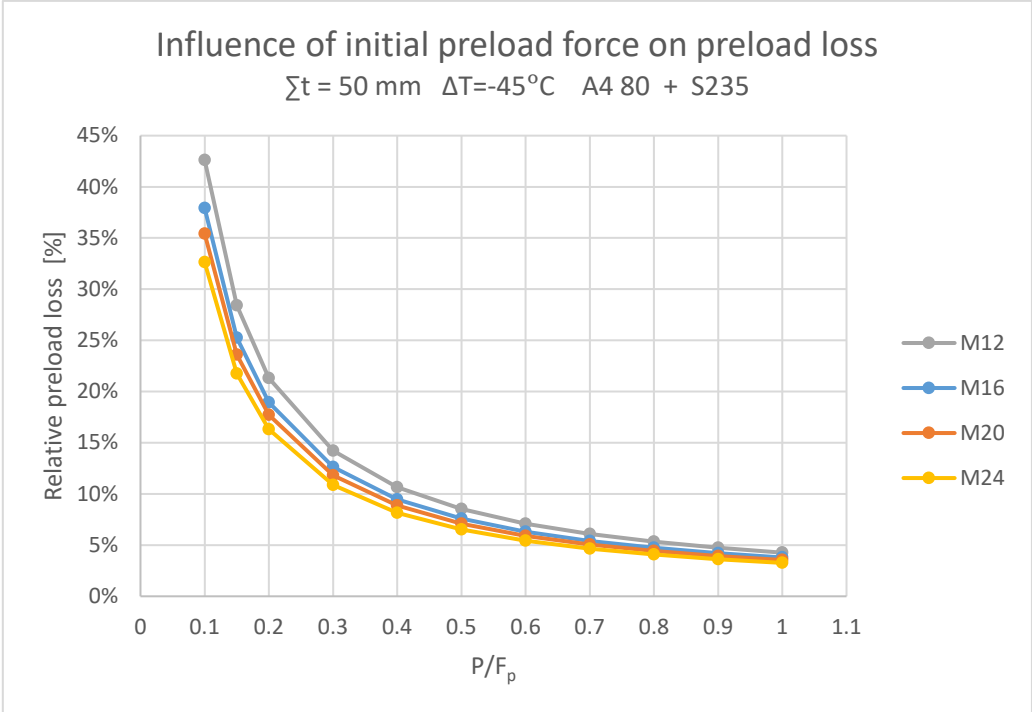


Figure 3.7.11: Influence of initial preload force vs. preload loss due to thermal effects (A4 80 + S235)

3.7.5 A4 80 stainless steel bolt + 5083O/6082T6 plates

The effect of the plate thickness on the absolute preload variation of a connection with an A4-80 bolt and aluminium plates is presented in figure 3.7.12. The preload variation is defined with $\Delta T = 1^\circ\text{C}$.

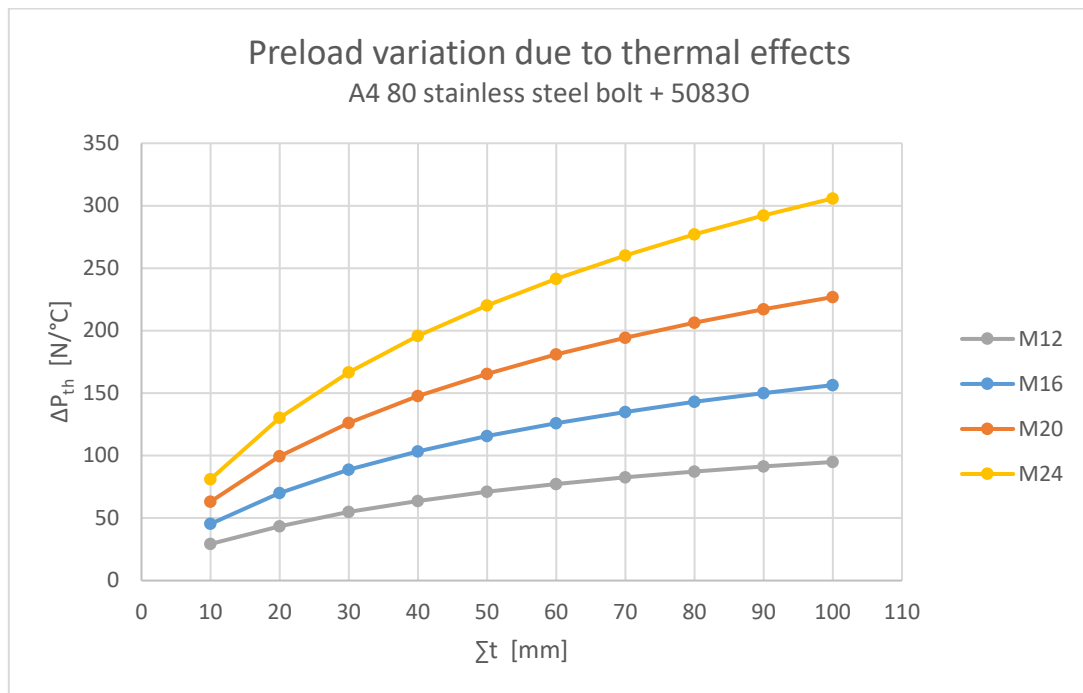


Figure 3.7.12: Influence of plate thickness vs. thermal effects (A4 80 bolt + 5083O plates)

Comparable with the previous reviewed material combinations, increasing the plate thickness results in increasing preload variation. Figure 3.7.13 represents the preload variation determined with the thermal VDI-model if $T_{\text{assembly}} = 15^\circ\text{C}$ and a total plate thickness $\Sigma t = 50\text{ mm}$ is applied.

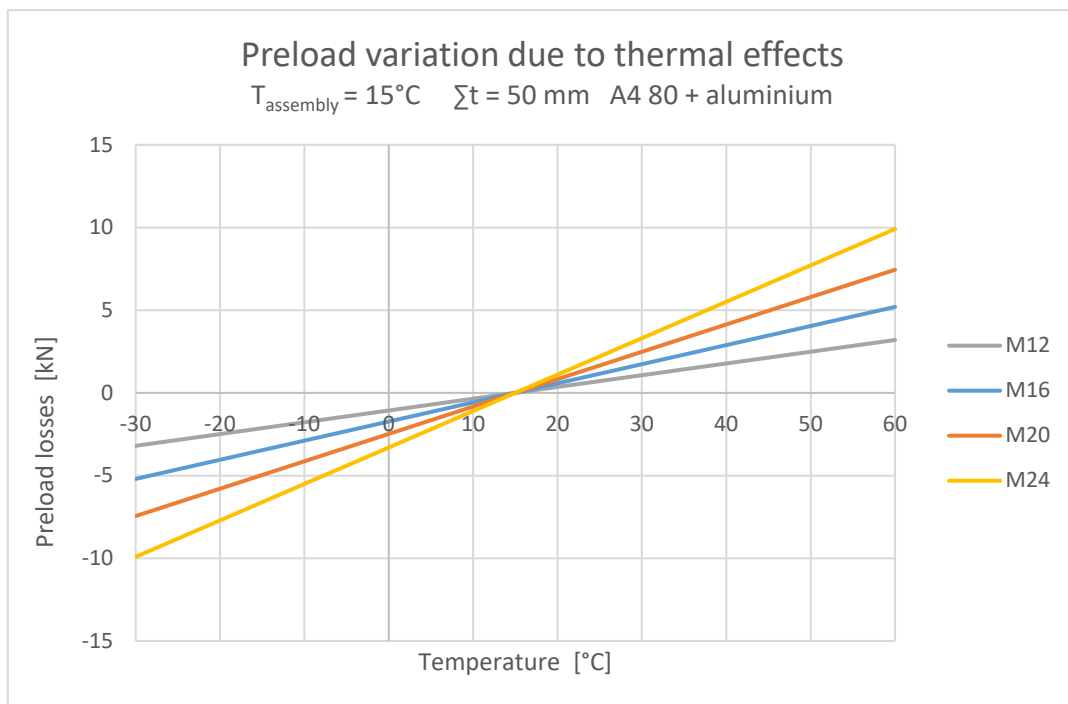


Figure 3.7.13: Preload variation of assumed connection (A4 80 bolt + 5083 O)

Assuming an initial preload force of P_{nom} , the relative preload losses of the reviewed connection are calculated. The results are presented in figure 3.7.14.

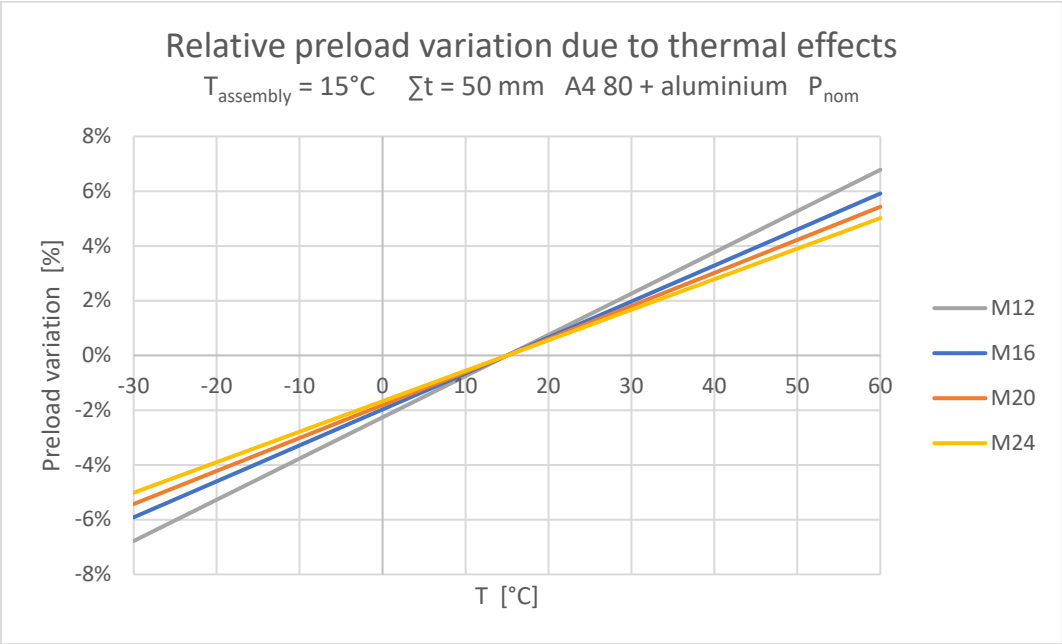


Figure 3.7.14: Preload variation of assumed connection with A4 80 bolt + 5083 O plates

The impact of the initial preload force on the relative preload losses is analyzed in figure 3.7.15. The preload losses are determined at a minimum temperature of $T=60^{\circ}\text{C}$ ($\Delta T= +45^{\circ}\text{C}$). The level of initial preload force is less dominant compared to the material combination 8.8 + aluminium, but more dominant compared to the material combination A4 80 + S235.

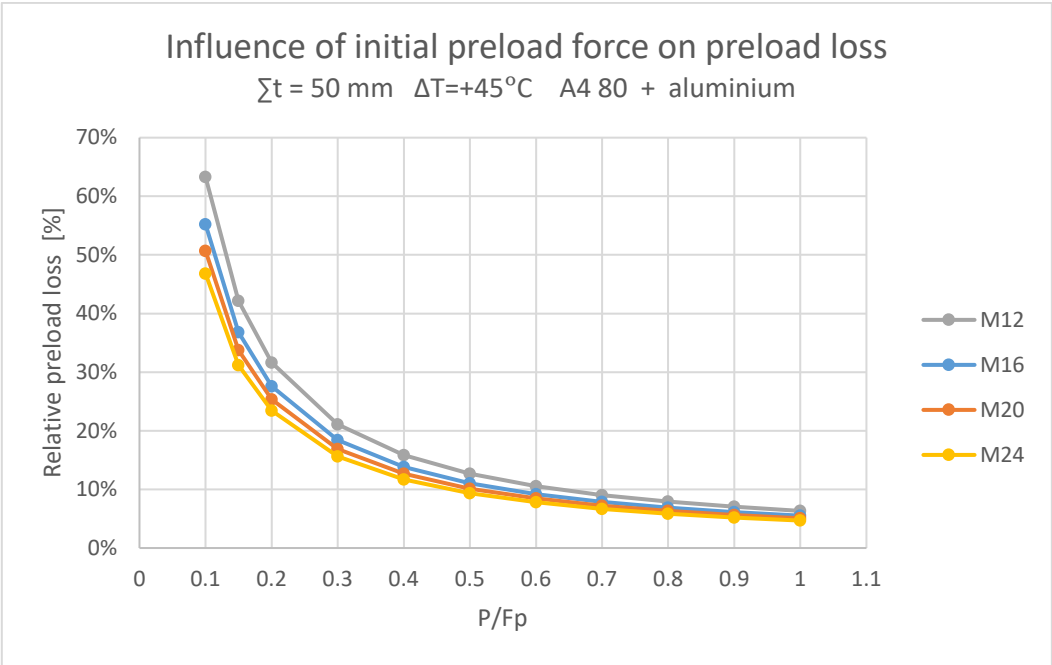


Figure 3.7.15: Influence of initial preload force vs. relative thermal preload losses (A4 80 + aluminium)

3.7.6 Comparison material combinations

The data found in section 3.7.3 – 3.7.5 can be compared to create an overview of the susceptibility of the various material combinations. The preload variation of an M16 bolt combined with a total plate thickness $\sum t = 50$ mm assembled at $T_{assembly} = 15^\circ\text{C}$ with P_{nom} is presented in figure 3.7.16, the relative preload losses are showed in figure 3.7.17.

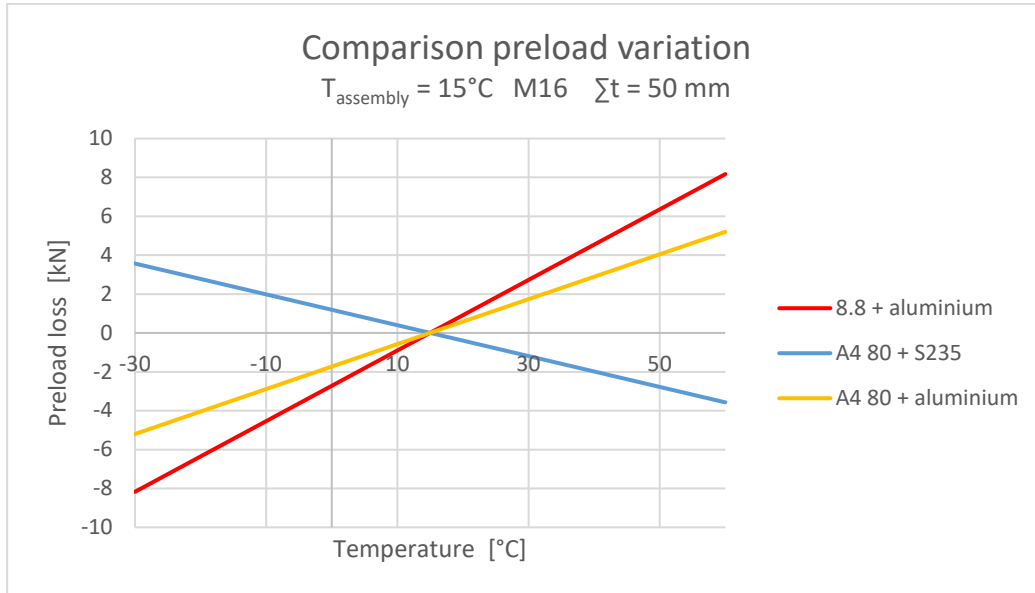


Figure 3.7.16: Comparison preload losses due to thermal effects with 3 material combinations

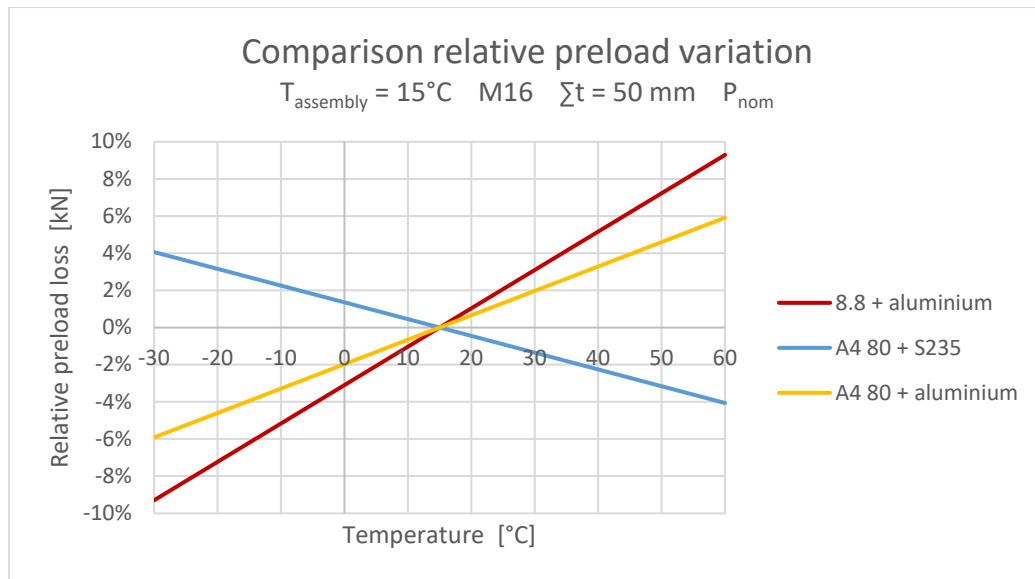


Figure 3.7.17: Comparison relative preload losses due to thermal effects with 3 material combinations

It can be concluded that the material combinations with aluminium plates are more susceptible to thermal variations compared to a combination with S235 steel plates. Furthermore, an increasing temperature has a positive effect on the preload force if aluminium plates are applied while a decreasing preload force is observed if steel plates are applied. If aluminium plates are applied, the preload loss can be minimized when retightening occurs at the lowest temperature experienced during the service life of the connection. On the contrary, combinations with S235 plates should be retightened at the highest temperature experienced during the service life of the connection. Finally, the initial preload force should be maximal to minimize relative preload variations irregardless of the considered material combination.

3.8 Poisson's effect

3.8.1 Theory

Preload variations due to poisson's effect occur when an axial parallel loading is applied to the plates. The perpendicular strain caused by Poisson's ratio reduces the clamping length of the joint. Comparable with embedment and plate creep, the resulting variation in clamping length will be less significant due to a decrease in preload force. This principle is visualized in figure 3.8.1.

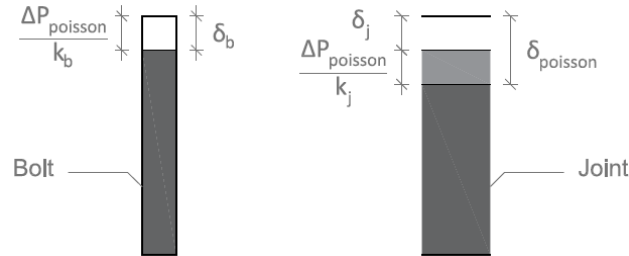


Figure 3.8.1: Visualization of equal deformations during poisson effect

The formulae regarding embedment creep are adjusted to be able to determine the impact of poisson's effect. Assuming joint separation will not occur, the loss of preload due to poisson's effect $\Delta P_{poisson}$ can be defined as:

$$\delta_b = \delta_j \rightarrow \frac{\Delta P_{poisson}}{k_b} = \delta_{poisson} - \frac{\Delta P_{poisson}}{k_j} \rightarrow \Delta P_{poisson} = \delta_{poisson} \left(\frac{k_b k_j}{k_b + k_j} \right) \quad (3.69)$$

With:

- $\Delta P_{poisson}$: loss of preload due to poisson's effect
- $\delta_{poisson}$: deformation due to poisson's effect

The deformation due to poisson's effect $\delta_{poisson}$ can be defined as the total amount of deformation generated by the perpendicular strain multiplied with the thickness of the separate plates. Since the stresses in the separate plates does not have to be equal, the strain in the plates has to be determined separately. The summation of the deformations will lead to an estimation of the total deformation:

$$\delta_{poisson} = \varepsilon_{\perp,1} t_1 + \varepsilon_{\perp,2} t_2 + \dots + \varepsilon_{\perp,i} t_i \quad (3.70)$$

With:

- t_i : thickness of plate i
- $\varepsilon_{\perp,i}$: perpendicular strain in plate i

The perpendicular strain ε_{\perp} in the elastic range can be calculated with the parallel strain multiplied with the Poisson's ratio:

$$\varepsilon_{\perp,i} = \nu \varepsilon_{\parallel,i} \quad (3.71)$$

With:

- $\varepsilon_{\parallel,i}$: parallel strain in plate i
- ν : Poisson's ratio

The parallel strain caused by the axial loading can be expressed with the Ramberg-Osgood stress-strain relationship (NASA Scientific and Technical Information Facility 1965):

$$\varepsilon_{//,i} = \frac{\sigma_{//,i}}{E_j} + K \left(\frac{\sigma_{//,i}}{E_j} \right)^n \quad (3.72)$$

$$K = 0.002 \cdot \left(\frac{f_{0.2}}{E_j} \right)^{-n} \quad (3.73)$$

With:

- E_j : Young's modulus plate material
- K : Ramberg-Osgood constant
- $f_{0.2}$: 0.2% proof strength plate material
- n : Ramberg-Osgood constant
- $\sigma_{//,i}$: remote stress in plate i

The properties of the considered aluminium alloys including 2024T3 are listed in table 3.8.1.

Material properties plate				
		5083O	6082T6	2024T3
E_j	[N/mm ²]	70000	70000	70000
ν	[-]	0.3	0.3	0.3
$f_{0.2}$	[N/mm ²]	125	260	345
n	[-]	6	25	12

Table 3.8.1: Proof and tensile properties (NEN-EN 1999-1-1 2013)

The elastic-plastic material behaviour of S235JR Steel is tested and modelled by Kossakowski (Kossakowski 2012). The true stress-strain behaviour is presented in figure 3.8.2 (left). The different branches representing the elastic-plastic stress-strain behaviour can be described by an approximation model proposed by Kossakowski:

$$\varepsilon = \frac{\sigma}{E} \quad \text{for } \sigma < \sigma_0 \quad (3.74)$$

$$\varepsilon = \frac{\varepsilon_1 - \varepsilon_0}{\sigma_1 - \sigma_0} (\sigma - \sigma_0) + \varepsilon_0 \quad \text{for } \sigma_0 \leq \sigma \leq \sigma_1 \quad (3.75)$$

$$\varepsilon = \varepsilon_0 + \frac{\sigma_{01}}{E} \left(\frac{\sigma}{\sigma_{01}} \right)^{1/N} \quad \text{for } \sigma > \sigma_1 \quad (3.76)$$

With:

- E : Young's modulus
- N : strain-hardening exponent
- ε : strain
- ε_0 : yield strain
- ε_1 : initial hardening strain
- σ : stress
- σ_0 : yield stress
- σ_{01} : initial stress at the beginning of the nonlinear part of the approximation curve
- σ_1 : initial hardening stress

To be able to match the nominal yield stress ($f_y = 235 \text{ N/mm}^2$) described in NEN-EN-1993-1-1, the true linear plastic $\sigma_0 - \sigma_1$ branch with a Young's modulus equal to $E = 1088 \text{ N/mm}^2$ is shifted downwards parallel to the original branch (i.e. matching $E = 1088 \text{ N/mm}^2$) to be able to intersect $f_y = 235 \text{ N/mm}^2$. The shift of the linear plastic branch is visualized in figure 3.8.2 (right). The parameters corresponding to figure 3.8.2 (right) are presented in table 3.8.2. The parameters are based on the data provided by Kossakowski and modified to be able to transpose the linear plastic branch.

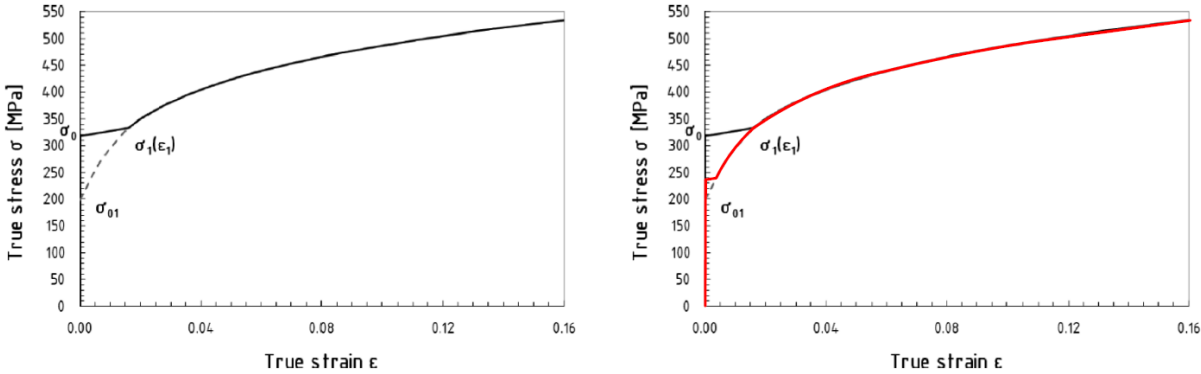


Figure 3.8.2: Approximation true stress-strain curve for S235JR steel (Kossakowski 2012) (left); shifted $\sigma_0 - \sigma_1$ branch to approximate nominal yield stress described in NEN-EN-1993-1-1.

Strength parameters S235JR steel					
ϵ_0	ϵ_1	σ_0	σ_{01}	σ_1	N
[-]	[-]	[N/mm ²]	[N/mm ²]	[N/mm ²]	[-]
0.001119	0.004041	235	198	238.18	0.195

Table 3.8.2: Modified strength parameters S235JR steel

The stress-strain relationship of the aluminium alloys presented in table 3.8.2 is plotted in figure 3.8.3 using the Ramberg-Osgood stress-strain relationship described in equations 3.72 and 3.73. The stress-strain relationship of S235 steel is added using the Kossakowski stress-strain relationship provided in equations 3.74, 3.75 and 3.76. More strain can be expected at medium stresses (100 - 125 N/mm²) with the application of 5083O compared to 6082T6 and S235. Subsequently, higher preload losses within the medium stress range can be expected if 5083O is applied. The medium stress range approaches the proof stress of 5083O and is therefore applicable if yielding around the bolt hole occurs. Yielding of the gross cross section is generally avoided. However, if stress concentrations around the bolt hole are considered, local yielding can occur.

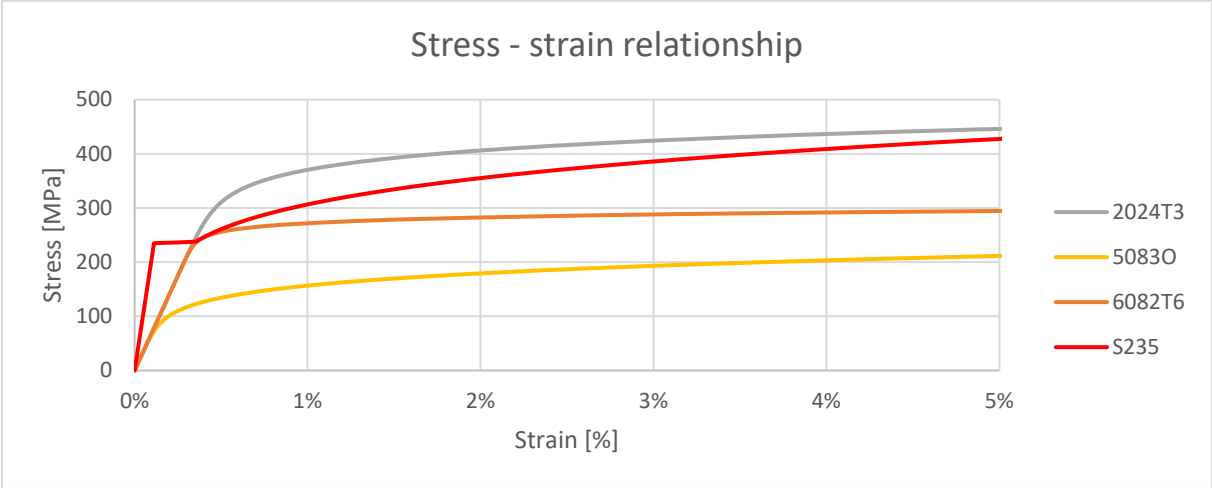


Figure 3.8.3: Engineering stress – strain relationship 2024T3, 5083O, 6082T6 and S235

3.8.2 Stress concentration at holes

Stress concentrations occur in abrupt geometrical changes if load is applied, resulting in an uneven stress distribution within the cross-section. Figure 3.8.4 visualizes the uniaxial normal stresses and stress concentrations around a hole without the application of a bolt (i.e. plate with hole). Peak stresses occur at the left and right side of the hole (red area), the top and the bottom are almost unstressed (blue area). Stress concentrations will have an impact on the deformations due to poisson's effect and should therefore be considered within the model.

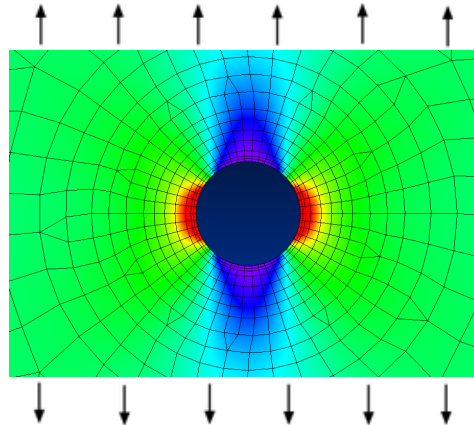


Figure 3.8.4: Stress concentrations at hole (McGinty 2010)

McGinty analyzed the effect of uneven distribution using Ernst Gustav Kirsch's linear elastic solution for stresses around a hole in an infinite plate. A plate with infinite width loaded with uniaxial tension contains the behaviour as indicated in figure 3.8.5. The ratio between the peak stress at the hole and the remote stress at the end of the plate σ_∞ appears to have a value of 3 in the case of a plate with infinite width. At a distance of one diameter from the edge of the hole, the stress concentration is relatively small. At two diameters distance the stress concentration is negligible and the occurring stress is equal to the remote stress σ_∞ . In the case of an infinite plate, the factor three is independent of the hole size; a relatively small hole introduces equal amounts of stress concentration compared with large holes (McGinty 2010).

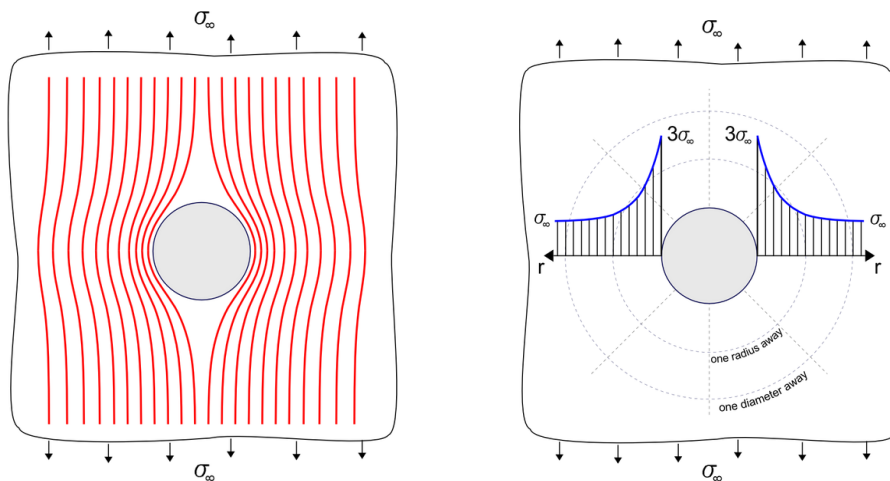


Figure 3.8.5: Stress concentrations at hole with infinite width (McGinty 2010)

A plate with finite width will result in an increase of stress concentration if the ratio between hole diameter and plate width increases as indicated in figure 3.8.6. Due to reduction of the cross-section, the average stress in the net section σ_{nom} is higher than the remote stress resulting in a higher stress concentration compared to a plate with infinite width.

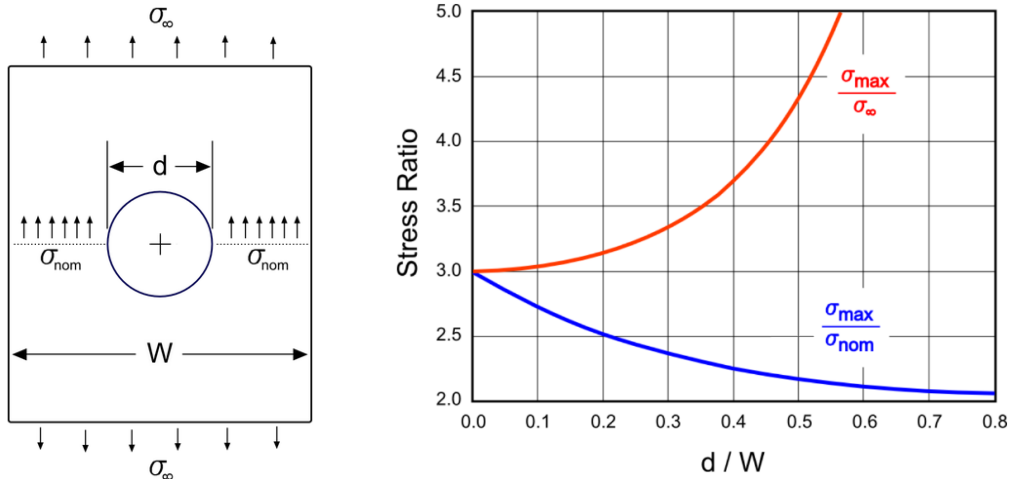


Figure 3.8.6: Stress concentrations at hole with finite width (McGinty 2010)

The stress concentration factor between the peak stress at the hole σ_{\max} and the remote stress σ_{∞} can be calculated with (McGinty 2010):

$$K_t = \frac{\sigma_{\max}}{\sigma_{\infty}} = \frac{1}{1 - \left(\frac{d}{W}\right)} \cdot \left(3 - 3.14 \left(\frac{d}{W}\right) + 3.667 \left(\frac{d}{W}\right)^2 - 1.527 \left(\frac{d}{W}\right)^3 \right) \quad (3.77)$$

With:

- K_t : Stress Concentration Factor (ratio between peak stress and remote stress)
- W : plate width
- d : hole diameter
- σ_{\max} : peak stress at edge hole
- σ_{∞} : unaffected remote stress

The stresses bypassing the hole in a plate loaded in tension are also referred to as bypass loading (Maljaars et al. 2019). The stress concentration factor corresponding to bypass loading $K_{t,byp}$ is described to be equal to (Pilkey and Pilkey 2008):

$$K_{t,byp} = \frac{2}{1 - \frac{d}{W}} + 0.284 - 0.6 \left(1 - \frac{d}{W}\right) + 1.32 \left(1 - \frac{d}{W}\right)^2 \quad (3.78)$$

With:

- $K_{t,byp}$: stress concentration factor in the case of bypass loading

Equations 3.77 and 3.78 give almost identical stress concentration factors with respect to the bolt hole diameter – width ratio as can be observed in table 3.8.3.

Comparison equations 3.74 and 3.75											
d/W	[-]	0	0.1	0.2	0.3	0.4	0.5	0.6	0.7	0.8	0.9
K_t	[-]	3	3.02	3.13	3.35	3.72	4.31	5.27	6.92	10.27	20.31
$K_{t,byp}$	[-]	3	3.04	3.15	3.37	3.73	4.31	5.26	6.89	10.22	20.24

Table 3.8.3: Comparison between output equation 3.74 and 3.75 vs. diameter-width ratio

If a bolt without a preload force is used to create a shear joint, higher peak stresses can be observed due to the local load transfer between the bolt and the plate. This case is described as pin loading with stress concentration factors equal to (Pilkey and Pilkey 2008):

$$K_{t,pin} = \frac{1}{1 - \frac{d}{W}} \left(\left(12.882 - 52.714 \frac{d}{W} \right) + 89.762 \left(\frac{d}{W} \right)^2 - 51.667 \left(\frac{d}{W} \right)^3 \right) \quad (3.79)$$

for $0.2 \leq \frac{d}{W} \leq 0.75$

With:

$K_{t,pin}$: stress concentration factor in the case of pin loading

Introducing a preload force in the bolt will have a decreasing effect on the stress concentration factor, since (part of) the tensile load will be transferred via friction. Once slip between the plate surfaces has occurred, the tensile load will be transferred through a combination of friction and bearing. The ratio between bearing and friction is defined as bearing ratio β and is defined as (Maljaars et al. 2019):

$$\beta = \max \left(\frac{F - F_{slip}}{F}, 0 \right) \quad (3.80)$$

With:

F : tensile force applied in the plate
 F_{slip} : theoretical slip load
 β : bearing ratio

The theoretical slip load F_{slip} can be calculated with (Maljaars et al. 2019):

$$F_{slip} = n_f \mu F_c \quad (3.81)$$

With:

F_c : preload force bolt
 n_f : number of friction planes
 μ : friction coefficient or slip factor

Since the preload force in the bolt will decrease with increasing tensile load due to poisson effect, the real slip load will decrease simultaneously. Equation 3.81 is modified to account for this effect:

$$F_{slip} = n_f \mu (P - \Delta P_{poisson}) \quad (3.82)$$

With:

P : initial preload force
 $\Delta P_{poisson}$: preload loss due to poisson's effect

The bearing ratio can be used to describe a combination of load transfer via bearing and/or friction by taking into account the distribution between pin loading and bypass loading. Taking into account the influence of the initial preload force, the stress concentration factor in a shear joint can be calculated with (Maljaars et al. 2019):

$$K_t = (2\beta - \beta^2) K_{t,pin} + 0.5(1 - \beta)^2 K_{t,byp} \quad (3.83)$$

Reviewing equation 3.83, two extreme cases regarding the bearing ratio β can be analyzed: if $\beta = 1$ (i.e. no preload force is applied), the tensile load is transferred via bearing only and $K_t = K_{t,pin}$; if $\beta = 0$ (i.e.

no slip has occurred), the tensile load is transferred via friction only and $K_t = 0.5 \cdot K_{t,byr}$. The 50% reduction of the stress concentration factor with respect to bypass loading in the case no slip has occurred ($\beta = 0$) can be explained with the load transfer in front of the bolt hole and behind the bolt hole: 50% of the load will be transferred via friction in front of the bolt hole introducing no stress concentrations at the bolt hole; the remaining 50% will be transferred via friction behind the bolt hole, introducing stress concentrations around the hole via bypass loading. Taking into account the stress concentration factor, equations 3.71 and 3.72 are combined and modified to be able to model the perpendicular strain around the bolt hole. As concluded from figure 3.8.4, parts of the circumference of the bolt hole exhibit peak stresses. Furthermore, almost unstressed areas can be found. It is unknown how much of the circumference can be considered stressed or unstressed. Therefore, a safe approximation will be regarded with peak stresses occurring over the full circumference. Furthermore, to include local yielding in the model, a plastic poisson ratio is introduced. The plastic poisson ratio is defined as $\nu_{pl} = 0.5$ (Gerard et al. 1952).

$$\epsilon_{\perp,i} = \nu \epsilon_{\parallel,i} = \nu_{el} \frac{K_t \sigma_{\parallel,i}}{E_j} + \nu_{pl} K \left(\frac{K_t \sigma_{\parallel,i}}{E_j} \right)^n \tag{3.84}$$

With:

- E_j : Young’s modulus plate material
- K : Ramberg-Osgood constant
- n : Ramberg-Osgood exponent
- $\epsilon_{\parallel,i}$: parallel strain in plate i
- $\epsilon_{\perp,i}$: perpendicular strain in plate i
- $\sigma_{\parallel,i}$: remote stress in plate i
- ν_{el} : elastic Poisson’s ratio
- ν_{pl} : plastic Poisson’s ratio

3.8.3 Verification with data Chakherlou

The validity of the poisson effect model formulated in 3.8.1 and the effect of stress concentration discussed in 3.8.2 can be analyzed by applying equations 3.69, 3.70, 3.83 and 3.84 on the sample tested by Chakherlou as shown in figure 3.8.7. The geometrical and mechanical properties of the bolt, joint and load cell (reported by Chakherlou) are listed in tables 3.8.4 and 3.8.5.

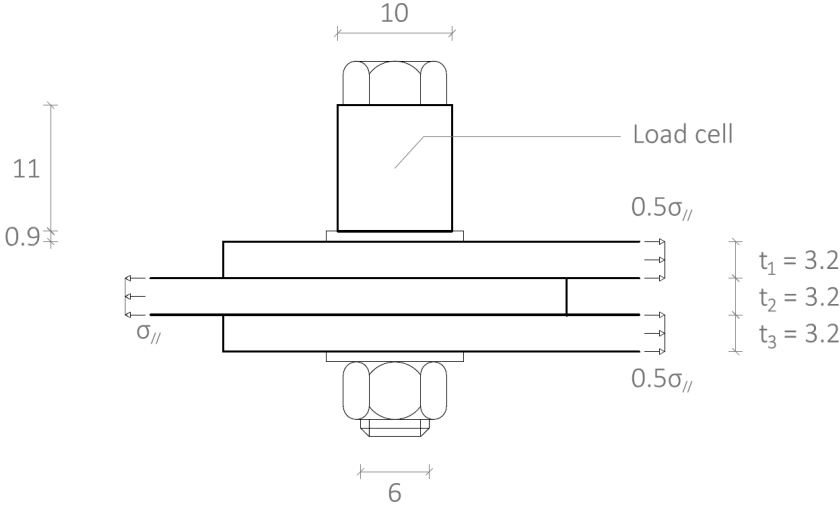


Figure 3.8.7: Double shear joint with longitudinal stress used by Chakherlou

Properties M6 bolt					
A_t	d_3	$f_{0.2}$	E	Case 1: $0.07F_p$	Case 2: $0.14F_p$
mm^2	mm	N/mm^2	N/mm^2	kN	kN
20.1	4.773	900	207000	1.296	2.548

Table 3.8.4: Geometrical and mechanical properties M6 bolt

Properties 2024 T3 joint and Load Cell								
Joint					Load Cell			
W	$t_1 = t_2 = t_3$	d_0	E	ν	Inner diameter	Outer diameter	E	Load Cell stiffness
mm	mm	mm	N/mm^2	-	mm	mm	N/mm^2	N/mm
18	3.2	6	71500	0.33	6.5	10	204000	841161

Table 3.8.5: Geometrical and mechanical properties 2024 T3 joint and Load Cell

Chakherlou experimentally determined: $\mu = 0.40$. The diameter – width ratio of the considered joint is equal to 0.33 ($d_0 / W = 0.33$), equation 3.79 is therefore applicable. The stress concentration factors $K_{t,pin}$ and $K_{t,byp}$ are equal to:

$$K_{t,byp} = \frac{2}{1 - \frac{6}{18}} + 0.284 - 0.6 \left(1 - \frac{6}{18}\right) + 1.32 \left(1 - \frac{6}{18}\right)^2 = 3.47 \quad (3.85)$$

$$K_{t,pin} = \frac{1}{1 - \frac{6}{18}} \left(\left(12.882 - 52.714 \cdot \frac{6}{18}\right) + 89.762 \left(\frac{6}{18}\right)^2 - 51.667 \left(\frac{6}{18}\right)^3 \right) = 5.06 \quad (3.86)$$

The bearing ratio is affected by the tensile force in the center plate:

$$F = \sigma_{II} A_g = \sigma_{II} \cdot (3.2 \cdot 18) \quad (3.87)$$

A comparison between the experimental data from Chakherlou and the theoretical preload force behaviour of the model involving case 1 and case 2 is presented in figure 3.8.8 and figure 3.8.9. A slip point is added to indicate the theoretical slip load. The tensile force when local yielding around the bolt hole occurs (i.e. $\sigma_{II} \cdot K_t = f_{0.2}$) is indicated for case 2. Local yielding did not occur in case 1.

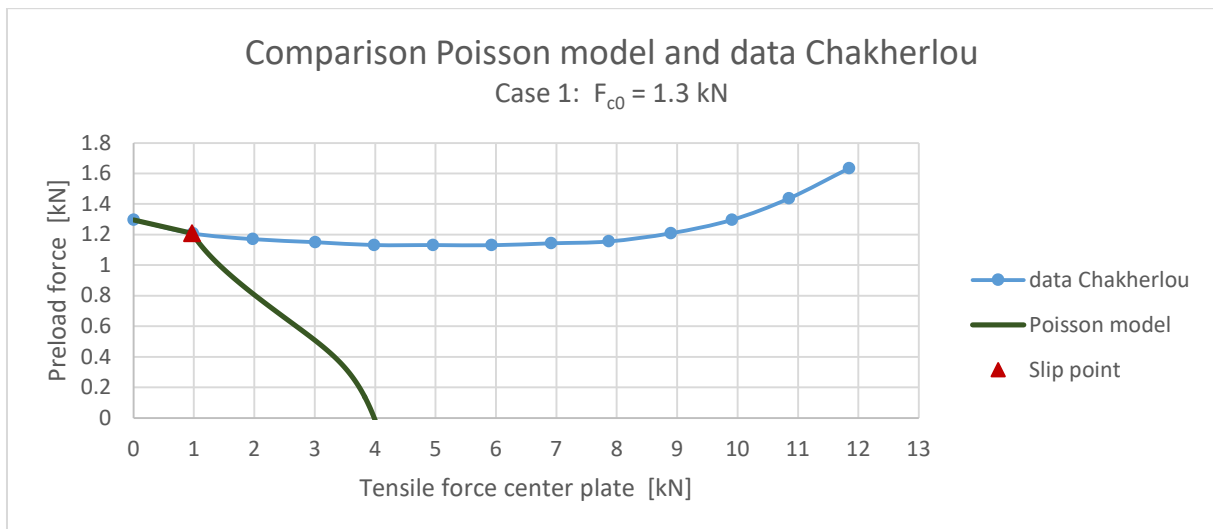


Figure 3.8.8: Comparison case 1 between Poisson model experimental data Chakherlou

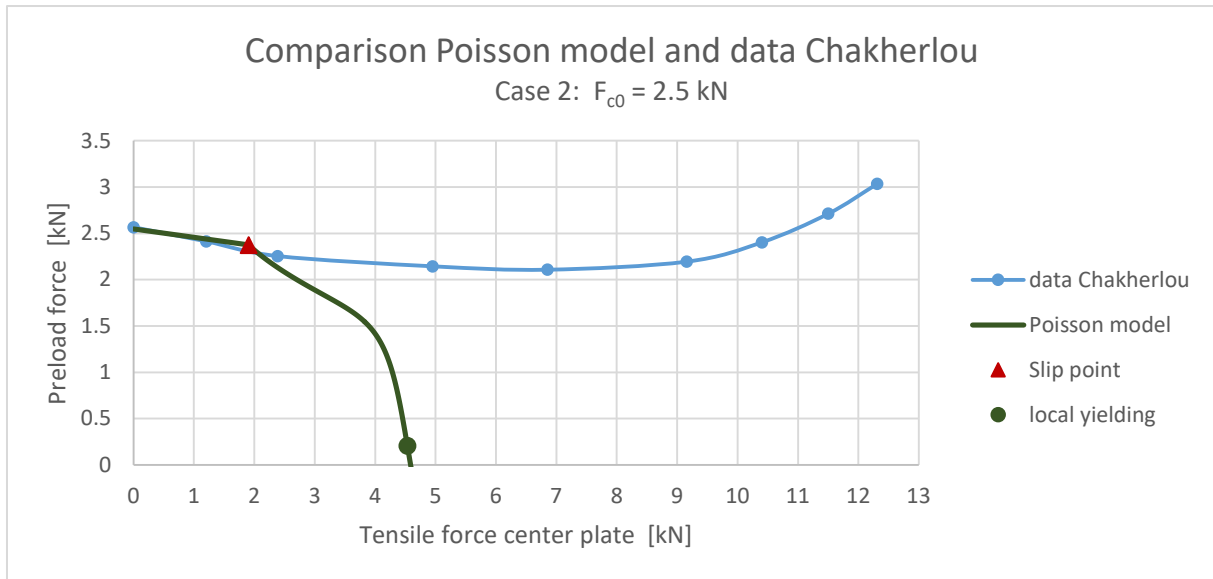


Figure 3.8.9: Comparison case 2 between Poisson model experimental data Chakherlou

The model predicts the preload behaviour prior to slip relatively well. If the slip load is exceeded, the stress concentration factor will increase since the load will be transferred partly via bearing. However, bolt bending and prying (figure 3.8.10) will have an increasing effect on the preload level, counterbalancing the decreasing preload force. These effects are not taken into account, resulting in differences between the model and the experimental data.

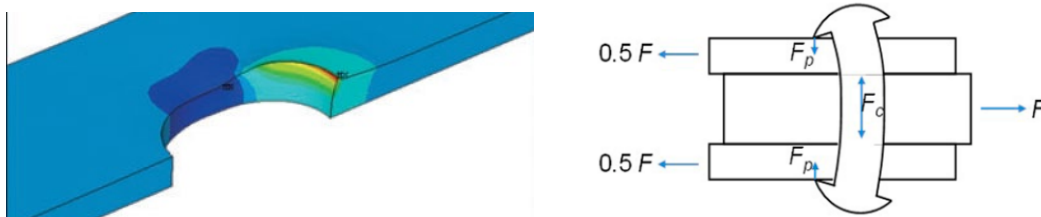


Figure 3.8.10: Bolt bending resulting in increasing thickness (Chakherlou, Razavi, and Aghdam 2012) (left) and prying (Maljaars, Leonetti, and Maas 2019) (right)

Chakherlou experimentally determined: $\mu = 0.40$. The theoretical slip loads corresponding to the two cases (case 1: $F_{c0} = 1.3$ kN; case 2: $F_{c0} = 2.5$ kN) are equal to:

$$F_{slip,1} = 0.97 \text{ kN} \quad (3.88)$$

$$F_{slip,2} = 1.90 \text{ kN} \quad (3.89)$$

It can be concluded that the preload losses due to poisson's effect are minimal if the theoretical slip load is not exceeded. According to NEN-EN-1999-1-1:

$$F_{s,Rd} = \frac{n\mu}{\gamma_{Ms}} F_{p,Cd} \quad (3.90)$$

With:

- $F_{p,Cd}$: design preloading force
- $F_{s,Rd}$: design slip resistance
- n : number of friction surfaces
- γ_{Ms} : partial safety factor for a slip resistant bolt
- μ : slip factor

The partial safety factor γ_{Ms} can be taken into account by determining whether slip is allowed in the Ultimate Limit State (ULS) or the Serviceability Limit State (SLS). The values for the partial safety factor γ_{Ms} are listed in table 3.8.6.

Partial safety factor γ_{Ms}	
ULS	SLS
1.25	1.1

Table 3.8.6: Values for partial safety factor γ_{Ms} (NEN-EN 1993-1-8 2010; NEN-EN 1999-1-1 2013)

The theoretical preload level corresponding to the remote stress at slip after taking into account the preload loss due to poisson's effect can be derived with:

$$P_s = F_{p,Cd} - \Delta P_{\text{poisson},s} \quad (3.91)$$

With:

P_s : theoretical preload force at slip
 $\Delta P_{\text{poisson},s}$: preload loss due to poisson's effect at $\sigma_{//} = \sigma_s$

The minimum preload force at slip and therefore maximum preload losses can be found if the partial safety factor is ignored (i.e. $\gamma_{Ms} = 1.0$). The remote stress corresponding to the slip load $\sigma_{//,s}$ can be determined by including the gross section of the plate:

$$F_{\text{slip}} = \frac{2 \cdot 0.40}{1.0} P_s = 0.80 P_s \quad (3.92)$$

$$\sigma_{//,s} = \frac{F_{\text{slip}}}{A_g} = \frac{0.80 P_s}{18 \cdot 3.2} = \frac{P_s}{72} \quad (3.93)$$

With:

A_g : gross cross-section
 $\sigma_{//,s}$: remote stress at slip

The maximum absolute and relative preload losses found at the theoretical slip force corresponding to the slip points of figures 3.8.8 and 3.8.9 are summarized in table 3.8.7.

Absolute and relative maximum preload losses at theoretical slip load F_s			
		Case 1	Case 2
$F_{p,Cd}$	[kN]	1.30	2.54
P_s	[kN]	1.20	2.36
$\Delta P_{\text{poisson},s}$	[kN]	0.093	0.19
$\Delta P_{\text{poisson},s}$	[%]	7.2%	7.5%

Table 3.8.7: Preload losses at slip using model and data Chakherlou

Increasing the preload force will increase the slip load and subsequently, the absolute preload loss at slip will increase. The maximum relative preload losses at slip are equal to 7 – 8 %. Whether the relative preload loss will be affected by the initial preload force can not be concluded from the limited data provided by Chakherlou.

The analysis is continued with a parametric study regarding the double shear joint presented in figure 3.8.11. The joint has equal nominal stresses in all three plates due to a dimensional ratio between the center plate thickness and cover plate thickness of 2:1. The analysis contains four material combinations (8.8 steel bolt + S235 plates / A4 80 stainless steel bolt + S235 plates / A4 80 stainless steel bolt + 5083O plates / A4 80 stainless steel bolt + 6082T6 plates) with material properties listed in 3.2. A friction coefficient $\mu = 0.40$ is applied.

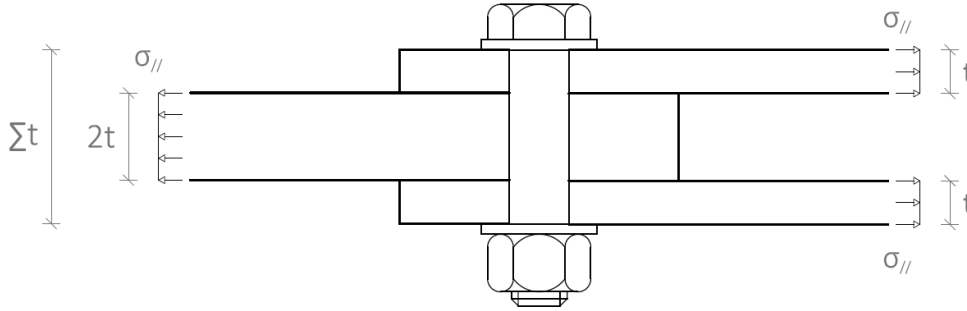


Figure 3.8.11: Double shear joint used in parametric study

The minimum possible width W_{min} is calculated using the minimum edge distance e_2 determined in NEN-EN-1993 and NEN-EN-1999. W_{min} is equal to twice the minimum edge distance with a bolt hole diameter equal to the bolt diameter:

$$e_2 = 1.2d_0 \quad (3.94)$$

$$W_{min} = 2 \cdot e_2 = 2.4d \quad (3.95)$$

As can be observed in figure 3.8.3, excessive strain deformation can occur once the proof stress has been exceeded. Subsequently, the preload force will decrease rapidly once local yielding occurs. This effect is taken into account in equation 3.82 by considering a decreasing theoretical slip load. If no slip is allowed, the tensile force in the center should not exceed the slip load:

$$F < F_{slip} \quad (3.96)$$

$$F < n_f \mu (P - \Delta P_{poisson})$$

The remote stresses at slip can be determined using the modified theoretical slip load:

$$\sigma_{||,s} < \frac{F_{slip}}{A_g} = \frac{n_f \mu (P - \Delta P_{poisson})}{W_{min} 2t} \quad (3.97)$$

Next to avoidance of slip, two additional requirements are considered. Firstly, yielding of the gross cross section is not allowed (yield limit). Secondly, the ultimate tensile strength of the net cross section should be respected to avoid cracking. To be able to avoid cracking, a crack limit can be considered by taking into account the stress concentrations around the bolt hole. It should be noted that the yield limit and crack limit are not governing in most cases since local yielding around the bolt hole will reduce the preload level significantly (i.e. resulting in slip).

$$\text{Yield limit: } \sigma_{||,s} < f_{0.2} \quad \text{or} \quad \sigma_{||,s} < f_y \quad (3.98)$$

$$\text{Crack limit: } \sigma_{||,s} < \frac{f_u}{K_t} \quad (3.99)$$

3.8.4 Poisson's effect 8.8 steel bolt + S235 plates

Using the material properties considering 8.8 steel bolts and S235 plates, the poisson's effect can be predicted. The relative preload losses of a joint with a total plate thickness $\sum t = 50$ mm, a plate width equal to W_{min} and an initial preload force $P = P_{nom} = 0.875F_p$ (determined in equation 3.23) are presented in figure 3.8.12. The preload behaviour of a joint with a total plate thickness $\sum t = 50$ mm and an M16 bolt with various levels of initial preload force is presented in figure 3.8.13. Slip points are added to the figures to indicated where slip will occur.

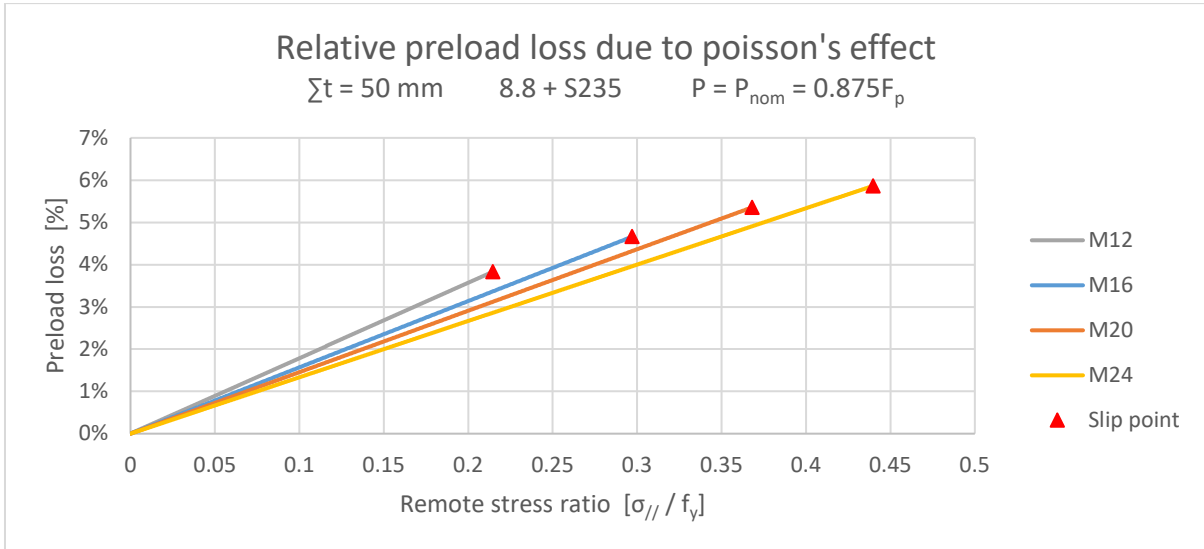


Figure 3.8.12: Relative preload loss due to poisson's effect ($\sum t = 50$ mm, 8.8 bolt + S235, $P = 0.875F_p$)

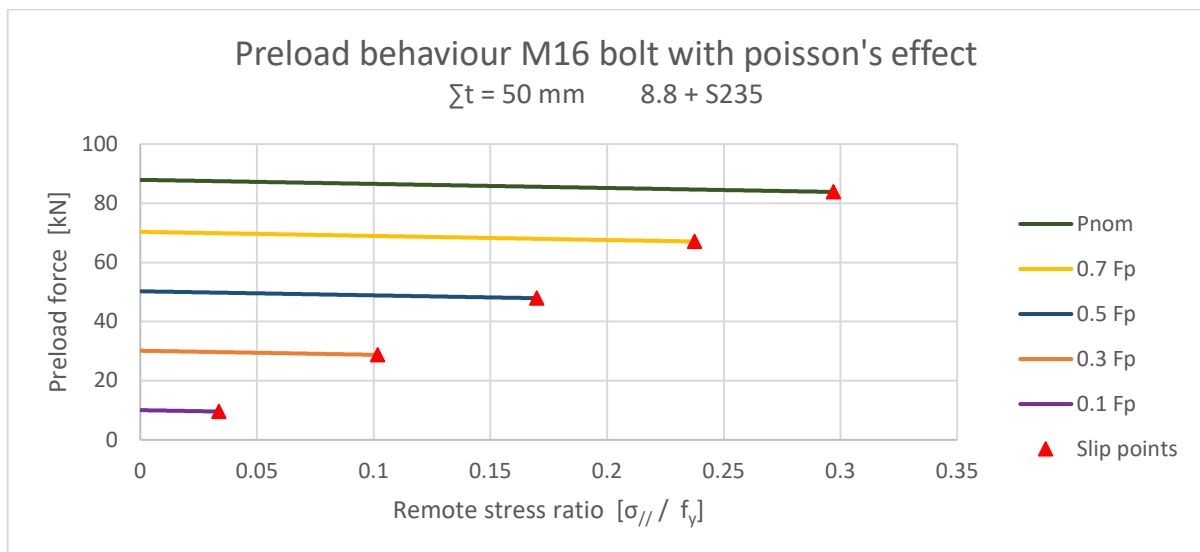


Figure 3.8.13: Preload behaviour due to poisson's effect ($\sum t = 50$ mm, M16, 8.8 bolt + S235)

It can be discovered that an increasing bolt diameter will lead to increasing relative preload losses, but will also improve the slip load and therefore the applicability of the joint since higher tensile forces in the plates can be allowed. Furthermore, an increasing initial preload force will lead to increasing applicability of the joint. Reviewing the low applicable remote stress ratios, limited tensile forces are allowed when slip has to be avoided. It can be concluded that the yield limit (i.e. yielding of the gross cross section) discussed in equation 3.98 and the crack limit (equation 3.99) are not governing in the reviewed case. The effect of the influence of the initial preload force versus relative preload loss at slip is reviewed considering a joint with a total plate thickness $\sum t = 50$ mm. The results are presented in figure 3.8.14. The preload variation appears to be independent of the initial preload force.

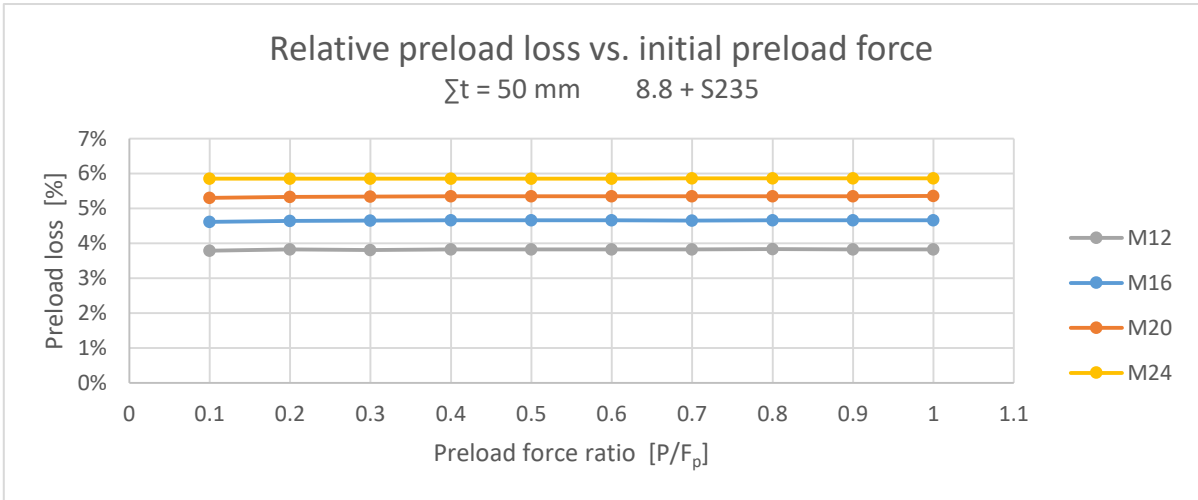


Figure 3.8.14: Relative preload loss vs. initial preload force ($\Sigma t = 50 \text{ mm}$, 8.8 bolt + S235)

Comparable with the influence of the initial preload force, a parametric study is performed considering the influence of the total plate thickness Σt at P_{nom} ($0.875F_p$) at slip or cracking. The relative preload losses at slip or cracking are presented in figure 3.8.15. Maximum susceptibility can be found at small total plate thicknesses. It can be concluded that the total plate thickness has a significant impact on the preload losses. At small plate thicknesses, the crack limit can be exceeded before the slip load is reached since the small cross section will allow higher remote stresses prior to slip, explaining the deviating decreasing trend at small total plate thicknesses.

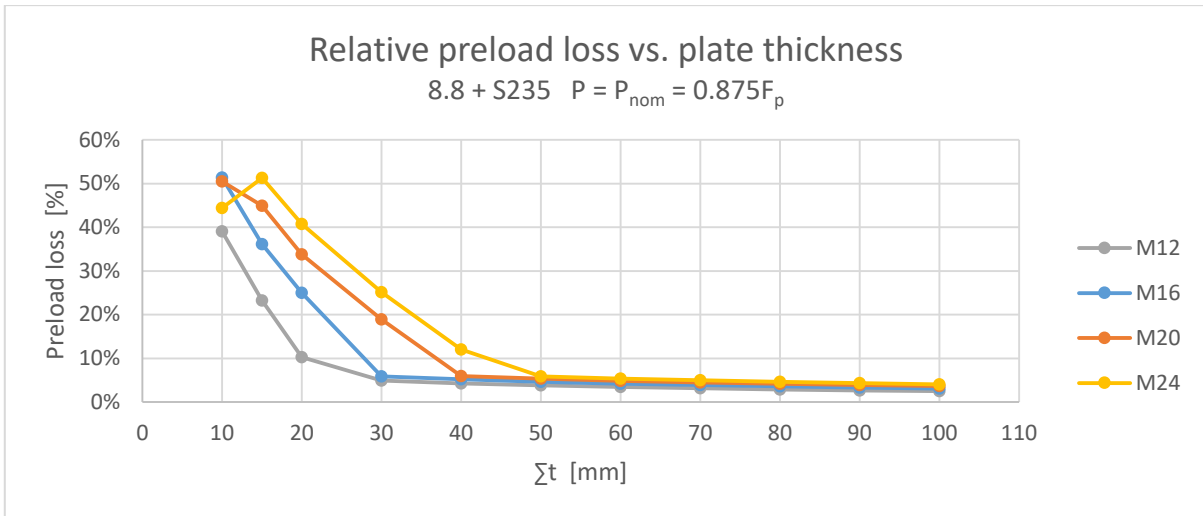


Figure 3.8.15: Relative preload loss vs. total plate thickness ($P = P_{nom}$, 8.8 bolt + S235)

Exceedance of the crack limit at small total plate thickness $\Sigma t = 10 \text{ mm}$ and high initial preload forces is visualized in figures 3.8.16 and 3.8.17. Figure 3.8.16 demonstrates that the slip load is reached prior to cracking for small bolt diameters. Furthermore, the yield limit is not reached ($\sigma_{//}/f_y < 1$) indicating that the relatively small width of the considered sample ($W_{min} = 2.4d$) leads to cracking of the net section before yielding of the gross cross section occurs. A sudden decrease of preload force can be observed at a remote stress ratio equal to 0.5 due to local yielding around the bolt hole. Figure 3.8.17 demonstrates that high initial preload losses can lead to exceedance of the crack limit before the slip load is reached if a small total thickness is combined with a large bolt diameter. It can be concluded that local yielding has a significant impact on the preload level. It should be noted that the model considers yielding over the full circumference leading to an overestimation of the preload losses. The stress concentrations are not uniform as can be noticed in figure 3.8.4.

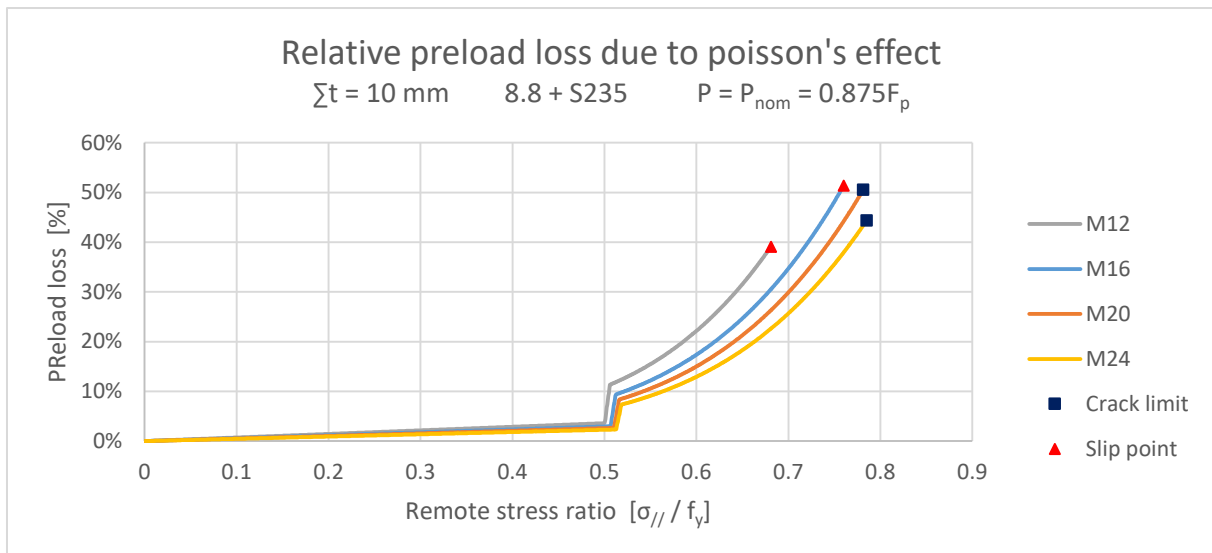


Figure 3.8.16: Relative preload loss due to poisson's effect ($\Sigma t = 10 \text{ mm}$, 8.8 bolt + S235, $P = 0.875F_p$)

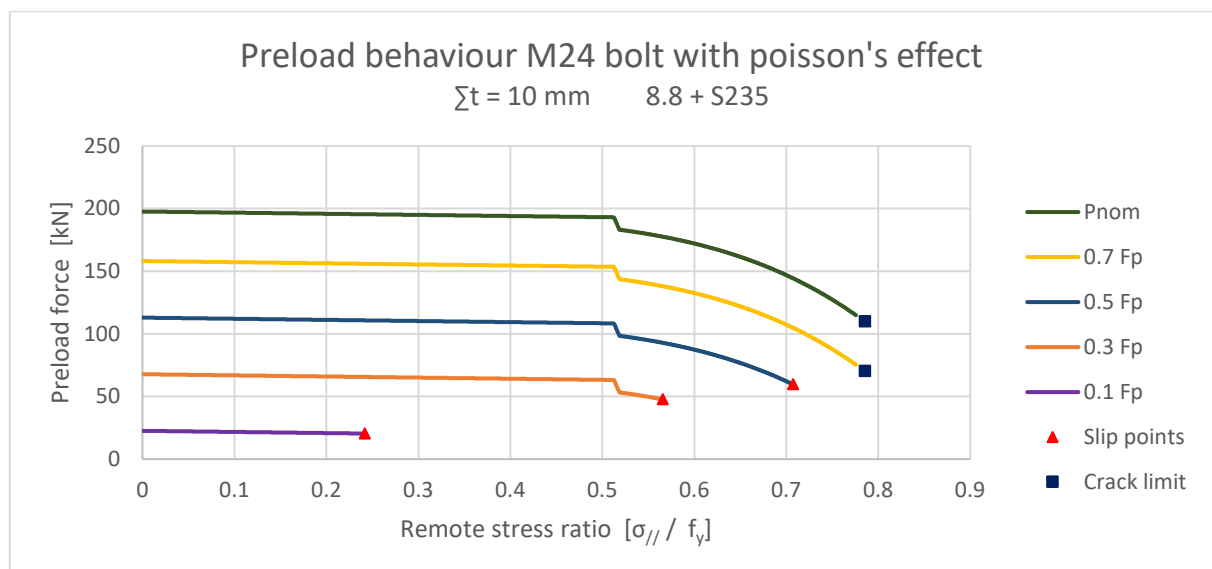


Figure 3.8.17: Preload behaviour due to poisson's effect ($\Sigma t = 10 \text{ mm}$, M24, 8.8 bolt + S235)

The impact of poisson's effect, local yielding and cracking can be minimized and prevented by formulating a minimum total plate thickness – bolt diameter requirement. The following requirement is assumed:

$$\frac{\Sigma t}{d} \geq 3 \quad (3.100)$$

The maximum relative preload losses corresponding to requirement described in equation 3.100 with $P = P_{nom}$ are listed in table 3.8.8.

Maximum preload losses with $\Sigma t/d$ requirement				
	M12	M16	M20	M24
Σt	>36 mm	>48 mm	>60 mm	>72 mm
$\Delta P_{poisson,max}$	4.52%	4.76%	4.88%	4.91%

Table 3.8.8: Maximum preload losses due to poisson's effect with $\Sigma t/d$ requirement (P_{nom} , 8.8 + S235)

3.8.5 Poisson's effect A4 80 stainless steel bolt + S235 plates

Using the material properties considering A4 80 bolts and S235 plates, the poisson's effect can be predicted. The relative preload losses of a joint with a total plate thickness $\Sigma t = 50$ mm and an initial preload force $P = P_{nom}$ ($P_{nom} = 0.933F_p$) are presented in figure 3.8.18. The preload behaviour of a joint with a total plate thickness $\Sigma t = 50$ mm and an M16 bolt with various levels of initial preload force is presented in figure 3.8.19. Slip points are added to the figures to indicated where slip will occur.

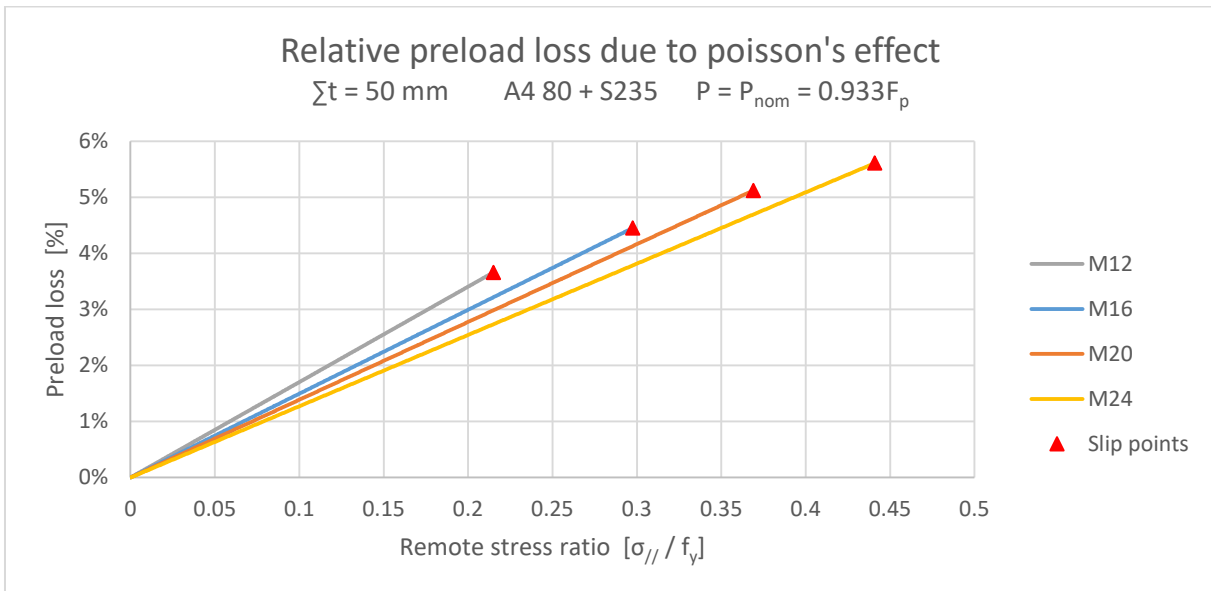


Figure 3.8.18: Relative preload loss due to poisson's effect ($\Sigma t = 50$ mm, A4 80 bolt + S235, $P = 0.933F_p$)

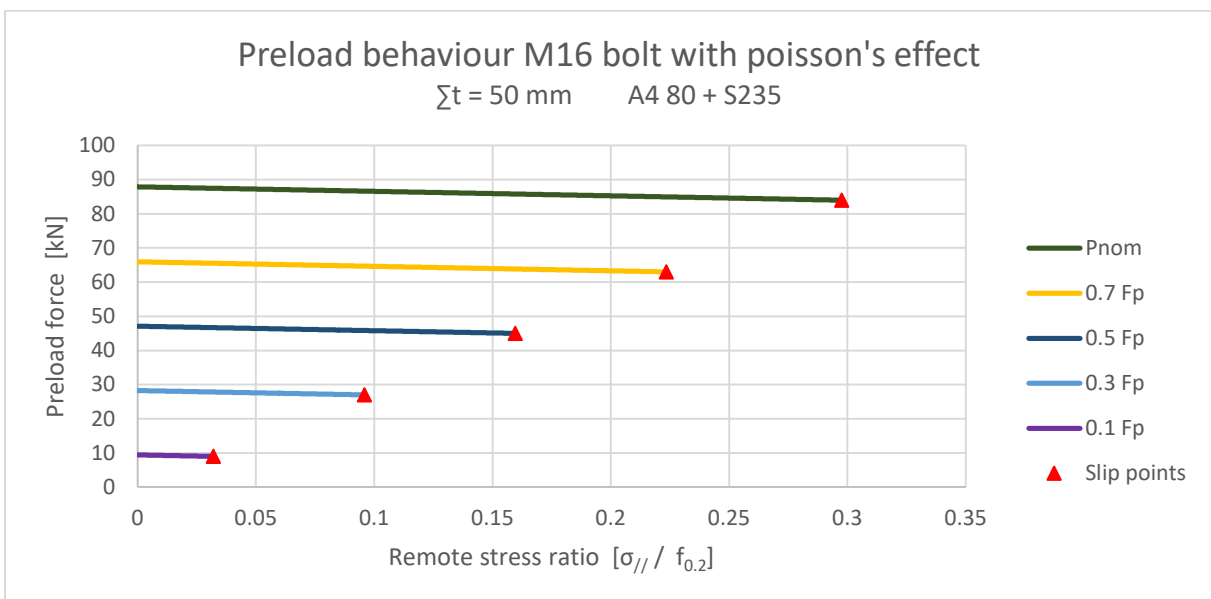


Figure 3.8.19: Preload behaviour due to poisson's effect ($\Sigma t = 50$ mm, M16, A4 80 bolt + S235)

Comparable with the results found in section 3.8.4, an increasing bolt diameter will lead to increasing relative preload losses, but will also improve the slip load and therefore the applicability of the joint since higher tensile forces can be allowed. Yielding of the gross cross section and failure of the net cross section will not occur if slip is prevented with this specific total plate thickness.

The effect of the influence of the initial preload force versus relative preload loss is reviewed considering a joint with a total plate thickness $\Sigma t = 50$ mm. The results are presented in figure 3.8.20. The preload variation appears to be independent of the initial preload force.

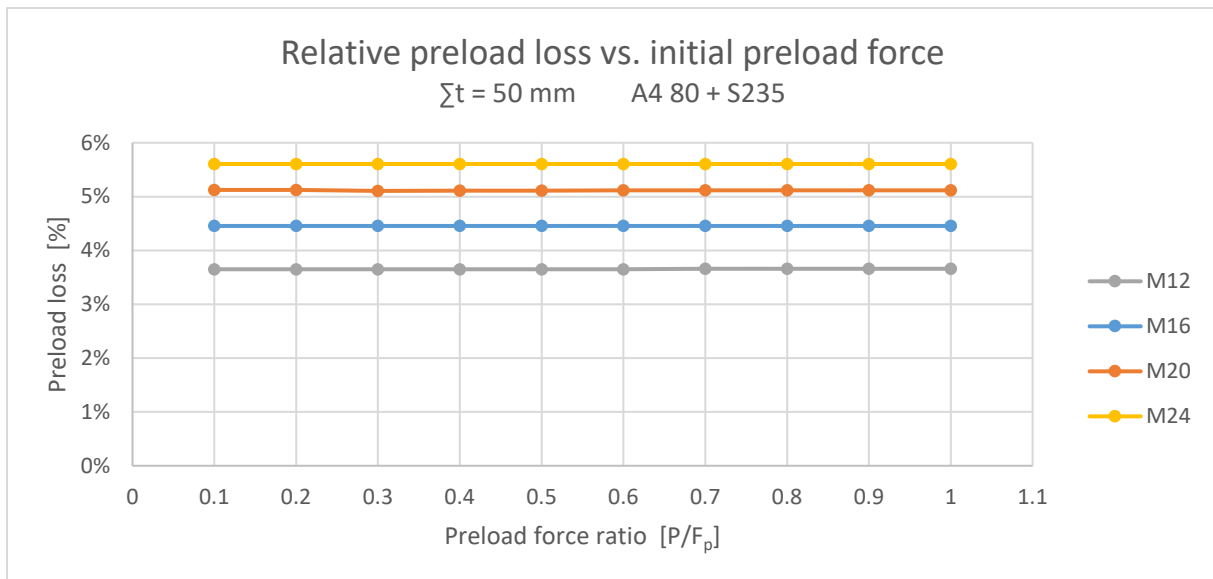


Figure 3.8.20: Relative preload loss vs. initial preload force ($\Sigma t = 50$ mm, A4 80 bolt + S235)

The influence of the total plate thickness Σt at P_{nom} ($0.933F_p$) on the relative preload losses is presented in figure 3.8.21. For every bolt diameter, maximum susceptibility can be found at a specific total plate thickness. Again, application of small total plate thicknesses will lead to exceedance of the crack limit before the slip load is reached.

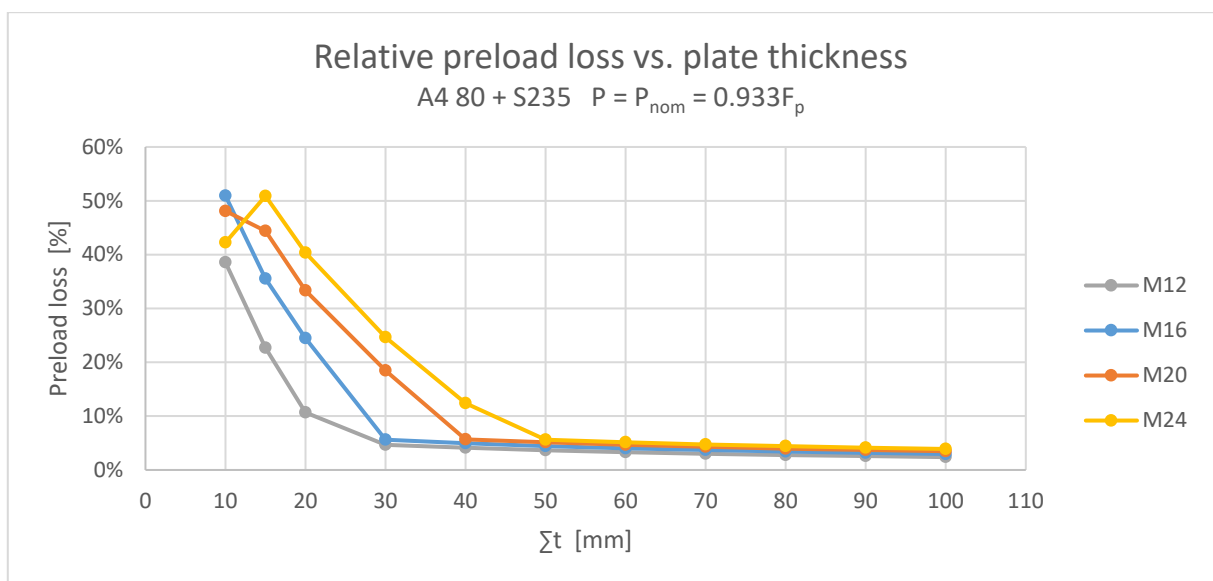


Figure 3.8.21: Relative preload loss vs. total plate thickness ($P = P_{nom}$, A4 80 bolt + S235)

Considering the $\Sigma t/d$ requirement formulated in equation 3.100, the maximum relative preload losses corresponding with $P = P_{nom}$ are determined and listed in table 3.8.9.

Maximum preload losses with $\Sigma t/d$ requirement				
	M12	M16	M20	M24
Σt	>36 mm	>48 mm	>60 mm	>72 mm
$\Delta P_{poisson,max}$	4.3%	4.6%	4.7%	4.7%

Table 3.8.9: Maximum preload losses poisson's effect with $\Sigma t/d$ requirement (P_{nom} , A4 80 + S235)

3.8.6 Poisson's effect A4 80 stainless steel bolt + 5083 O plates

Using the material properties considering A4 80 bolts and 5083O plates, the poisson's effect can be predicted. The relative preload losses of a joint with a total plate thickness $\Sigma t = 50$ mm and an initial preload force $P = P_{nom}$ ($P_{nom} = 0.933F_p$) are presented in figure 3.8.22. The preload behaviour of a joint with a total plate thickness $\Sigma t = 50$ mm and an M16 bolt with various levels of initial preload force is presented in figure 3.8.23. Slip points are added to the figures to indicated where slip will occur. The preload behaviour follows the stress strain relationship of 5083O explaining the curved trend.

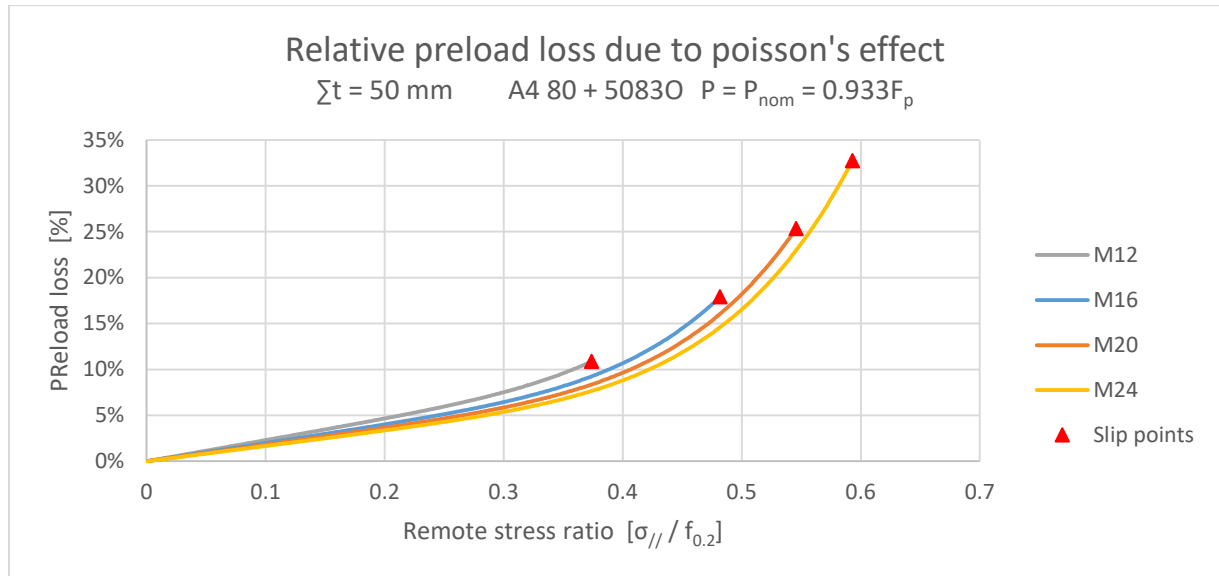


Figure 3.8.22: Relative preload loss due to poisson's effect ($\Sigma t = 50$ mm, A4 80 bolt + 5083O, $P = 0.933F_p$)

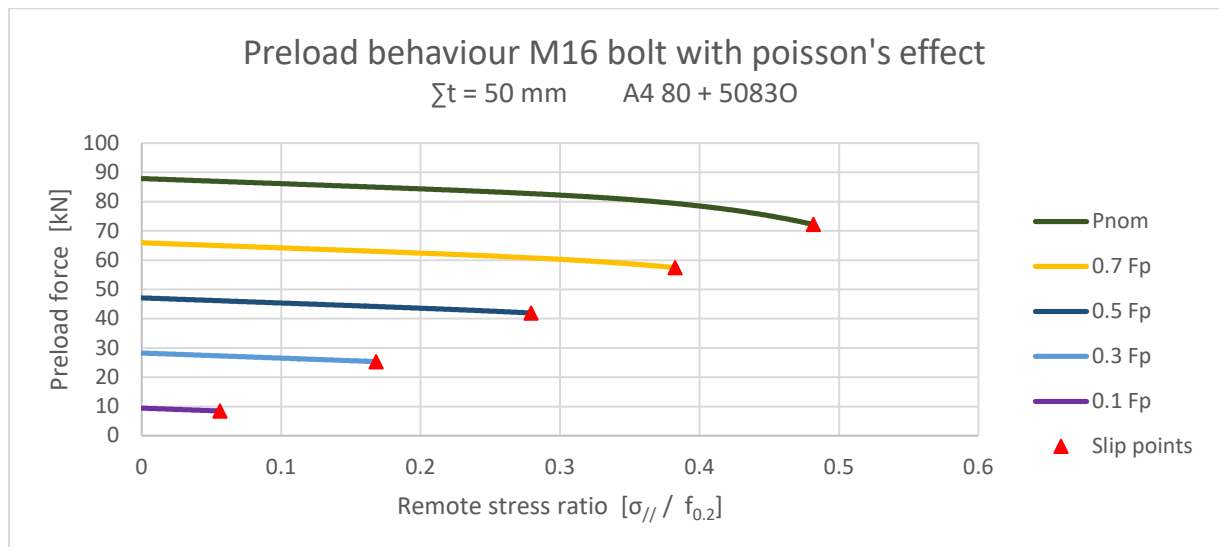


Figure 3.8.23: Preload behaviour due to poisson's effect ($\Sigma t = 50$ mm, M16, A4 80 bolt + 5083O)

Comparable with the results found in sections 3.8.4 and 3.8.5, an increasing bolt diameter will lead to increasing relative preload losses, but will also improve the slip load and therefore the applicability of the joint since higher tensile forces can be allowed. The non-linear behaviour indicates that yielding occurs around the bolt hole due the relatively low proof stress of 5083O. The excessive deformations caused by yielding will lead to higher preload losses at slip as compared to S235.

The effect of yielding can also be observed by considering the influence of the initial preload force versus relative preload loss. The impact is reviewed considering a joint with a total plate thickness $\Sigma t = 50$ mm. The results are presented in figure 3.8.24. Yielding occurs if $P/F_p > 0.3$.

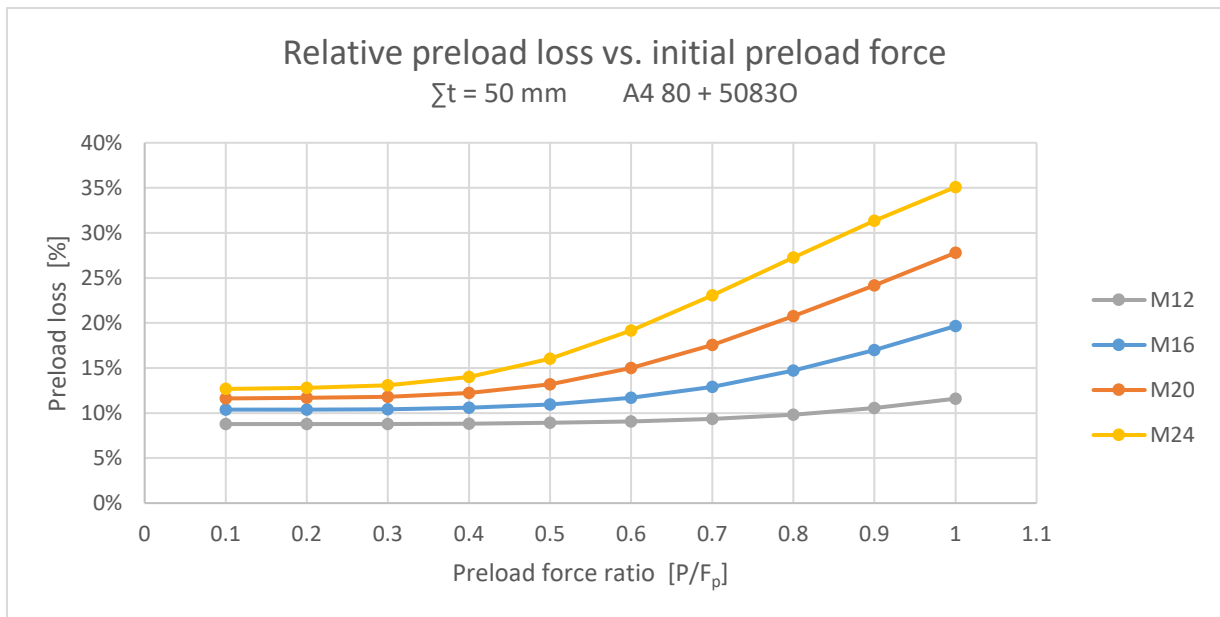


Figure 3.8.24: Relative preload loss vs. initial preload force ($\Sigma t = 50$ mm, A4 80 bolt + 50830)

The influence of the total plate thickness Σt at P_{nom} ($0.933F_p$) on the relative preload losses is presented in figure 3.8.25. Yielding around the bolt hole will occur prior to cracking at relatively low remote stresses leading to extensive deformations around the bolt hole. Subsequently, the preload level will drop significantly resulting in slip.

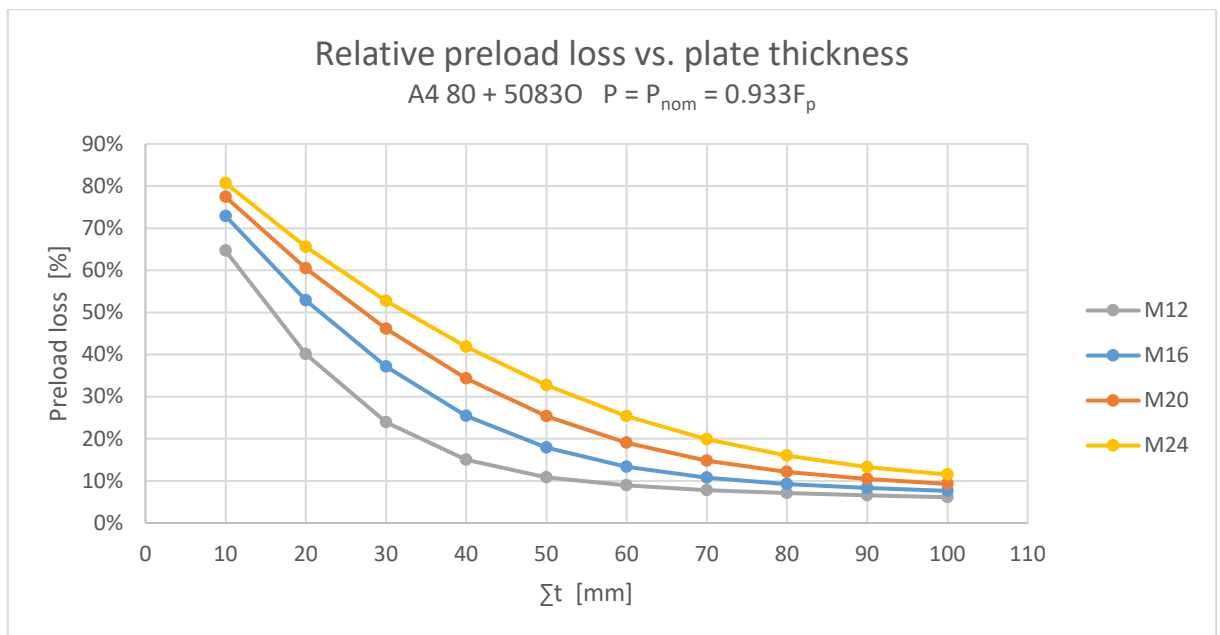


Figure 3.8.25: Relative preload loss vs. total plate thickness ($P = P_{nom}$, A4 80 bolt + 50830)

Considering the $\Sigma t/d$ requirement formulated in equation 3.100, the maximum relative preload losses corresponding with $P = P_{nom}$ are determined and listed in table 3.8.10.

Maximum preload losses with $\Sigma t/d$ requirement				
	M12	M16	M20	M24
Σt	>36 mm	>48 mm	>60 mm	>72 mm
$\Delta P_{poisson,max}$	17.8%	19.1%	19.0%	19.0%

Table 3.8.10: Maximum preload losses poisson's effect with $\Sigma t/d$ requirement (P_{nom} , A4 80 + 50830)

3.8.7 Poisson's effect A4 80 stainless steel bolt + 6082T6 plates

Using the material properties considering A4 80 bolts and 6082T6 plates, the poisson's effect can be predicted. The relative preload losses of a joint with a total plate thickness $\sum t = 50$ mm and an initial preload force $P = P_{nom}$ ($P_{nom}=0.933F_p$) are presented in figure 3.8.26. The preload behaviour of a joint with a total plate thickness $\sum t = 50$ mm and an M16 bolt with various levels of initial preload force is presented in figure 3.8.27. Slip points are added to the figures to indicated where slip will occur.

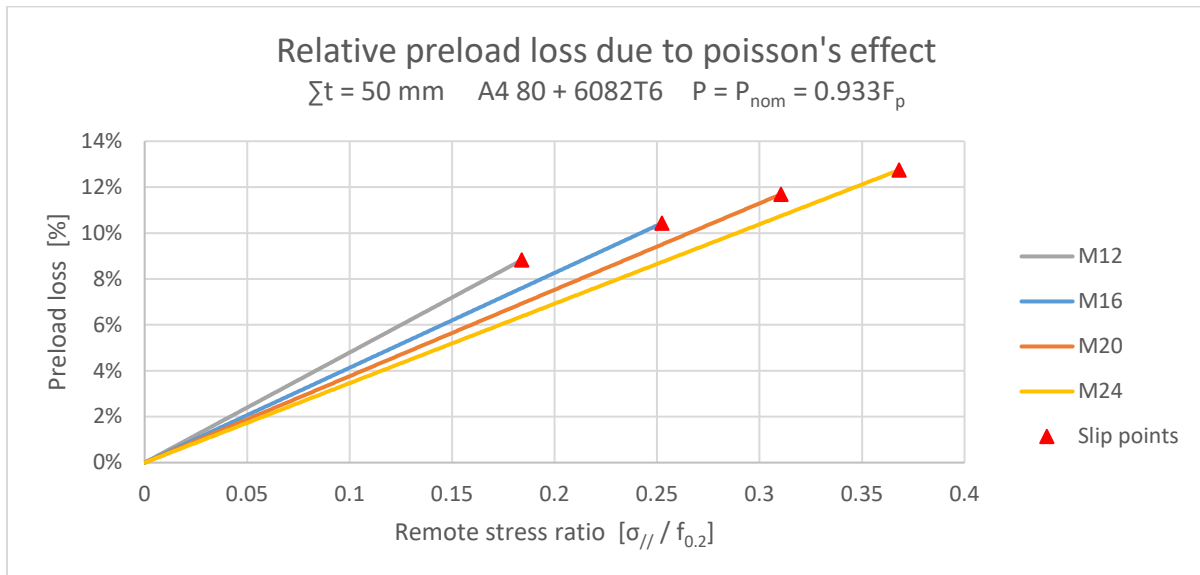


Figure 3.8.26: Relative preload loss poisson's effect ($\sum t = 50$ mm, A4 80 bolt + 6082T6, $P = 0.933F_p$)

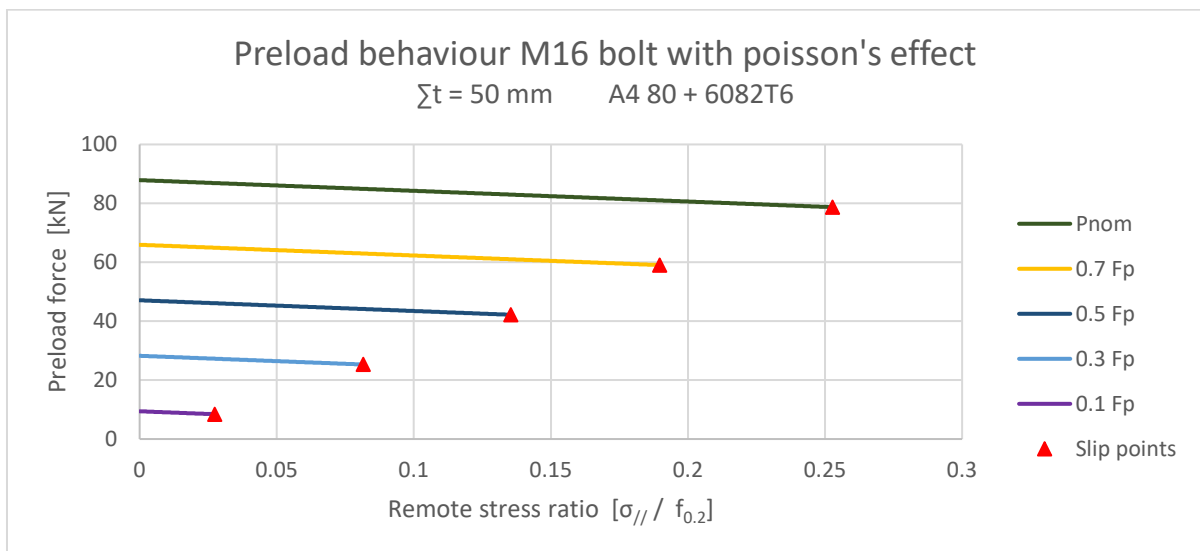


Figure 3.8.27: Preload behaviour due to poisson's effect ($\sum t = 50$ mm, M16, A4 80 bolt + 6082T6)

Comparable with the results found in sections 3.8.4, 3.8.5 and 3.8.6, an increasing bolt diameter will lead to increasing relative preload losses, but will also improve the slip load and therefore the applicability of the joint since higher tensile forces can be allowed. Non-linear preload behaviour does not occur with the considered total plate thickness and initial preload force, indicating that yielding around the bolt hole will not occur prior to slip.

The effect of the influence of the initial preload force versus relative preload loss is reviewed considering a joint with a total plate thickness $\sum t = 50$ mm. The results are presented in figure 3.8.28. Comparable with the application of S235 plates, the preload variation appears to be independent of the initial preload force.

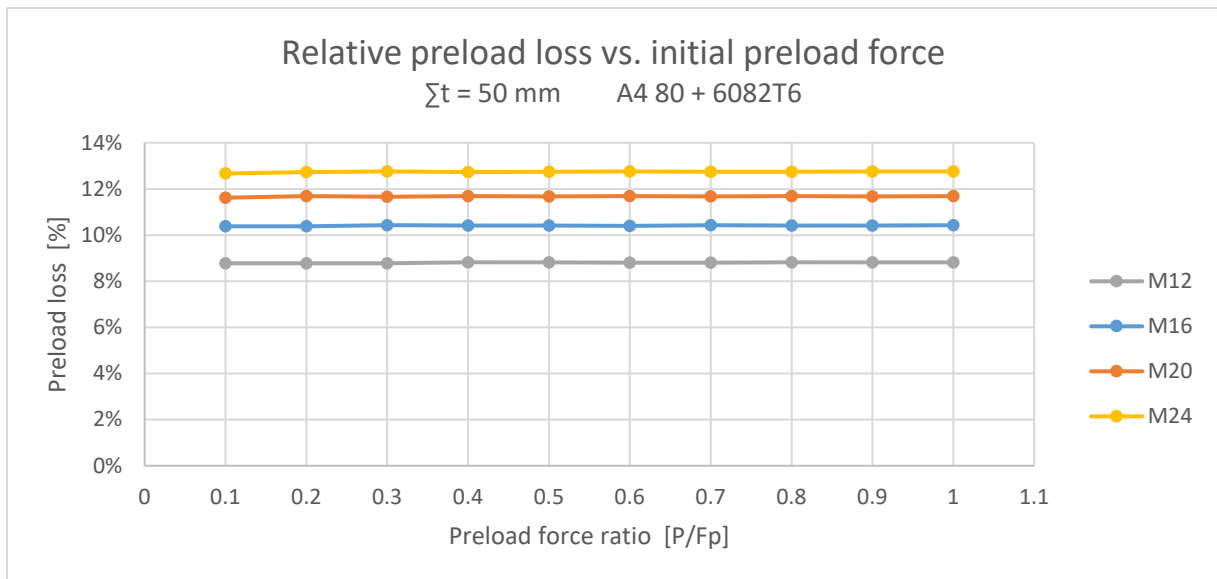


Figure 3.8.28: Relative preload loss vs. initial preload force ($\Sigma t = 50 \text{ mm}$, A4 80 bolt + 6082T6)

The influence of the total plate thickness Σt at P_{nom} ($0.933F_p$) on the relative preload losses is presented in figure 3.8.29. Yielding will occur at small total plate thicknesses. Again, the preload level will drop significantly due to local yielding around the bolt hole.

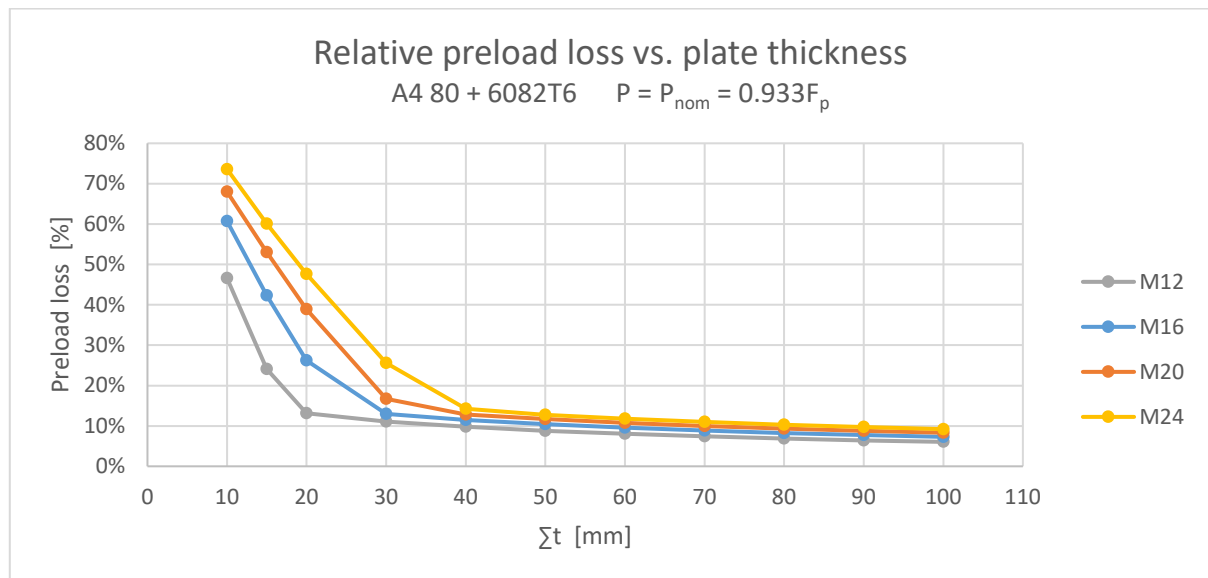


Figure 3.8.29: Relative preload loss vs. total plate thickness ($P = P_{nom}$, A4 80 bolt + 6082T6)

Considering the $\Sigma t/d$ requirement formulated in equation 3.100, the maximum relative preload losses corresponding with $P = P_{nom}$ are determined and listed in table 3.8.11.

Maximum preload losses with $\Sigma t/d$ requirement				
	M12	M16	M20	M24
Σt	>36 mm	>48 mm	>60 mm	>72 mm
$\Delta P_{poisson,max}$	10.2%	10.6%	10.8%	10.8%

Table 3.8.11: Maximum preload losses poisson's effect with $\Sigma t/d$ requirement (P_{nom} , A4 80 + 6082T6)

3.8.8 Comparison material combinations

Combining the data of the preload behaviour of a joint with a total plate thickness of $\Sigma t = 50$ mm and an M16 bolt preloaded up to P_{nom} will give the opportunity to compare the results of the four material combinations. The relative preload losses are presented in figure 3.8.30, the preload behaviour is presented in figure 3.8.31. It can be concluded that a combination of aluminium plates combined with a stainless steel bolt is most susceptible to poisson's effect as can be expected due to the relatively low young's modulus of aluminium. With normalization with respect to the proof stress, 6082 T6 is most susceptible to poisson's effect. When the remote stress is plotted without normalization, as shown in figure 3.8.32, it can be observed that a combination of 5083O with A4 80 will lead to extreme preload losses at low remote stresses.

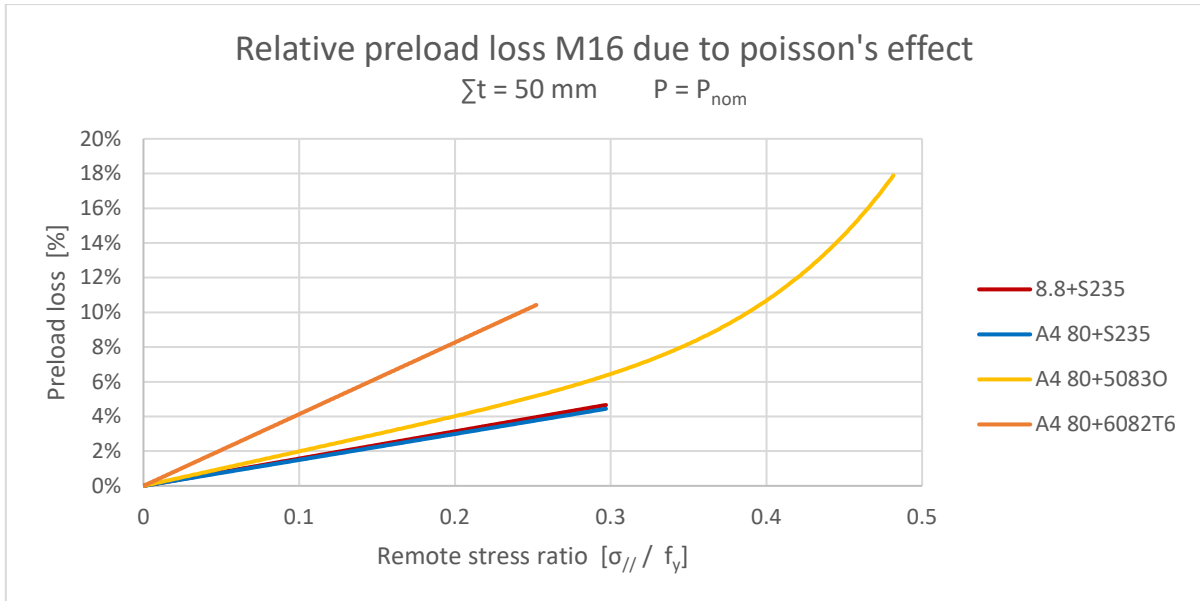


Figure 3.8.30: Comparison relative preload losses poisson's effect with normalized remote stresses

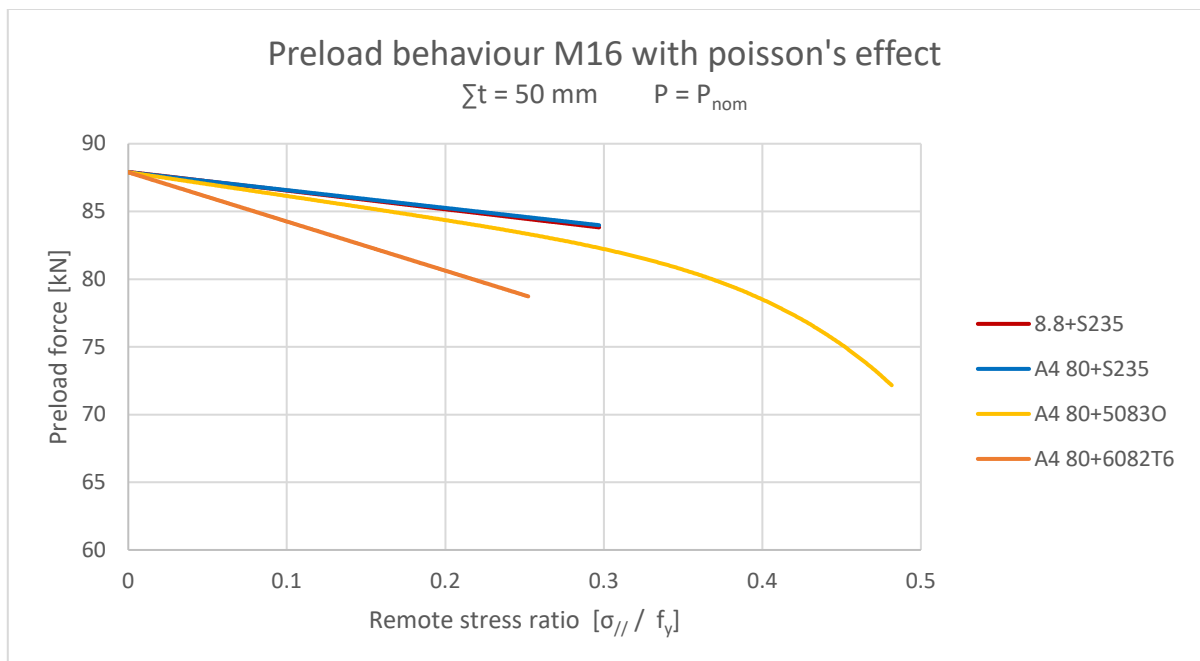


Figure 3.8.31: Comparison preload behaviour poisson's effect with normalized remote stresses

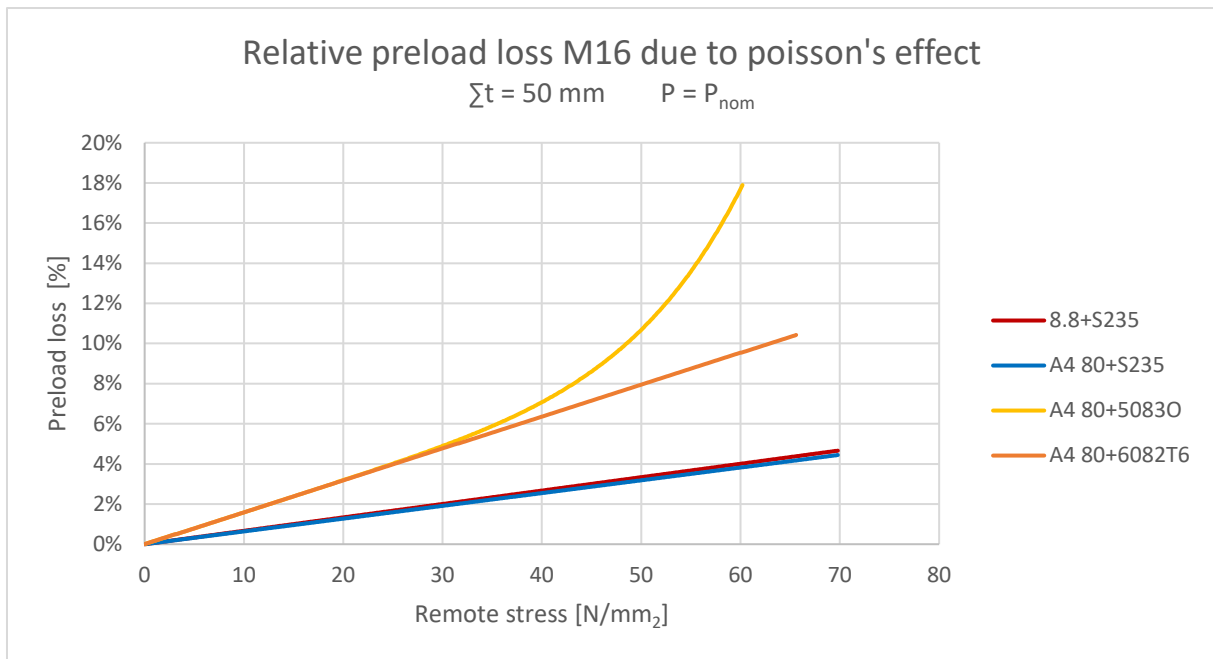


Figure 3.8.32: Comparison relative preload losses poisson's effect with 4 material combinations

The preload losses of the four material combinations determined with the total thickness – bolt diameter requirement of equation 3.100 ($\sum t/d > 3$) are presented in table 3.8.12. Again, it can be observed that joints with aluminium alloys are more susceptible to poisson's effect as compared to joints with steel plate material.

Maximum preload losses with $\sum t/d > 3$				
	M12	M16	M20	M24
	$\sum t > 36 \text{ mm}$	$\sum t > 48 \text{ mm}$	$\sum t > 60 \text{ mm}$	$\sum t > 72 \text{ mm}$
8.8 + S235	4.5%	4.8%	4.9%	4.9%
A4 80 + S235	4.3%	4.6%	4.7%	4.7%
A4 80 + 50830	17.8%	19.1%	19.0%	19.0%
A4 80 + 6082T6	10.2%	10.6%	10.8%	10.8%

Table 3.8.12: Comparison maximum preload losses poisson's effect with $\sum t/d$ requirement

Application of a slightly higher requirement for the thickness – diameter ratio will reduce the preload losses of A4 80 + 50830 significantly. Table 3.8.13 presents the maximum preload losses for $\sum t/d > 4$.

Maximum preload losses with $\sum t/d > 4$				
	M12	M16	M20	M24
	$\sum t > 48 \text{ mm}$	$\sum t > 64 \text{ mm}$	$\sum t > 80 \text{ mm}$	$\sum t > 96 \text{ mm}$
8.8 + S235	3.9%	4.1%	4.2%	4.2%
A4 80 + S235	3.7%	3.9%	4.0%	4.0%
A4 80 + 50830	11.4%	12.1%	12.1%	12.1%
A4 80 + 6082T6	9.0%	9.3%	9.4%	9.4%

Table 3.8.13: Comparison maximum preload losses poisson's effect with $\sum t/d > 4$

3.9 Case Study

The theoretical preload behaviour of a double lap joint with a total plate thickness $\Sigma t = 50$ mm is analyzed for two material combinations containing aluminium alloys and one A4 80 bolt with $d=M16$. The width is assumed to be equal to W_{\min} ($W = 2.4 \cdot d = 38.4$ mm). The double lap joint is illustrated in figure 3.9.1.

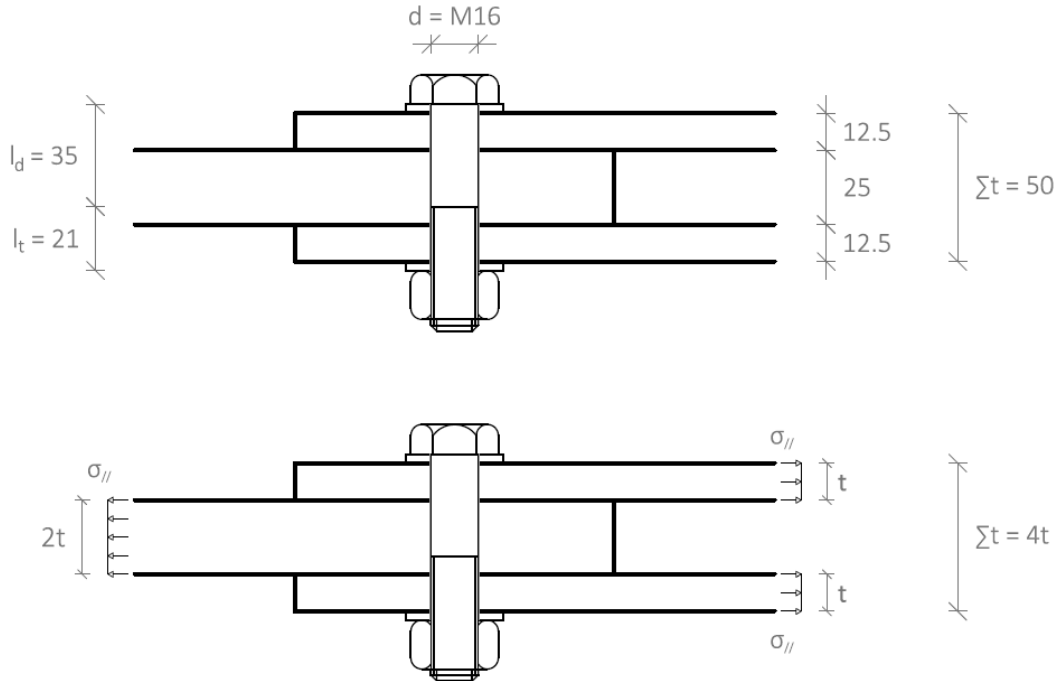


Figure 3.9.1: Double lap joint applied in case study

The bolted joint is subjected to various effects in successive order (e.g. the preload force at the end of phase 1 will be applied at the start of phase 2). The effects and phases used during this analysis are:

- Phase 1: Application of preload force P_{nom} (88 kN) at $T_{\text{assembly}} = 20^\circ\text{C}$ with duration of 1000 hours; embedment effects are ignored since retightening can neutralize embedment creep
- Phase 2: Tensile force up to slip load after 42 days
- Phase 3: Temperature drop to 5°C
- Phase 4: Structure life time 50 years

3.9.1 Bolt and joint characteristics

The characteristics of the joint can be determined with the VDI-model derived in section 3.1. The stiffness of the subdivided bolt parts is calculated with:

$$k_{SK} = \frac{E_b A_d}{0.5d} = \frac{200000 \cdot 201}{0.5 \cdot 16} = 5.027 \cdot 10^6 \text{ N/mm} \quad (3.101)$$

$$k_d = \frac{E_b A_d}{l_d} = \frac{200000 \cdot 201}{35} = 1.149 \cdot 10^6 \text{ N/mm} \quad (3.102)$$

$$k_t = \frac{E_b A_t}{l_t} = \frac{200000 \cdot 157}{21} = 1.495 \cdot 10^6 \text{ N/mm} \quad (3.103)$$

$$k_{GM} = \frac{1}{\frac{0.5d}{E_b \frac{\pi}{4} d^3} + \frac{0.4d}{E_b A_d}} = \frac{1}{\frac{8}{157080 \cdot 13.546^2} + \frac{3.4}{200000 \cdot 201}} = 2.290 \cdot 10^6 \text{ N/mm} \quad (3.104)$$

The total stiffness of the bolt is equal to:

$$k_b = \frac{1}{\frac{1}{k_{SK}} + \frac{1}{k_d} + \frac{1}{k_t} + \frac{1}{k_{GM}}} = 4.598 \cdot 10^5 \text{ N/mm} \quad (3.105)$$

Since the joint is symmetrical, the joint can be calculated with two identical frusta with a height of $0.5\sum t$. The stiffness of a frustum is equal to:

$$\begin{aligned} k_t &= \frac{\pi E_j d_0 \tan 30}{\ln \left(\frac{(2t_1 \tan 30 + (1.5d + 2t_w \tan 30) - d_0) \cdot ((1.5d + 2t_w \tan 30) + d_0)}{(2t_1 \tan 30 + (1.5d + 2t_w \tan 30) + d_0) \cdot ((1.5d + 2t_w \tan 30) - d_0)} \right)} \\ &= \frac{\pi \cdot 70000 \cdot 17 \cdot \tan 30}{\ln \left(\frac{(50 \cdot \tan 30 + (24 + 6 \cdot \tan 30) - 17) \cdot ((24 + 6 \cdot \tan 30) + 17)}{(50 \cdot \tan 30 + (24 + 6 \cdot \tan 30) + 17) \cdot ((24 + 6 \cdot \tan 30) - 17)} \right)} \\ &= 2.623 \cdot 10^6 \text{ N/mm} \end{aligned} \quad (3.106)$$

The combined plate stiffness is equal to:

$$k_{\sum t} = \frac{1}{\frac{1}{k_t} + \frac{1}{k_t}} = \frac{1}{\frac{1}{2.623 \cdot 10^6} + \frac{1}{2.623 \cdot 10^6}} = 1.312 \cdot 10^6 \text{ N/mm} \quad (3.107)$$

The washer stiffness is equal to:

$$\begin{aligned} k_w &= \frac{\pi E_w d_{w1} \tan 30}{\ln \left(\frac{(2t_w \tan 30 + 1.5d - d_{w1}) \cdot (1.5d + d_{w1})}{(2t_w \tan 30 + 1.5d + d_{w1}) \cdot (1.5d - d_{w1})} \right)} \\ &= \frac{\pi \cdot 200000 \cdot 17 \cdot \tan 30}{\ln \left(\frac{(2 \cdot 3 \cdot \tan 30 + 1.5 \cdot 16 - 17) \cdot (1.5 \cdot 16 + 17)}{(2 \cdot 3 \cdot \tan 30 + 1.5 \cdot 16 + 17) \cdot (1.5 \cdot 16 - 17)} \right)} \\ &= 1.927 \cdot 10^7 \text{ N/mm} \end{aligned} \quad (3.108)$$

The joint stiffness is equal to the summation of the 2 washers and 2 frusta and is equal to:

$$k_j = \frac{1}{\frac{1}{k_w} + \frac{1}{k_{\sum t}} + \frac{1}{k_w}} = \frac{1}{\frac{1}{1.927 \cdot 10^7} + \frac{1}{1.312 \cdot 10^6} + \frac{1}{1.927 \cdot 10^7}} = 1.154 \cdot 10^6 \text{ N/mm} \quad (3.109)$$

3.9.2 50830 + M16 A4 80 bolt

Phase 1 contains the application of a preload of force of P_{nom} resulting in bolt relaxation and plate creep over 1000 hours assuming $t_{assembly} = 3s$. A combined model is created and the bolt relaxation and plate creep is calculated per time increment dt . At the start of the next time increment, the preload losses of both effects are taken into account. Figure 3.9.2 gives the preload behaviour in the first 42 days. Since retightening is assumed, embedment effects will be ignored.

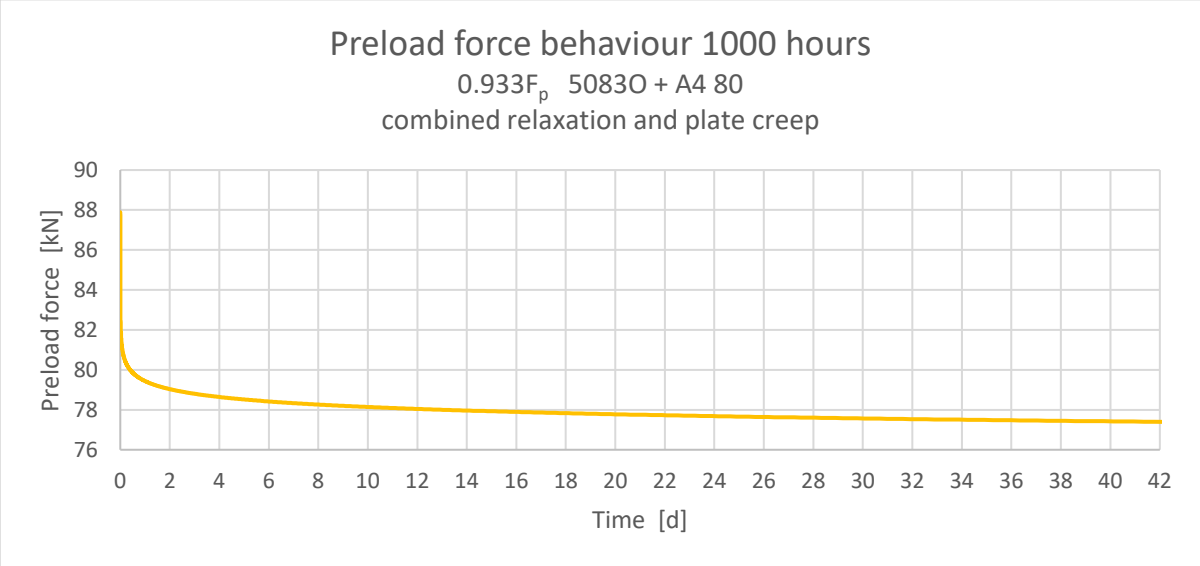


Figure 3.9.2: Preload behaviour 42 days combined relaxation A4 80 and plate creep 50830

The remaining preload level after 42 days is 77.4 kN which corresponds to a preload loss of 10.5 kN. The relative preload losses due to combined relaxation and plate creep are therefore equal to 11.9%.

Phase 2 takes into account a tensile force up to the slip load. The preload force at the start of phase 2 is equal to 77.4 kN. The preload behaviour versus the normalized stress is visualized in figure 3.9.3.

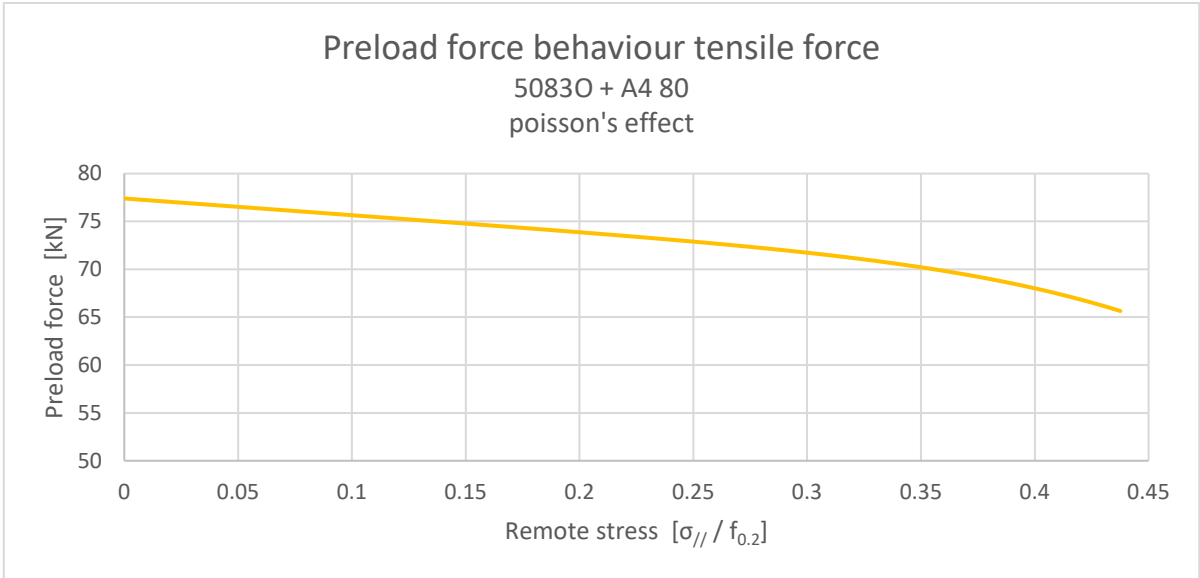


Figure 3.9.3: Preload behaviour poisson's effect 50830 + A4 80

The remaining preload level after the application of the tensile force is 65.6 kN which is equal to a preload loss of 11.8 kN. The relative preload loss due to poisson's effect, estimated with respect to the initial preload force of 87.9 kN, is therefore equal to 13.4%.

Phase 3 contains a temperature variation of $\Delta T = -15^{\circ}\text{C}$ up to $T = 5^{\circ}\text{C}$. The preload force at the start of phase 3 is equal to 58.6 kN. The preload behaviour versus temperature is visualized in figure 3.9.4.

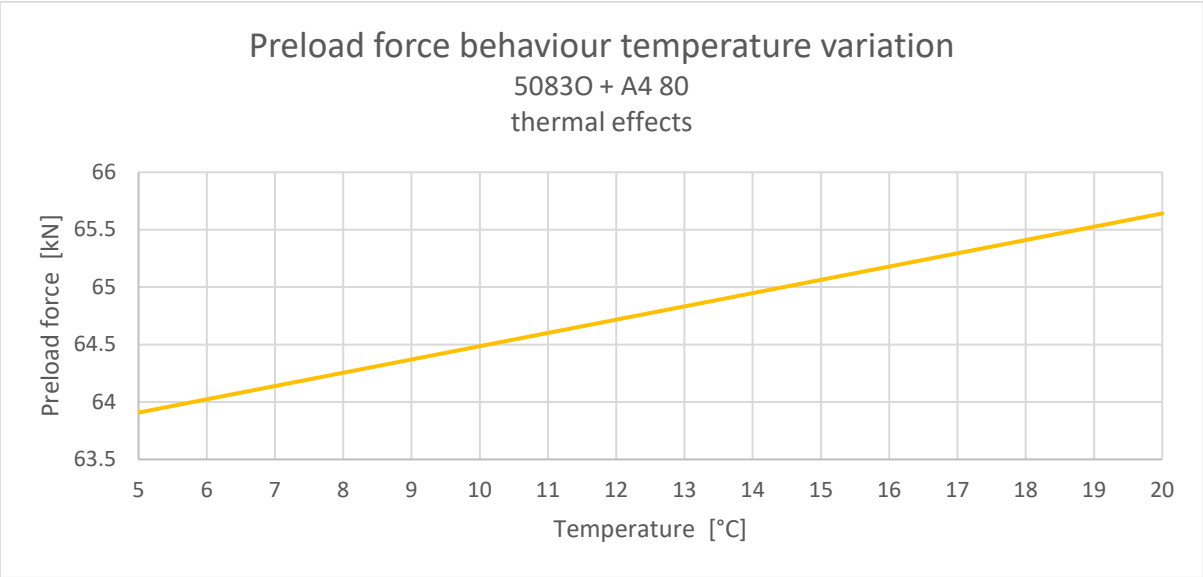


Figure 3.9.4: Preload behaviour thermal effects 50830 + A4 80

The remaining preload level after a temperature variation of 15°C is 63.9 kN which corresponds to a preload loss of 1.7 kN. The relative preload loss due to thermal effects, estimated with respect to the initial preload force of 87.9 kN, is therefore equal to 1.9%.

Phase 4 takes into account the relaxation and plate creep in the remaining 50 years of the structure life time. The preload force at the start of phase 4 is equal to 63.9. The preload behaviour versus time is visualized in figure 3.9.5.

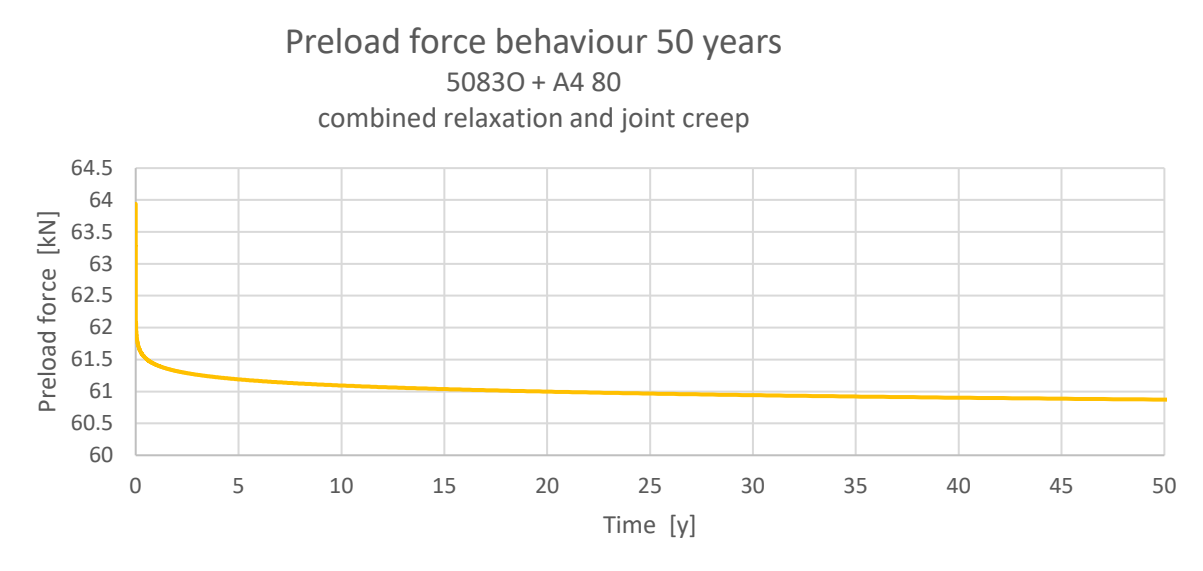


Figure 3.9.5: Preload behaviour 50 years days combined relaxation A4 80 and plate creep 50830

The remaining preload level after 50 years of service is 60.9 kN which corresponds to a preload loss of 3.1 kN. The relative preload losses due to relaxation and plate creep are therefore equal to 3.5%.

The combined preload loss of all 4 phases is equal to 27.0 kN which is equal to 30.7% relative preload loss. Preload losses due to poisson’s effect are most dominant with a relative preload loss of 13.4%.

3.9.3 6082T6 + M16 A4 80 bolt

Similar to the analysis of a joint containing 6082T6 aluminium plates and an M16 A4 80 bolt, an identical joint with 6082T6 plates is regarded containing all 4 phases. Figure 3.9.6 gives the preload behaviour during phase 1. Embedment effects are not taken into account.

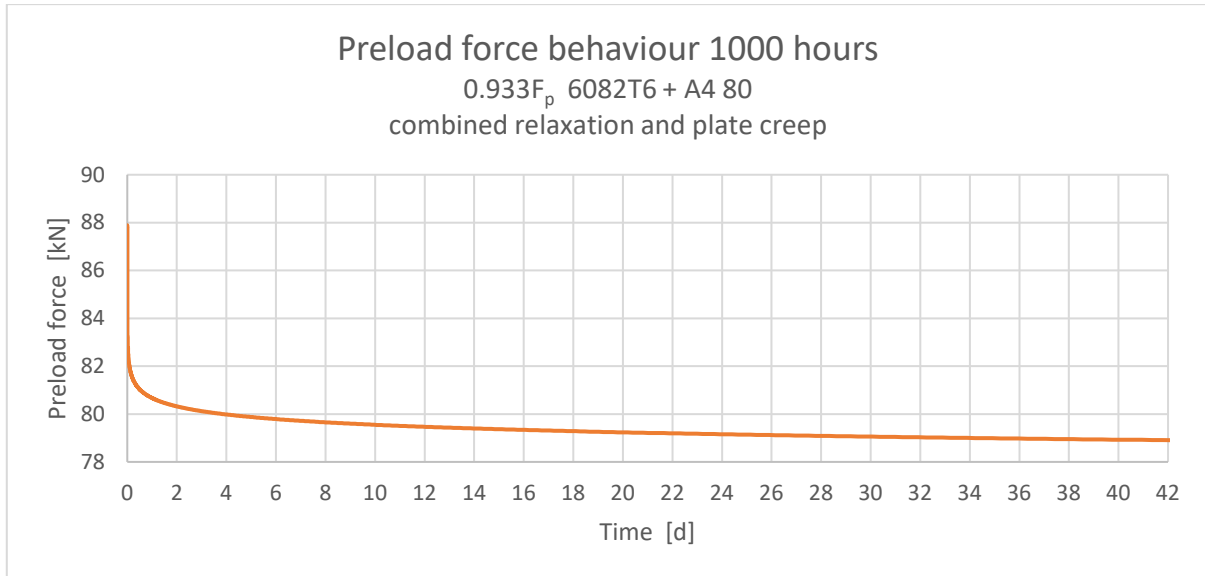


Figure 3.9.6: Preload behaviour 42 days combined relaxation A4 80 and plate creep 6082T6

The remaining preload level after 42 days is 78.9 kN which corresponds to a preload loss of 9.0 kN. The relative preload losses due to combined relaxation and plate creep are therefore equal to 10.2%.

A tensile load up to the slip load is applied in phase 2. The preload force at the start of phase 2 is equal to 78.9 kN. The preload behaviour versus the normalized remote stress is visualized in figure 3.9.7.

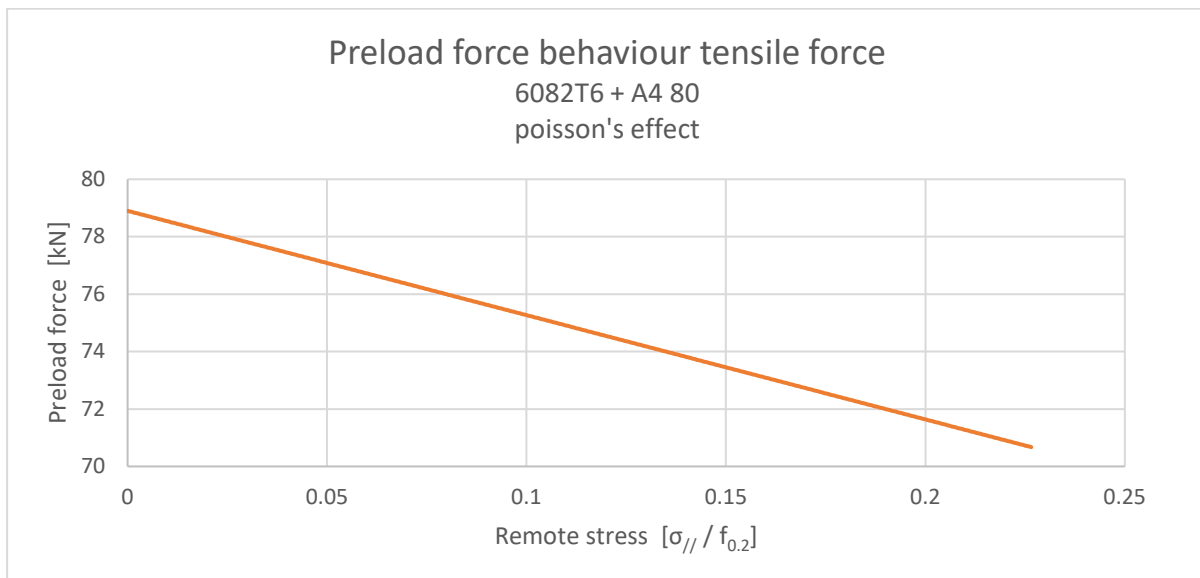


Figure 3.9.7: Preload behaviour poisson's effect 6082T6 + A4 80

The remaining preload level at slip after the application of the tensile force is equal to 70.7 kN which is equal to a preload loss of 8.2 kN during phase 2. The relative preload loss due to poisson's effect, estimated with respect to the initial preload force of 87.9 kN, is therefore equal to 9.3%.

The temperature variation during phase 3 results in equal absolute preload losses compared with 50830 since the coefficient of thermal expansion is identical. The preload force at the start of phase 3 is equal to 70.7 kN. The preload behaviour versus temperature is visualized in figure 3.9.8.

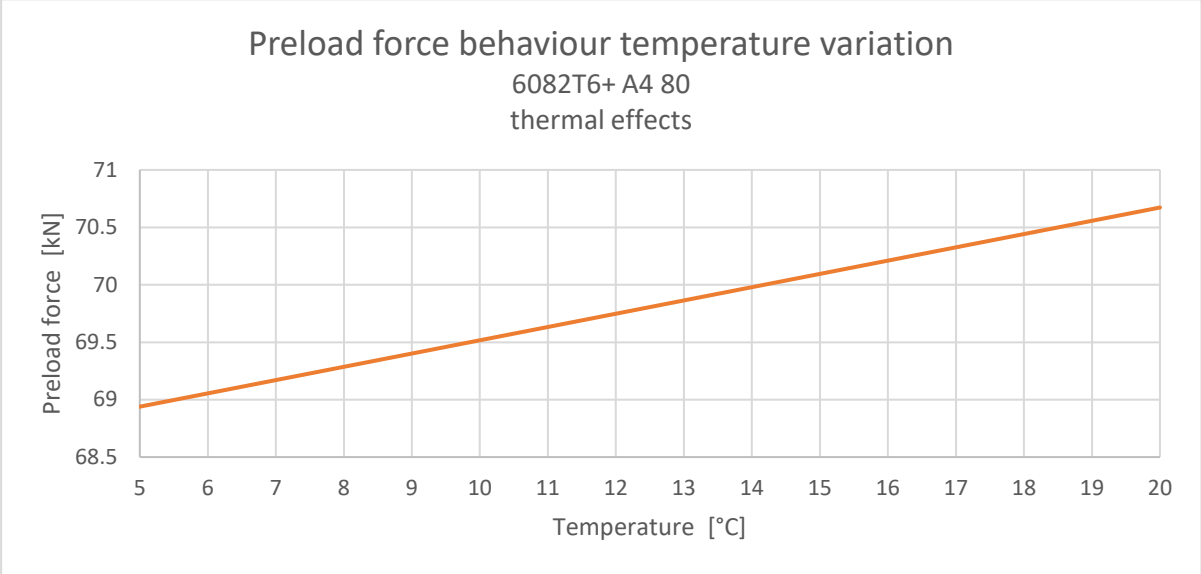


Figure 3.9.8: Preload behaviour thermal effects 6082T6 + A4 80

The remaining preload level after a temperature variation of 15°C is 68.9 kN which corresponds to a preload loss of 1.7 kN. The relative preload loss due to thermal effects, estimated with respect to the initial preload force of 87.9 kN, is therefore equal to 1.9%.

The relaxation and plate creep in the remaining 50 years of the structure life time during phase 4 are visualized in figure 3.9.9. The preload force at the start of phase 4 is equal to 68.9 kN.

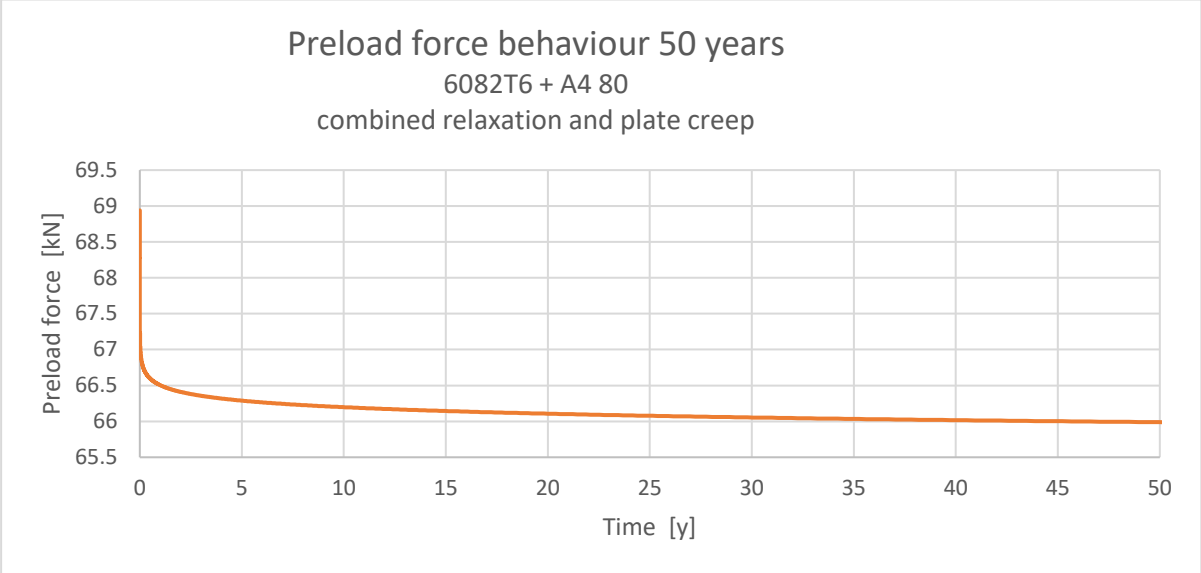


Figure 3.9.9: Preload behaviour 50 years days combined relaxation A4 80 and plate creep 6082T6

The remaining preload level after 50 years of service is 66.0 kN which corresponds to a preload loss of 2.9 kN. The relative preload losses due to relaxation and plate creep are therefore equal to 3.3%.

The combined preload loss of all 4 phases is equal to 21.9 kN which is equal to 24.9% relative preload loss. Preload losses due to relaxation (plate creep of 6082T6 is insignificant) in the first 1000 hours are most dominant with a relative preload loss of 10.2%.

3.10 Summary and conclusions analytical modelling

The construction of a spring model with characteristics described in VDI 2230 is relatively simple due to available data regarding material properties and dimensional data of bolts and joints. A variation in bolt diameter and plate thickness results in varying elastic stiffnesses which can be used in the analysis of the time-dependent and time-independent effects. The ratio between bolt stiffness and joint stiffness will have an impact on the force distribution between joint and bolt. Since aluminium has a lower Young's modulus than steel, the joint stiffness of an aluminium joint will be lower than an identical joint in carbon steel resulting in a lower stiffness ratio. Preload losses can be calculated with the application of contraction and/or extension of the bolt parts and/or joint parts. The contraction and extension due to embedment creep, relaxation, plate creep, thermal effects and poisson's effect are estimated and used to predict preload losses.

Guide values regarding embedment creep are only available for carbon steel joints and bolt. Preload losses in accordance with literature are found if $\sum t > 50$ mm. If $\sum t < 50$ mm, the model output is conservative compared to literature. The available creep data of 316 (A4 80) bolt material and 50830 / 6082T6 alloys are insufficient to take into account in a model. Therefore, the creep data of 314L (wire) are used to estimate the relaxation in A4 80 bolts. Both materials show comparable proof and strength properties. A comparison between 5454O and 6061T6 is made to estimate the plate creep of 50830 and 6082T6. The preload losses due to poisson's effect are determined at slip taking into account the stress concentrations at the bolt hole. After slip, the tensile load will be transferred through a combination of friction and bearing introducing higher peak stresses due to the local load transfer between the bolt and the plate resulting in increasing preload losses. Therefore, slip should be avoided to minimize the preload losses and a high initial preload force should be applied. Preload losses due to poisson's effect are higher in the case of aluminium than in the case of steel due to the lower Young's modulus and (in some alloys) lower proof strength. Bolt bending and prying is not taken into account in the model and should be studied with further research.

A case study containing the theoretical preload behaviour of a double lap joint with a total plate thickness $\sum t = 50$ mm is analyzed for two material combinations containing aluminium alloys and one A4 80 bolt with $d=M16$. The initial preload level is in accordance with the nominal preload force P_{nom} which is determined with 70% of the ultimate design strength of the bolt material f_{ub} multiplied with the reduced-shank cross section A_t . Assuming $t_{assembly} = 3s$, the preload losses due to relaxation and plate creep are approximately 12% with the majority of the losses occurring in the first 10 hours after application of the preload force. Plate creep in both alloys has a minor impact on the preload level. The influence of a thermal variation of $-15^{\circ}C$ is small, resulting in 2% preload loss. The impact of poisson's effect is dominant with relative preload losses up to 13%.

Reviewing the impact of the initial preload force, it can be concluded that a high initial preload force is required to neutralize embedment creep and thermal effects and for applicability of a shear joint if slip-resistance is required. A high initial preload force will introduce significant bolt relaxation and plate creep, but the relative preload losses of these effects are minor compared to the extreme relative losses of embedment creep and thermal variations if a low preload force is applied. The impact of the joint thickness – bolt diameter ratio on the relative preload loss is determined for all considered aspects and summarized in tables 3.10.1 and 3.10.2. Respecting a minimum total plate thickness – bolt diameter ratio ($\sum t/d$) will minimize the preload losses in most of the considered aspects with the exception of thermal variations since an increasing thickness will lead to increasing preload variations in the case of thermal variations. Increasing the bolt diameter, while keeping $\sum t/d$ constant, will have a positive effect (i.e. less decreasing impact) on the preload level considering embedment creep, relaxation/plate creep and thermal effects, but has a negative impact in the case of poisson's effect.

Relative preload losses $\Sigma t/d = 3$ with $P = P_{nom}$				
	M12	M16	M20	M24
	$\Sigma t=36$ mm	$\Sigma t=48$ mm	$\Sigma t=60$ mm	$\Sigma t=72$ mm
Embedment creep				
8.8 + S235	14.8%	11.3%	9.4%	7.9%
Combined bolt relaxation and plate creep (50 years)				
A4 80 + 50830	15.7%	15.2%	14.2%	12.7%
A4 80 + 6082T6	14.0%	13.0%	11.3%	9.8%
Thermal variations ($\Delta T = 45^\circ\text{C}$)				
8.8 + aluminium	9.7%	9.7%	9.9%	10.1%
A4 80 + S235	3.8%	3.9%	4.0%	4.0%
A4 80 + aluminium	5.6%	5.6%	5.8%	5.9%
Poisson effect				
8.8 + S235	4.5%	4.8%	4.9%	4.9%
A4 80 + S235	4.3%	4.6%	4.7%	4.7%
A4 80 + 50830	17.8%	19.1%	19.0%	19.0%
A4 80 + 6082T6	10.2%	10.6%	10.8%	10.8%

Table 3.10.1: Comparison relative preload losses with $\Sigma t/d = 3$

Relative preload losses $\Sigma t/d = 4$ with $P = P_{nom}$				
	M12	M16	M20	M24
	$\Sigma t=48$ mm	$\Sigma t=64$ mm	$\Sigma t=80$ mm	$\Sigma t=96$ mm
Embedment creep				
8.8 + S235	12.7%	9.6%	8.0%	6.7%
Combined bolt relaxation and plate creep (50 years)				
A4 80 + 50830	14.8%	14.4%	13.5%	12.1%
A4 80 + 6082T6	13.3%	12.5%	10.9%	9.6%
Thermal variations ($\Delta T = 45^\circ\text{C}$)				
8.8 + aluminium	11.1%	11.1%	11.3%	11.5%
A4 80 + S235	4.3%	4.4%	4.5%	4.6%
A4 80 + aluminium	6.5%	6.5%	6.6%	6.7%
Poisson effect				
8.8 + S235	3.9%	4.1%	4.2%	4.2%
A4 80 + S235	3.7%	3.9%	4.0%	4.0%
A4 80 + 50830	11.4%	12.1%	12.1%	12.1%
A4 80 + 6082T6	9.0%	9.3%	9.4%	9.4%

Table 3.10.2: Comparison preload losses with $\Sigma t/d = 4$

4 Experimental verification

4.1 Introduction

The analytical model derived in section 3 is based on both literature and assumptions regarding the material behaviour. Experimental research can verify the validity of the model. Furthermore, unknown aspects as the impact of the tightening procedure and preload force behaviour after slip can give insight in the to be expected preload losses under normal circumstances.

A common assembly technique of bolted joints is the utilization of a torque wrench during construction. Turning the nut after the joint is snug-tight will result in introduction of a preload force. Deviations in preload force can occur while applying torque, section 4.4 will therefore focus on the determination of a relationship between torque and preload force of A4 80 bolts.

The assumption regarding a comparison between the creep behaviour of 5454O and 5083O is examined in section 4.5. Compressive tests with a duration of 6-22 hours are performed on both grit-blasted and as-delivered plates. The surface conditions of the plates are discussed in section 4.3.

The preload force level of a 5083O aluminium joint connected with a preloaded M16 A4 80 bolt is monitored to identify the long-term preload force behaviour under realistic circumstances. The expected preload losses will include embedment creep, bolt relaxation and plate creep. Various initial preload forces will be applied to distinguish the impact of the initial preload force. The results can be used to verify the model. The preload force is mainly monitored with a load cell, section 4.6 will consider this method. Section 4.2 will discuss the properties of the Load Cell. An alternative monitoring method is applied in section 4.7. A strain gauge is embedded into the bolt shaft to be able to compare bolts applied with a load cell with bolts measured with a strain gauge

A double lap joint containing 5083O plates is subjected to a longitudinal force introducing preload losses due to poisson’s effect. The plates are grit-blasted to increase the slip limit. Two varying initial preload levels are applied. The results can be found in section 4.8.

The actual tensile strength properties of the used bolts and plates are reported in certificates. The (minimum) reported values are summarized in table 4.1.1.

Strength properties plates and bolts - Certificate					
5083 O/H111 Plates			A4 80 Bolts		
t	f _{0.2}	f _u	d x L	f _{0.2}	f _u
[mm]	[N/mm ²]	[N/mm ²]	[mm]	[N/mm ²]	[N/mm ²]
10	165	287	M16x75	736.45	946.52
20	153	296	M16x110	645.52	867.44
25	168	310	M20x100	710.01	803.21

Table 4.1.1: Proof and tensile strength 5083O/H111 plates and A4 80 bolts

4.2 Load Cell application and properties

The majority of the experiments conducted in this research include monitoring of the preload level with a Load Cell. A load cell is able to measure the (compressive) clamping force introduced by the preload force and is positioned between a bolt head and adjacent plate. The 4 Load Cells used in this research are manufactured by *BoltSafe*. Centering of the Load Cell is required to be able to measure the preload force correctly. The Bolt Safe Load Cell was originally designed for M20 bolts. Adapter rings are provided to center the Load Cell with the application of M16 bolts. The Load Cell and adapter rings are visualized in figure 4.2.1. Centering of the Load Cell is shown in figure 4.2.2 (left). Adapter rings are positioned on both sides of the sensor as can be observed in figure 4.2.2 (right).



Figure 4.2.1: Bolt Safe Load Cell and Adapter rings

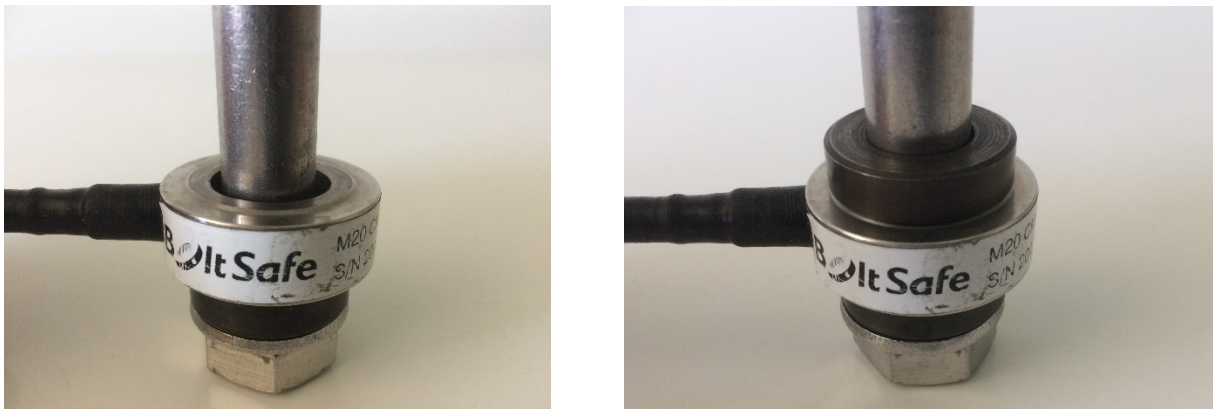


Figure 4.2.2: Centering of the Load Cell by adapter ring (left); application of adapter ring on either side of the Load Cell (right)

A washer is placed between bolt head and adapter ring. An additional washer is placed between the adapter ring and the adjacent plate surface to be able to preserve contact between a washer and adjacent plate and to generate a realistic load distribution in the washer. The side view and schematization of the Load Cell composition are presented in figure 4.2.3 and figure 4.2.4.



Figure 4.2.3: Side view Load Cell, adapter rings and additional washer

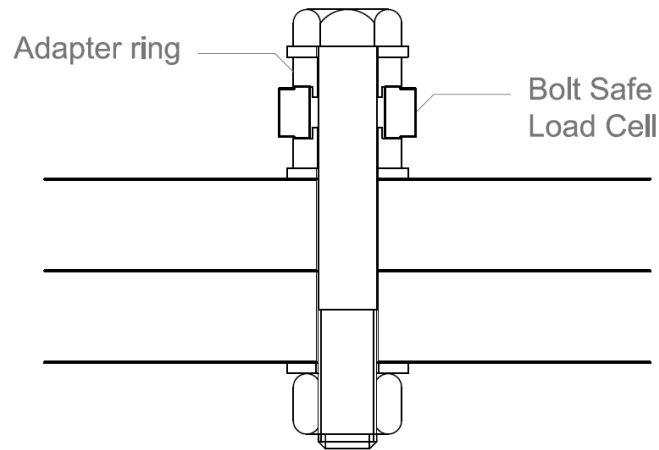


Figure 4.2.4: Schematization Load Cell, adapter rings and additional washer

4.2.1 Load Cell dimensions and properties

The Load Cell has a height of 14.10 mm and is composed of 17-PH Stainless Steel, Condition H1025. The adapter used to position the bolt in the Load Cell has an effective height of 8.10 mm and is made of 1.2312 stainless steel. The specifications of the Load Cell are added in Annex B1. A minimal creep loss of 0.1% of the Full Scale Load of the Load Cell (166 kN) can be expected (= 0.17 kN). The creep impact is therefore ignored. The dimensions of the Load Cell and adapter rings are visualized in figure 4.2.5, the material properties are summarized in table 4.2.1. The effective (contact) width of the interface between the Load Cell and the adapter ring is equal to 4.25 mm. To be able to take into account the stiffness of the Load Cell – Adapter combination, the combination will be simplified into 3 cylinders as visualized in figure 4.2.6.

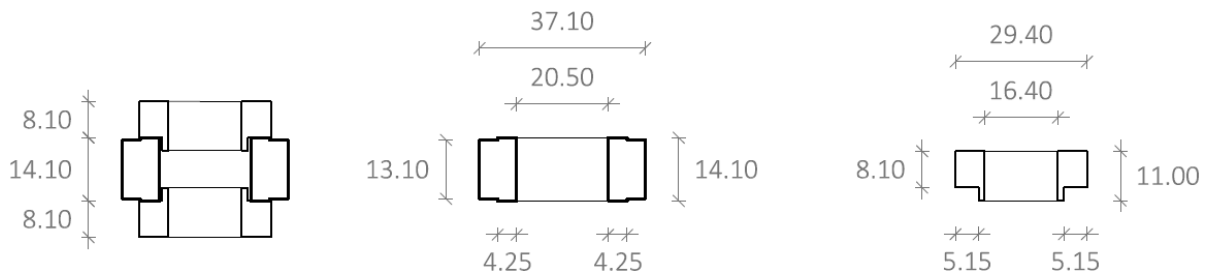


Figure 4.2.5: Dimensions [mm] Load Cell and adapter ring

Material properties Load Cell / Adapter ring			
		17-PH H1025 ¹	1.2312 ²
E	[N/mm ²]	196000	210000
α_T	[mm/mm/°C]	0.0000108	0.0000128

Table 4.2.1: Material properties LC/ Adapter ring (¹ Metallurgica Veneta 1980; ² TelmaStainless BV)

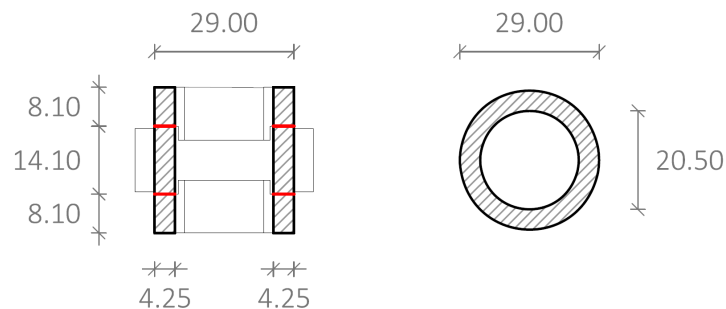


Figure 4.2.6: Dimensions [mm] and simplification Load Cell – Adapter ring combination

The effective bearing area corresponding to the effective (contact) width of the interface of the Load Cell – Adapter ring combination is equal to:

$$A_{LC} = \frac{\pi}{4} (29.00^2 - 20.50^2) = 330.46 \text{ mm}^2 \quad (4.1)$$

With:

A_{LC} : effective bearing area interface Load Cell – Adapter ring

The elastic stiffness of the Load Cell can be estimated with:

$$k_L = \frac{E_L A_{LC}}{h_L} = \frac{196000 \cdot 330.46}{14.10} = 4.594 \cdot 10^6 \text{ N/mm} \quad (4.2)$$

With:

A_{LC} : effective bearing area interface Load Cell – Adapter ring

E_L : Young's modulus Load Cell material

h_L : effective height Load Cell

k_L : elastic stiffness Load Cell

The elastic stiffness of the Adapter ring can be estimated with:

$$k_A = \frac{E_A A_{LC}}{h_A} = \frac{210000 \cdot 330.46}{8.10} = 8.567 \cdot 10^6 \text{ N/mm} \quad (4.3)$$

With:

E_A : Young's modulus Adapter ring material

h_A : effective height Adapter ring

k_A : elastic stiffness Adapter ring

The total Load Cell – Adapter ring combination stiffness, represented by k_{LC} , is determined by combining the Load Cell stiffness with the two Adapter ring stiffnesses:

$$k_{LC} = \frac{1}{\frac{1}{k_A} + \frac{1}{k_L} + \frac{1}{k_A}} = \frac{1}{\frac{1}{8.567 \cdot 10^6} + \frac{1}{4.594 \cdot 10^6} + \frac{1}{8.567 \cdot 10^6}} = 2.217 \cdot 10^6 \text{ N/mm} \quad (4.4)$$

With:

k_A : elastic stiffness Adapter ring

k_L : elastic stiffness Load Cell

k_{LC} : elastic stiffness Load Cell - Adapter ring combination

4.2.2 Comparison Load Cell output and calibrated Instron system

A discrepancy is noticed between the output from the Load Cells and a calibrated Instron Testing System. The deviations are analyzed in a compression test using the Instron System and the Load Cells as indicated in figure 4.2.7. The results of the input of the Instron System versus the output of the 4 Load Cells are presented in figure 4.2.8. A line representing perfect calibration of both systems is added. It can be concluded that the Load Cell overestimates the Instron input. The deviations of the separate Load Cells are equal to:

- Load Cell 1: 2 - 8 kN
- Load Cell 2: 0 - 5 kN
- Load Cell 3: 2 kN
- Load Cell 4: 2 - 3 kN

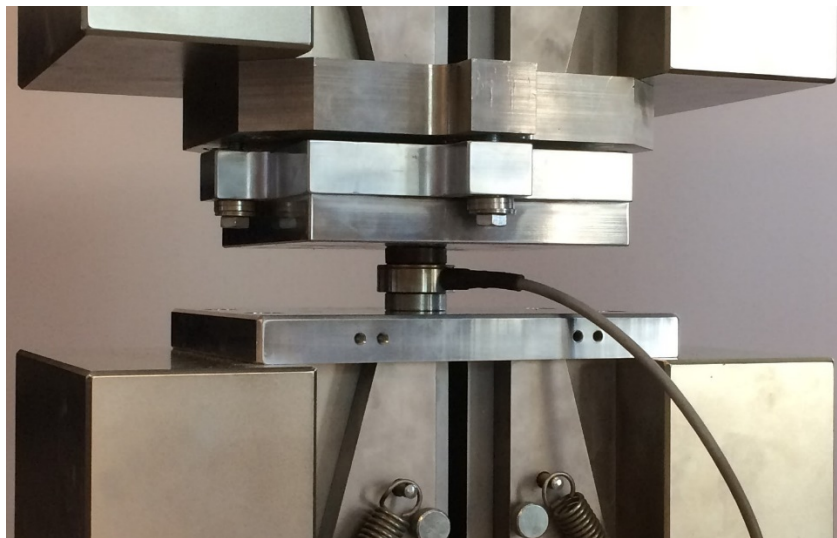


Figure 4.2.7: Test setup comparison Instron input vs. Load Cell output

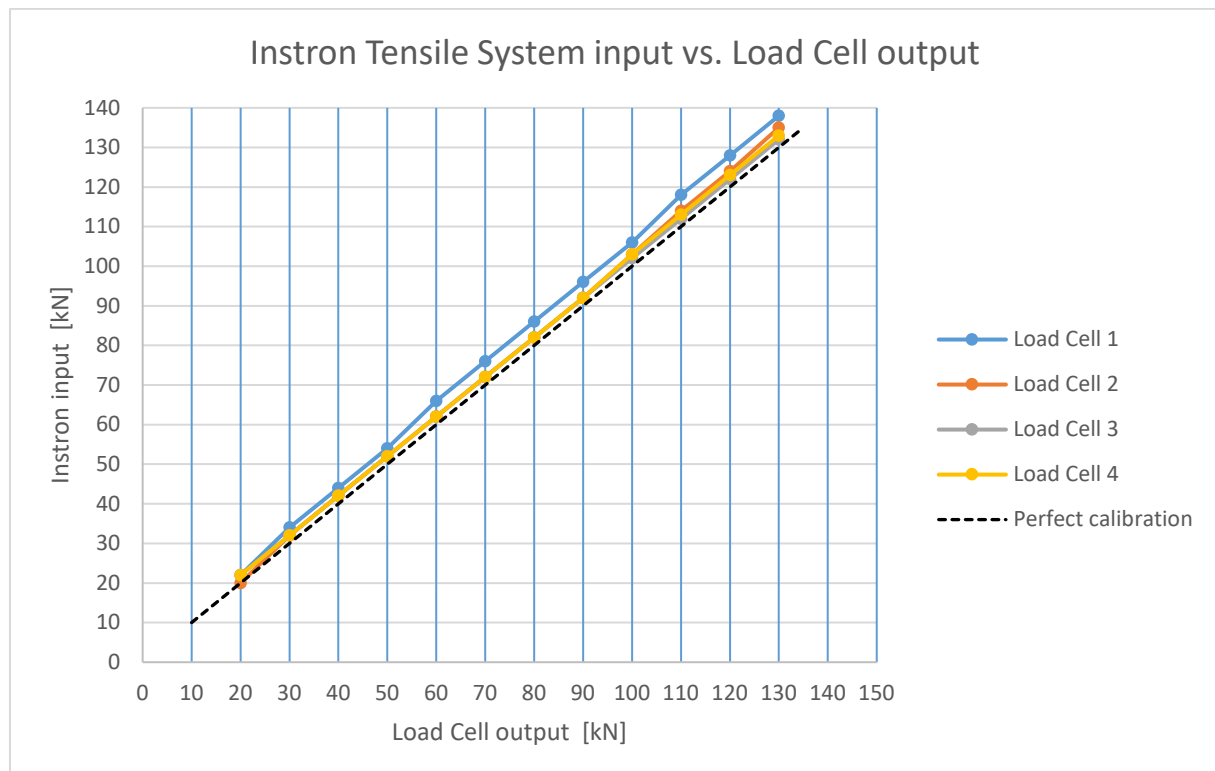


Figure 4.2.8: Results regarding deviations between Instron System and Load Cells

The deviations of the Load Cell output of all four Load Cells compared to the Instron System input are presented in figure 4.2.9 and table 4.2.2. Load Cell 1 is abbreviated to 'LC1', Load Cell 2 to 'LC2', etc. The discrepancies of the Load Cell output are taken into account in the conducted experiments in the following sections in order to present accurate results.

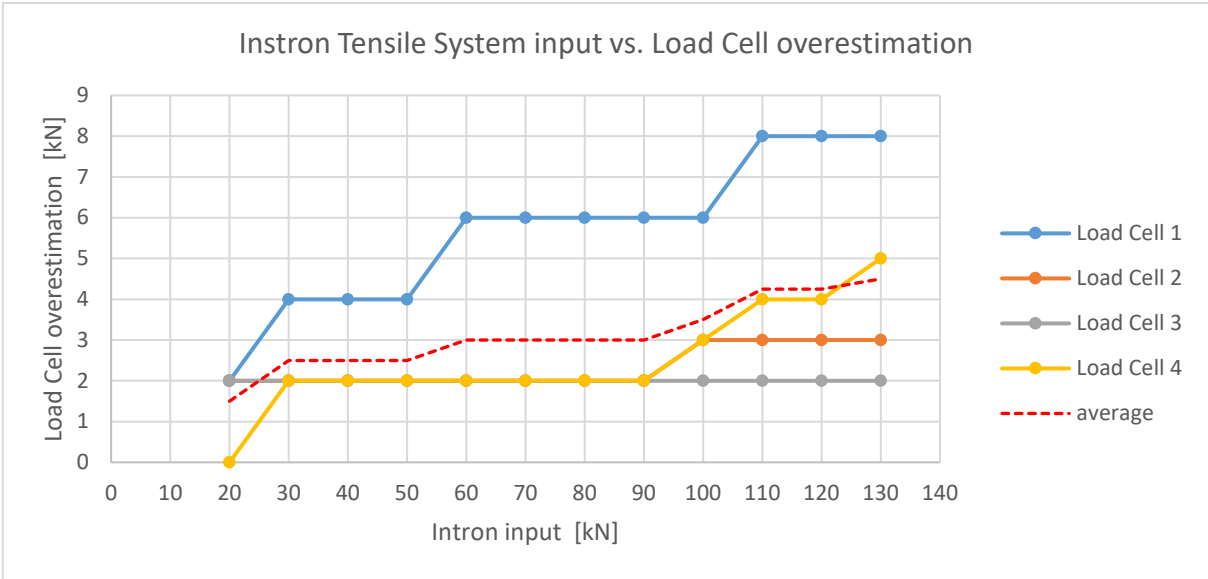


Figure 4.2.9: Overestimation of Load Cell compared to calibrated input

Calibrated Instron input vs. Load Cell output and discrepancies									
Calibrated input	Load Cell output				Discrepancies				
	LC1	LC2	LC3	LC4	LC1	LC2	LC3	LC4	Average
[kN]	[kN]	[kN]	[kN]	[kN]	[kN]	[kN]	[kN]	[kN]	[kN]
20.0	22	20	22	22	2.0	0.0	2.0	2.0	1.50
30.0	34	32	32	32	4.0	2.0	2.0	2.0	2.50
40.0	44	42	42	42	4.0	2.0	2.0	2.0	2.50
50.0	54	52	52	52	4.0	2.0	2.0	2.0	2.50
60.0	66	62	62	62	6.0	2.0	2.0	2.0	3.00
70.0	76	72	72	72	6.0	2.0	2.0	2.0	3.00
80.0	86	82	82	82	6.0	2.0	2.0	2.0	3.00
90.0	96	92	92	92	6.0	2.0	2.0	2.0	3.00
100.0	106	103	102	103	6.0	3.0	2.0	3.0	3.50
110.0	118	114	112	113	8.0	4.0	2.0	3.0	4.25
120.0	128	124	122	123	8.0	4.0	2.0	3.0	4.25
130.0	138	135	132	133	8.0	5.0	2.0	3.0	4.50

Table 4.2.2: Comparison calibrated input and Load Cell output with corresponding discrepancies

4.3 Plate surface conditions

The joints used during the experiments contain 5083O/H111 plates in various thicknesses with an as-delivered or grit blasted surface. Grit blasting will increase the roughness of the surface. The plate roughness is defined using the arithmetical mean roughness value R_a . The value for R_a can be calculated by averaging the absolute distance from the mean line as indicated in figure 4.3.1.

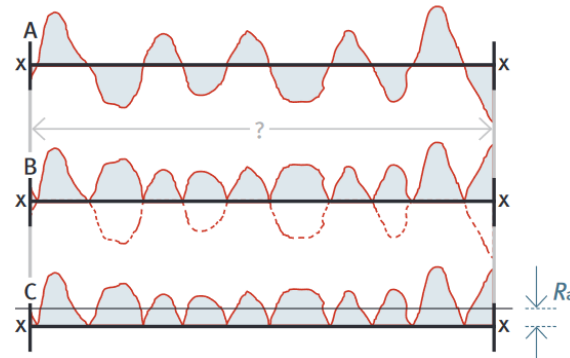


Figure 4.3.1: The principle of measuring average roughness R_a (Euro Inox 2014)

In accordance with ISO 1997, the surface roughness is experimentally determined using a surface roughness meter Mitutoyo SJ210. Figure 4.3.2 shows the application of the surface roughness meter on an as-delivered surface (left) and a grit blasted plate surface (right).

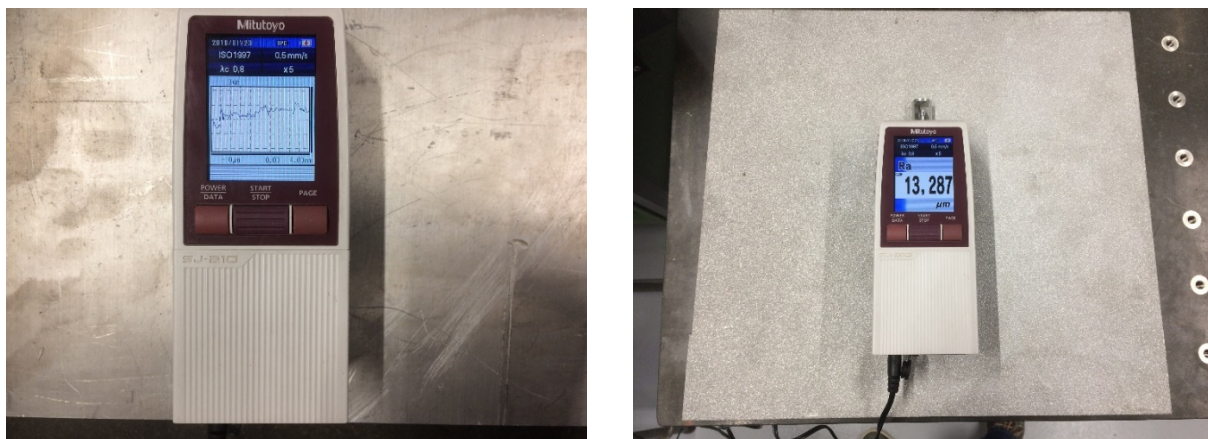


Figure 4.3.2: Determination of surface roughness as-delivered (left) and grit blasted surface (right)

The surface of the as-delivered plate was monitored parallel to the rolling direction and perpendicular to the rolling direction. The grit blasted surface did not show variations with respect to the rolling direction. The results of the measurements are presented in table 4.3.1. An average value is determined at the bottom row of the table.

Results measurements arithmetical mean roughness R_a [μm]					
Measurement		As-delivered		Grit blasted	
		Parallel to rolling direction	Perpendicular to rolling direction		
1	[μm]	0.558	1.470	13.287	
2	[μm]	0.442	1.264	17.037	
3	[μm]	0.691	1.061	15.731	
R_a (average)		[μm]	0.564	1.265	15.352

Table 4.3.1: Results surface roughness experiment

4.4 Relationship torque – bolt force

Within Bayards, the torque method is selected to introduce preload forces in bolts. To assure sufficient preload force in the bolt after installation, the relationship between applied torque and corresponding preload force has to be determined. To gain insight into the effect of the application of lubrication during assembly, 4 lubrication types are tested with A4 80 M16x110 and M20x100 bolts. Table 4.4.1 gives an overview of the amount of bolts tested per lubrication type. The lubrication types are:

- 1) Unlubricated bolts
- 2) Lubrication of bolt using silicon free anti-spatter spray
- 3) Lubrication of outer threads bolt using lubrication paste (HY52 Special lubrication Paste White)
- 4) Lubrication of inner threads nut using lubrication paste (HY52 Special lubrication Paste White)

Overview amount of bolts tested per lubrication type	
Lubrication type	Amount of tests
Unlubricated	8
Lubrication with spray	8
Lubrication with paste (bolt)	4
Lubrication with paste (nut)	4

Table 4.4.1: Overview of performed amount of tests per lubrication type

The tested joint contains two as-delivered aluminium plates 5083O/H111 with dimensions 360 x 440 x 25 mm with 4 bolt holes and is held into position using a bench vise. The 4 bolts are tested successively with the following procedure:

- Bolt head is locked with a wrench to prevent rotation of the bolt head
- A torque wrench is used to gradually increase the preload force
- During the test the bolt force under the bolt head is measured continuously with *BoltSafe* Load Cells and a *BoltSafe* Load Measuring System

The test setup is illustrated in figure 4.4.1 showing the clamped plates with the Load Cells (left) and the *BoltSafe* Load Measuring System (right).



Figure 4.4.1: Test setup experiments torque – preload force

4.4.1 Relationship A4 80 M16x110

As discussed in section 4.3, the monitoring of M16 bolts requires adapters to be able to center the bolt. The joint dimensions and Load Cell applications are illustrated in figure 4.4.2.

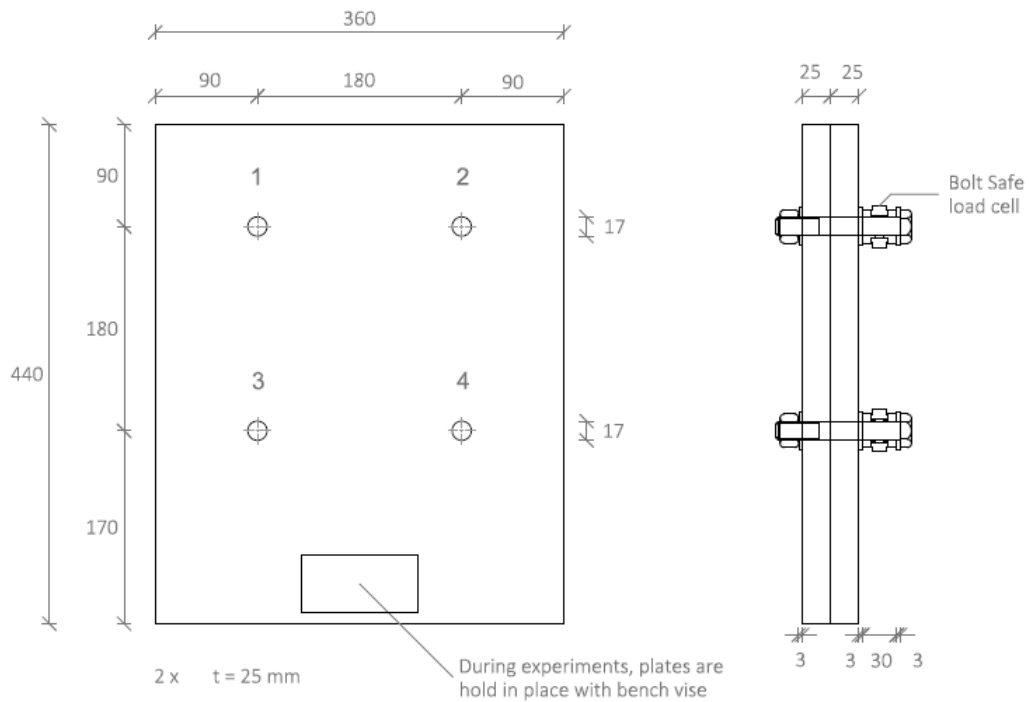


Figure 4.4.2: Test setup and joint dimensions including A4 80 M16 x 110 bolts

The torque-experiment is performed with the procedure described in section 4.4. Figure 4.4.3 presents the average preload force versus applied torque per lubrication type. Figure 4.4.4 gives the corresponding standard deviations of the preload force per lubrication type and applied torque. The value representing the nominal preload force of M16 bolts ($P_{nom} = 88 \text{ kN}$) is added to figure 4.4.3.

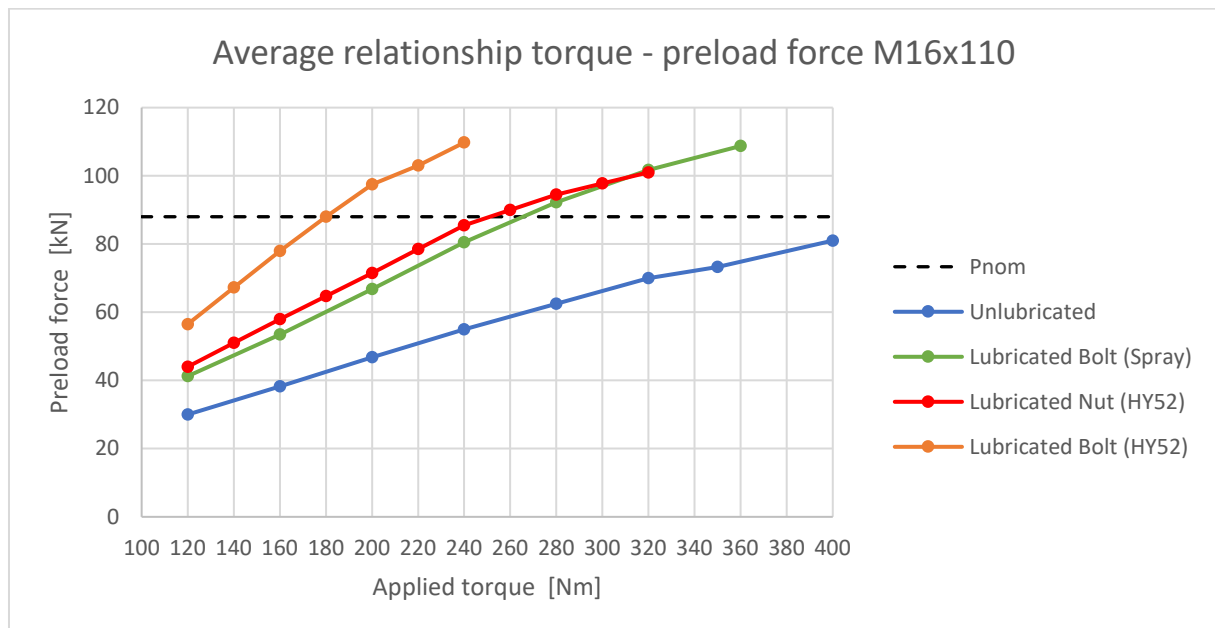


Figure 4.4.3: Average relationship M16x110 per lubrication type

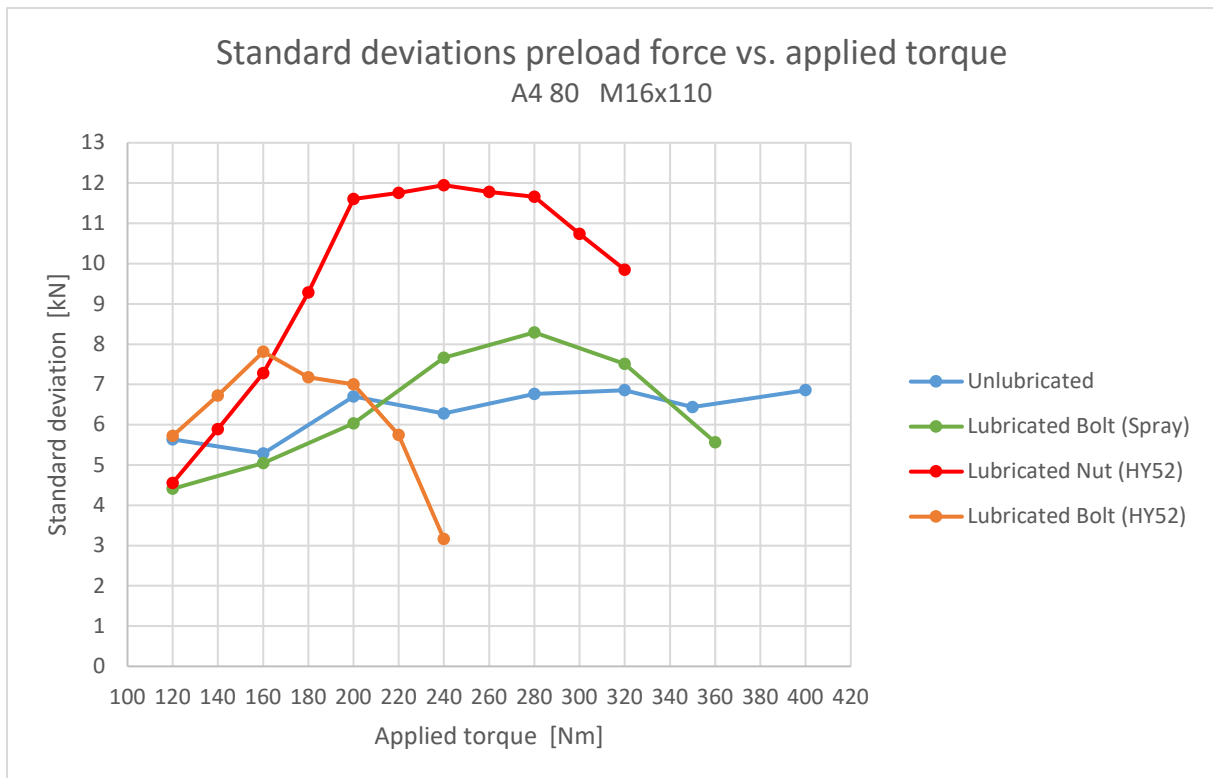


Figure 4.4.4: Standards deviations preload force A4 80 M16x110 bolts per lubrication type

The average linear relationship between torque and bolt force is determined with the average coefficient of friction k_{avg} . The coefficient of friction can be determined with the following formula (NEN-EN 1090-2 2018):

$$M = k_{avg} \cdot d \cdot P \rightarrow k_{avg} = \frac{M}{16P} \quad (4.5)$$

With:

- M : applied torque
- P : preload force
- d : diameter bolt
- k_{avg} : average coefficient of friction

Within the range 0 – 85 kN (0.9F_p), the values for the average coefficient of friction k_{avg} are determined for every data point. The values for k_{avg} per lubrication type are summarized in table 4.4.2.

Coefficients of friction M16x110	
Lubrication type	k_{avg}
Unlubricated	0.25 – 0.31
Lubrication with spray	0.18 – 0.21
Lubrication with paste (bolt)	0.13 – 0.14
Lubrication with paste (nut)	0.17 – 0.20

Table 4.4.2: Overview of values k_{avg} per lubrication type M16 x 110

It can be concluded that a linear torque – preload force relationship can be discovered from the average values up to 0.9F_p. Furthermore, the application of lubrication does not have a decreasing impact on the deviations as compared to unlubricated bolts as can be concluded from figure 4.4.4.

4.4.2 Relationship A4 80 M20x100

The experiment conducted in section 4.4.1 is repeated for bolts with $d = 20$ mm. The test setup, joint dimensions and application of the Load Cells are illustrated in figure 4.4.5. The addition of adapters to fit the bolts is not necessary, therefore only an extra washer and the installation of a Load Cell is needed to be able to measure the preload force in the bolt.

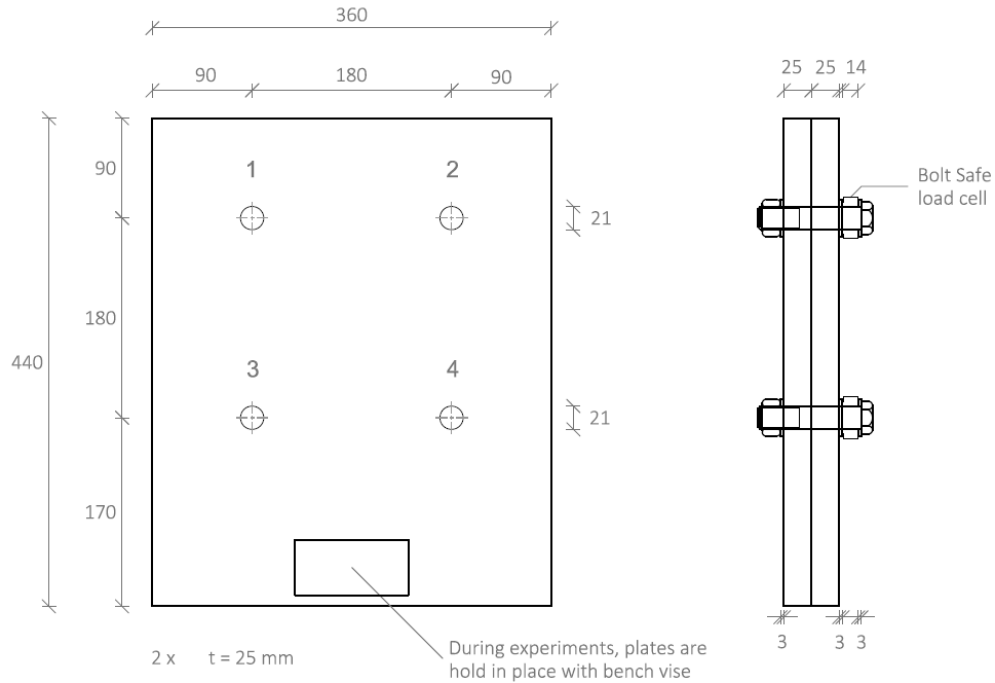


Figure 4.4.5: Test setup combined results lubricated M20 x 100 bolt sets

The test is repeated with the procedure described in section 4.4. Figure 4.4.6 presents the average preload force versus applied torque per lubrication type. Figure 4.4.7 gives the corresponding standard deviations of the preload force per lubrication type and applied torque. The preload level representing the nominal preload force of M20 bolts ($P_{nom} = 137$ kN) was not reached, therefore lines representing a preload level of $0.5F_p$ (74 kN) and $0.7F_p$ (103 kN) are added to figure 4.4.6.

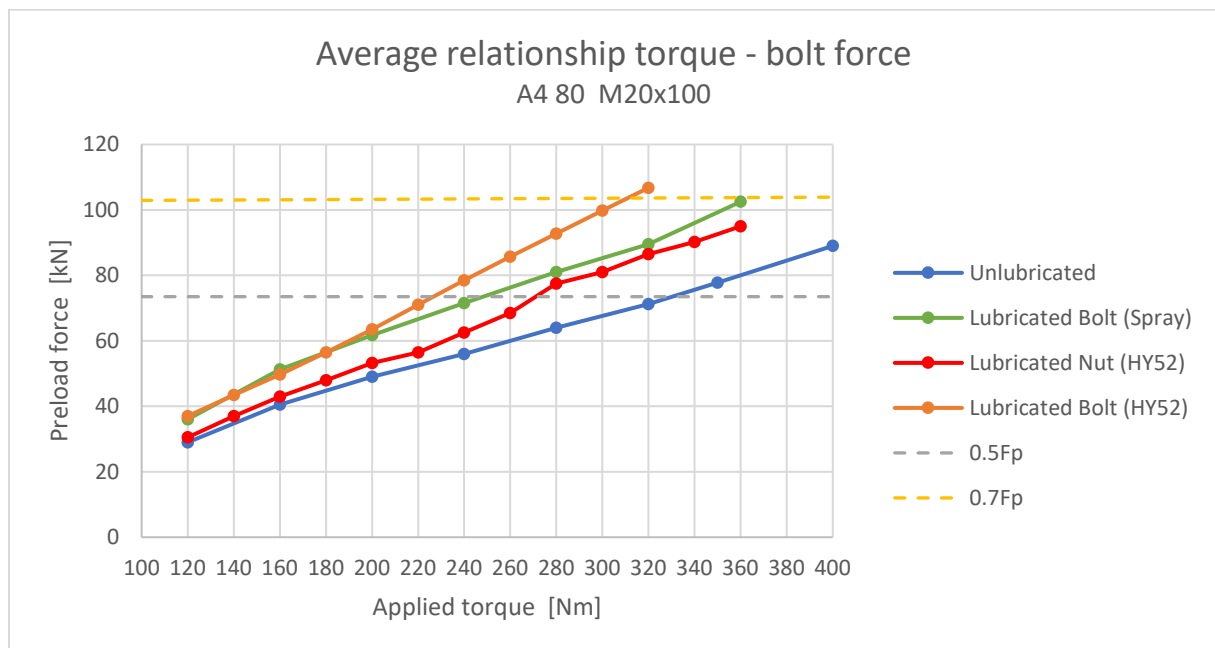


Figure 4.4.6: Average relationship M20 x 100 with varying type of lubrication

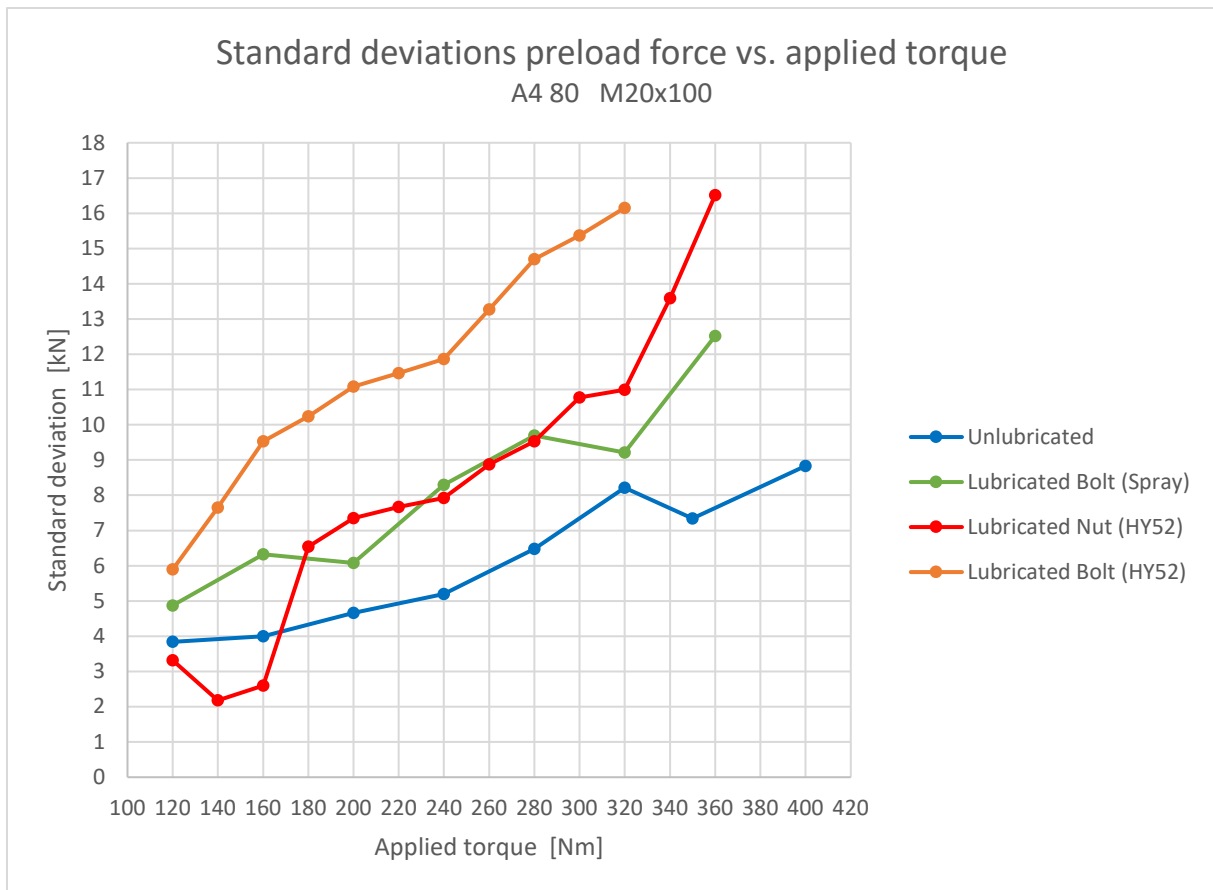


Figure 4.4.7: Maximal positive and negative deviations results M20x100 compared with average

The average relationship (shown in figure 4.4.6) contains linear behaviour up to $0.7F_p$ ($= 103$ kN). The relationship between torque and bolt force is determined using equation 4.5 with $d = 20$ mm. Within the range $0 - 103$ kN, the values for k_{avg} are determined for every data point. The ranges of the values for k_{avg} per lubrication type are summarized in table 4.4.3.

Coefficients of friction M20x100	
Lubrication type	k_{avg}
Unlubricated	0.21 – 0.23
Lubrication with spray	0.16 – 0.18
Lubrication with paste (bolt)	0.15 – 0.16
Lubrication with paste (nut)	0.18 – 0.20

Table 4.4.3: Overview of values k_{avg} per lubrication type M20x100

It can be concluded that the coefficients of friction for M20x100 bolts are comparable with M16x110 bolts per lubrication type. Again, the application of lubrication does not have a decreasing impact on the deviations as compared to unlubricated bolts for both bolt diameters.

4.5 Creep experiment aluminium

During the analysis of plate creep in section 3.6, a comparison between the creep behaviour of 5454O and 5083O is made due to insufficient creep data of 5083 O/H111. Alloys 5454O and 5083 O/H111 show comparable proof and strength properties, but no literature is found to support the possibility to compare the creep data. The comparison is verified with a compressive creep test of 6 – 22 hours on both as-delivered and grit-blasted plates. The tested plates consists of small aluminium 5083 O/H111 blocks with dimensions 28 x 28 x 25 mm. The blocks are cut out of a plate with a thickness of 25 mm. Figure 4.5.1 shows the blocks with an as-delivered and a grit-blasted surface.

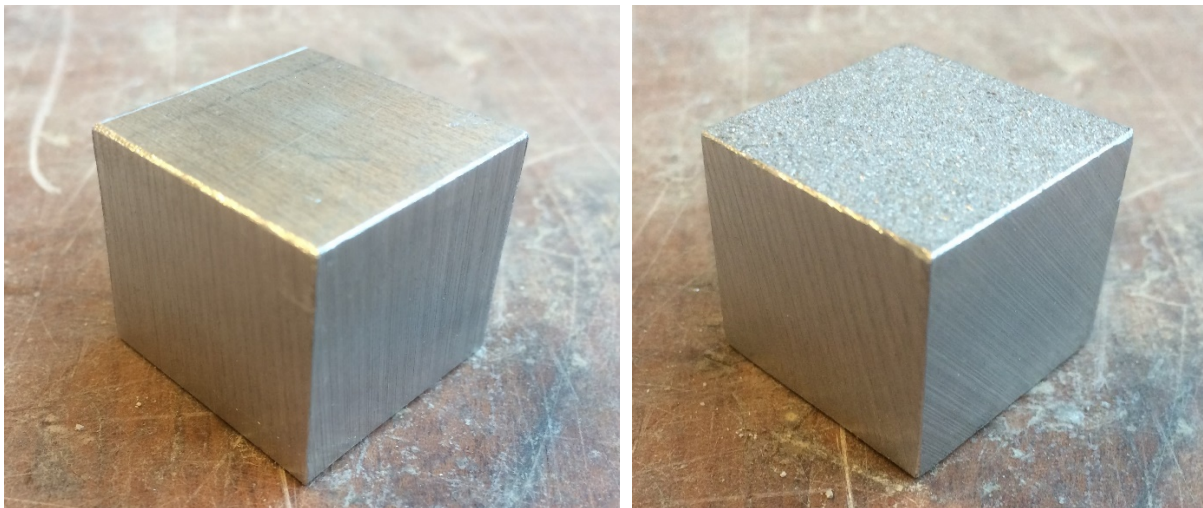


Figure 4.5.1: Block used in creep experiment with as-delivered (left) and grit-blasted surface (right)

The test setup contains 4 blocks with either as-delivered or grit-blasted surfaces. The blocks are stacked to create a sample with dimensions 28 x 28 x 100 mm. To be able to measure the creep strain, 4 LVDT sensors are attached to the sample as visualized in figure 4.5.2. Since a compressive force can lead to instability of the sample, all 4 sides are monitored to be able to calculate the average creep strain of the sample. The impact of the treatment of the surface is distinguished by taking into account one interface combined with 25 mm of plate within the original length L_0 .

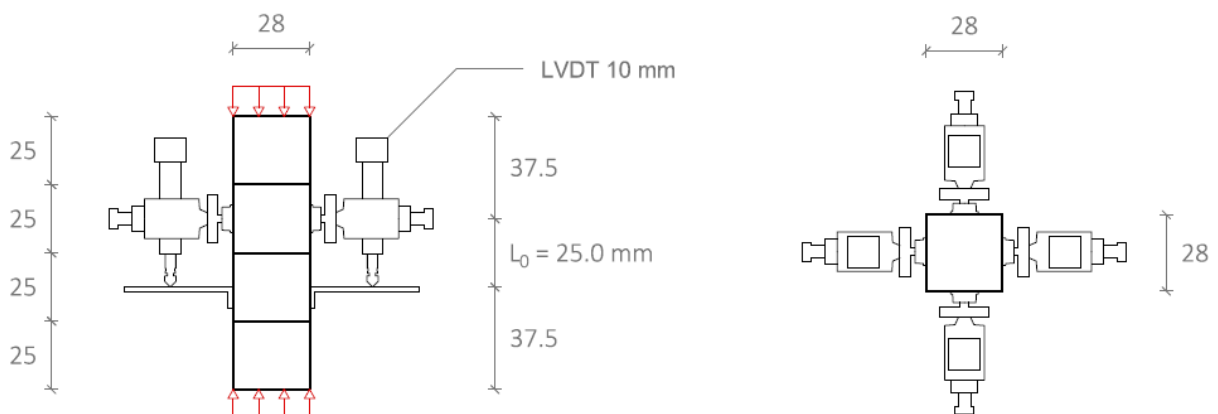


Figure 4.5.2: Test setup section (left) and top view (right)

As indicated in figure 4.5.2, a compressive force will be applied at the top and bottom of the sample. The compressive force is introduced at the top of the sample with an Instron 5985 Universal Testing System. The test setup including the Instron Testing System is shown in figure 4.5.3.

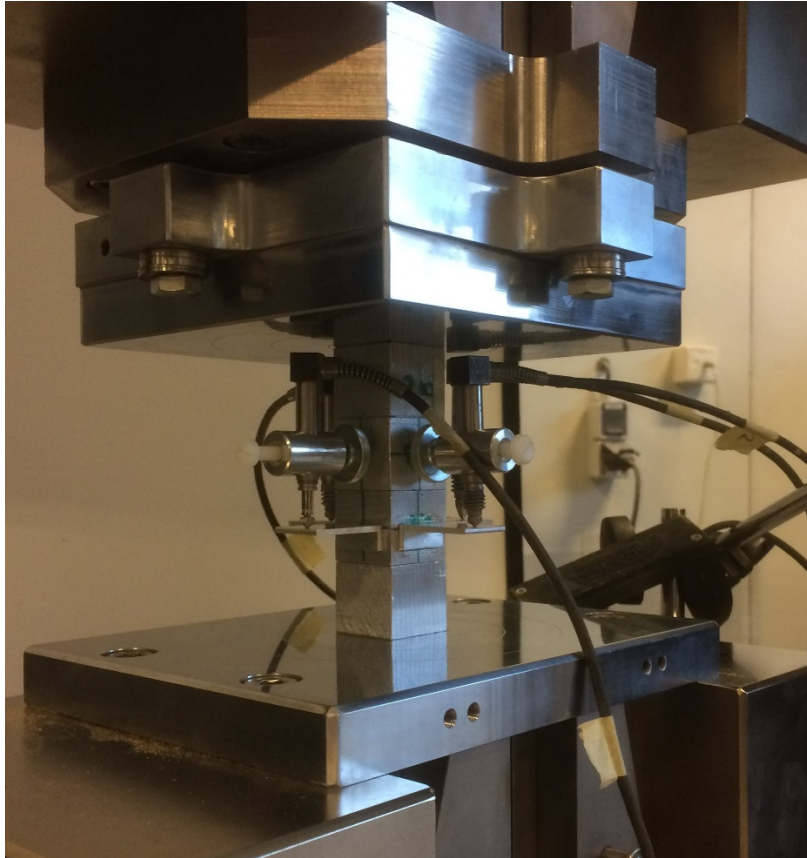


Figure 4.5.3: Test setup compressive creep test including Instron Testing System

Since the Instron Testing system is positioned outside the conditioned lab, temperature fluctuations can occur resulting in deviating creep strain behaviour. Therefore, an unloaded strip of 50830/H111 is placed next to the loaded sample. The strip is equipped with an LVDT measuring over an original length of $L_0 = 25$ mm. The occurring creep strain can be subtracted or added by the creep strain measured in the loaded sample to account for temperature variations. The setup for parallel temperature monitoring is visualized in figure 4.5.4.

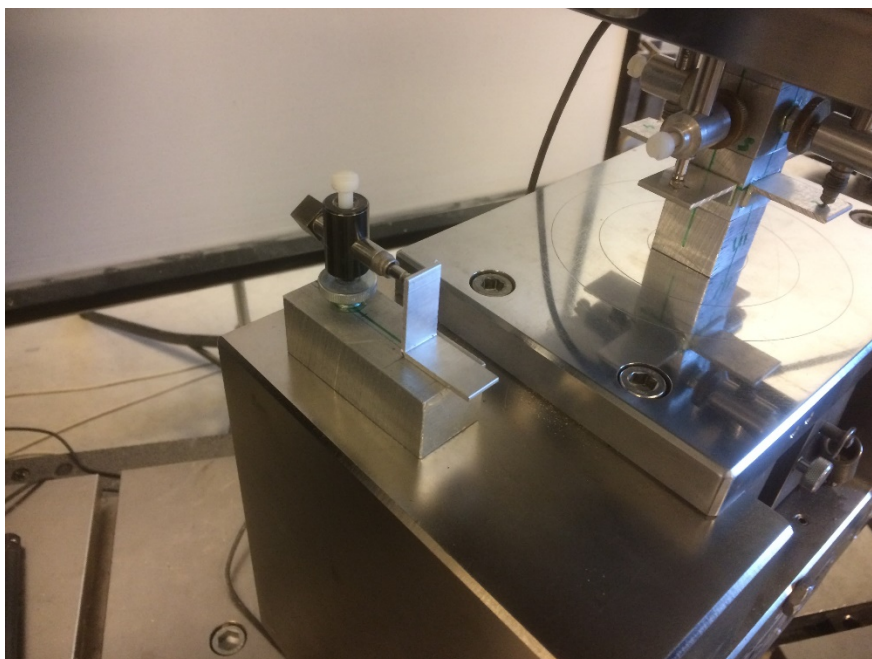


Figure 4.5.4: Test setup parallel temperature monitoring

As discussed in figure 3.2.7, the critical bearing surface outside diameter at the top of the plate frustum and corresponding bearing area in the interface between washer and plate is equal to:

$$d_w = 1.5d + 2t_w \tan 30 = 27.46 \text{ mm}^2 \quad (4.6)$$

$$A_{dW} = \frac{\pi}{4} \cdot (d_w^2 - d_0^2) = \frac{\pi}{4} \cdot (27.46^2 - 17.0^2) = 365 \text{ mm}^2 \quad (4.7)$$

Where:

- A_{dW} : critical bearing area interface washer-plate
- d : bolt diameter
- d_w : critical bearing surface outside diameter
- t_w : washer thickness

With the application of a preload force of $0.93F_p$, the maximum occurring bearing stress is equal to:

$$\sigma_{\max} = \frac{0.93F_p}{A_{dW}} = \frac{88 \cdot 10^3}{365} = 241 \text{ MPa} \quad (4.8)$$

The impact of 241 MPa compressive stress will be examined with the sample shown in figure 4.5.2. To be able to introduce 241 MPa, the sample is loaded up to:

$$F = \sigma_{\max} A = 241 \cdot 28^2 = 188.6 \text{ kN} \quad (4.9)$$

The load is applied with a constant displacement rate of 1 mm/min, which corresponds to a strain rate of $1.7 \cdot 10^{-4} \text{ s}^{-1}$. In total, two samples with as-delivered surfaces and two samples with grit blasted surfaces are examined. The average stress – strain behaviour of the 4 LVDT sensors per sample during the loading phase is presented in figure 4.5.5.

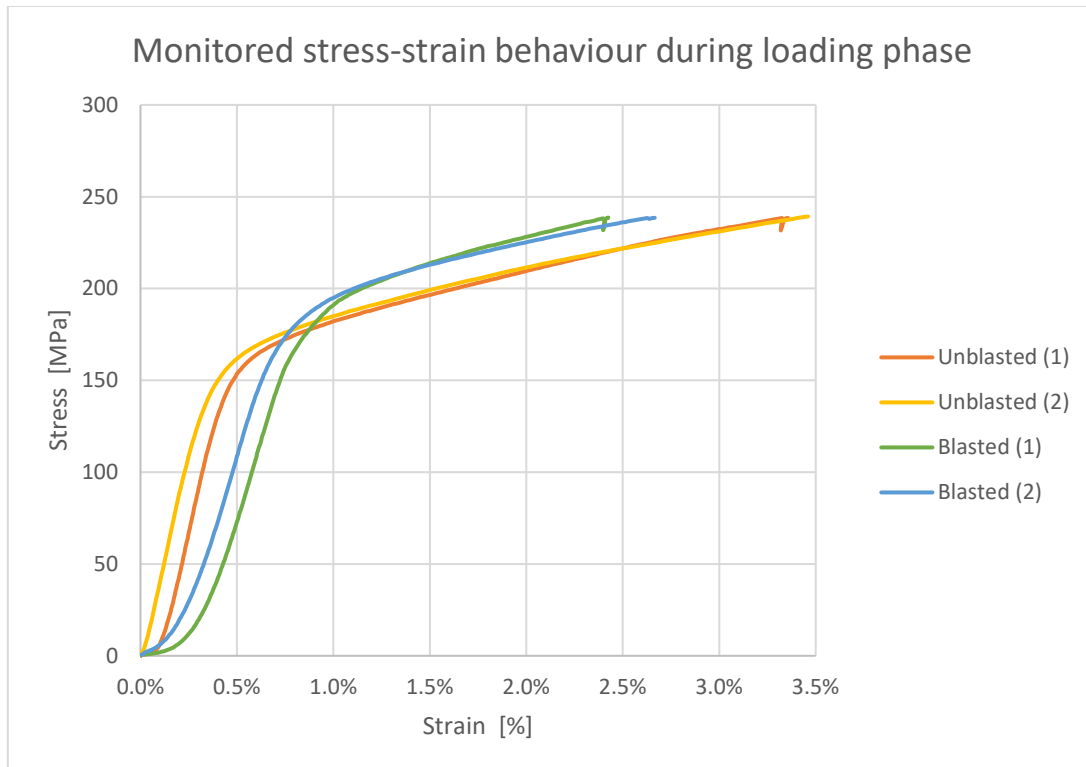


Figure 4.5.5: Monitored stress-strain relationship during loading sample

It can be discovered that a grit-blasted surface deforms more during loading due to settling of the roughness compared to an as-delivered surface. On the other hand, the total amount of strain needed to reach a compressive stress of 241 MPa is less for samples with blasted surfaces than for as-delivered surfaces. A possible explanation for this phenomenon is that grit-blasting has a hardening effect on the physical properties resulting in a stiffer material behaviour.

The creep strain behaviour is analyzed in 10 – 22 hour creep tests. After loading the sample with 1 mm/min, the compressive force is held constant over time. The average creep strain of the 4 samples determined with the 4 LVDT sensors can be found in figure 4.5.6. The theoretical creep behaviour of 54540 is added for comparison.

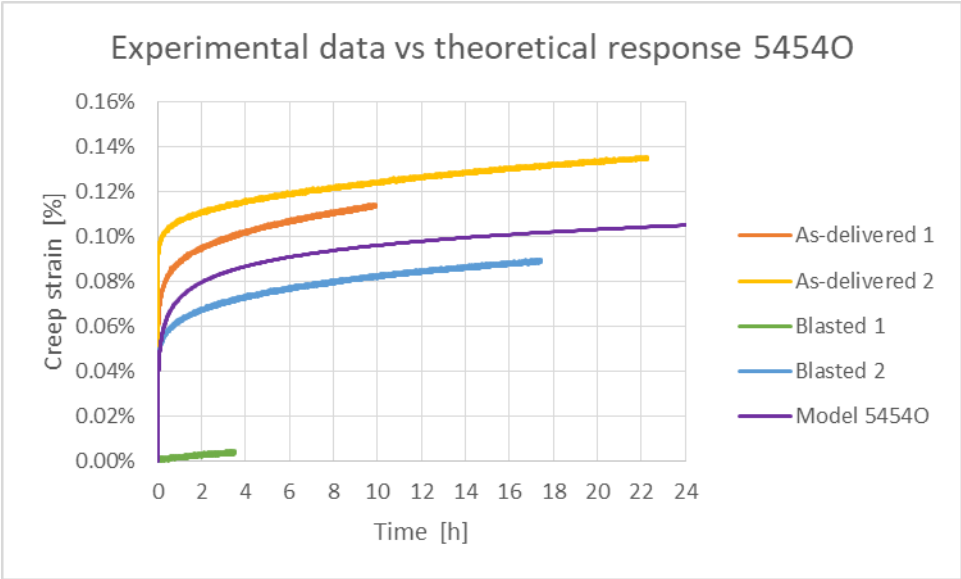


Figure 4.5.6: Experimental creep strain behaviour 50830 versus theoretical response 54540

The majority of the creep occurs within the first 2 hours after application of the compressive force and increases gradually over time. Comparable with the stress-strain behaviour during loading, the samples with a blasted surface show less sensitivity indicating a hardening impact of grit-blasting. The model based on creep data of 54540 predicts the creep behaviour of 50830/H111 relatively well with the exception of sample 1 with a blasted surface. The sample exhibited shear deformation behaviour due to off-center positioning in the Instron Testing System possibly resulting in deviating results.

The amount of embedment creep occurring in the plate interface can be estimated by considering the difference between the model and the data corresponding to maximum creep discovered in the as-delivered surface (i.e. as-delivered 2) at t = 22h:

$$\delta_{em} = (0.00135 - 0.00104) \cdot 25 \text{ mm} \hat{=} 7.75 \text{ } \mu\text{m} \tag{4.10}$$

4.6 Relaxation experiments with Load Cell Method

The relaxation/creep model is tested in a long-term relaxation experiment containing as-delivered and grit-blasted aluminium 5083O/H111 plates and A4 80 M16 bolts. The bolt threads are lubricated using HY52 Special lubrication Paste White and a Nyloc-nut is used. The tests are performed in a conditioned lab with a constant temperature of 20°C and a constant relative humidity of 60%. Several levels of initial preload force are considered and both as-delivered and grit-blasted plate surfaces are applied. The bolt force is monitored using the Load Cells described in section 4.2. The discrepancies of the Load Cells described in section 4.2.2 are taken into account.

4.6.1 Load Cell relaxation experiment 1 ($P = 63 \text{ kN} = 0.7F_p$)

Relaxation experiment 1 contains four sets of two as-delivered aluminium plates 5083 O/H111 with dimensions 180x220x25 mm assembled with a lubricated (Lubrication Paste Bolt Thread) bolt A4 80 M16x110 mm preloaded up to 63 kN ($0.7F_p$). The test setup is visualized in figure 4.6.1 and figure 4.6.2. During assembly the joint is held into position using a bench vise. The tightening procedure is comparable with the tests conducted in section 4.4:

- Bolt head is locked to prevent rotation of the bolt head
- A wrench is used for tightening
- During the test the bolt force is measured with Bolt Safe Load Cells and a BoltSafe Load Measuring System SM-200

As can be observed in figure 4.6.1, the edge distance is sufficient for the development of a load distribution cone with an angle of 30°. The stiffness equations discussed in section 2.2 are therefore applicable to compare the relaxation model with the experimental results.

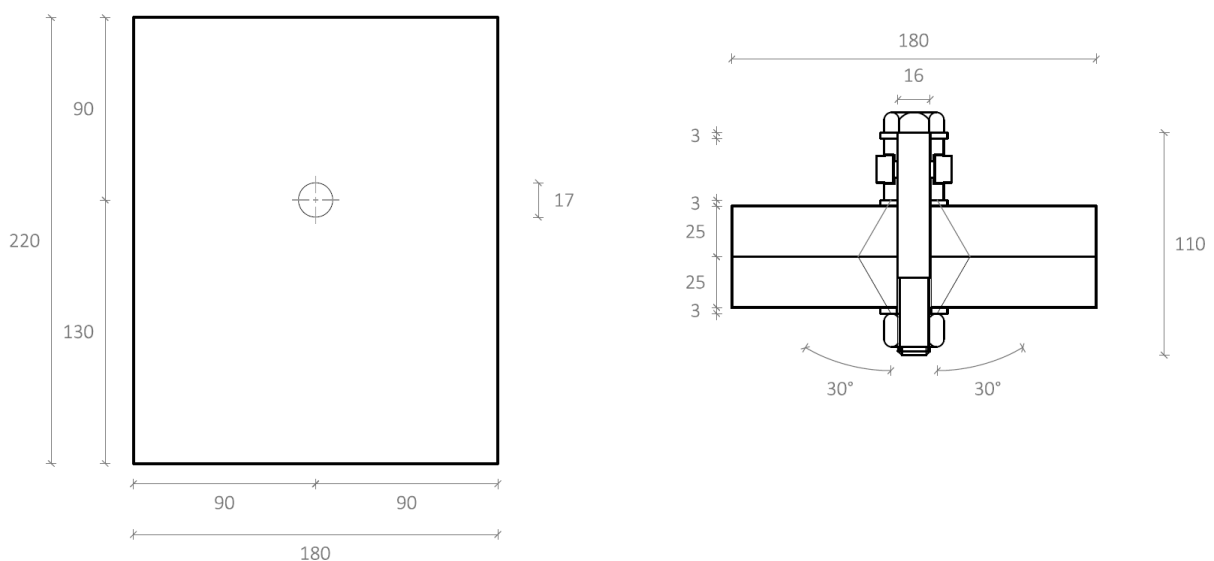


Figure 4.6.1: Joint dimensions [mm], top and side view sample relaxation test

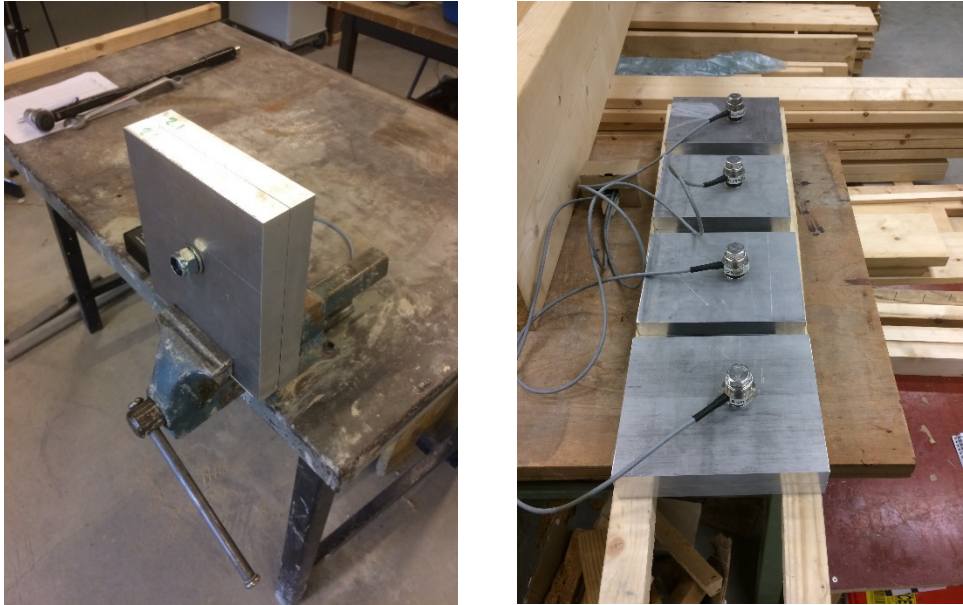


Figure 4.6.2: Assembly of joint (left); Samples stored in conditioned lab (right)

The Load Cell rounds off the preload force to the nearest value with steps of 2 kN (i.e. display accuracy of 2 kN). A fluctuating output is noticed once the current preload force is equal to the average of the adjacent output levels. For example, a fluctuating current force of 60 – 62 kN can be interpreted as 61 kN. Monitoring was started immediately after tightening. The experimental data corresponding to the four samples are summarized in table 4.6.1. Sample 1 was monitored with Load Cell 1, sample 2 with Load Cell 2, sample 3 with Load Cell 3 and sample 4 with Load Cell 4.

Results relaxation test 1 with $P = 63 \text{ kN} = 0.7F_p$						
Time	Preload force per sample				Average preload force	Average preload loss
	Sample 1	Sample 2	Sample 3	Sample 4		
[h]	[kN]	[kN]	[kN]	[kN]	[kN]	[kN]
0.0	61	64	64	64	63.25	0
0.1	59	62	62	62	61.25	2
0.2	59	62	62	62	61.25	2
0.7	59	60	62	62	60.75	2.5
0.8	59	60	62	61	60.5	2.8
1.7	59	60	62	60	60.25	3
3.7	57	60	62	60	59.75	3.5
7.8	57	60	62	60	59.75	3.5
25.3	57	60	60	60	59.25	4
30.2	57	58	60	60	58.75	4.5
97.3	57	58	60	60	58.75	4.5
195.3	57	58	60	60	58.75	4.5
339.4	57	58	60	58	58.25	5
673.3	57	58	60	58	58.25	5
940.4	57	58	60	58	58.25	5
1417.3	57	58	60	58	58.25	5
2018.8	56	58	60	58	58	5.3

Table 4.6.1: Results relaxation test 1 with $P = 63 \text{ kN} = 0.7F_p$

The average preload losses are presented in figures 4.6.3, 4.6.4 and 4.6.5 including the output from the spring model with bolt relaxation and plate creep. The spring model includes the bolt, two 25 mm plates, 3 washers and the Load Cell – adapter rings combination discussed in section 4.2.1. To be able to account for embedment creep, the guide value of table 3.4.1 can be used or the embedment effects noticed during the creep experiment in section 4.5 can be applied. Using the guide values of table 3.4.1, the expected amount of embedment creep is equal to:

- Embedment in the threads: $3 \mu m$
- Embedment under the head/nut area: $3 \cdot 6.5 = 19.5 \mu m$
- Embedment in the interface of the plates: $3.5 = 3.5 \mu m$

A total embedment creep of $26.0 \mu m$ is expected to occur. Therefore:

$$\Delta P_{em} = 0.0260 \left(\frac{k_b k_j}{k_b + k_j} \right) = 0.0260 \left(\frac{3.34 \cdot 10^5 \cdot 7.30 \cdot 10^5}{3.34 \cdot 10^5 + 7.30 \cdot 10^5} \right) = 6.0 \text{ kN} \quad (4.11)$$

The embedment creep noticed during the creep experiment in section 4.5 is equal to $7.75 \mu m$ per interface. The total amount of embedment creep of 3 interfaces (area under nut, bolt head and interface of plates) is therefore equal to $23 \mu m$. Therefore:

$$\Delta P_{em} = 0.0230 \left(\frac{k_b k_j}{k_b + k_j} \right) = 0.0230 \left(\frac{3.34 \cdot 10^5 \cdot 7.30 \cdot 10^5}{3.34 \cdot 10^5 + 7.30 \cdot 10^5} \right) = 5.3 \text{ kN} \quad (4.12)$$

The output from the model is presented for 3 cases: without embedment creep and with the preload loss found in equations 4.11 and 4.12. The model was generated with $t_{assembly} = 3 \text{ s}$ suggested by Afzali (Afzali et al. 2017).

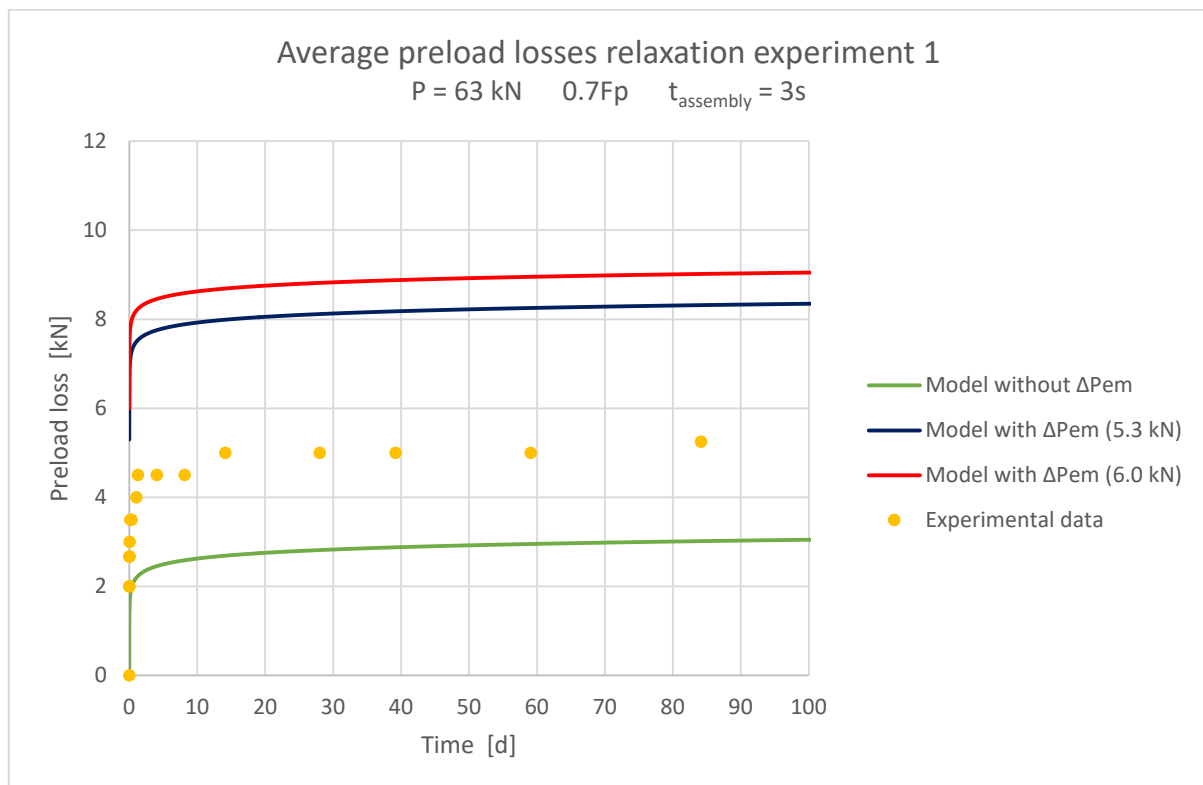


Figure 4.6.3: Average preload losses experiment 1 versus output model $P = 0.7F_p$

Figure 4.6.4 presents the preload losses within the first 8 hours after tightening, figure 4.6.5 presents the preload losses on a logarithmic scale. The slope of the experimental data on a logarithmic scale becomes parallel with the output from the model 10 hours after tightening ($t > 10h$). Before the 10 hour mark, a steeper slope can be discovered, indicating that embedment effects are present within the first 10 hours.

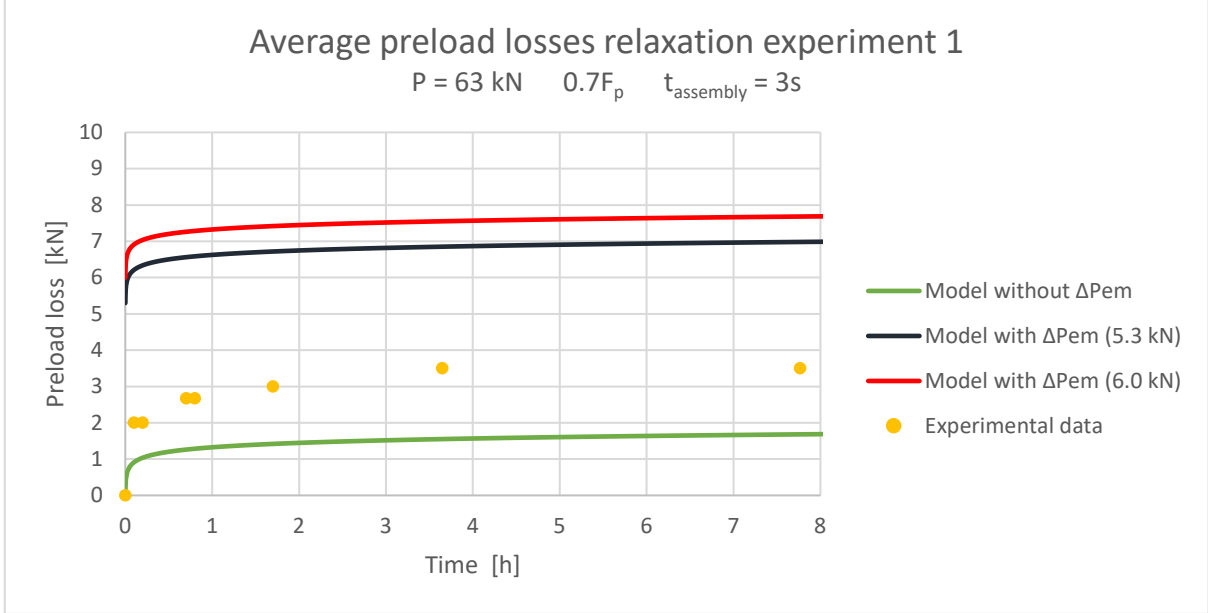


Figure 4.6.4: Average preload losses experiment 1 within first 8 hours after tightening

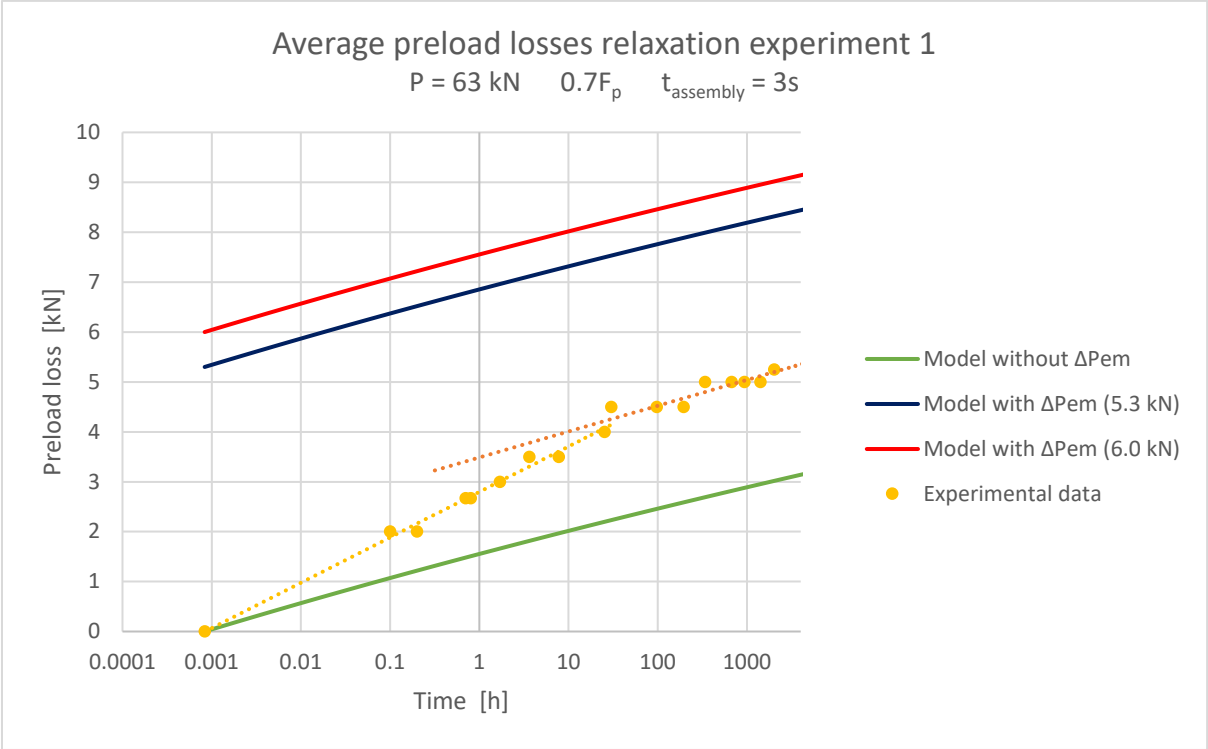


Figure 4.6.5: Average preload losses experiment 1 presented on logarithmic scale

The model captures the shape of the preload loss curve relatively well, but does underestimate the preload losses with approximately 2.5 kN if no embedment creep is taken into account. The addition of embedment creep will lead to overestimation of the preload losses as can be observed in figure 4.6.3. The discrepancies can be explained with the inaccuracy of the creep parameter functions $f_1(\sigma)$,

overestimation of the expected amount of embedment creep. Furthermore, the assembly time can have an influence as discussed in section 3.5.4. The approximate assembly time was equal to 30 seconds instead of the adopted 3 seconds mentioned by Afzali (Afzali et al. 2017). The influence of a variation of the time needed for assembly is visualized in figure 4.6.6. Next to the output corresponding to $t_{assembly} = 3s$, the data corresponding to $t_{assembly} = 30s$ is added.

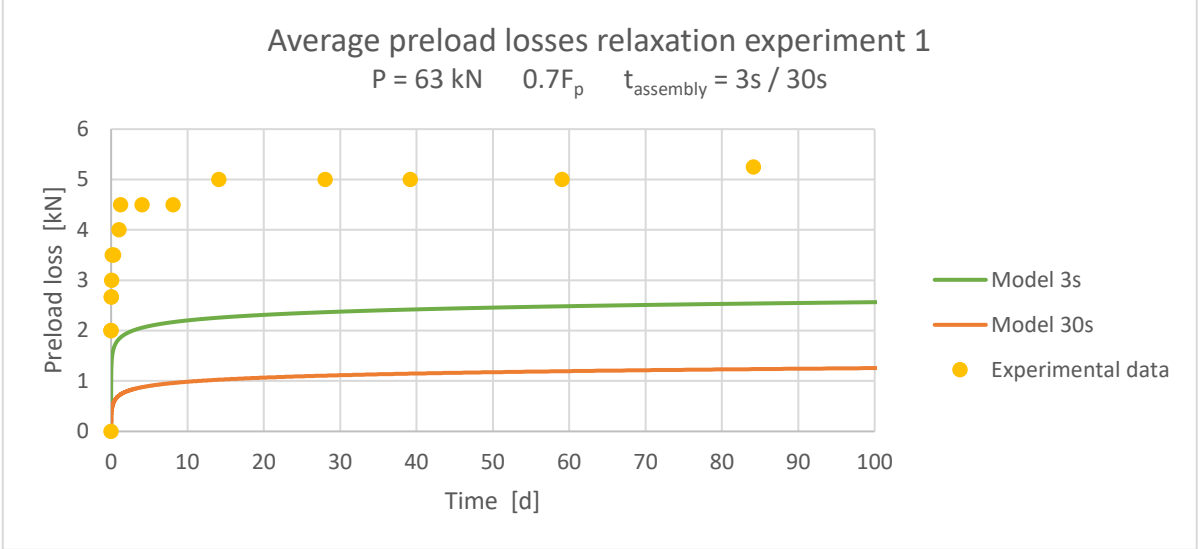


Figure 4.6.6: Average preload losses experiment 1 with varying starting point ($t_{assembly}$)

It can be discovered that the model output has a significant sensitivity to the assembly time, supporting the observations made in section 3.5.4. However, since significant relaxation occurs only at higher preload levels, only the last part of the assembly time should be considered. Next to that, as discussed in section 2.3.4, (re)tightening has no significant influence on the preload loss behaviour indicating that neutralization of relaxation during tightening is minimal. Therefore, it is uncertain what value for $t_{assembly}$ is applicable. A curve fit with $t_{assembly} = 10s$ and $\Delta P_{em} = 3.5 \text{ kN}$ gives a good approximation of the preload force behaviour as can be discovered in figure 4.6.7.

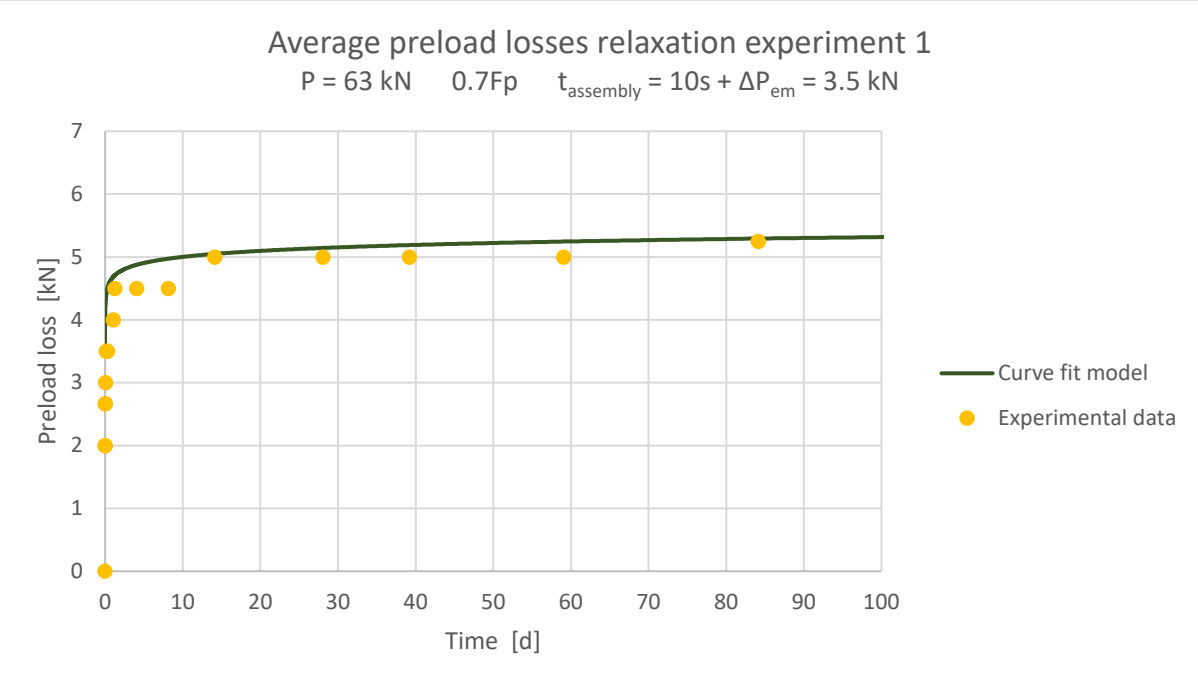


Figure 4.6.7: Average preload losses experiment 1 with curve fit model including $t_{assembly}$ and ΔP_{em}

4.6.2 Load Cell relaxation experiment 2 ($P = 82 \text{ kN} = 0.9F_p$)

Relaxation experiment 2 contains an identical setup compared with relaxation test 1 with the exception of the level of the initial preload force and the lubrication type. Four sets of two as-delivered aluminium plates 5083 O/H111 with dimensions 180x220x25 mm are assembled with a bolt A4 80 M16x110 mm and preloaded up to 82 kN ($0.9F_p$). The samples are stored in a conditioned lab with a constant temperature of 20°C to exclude thermal variations.

To be able to identify the influence of the lubrication type, two lubrication types are used: two samples contain unlubricated bolts and two samples contain lubrication (bolt threads are lubricated with HY52 paste). The amount of torque needed to introduce the preload force will therefore vary. The tightening procedure is identical to the procedure described in section 4.6.1:

- Bolt head is locked to prevent rotation of the bolt head
- A wrench is used for tightening
- During the test the bolt force is measured with Bolt Safe Load Cells and a BoltSafe Load Measuring System SM-200

The experimental data corresponding to the four samples are summarized in table 4.6.2.

Results relaxation test 2 with $P = 82 \text{ kN} = 0.9F_p$						
Time	Unlubricated			Lubricated		
	Preload force		Average preload loss	Preload force		Average preload loss
	Sample 1	Sample 2		Sample 3	Sample 4	
[h]	[kN]	[kN]	[kN]	[kN]	[kN]	[kN]
0.0	79	83	0	83	83	0
0.2	76	79	3.5	80	80	3
0.4	75	79	4	80	80	3
0.9	74	78	5	80	80	3
2.4	74	78	5	79	79	4
5.8	74	78	5	78	78	5
51.3	73	77	6	77	78	5.5
192.7	72	76	7	76	78	6
295.0	72	76	7	76	77	6.5
531.4	72	76	7	76	77	6.5
627.5	72	76	7	76	76	7
1158.7	72	75	7.5	76	76	7
1467.7	72	75	7.5	76	76	7
2139.7	72	74	8	76	76	7

Table 4.6.2: Results relaxation test 2 with $P = 82 \text{ kN} = 0.9F_p$

The average preload losses of both lubrication types are presented in figure 4.6.8 with a logarithmic time scale. Both types show parallel relaxation behaviour, indicating that the amount of initial torque does not have an influence on the preload force behaviour. The small offset can be explained with discrepancies of the initial preload force due to the Load Cell display accuracy of 2 kN discussed in section 4.6.1.

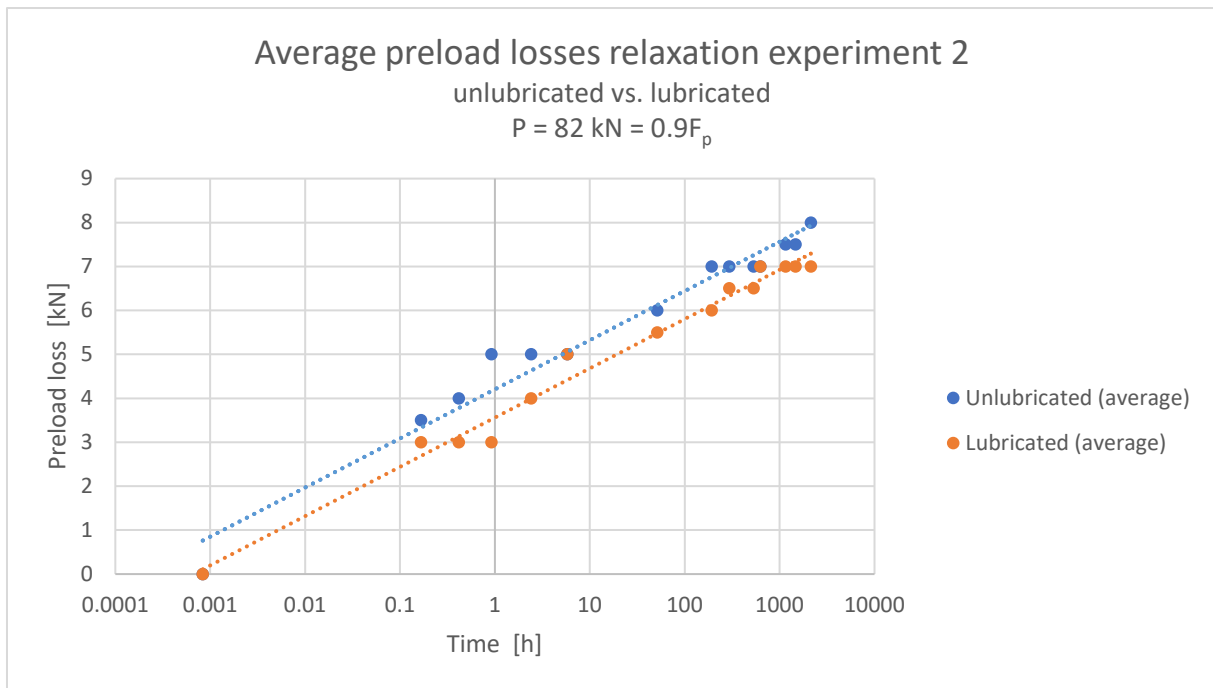


Figure 4.6.8: Average preload losses experiment 2 unlubricated versus lubricated $P = 0.9F_p$

The average preload losses of all 4 samples are presented in figure 4.6.9. The output from the model is presented with the parameters used in relaxation experiment 1 ($t_{\text{assembly}} = 10\text{s}$ and $\Delta P_{\text{em}} = 3.5 \text{ kN}$). The shape of the theoretical preload loss behaviour matches relatively well with the experimental data. An overestimation of 2 kN is observed, indicating an overestimation of the approximated amount of embedment creep or underestimation of t_{assembly} . Since the proof strength of 50830/H111 is relatively low, imperfections could be leveled already during tightening. Next to the inaccuracies of the model discussed in section 4.6.1, neutralization of embedment effects and during tightening can therefore lead to deviating results.

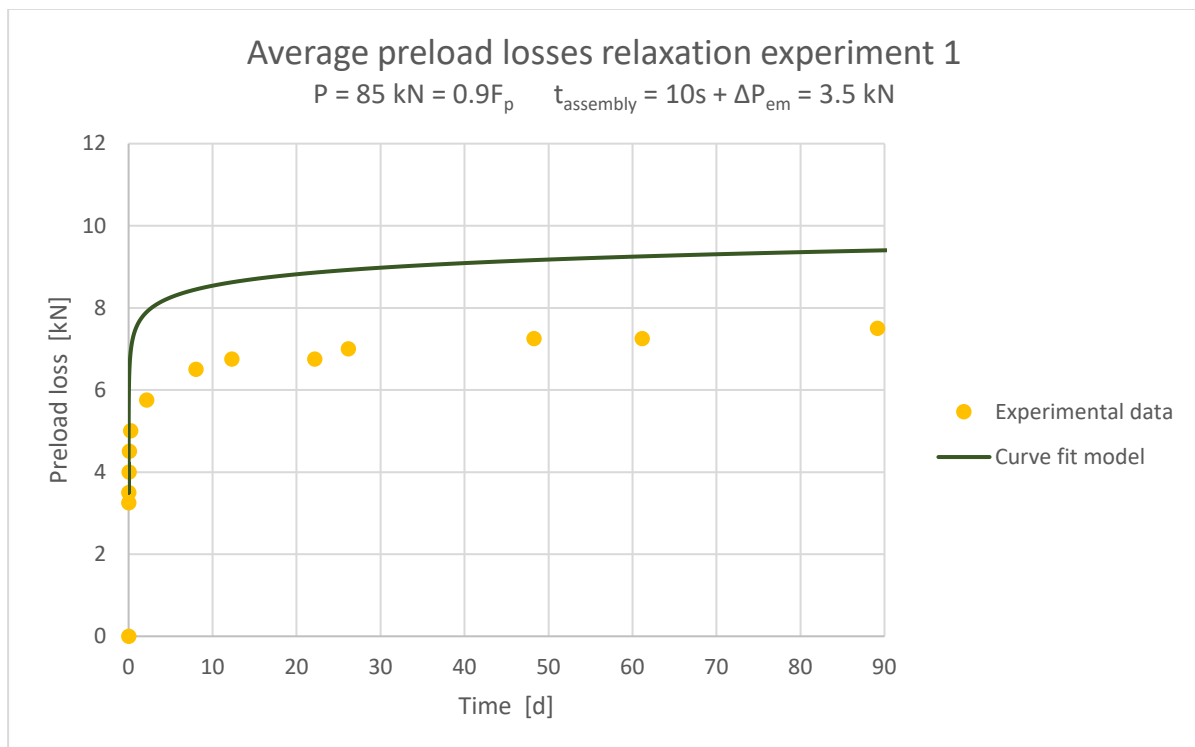


Figure 4.6.9: Average preload losses experiment 2 with curve fit model including t_{assembly} and ΔP_{em}

4.6.3 Load Cell relaxation experiment 3 ($P \approx 32 \text{ kN} = 0.34F_p$)

Relaxation experiment 3 contains two grit blasted double lap joints assembled with 1 lubricated bolt A4 80 M16x110 mm and 1 lubricated bolt A4 80 M16x75mm preloaded up to approximately $0.34F_p$. The bolt with a length of 110 mm is equipped with a Load Cell. Next to the application of a Load Cell, the bolts are equipped with strain gauges to perform a parallel measurement of the preload force. Since the strain gauge method has limitations with respect to the preload level, a relatively low initial preload force was introduced. The bolt with a length of 75 mm is tightened with a torque wrench up to 70 Nm to introduce a preload force of approximately 32 kN (theory can be found in section 4.4.1). The joint dimensions, plate dimensions and test setup are visualized in figure 4.6.10 – 4.6.13. As can be observed in figure 4.6.11, the edge distance is sufficient for the development of a load distribution cone with an angle of 30° . The stiffness equations discussed in section 2.2 are therefore applicable to compare the spring model with the experimental results. The results of the strain gauge method are discussed in section 4.7. This section focusses on the results of the Load Cells used in the 110 mm bolts.

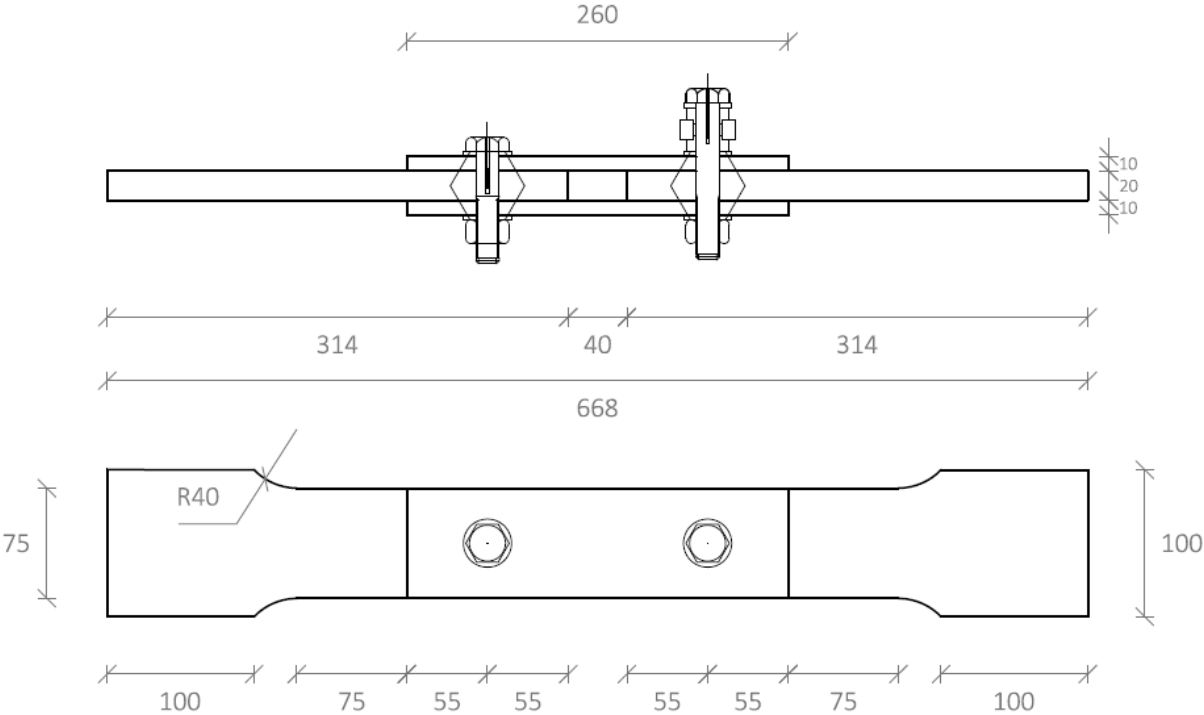


Figure 4.6.10: Joint dimensions top and side view sample relaxation test 3

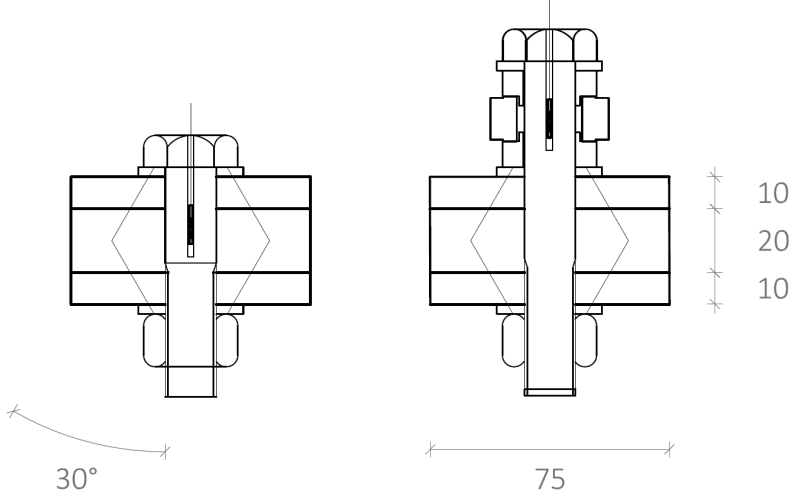


Figure 4.6.11: Joint dimensions section sample

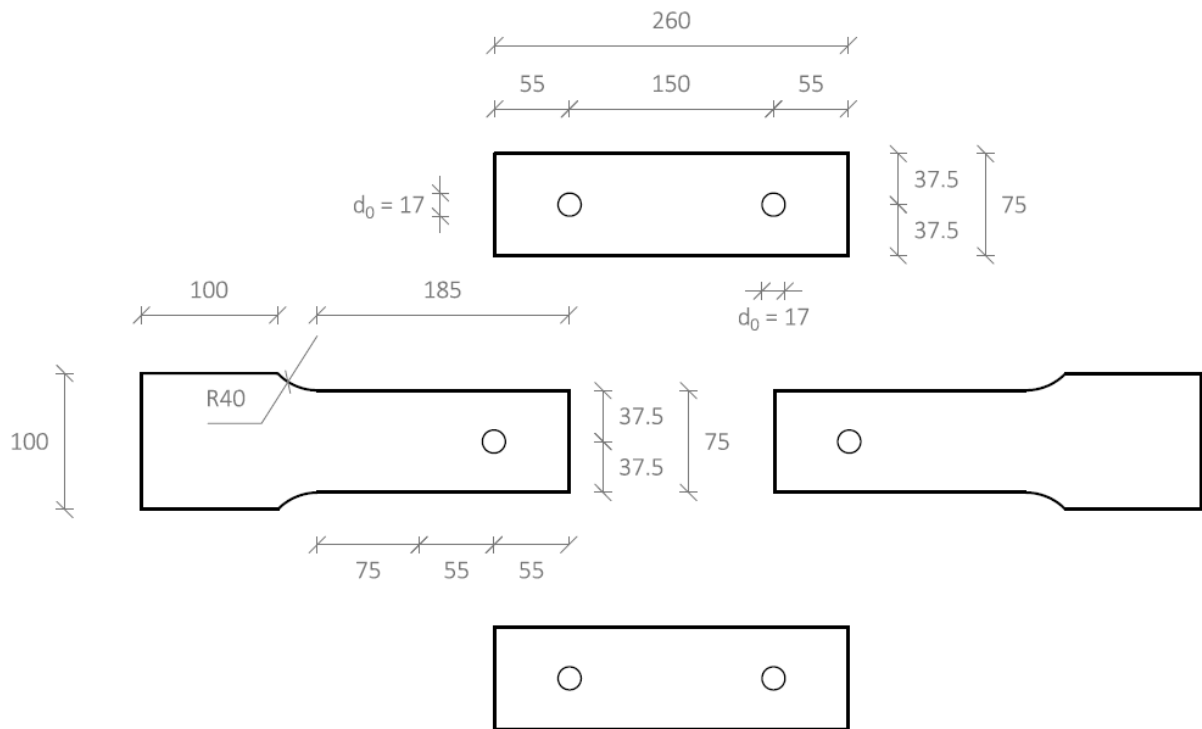


Figure 4.6.12: Plate dimensions sample

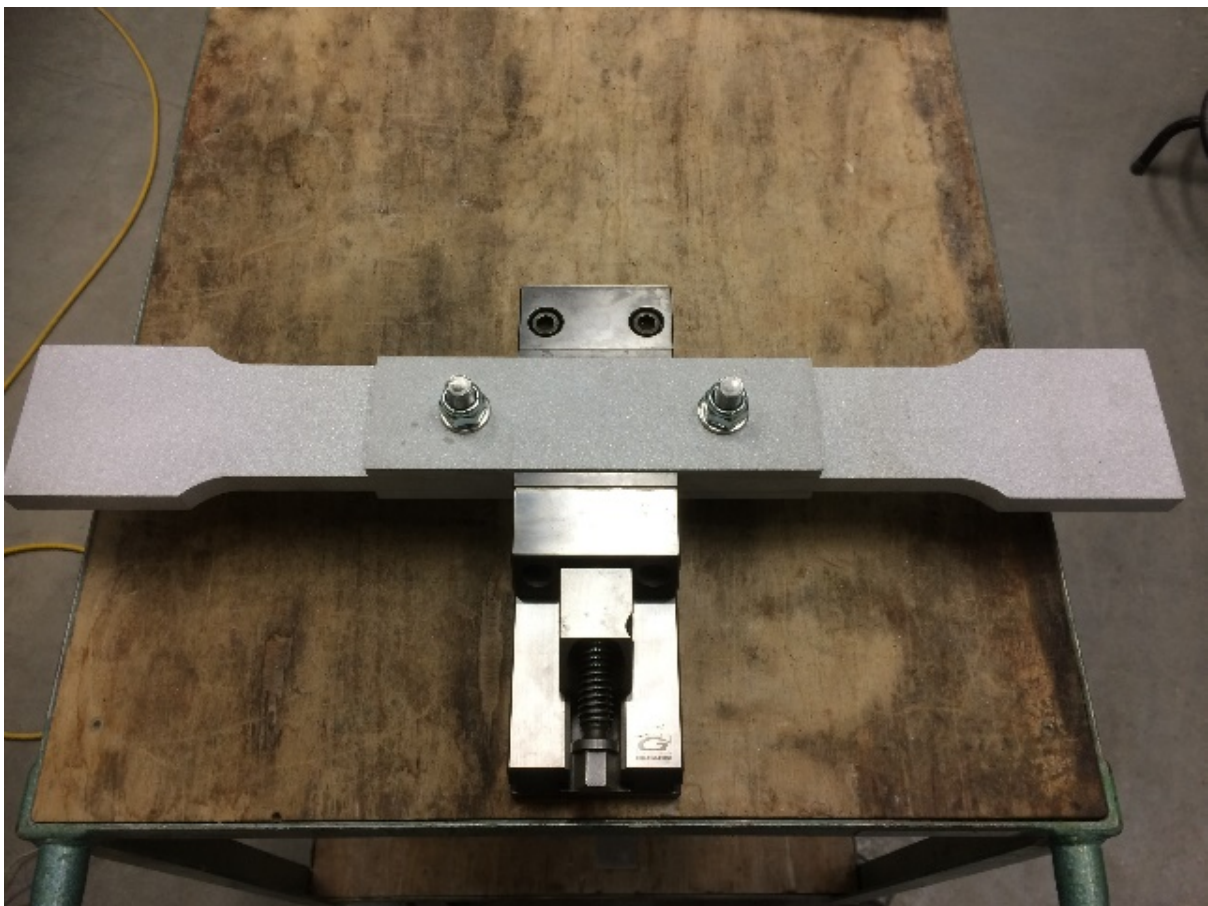


Figure 4.6.13: Assembly of joint using bench vice

Two samples are monitored with a Load Cell. The 110 mm bolt of sample 3 is monitored with Load Cell 3, the 110 mm bolt of sample 4 is monitored with Load Cell 4. The experimental data corresponding to the two samples are summarized in table 4.6.3.

Results relaxation test 3 with $P \approx 32 \text{ kN} = 0.34F_p$			
Time	Preload force per sample		Average preload loss
	Sample 3	Sample 4	
[h]	[kN]	[kN]	[kN]
0.0	36	32	0
0.4	34	31	1.5
1.4	34	31	1.5
2.4	34	31	1.5
4.1	34	30	2.0
77.1	34	30	2.0
143.9	34	30	2.0
314.2	34	30	2.0
406.7	34	30	2.0

Table 4.6.3: Results relaxation test 3 with $P \approx 32 \text{ kN} = 0.34F_p$

The output from the model is presented in figure 4.6.14 with the parameters used in relaxation experiment 1 ($t_{assembly} = 10\text{s}$ and $\Delta P_{em} = 3.5 \text{ kN}$). The model predicts a negligible increasing amount of preload loss, with the majority of the preload losses caused by embedment creep. The experimental data exhibit a stable preload level 5 hours after tightening with a preload loss of 2 kN, following a comparable trend with the model output. Assuming $t_{assembly} = 10\text{s}$, the amount of embedment creep appears to be equal to approximately 2 kN, indicating that a lower amount of embedment creep can be expected with low initial preload forces.

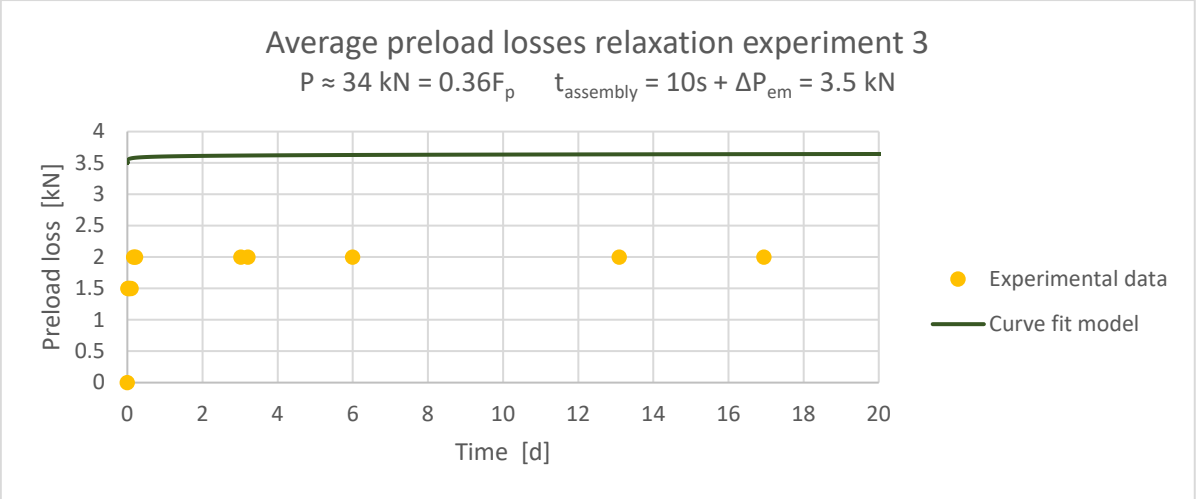


Figure 4.6.14: Average preload losses experiment 3 with curve fit model including $t_{assembly}$ and ΔP_{em}

4.6.4 Load Cell relaxation experiment 4 ($P \approx 85 \text{ kN} = 0.9F_p$)

Relaxation experiment 4 contains an identical setup compared with relaxation test 3 with the exception of the level of the initial preload force. Two samples containing a double lap joint with grit-blasted aluminium plates 5083 O/H111 are assembled with a lubricated A4 80 M16 bolt preloaded up to 88 kN ($0.9F_p$). The bolt with a length of 110 mm is equipped with a Load Cell. The bolt with a length of 75 mm is tightened with 175 Nm to introduce a preload force of approximately 88 kN (background:

section 4.4.1). Both samples are monitored with a Load Cell. The 110 mm bolt of sample 1 was monitored with Load Cell 1, the 110 mm bolt of sample 2 was monitored with Load Cell 2. The experimental data corresponding to the two samples are summarized in table 4.6.4.

Results relaxation test 4 with $P \approx 85 \text{ kN} = 0.9F_p$			
Time	Preload force per sample		Average preload loss
	Sample 1	Sample 2	
[h]	[kN]	[kN]	[kN]
0.0	82	88	0
0.2	80	85	2.5
0.5	80	84	3
1.2	80	84	3
2.2	78	84	4
4.0	78	83	4.5
5.1	78	83	4.5
72.5	77	82	5.5
77.0	77	81	6
143.7	76	81	6.5
314.0	76	80	7
406.5	76	80	7

Table 4.6.4: Results relaxation test 4 with $P \approx 85 \text{ kN} = 0.9F_p$

The average preload losses of table 4.6.4 are presented in figure 4.6.15. The output from the model is presented with the approximated parameters ($t_{assembly} = 10\text{s}$ and $\Delta P_{em} = 3.5 \text{ kN}$). Comparable with relaxation experiment 2, the model output overestimates the experimental preload losses with 2 kN .

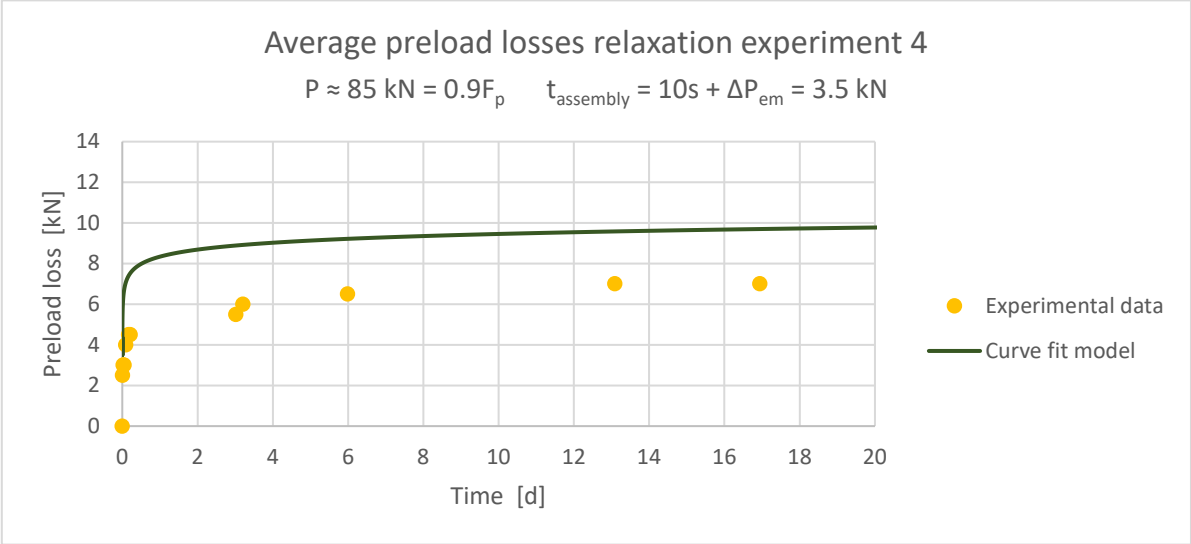


Figure 4.6.15: Average preload losses experiment 4 with curve fit model including $t_{assembly}$ and ΔP_{em}

The initial preload force of relaxation experiment 2 (as-delivered plates) is comparable to the initial preload force of relaxation experiment 4 (grit-blasted plates). The average results obtained from both samples exhibit identical preload losses. Grit-blasting the plates has therefore no increasing effect on the preload loss. This conclusion is in accordance with the results found in section 4.5, where a hardening effect was noticed in grit-blasted plates. Overall, conservative results can be obtained by considering a preload loss of 3.5 kN due to embedment creep and $t_{assembly} = 10\text{s}$.

4.7 Relaxation experiments with Strain Gauge Method

An alternative method to measure preload behaviour of bolts is the Strain Gauge Method. An embedded strain gauge can measure the axial strain within the bolt during tightening and service life. To be able to install the strain gauges, a 2 mm hole with a depth of 38 mm has been drilled into A4 80 M16x75 and M16x110 mm bolts. A BTM-6C strain gauge with a strain limit of 5000 $\mu\text{m}/\text{m}$ is embedded with Adhesive Type A-2. The bolts with 110 mm length were equipped with both a strain gauge and a Load Cell to be able to compare the results of both measuring systems. Since 8 strain gauges were available, 4 instrumented M16x75 mm bolts and 4 instrumented M16x110mm were obtained. The application is illustrated in figure 4.7.1, preparation and installation is shown in figure 4.7.2.

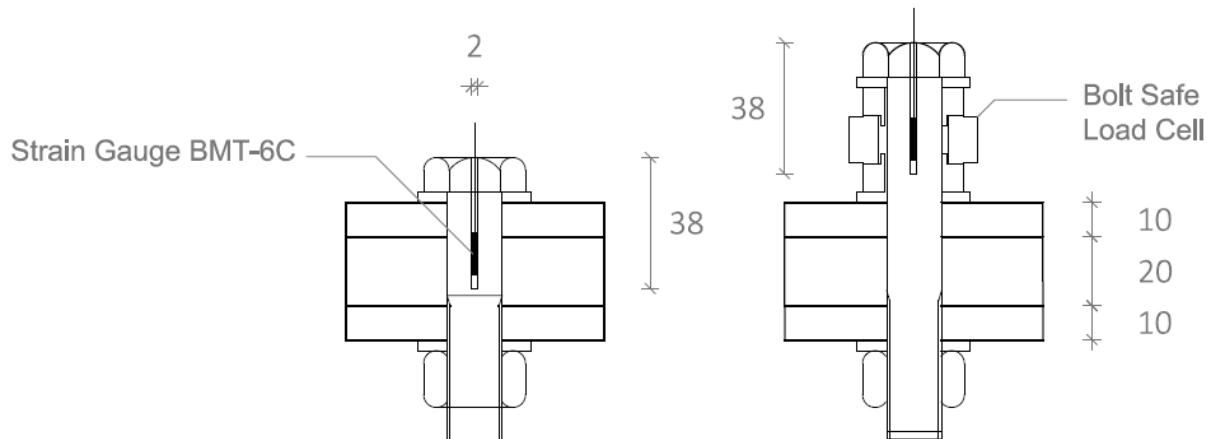


Figure 4.7.1: Application BMT-6C strain gauge



Figure 4.7.2: Bolts before (left) and after (right) installation

4.7.1 Stress – strain behaviour 316 (A4) bolt material

The output of the strain gauge should follow the stress – strain behaviour of 316 (A4) bolt material closely to be able to measure the preload force in the bolt. The stress – strain behaviour of an A4 80 M16x110 mm bolt without a strain gauge and hole is determined in a tensile test. The shank of the bolt is reduced to $d = 12.503$ mm to create a minimum surface where the strain will be maximal. Furthermore, an as-delivered surface is needed to be able to monitor the strain. The reduced shank is equipped with 2 dots for optical measurement. The original length L_0 between the dots is equal to 12.0 mm. The specimen and dimensions are shown in figure 4.7.3 and figure 4.7.4.

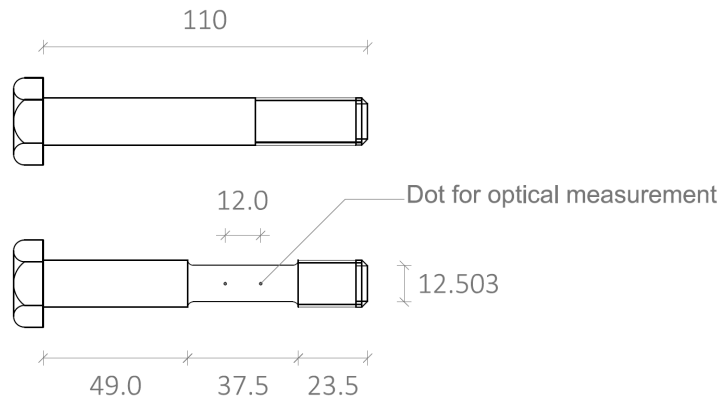


Figure 4.7.3: Original bolt dimensions and dimensions specimen used in tensile test



Figure 4.7.4: M16x110mm bolt with reduced shank used in tensile test

The strain is measured with an Instron 5985 Universal Testing System with an optical video gauge. A ball joint is used at both ends of the specimen to minimize horizontal displacements. The test setup is visualized in figure 4.7.5. The ball joints are shown in figure 4.7.6.

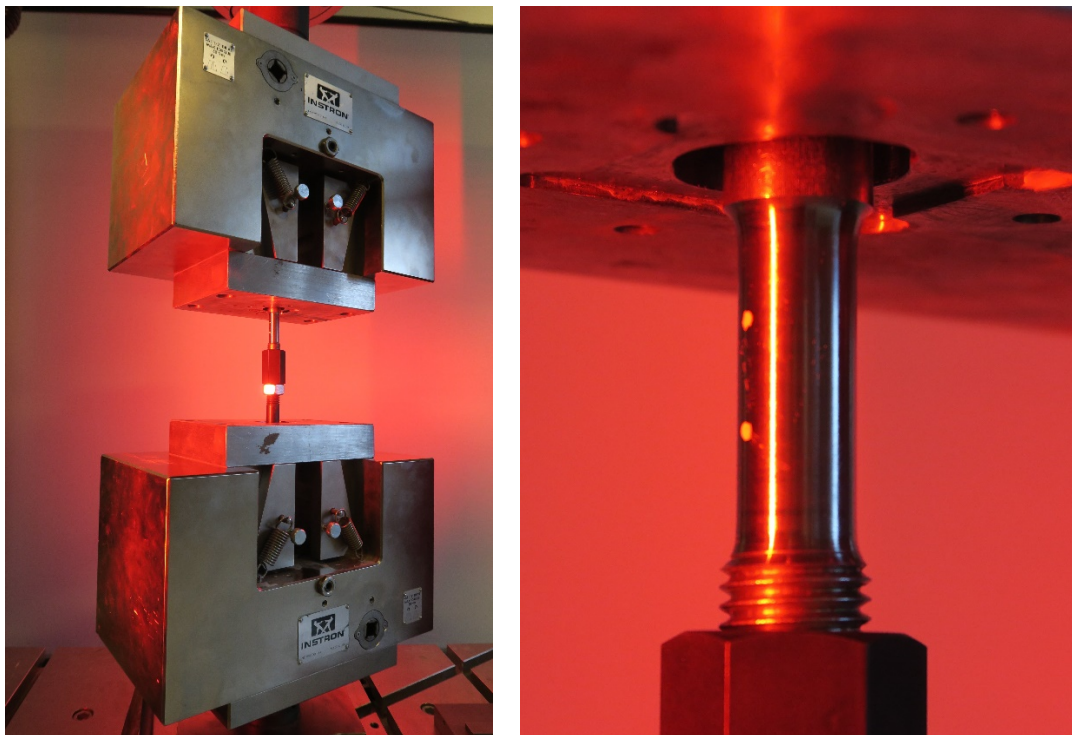


Figure 4.7.5: Test setup including Instron 5985 Universal Testing System (left) and specimen (right)

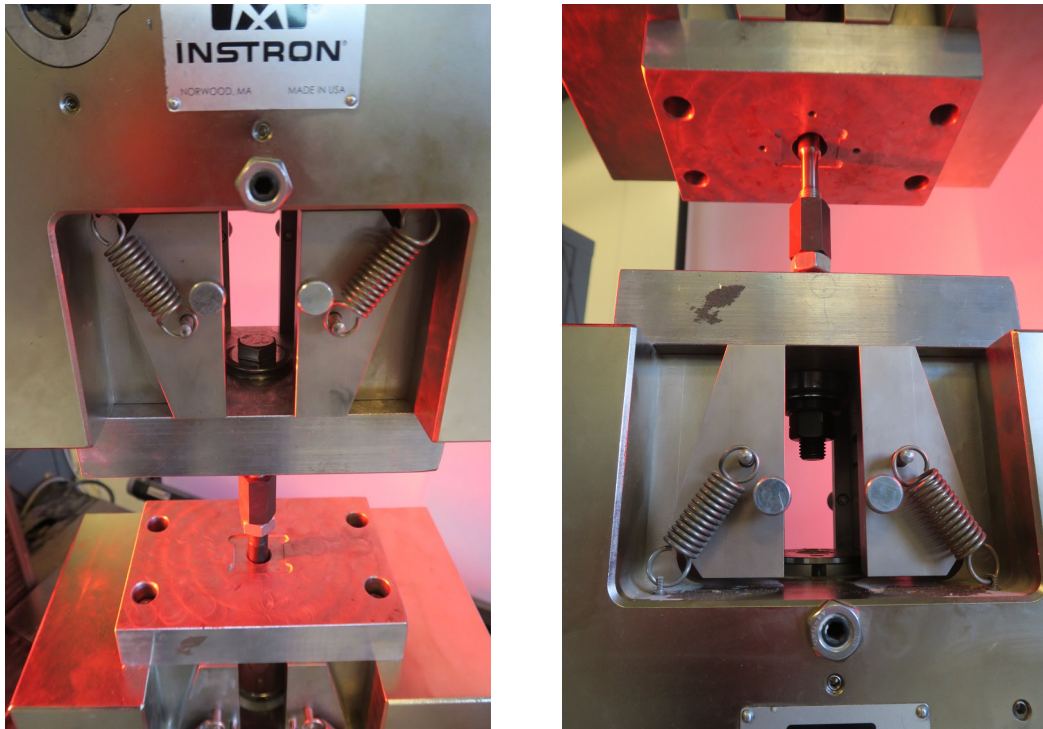


Figure 4.7.6: Ball joints used at top specimen (left) and at bottom of specimen (right)

The tensile test is performed with a constant displacement rate of 1 mm/min, which corresponds to a strain rate of approximately $5.3 \cdot 10^{-4} \text{ s}^{-1}$ measured in the reduced cross section. Four specimens are tested, the results can be found in figure 4.7.7. An 0.2% offset is added with a Young's Modulus equal to the value found in table 3.3.2 ($E_b = 1.93 \cdot 10^5 \text{ N/mm}^2$). As can be noticed from figure 4.7.7, the tensile tests of specimen 1 and 2 are ended relatively soon. These specimen are used to test the setup and Instron system programming. Specimen 2 shows a fluctuating trend, which disappears in specimen 3 and 4 by adjusting the Instron system programming.

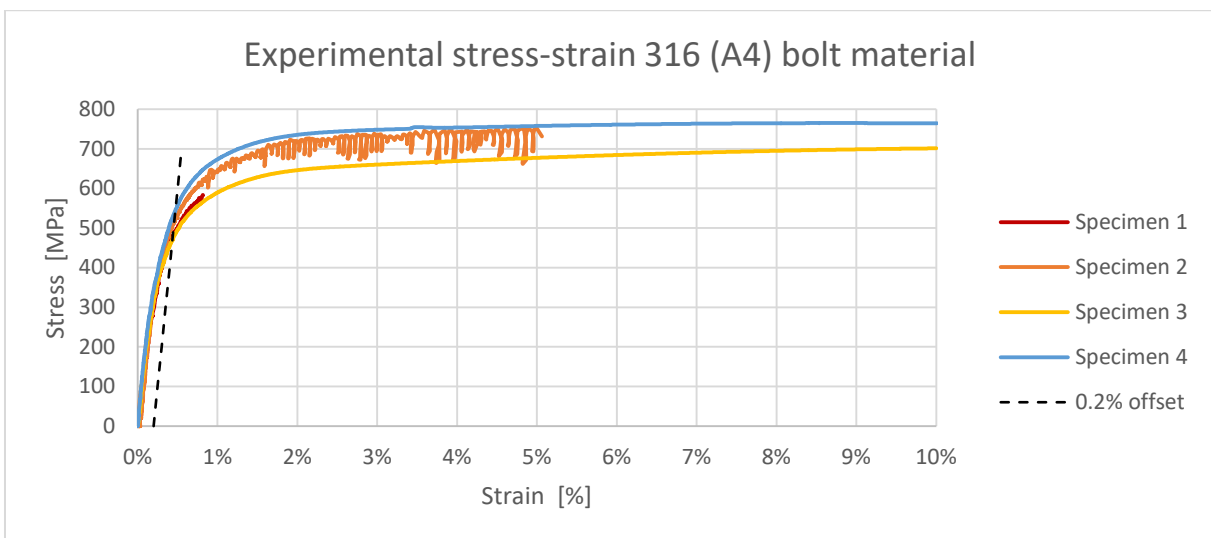


Figure 4.7.7: Experimental stress – strain behaviour of 316 (A4) bolt material with 0.2% offset

The stress-strain behaviour of 316 (A4) appears to be non-linear, therefore a Ramberg-Osgood equation will be constructed to describe the average stress-strain behaviour. Since in practical cases the bolt will be loaded to stresses less than the proof stress, an upper limit where the Ramberg-Osgood equation is determined is set to 1%. An average Ramberg-Osgood relationship derived from the experimental data can be found in figure 4.7.7. The 0.2% offset is based on the found Young's Modulus.

The parameters corresponding to the derived relationship are listed in table 4.7.1. The theoretical ultimate strength was derived from the average ultimate strength values of specimen 2, 3 and 4. No literature was found regarding a theoretical value of n .

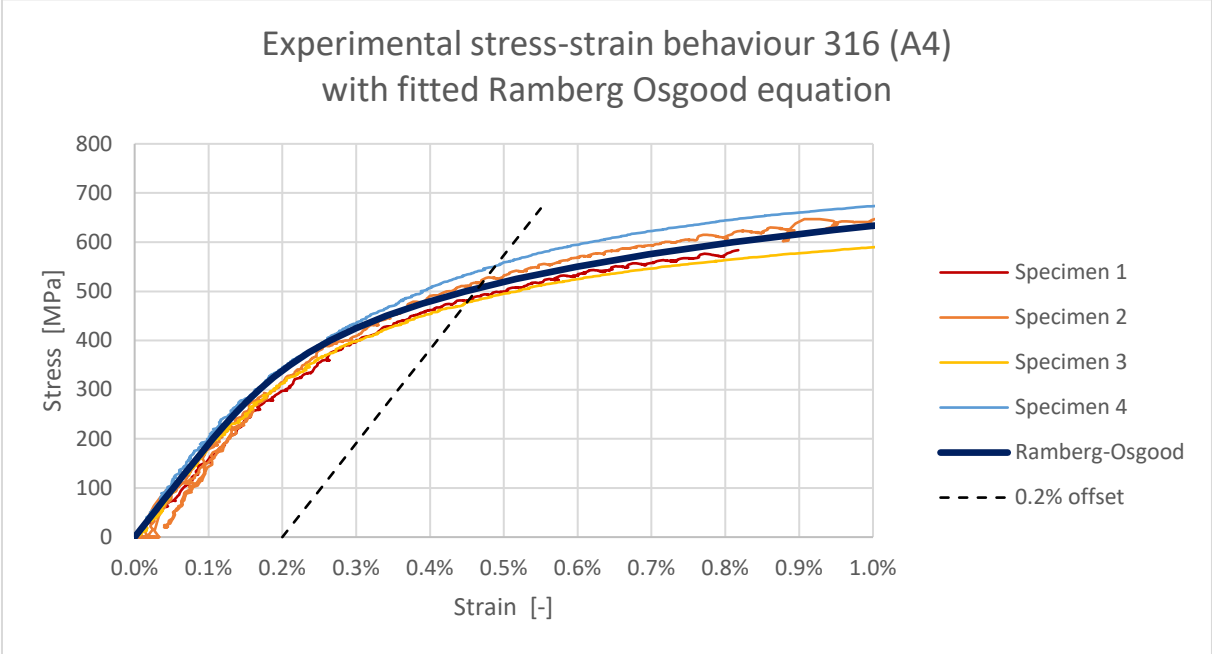


Figure 4.7.8: Experimental stress – strain behaviour 316 (A4) with Ramberg-Osgood equation

Ramberg-Osgood parameters 316 (A4) bolt material			
		Experimental	Nominal ^{1,2}
E	[N/mm ²]	191006	193000
f _{0.2}	[N/mm ²]	507	600
f _u	[N/mm ²]	758	800
n	[-]	5.4	-

Table 4.7.1: Experimental vs. nominal values (¹NEN-EN 1993-1-4 2006) (²Atlas Specialty Metals 2006)

It can be concluded that the average experimental results are inferior compared to the nominal data. Necking and fracture occurred close to the transition of unthreaded and threaded part of the original bolt (visualized in figure 4.7.9), possibly indicating that a weak point exists in the bolt. Since this weak point originates within the original length L_0 , the output could have been influenced



Figure 4.7.9: Necking and fracture of specimens (left) and detailed fracture (right)

4.7.2 Calibration of bolts equipped with strain gauge

A calibration of the instrumented bolts is necessary to determine the stiffness of the combination of the strain gauge and adhesive. A comparison with the experimental stress-strain behaviour determined in section 4.7.1 should give a verification whether the strain gauge output is realistic. Therefore, all 8 instrumented bolts are examined in a tensile test with an Instron 5985 Universal Testing System. The test setup and connection with the strain gauge is shown in figure 4.7.10.

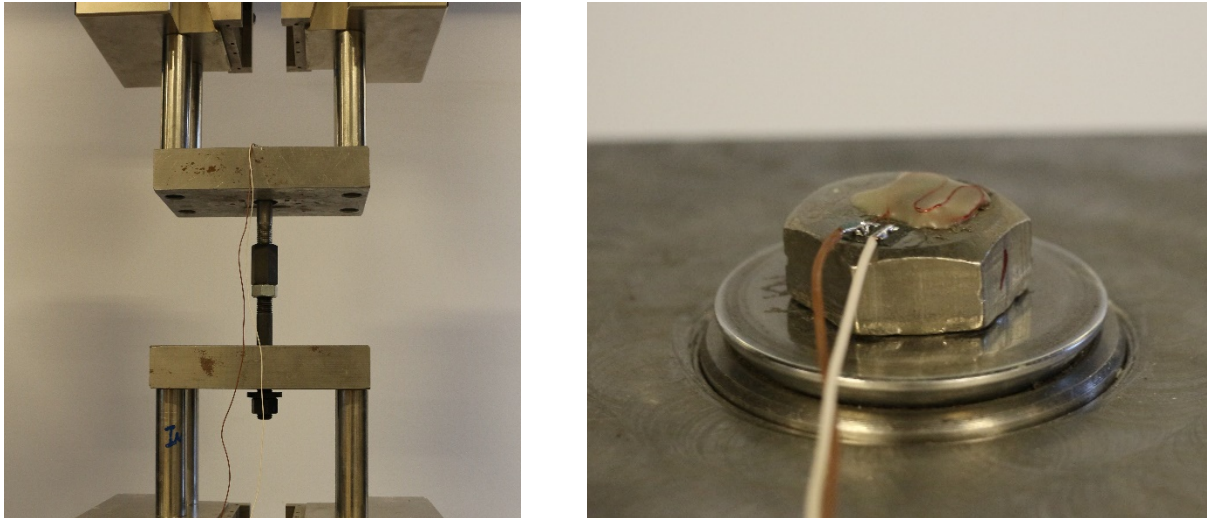


Figure 4.7.10: Test setup calibration instrumented bolts (left) and connected strain gauge (right)

A load rate of 0.1 kN/s is applied corresponding to a stress rate of 0.52 MPa/s. An upper limit of 175 MPa was taken into account to avoid the occurrence of plastic strain and possible disturbance of the relaxation behaviour. An exception was made for 1 bolt M16x110mm to be able to analyze and compare the non-linear stress-strain behaviour up to 385 MPa. M16x75mm bolts are coded with #S (sample number S(Short bolt)). The calibration of the bolts with a length of 75 mm can be found in figures 4.7.11 – 4.7.14. The Ramberg-Osgood relationship is added for comparison. The axial strain is presented in $\mu\text{m}/\text{m}$.

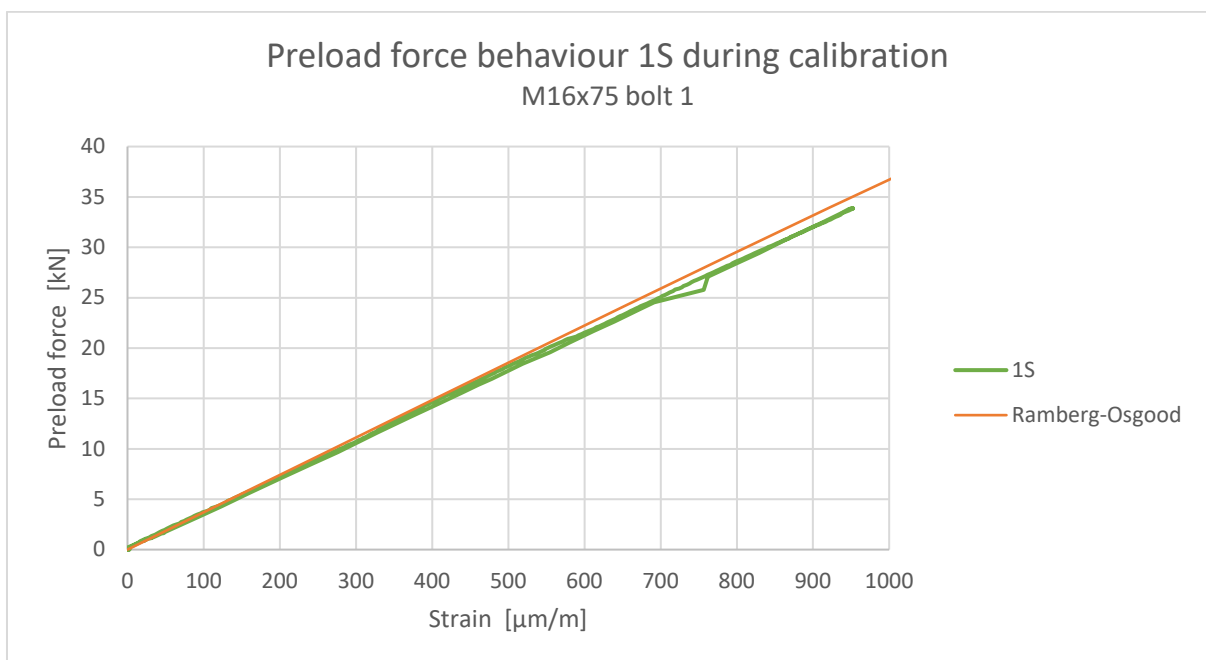


Figure 4.7.11: Preload force – strain relationship instrumented bolt 1S

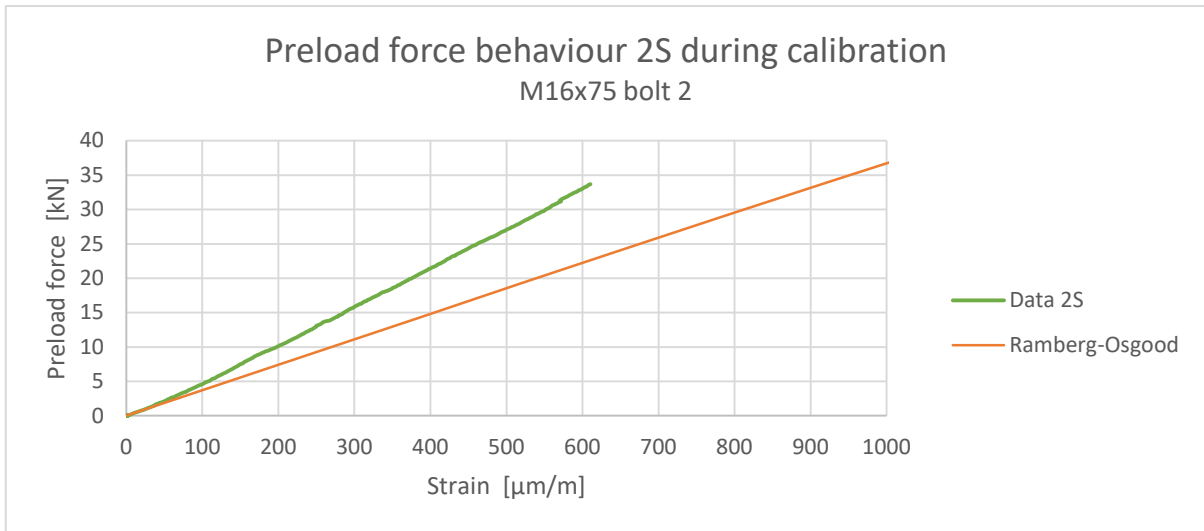


Figure 4.7.12: Preload force – strain relationship instrumented bolt 2S

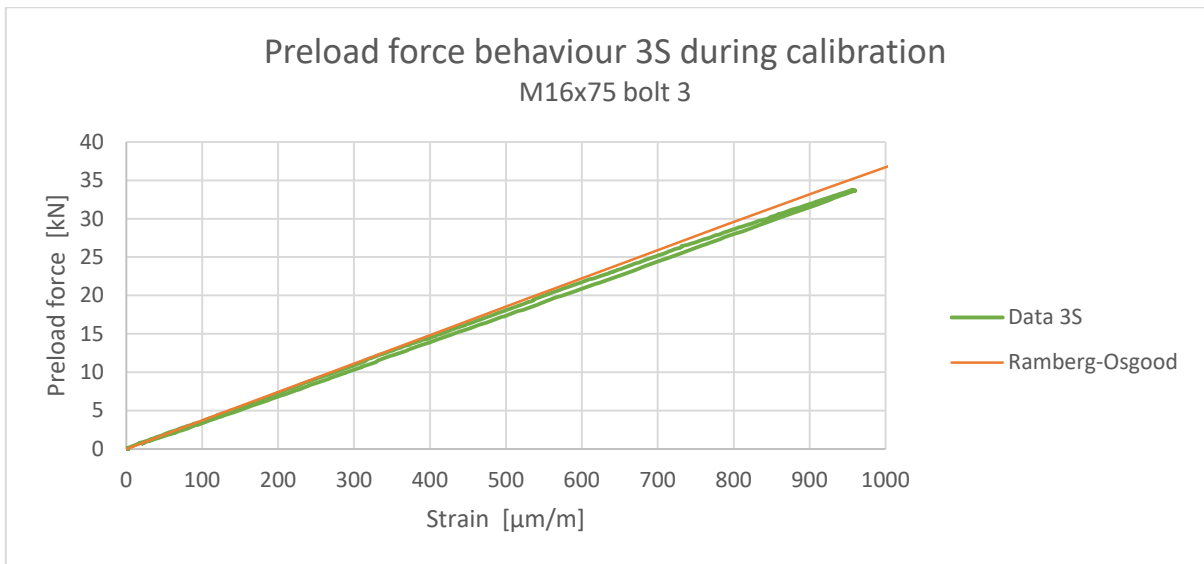


Figure 4.7.13: Preload force – strain relationship instrumented bolt 3S

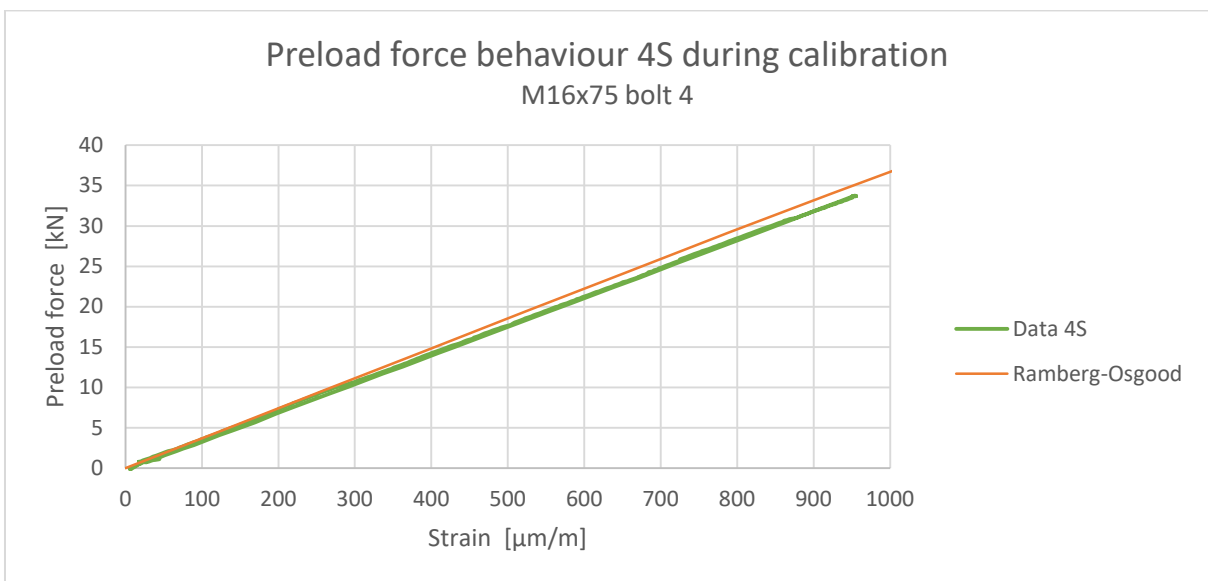


Figure 4.7.14: Preload force – strain relationship instrumented bolt 4S

The preload force – strain behaviour of the short M16x75mm instrumented bolts is in good agreement with the experimental Ramberg-Osgood behaviour derived in 4.7.1 with the exception of bolt 2S. The stiffness of bolt 2S showed deviating behaviour compared to bolt 1S, 3S and 4S and is not in accordance with realistic behaviour of stainless steel resulting in disregarding of bolt 2S. Table 4.7.2 summarizes the obtained Young’s Modulus of the bolts showing a 50% deviation of the Young’s modulus of bolt 2S with respect to the experimentally derived Young’s Modulus of $E_b = 191006 \text{ N/mm}^2$.

Young’s modulus M16x75 instrumented bolts					
		1S	2S	3S	4S
E_b	[N/mm ²]	183006	285890	182374	182505

Table 4.7.2: Young’s modulus M16x75mm (#S) instrumented bolts

The calibration of the bolts with a length of 110 mm can be found in figures 4.7.15 – 4.7.18. As mentioned earlier, bolt 1L is tested well into the plastic range to be able to analyze the non-linear behaviour of an instrumented bolt. Furthermore, the bolt was unloaded two times to discover the impact of unloading and subsequently loading the bolt.

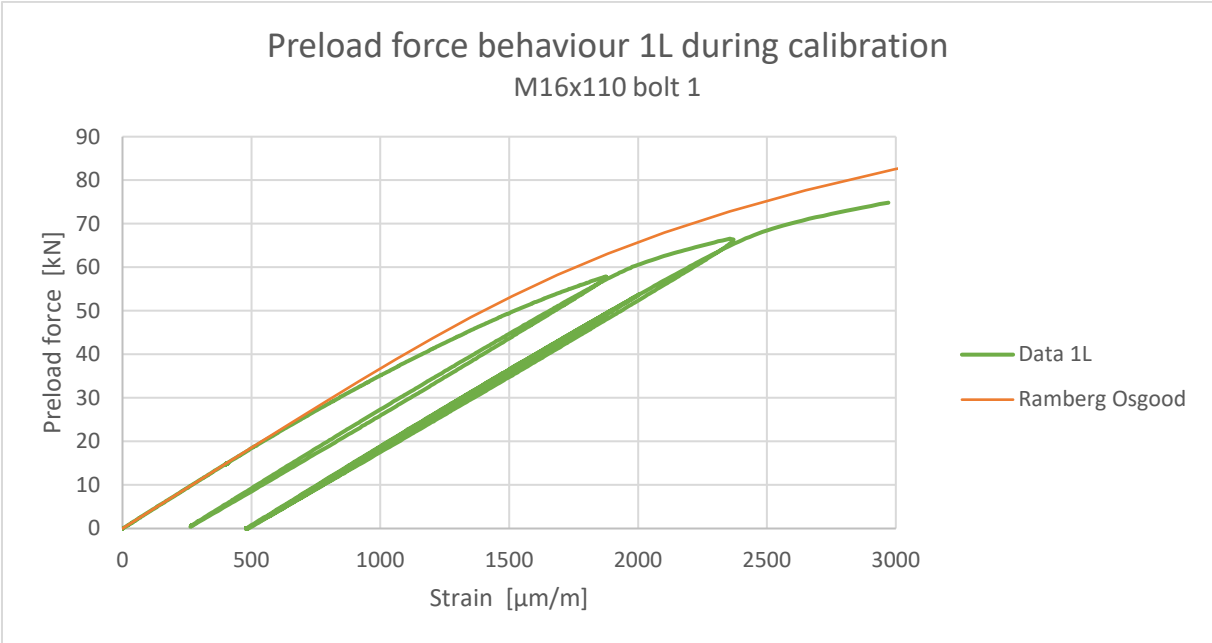


Figure 4.7.15: Preload force – strain relationship instrumented bolt 1L

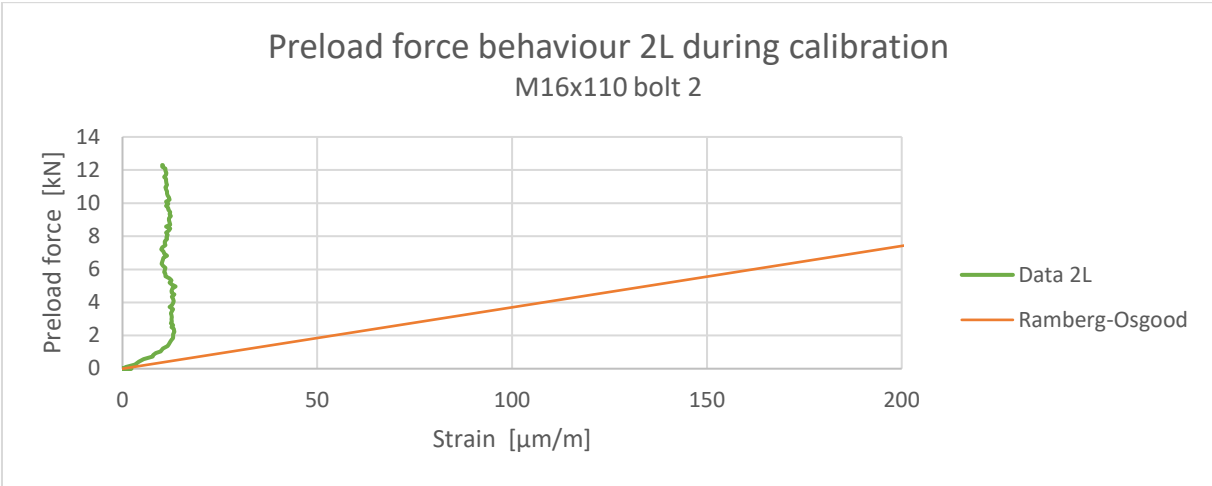


Figure 4.7.16: Preload force – strain relationship instrumented bolt 2L

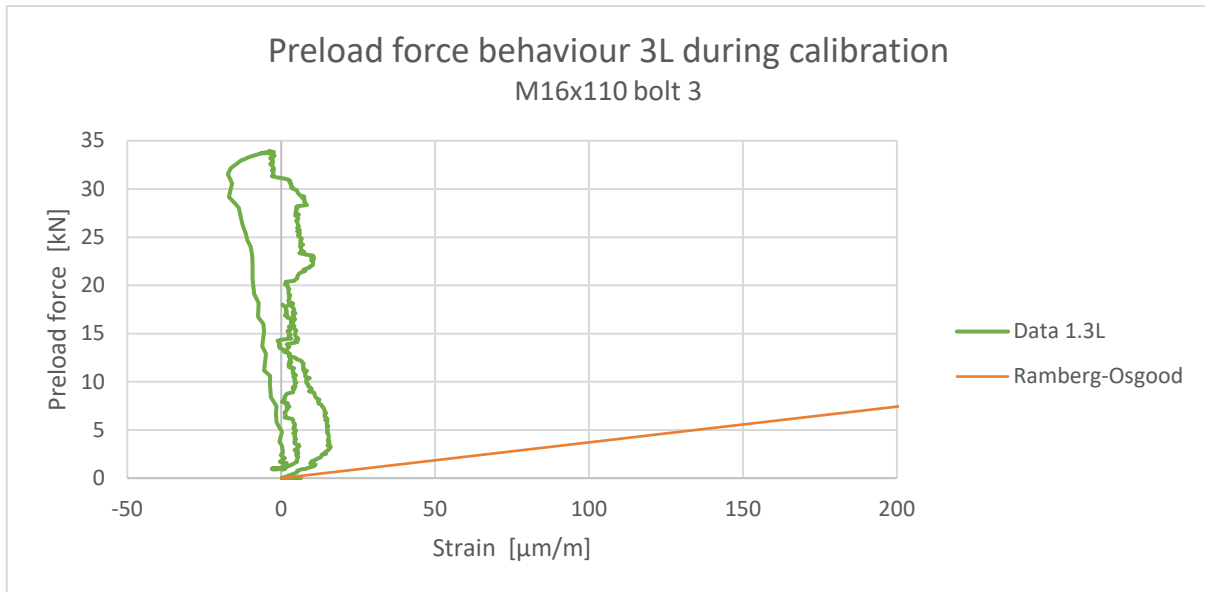


Figure 4.7.17: Preload force – strain relationship instrumented bolt 3L

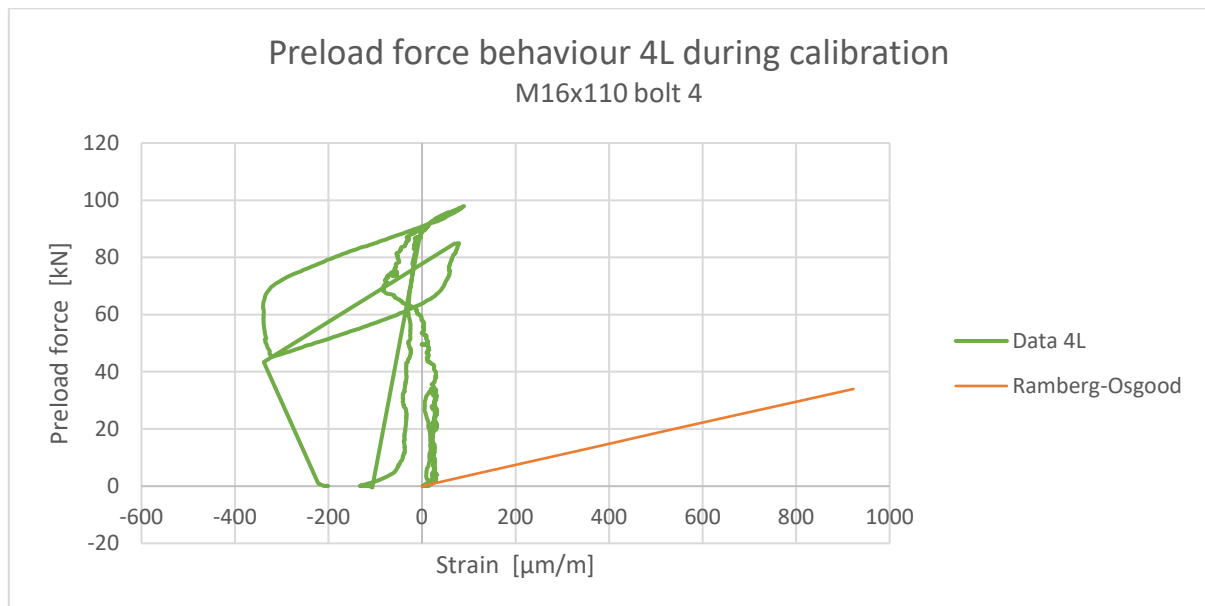


Figure 4.7.18: Preload force – strain relationship instrumented bolt 4L

The preload force – strain behaviour of bolt 1L (M16x110mm instrumented bolt 1) is in good agreement with the experimental Ramberg-Osgood behaviour derived in section 4.7.1. A hysteresis behaviour was found, with a curve describing unloading-loading with a stiffness comparable to the initial Young’s modulus of the instrumented bolt. Bolt 2L, 3L and 4L showed an unrealistic reaction with respect to the applied tensile force resulting in disregarding of all 3 bolts. No explanation can be given for the dysfunctioning behaviour of the strain gauges. After dismantling the strain gauge of 1 of the bolts, no irregularities were found with the adhesive or strain gauge. Table 4.7.3 summarizes the obtained Young’s Modulus of bolt 1L.

Young’s modulus M16x110 instrumented bolts					
		1L	2L	3L	4L
E_b	[N/mm ²]	187088	-	-	-

Table 4.7.3: Young’s modulus M16x110mm (#L) instrumented bolts

4.7.3 Strain gauge relaxation experiment 5 ($P \approx 32 \text{ kN} = 0.34F_p$)

The 4 functioning strain gauges are used in a relaxation experiment with an initial preload force of approximately $0.36F_p$. The M16x110 mm bolt is used parallel with a Load Cell to be able to compare the results of both measuring methods. The samples are composed of the plates illustrated in figure 4.3.11 and an identical joint is created. The surfaces are grit blasted with an average surface roughness of $R_a = 15.532 \mu\text{m}$ (table 4.3.4). The samples contain a combination of the following bolts:

- Sample 3: 1L (also monitored with LC 3) + 1S
- Sample 5: 3S + 4S

Sample 4 contains uncalibrated bolt 2S and bolt 2L applied with a Load Cell. The results of the Load Cell of sample 4 are discussed in 4.6.3. As mentioned earlier, bolt 1L is tested well into the plastic range to be able to analyze the non-linear behaviour. However, as concluded in section 2.3.4, retightening does not have a significant impact on the relaxation behaviour. The results of bolt 1L should therefore be comparable with the results found in the 75 mm bolts. Using the experimentally derived Young's moduli of the strain gauge – bolt combinations, the preload force is applied by introducing a specific amount of strain. The bolt threads are lubricated using HY52 Special Lubrication Paste White and a Nyloc-nut is used. The samples are stored in a conditioned lab with a constant temperature of 19.5°C and a constant relative humidity of 60%. Continuous monitoring is possible by attaching the strain gauges with a monitoring system. The experimental setup is shown in figure 4.7.19.



Figure 4.7.19: Test setup relaxation experiment instrumented bolts

Figure 4.7.19 shows the storage of 5 samples since relaxation experiment 4 is performed simultaneously with the relaxation experiment discussed in this topic. Since the bolts are loaded within the elastic branch of the stress-strain behaviour, the decreasing preload force due to relaxation/plate creep/embedment creep can be estimated with the experimentally determined Young's moduli summarized in table 4.7.2 and table 4.7.3. Possible occurring creep of the adhesive is not taking account. The preload losses of the successfully calibrated bolts are presented in figure 4.7.20. The output from the model without embedment creep is added as well as the output from the model with modified parameters ($t_{\text{assembly}} = 10\text{s}$ and $\Delta P_{\text{em}} = 3.5 \text{ kN}$).

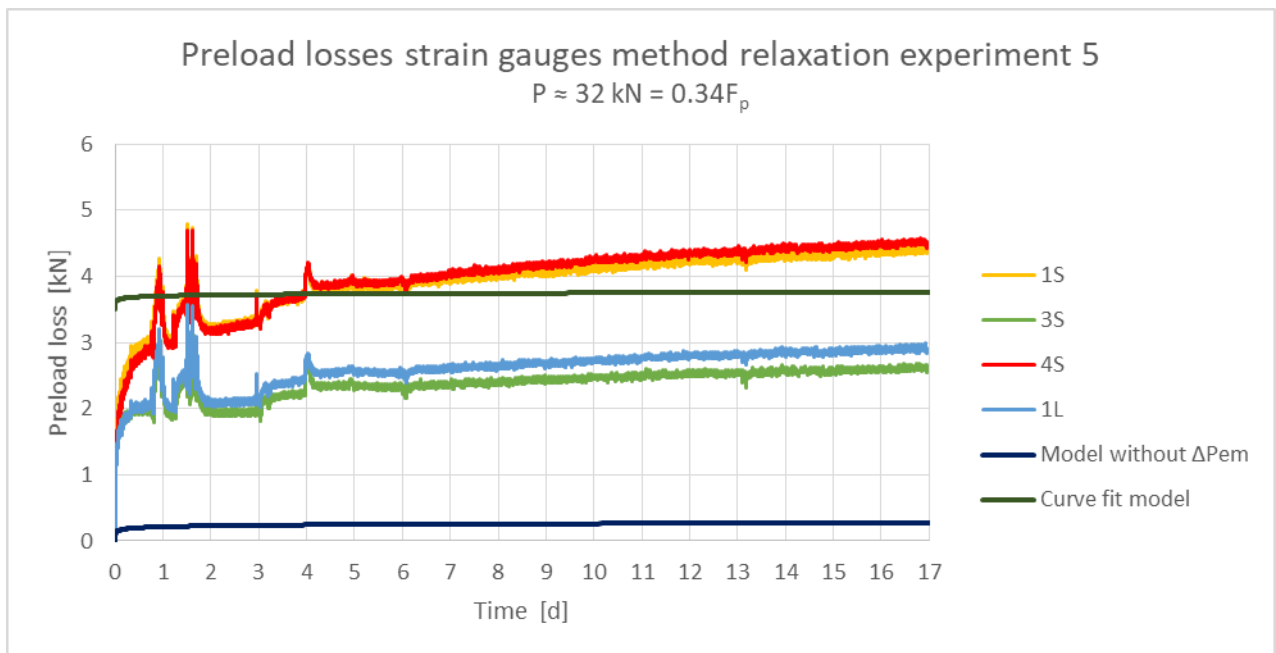


Figure 4.7.20: Preload losses experiment 5 measured with strain gauges versus output model $P \approx 0.34F_p$

The strain gauges used in this experiment are not temperature compensated. The extreme deviations found 1-2 days after starting the test are caused by an insufficient conditioning of the temperature resulting in deviating results. Figure 4.3.21 presents the temperature of the conditioned lab indicating the unstable temperature.

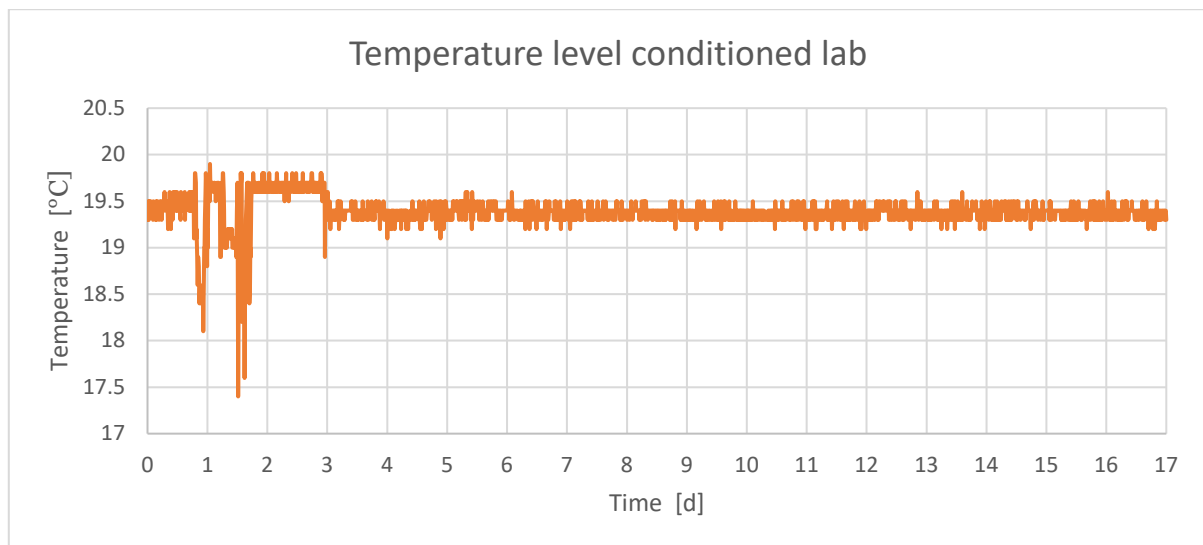


Figure 4.7.21: Temperature level conditioned lab

The experiments show significant deviations compared to the model without embedment creep which is comparable to the results of relaxation experiment 3 in section 4.6.3. Using the modified parameters, the model is able to give a rough estimation of the preload losses. The model predicts a more or less preload level, while the experimental data exhibit an increasing preload losses. Next to inaccuracy of the model, the discrepancies could be explained with creep of the adhesive.

Bolt 1S and 4S exhibit comparable preload losses. The preload losses of bolt 1L and bolt 3S are comparable as well. The differences between both bolt sets can not be explained. All 4 bolts received a similar tightening procedure. As mentioned in section 4.7.2, bolt 1L was tested well into the plastic branch. As expected, retightening of the bolt has no influence on the preload behaviour.

4.7.4 Comparison Load Cell method with Strain Gauge method

Bolt 1L is monitored with both a strain gauge and a strain gauge. A comparison between both measuring methods is presented in figure 4.7.22. The Load Cell method and Strain Gauge method show comparable results. The Load Cell rounds off the measured data to the nearest value, leading to underestimation of the preload losses after 4 days.

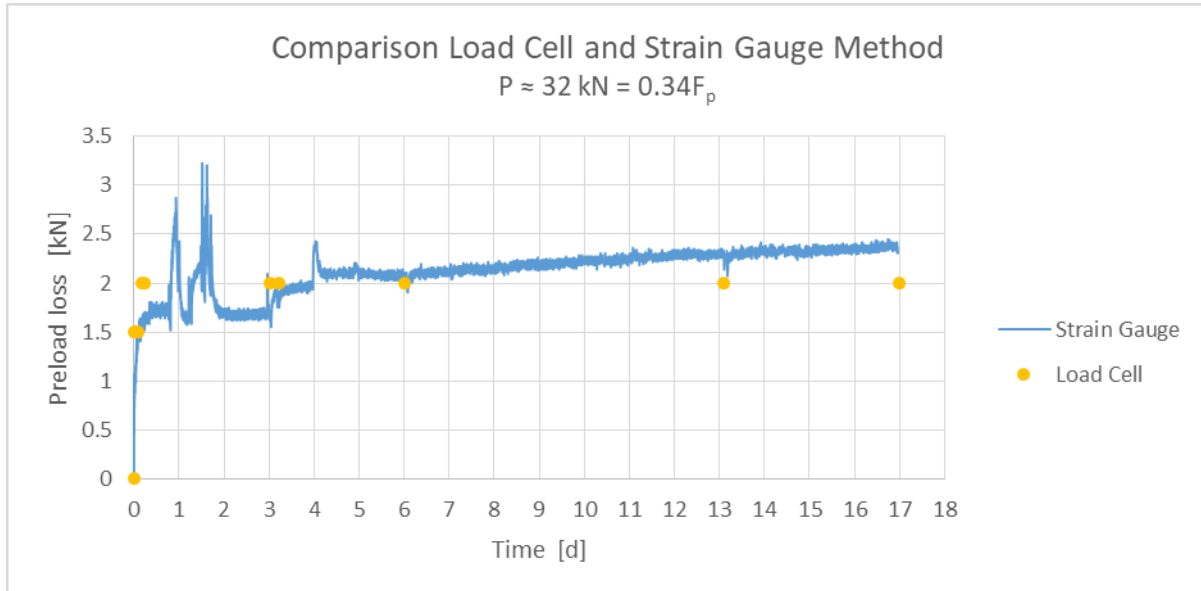


Figure 4.7.22: Comparison between Load Cell Method and Strain Gauge Method

4.8 Tensile test introducing poisson's effect

After finishing relaxation experiment 3, 4 and 5, the samples are analyzed in a tensile test to obtain the preload behaviour under influence of poisson's effect. The initial preload level of each sample at the start of the tensile test is therefore equal to the preload level at the end of the relaxation experiments. The samples are clamped at both free ends as visualized in figure 4.8.1 and equipped with an LVDT sensor at either side to be able to monitor the slip between the main plate and cover plates. Figure 4.8.1 shows that the strain gauge of the short bolts is located within the shear plane. Validity of the output of the strain gauges of the short bolts can therefore not be guaranteed if the bolt is subjected to shear which occurs once slip is noticed. Determination of the slip is therefore relevant in the application of bolts with strain gauges. During the tensile test, the load is gradually increased with 0.15 kN/s which corresponds to a stress rate of 0.1 MPa/s determined at the gross cross section of the center plate ($A = 1500 \text{ mm}^2$).

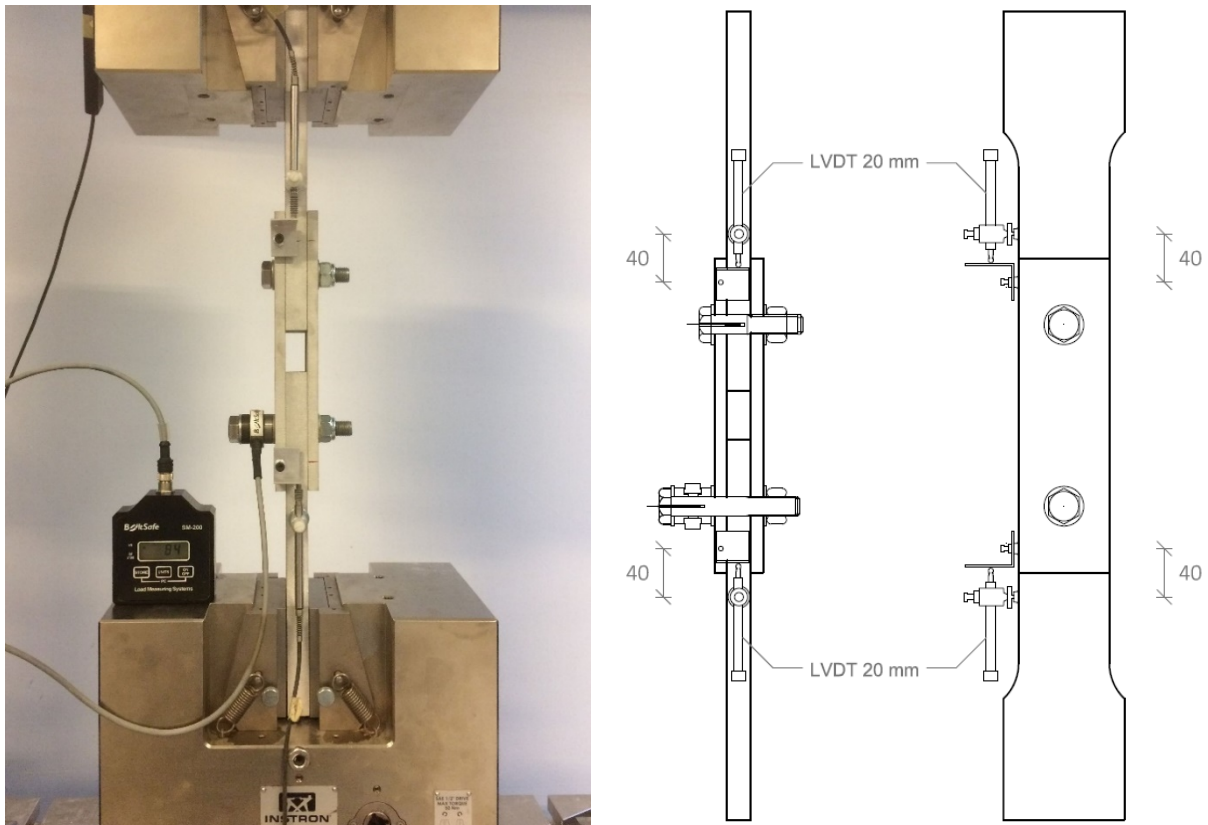


Figure 4.8.1: Test setup poisson test (left) and side views sample equipped with LVDT sensors (right)

To be able to gain insight into the forces corresponding to the failure modes of the sample, the following resistances are determined following NEN-EN 1999-1-1 and NEN-EN 1993-1-1:

- $N_{o,Rd}$ Yield resistance gross cross section plate(s)
- $N_{u,Rd}$ Tensile resistance netto cross section plate(s) at bolt hole
- $F_{b,Rd}$ Bearing resistance plate(s)
- $F_{v,Rd}$ Shear resistance bolt

Since the samples are tested experimentally, the partial safety factors γ_{M1} and γ_{M2} are ignored and assumed to be 1.0. The yield strength of the 20 mm center plate is equal to:

$$N_{o,Rd} = \frac{A_g f_o}{\gamma_{M1}} \rightarrow N_{o,Rd} = \frac{75 \cdot 20 \cdot 125}{1.0} \triangleq 187.5 \text{ kN} \quad (4.14)$$

With:

- A_g : Gross cross section plate
 f_o : Proof strength plate material

The cumulative yield strength of the 10 mm side plates is equal to the yield strength of the 20 mm center plate:

$$N_{o,Rd} = 2 \cdot \frac{75 \cdot 10 \cdot 125}{1.0} \hat{=} 187.5 \text{ kN} \quad (4.15)$$

According to NEN-EN 1999-1-1, the tensile resistance of the net section of the 20 mm plate at the bolt hole is equal to:

$$N_{u,Rd} = \frac{0.9 A_{net} f_u}{\gamma_{M2}} \rightarrow N_{u,Rd} = \frac{0.9 \cdot (75 - 17) \cdot 20 \cdot 275}{1.0} \hat{=} 287.1 \text{ kN} \quad (4.16)$$

With:

- A_{net} : Net section plate at bolt hole
 f_u : Tensile strength plate material

Comparable with the determination of the yield strength, the cumulative tensile strength of the 10 mm cover plates is equal to the tensile strength of the 20 mm center plate:

$$N_{u,Rd} = 2 \cdot \frac{0.9 \cdot (75 - 17) \cdot 10 \cdot 275}{1.0} \hat{=} 287.1 \text{ kN} \quad (4.17)$$

The bearing resistance of the 20 mm plate and cumulative bearing resistance of the cover plates are equal and can be determined with:

$$F_{b,Rd} = \frac{k_1 \alpha_b f_u d t}{\gamma_{M2}} \rightarrow F_{b,Rd} = \frac{2.5 \cdot 1.0 \cdot 275 \cdot 16 \cdot 20}{1.0} \hat{=} 220.0 \text{ kN} \quad (4.18)$$

With:

- d : diameter bolt
 f_u : tensile strength plate material
 t : thickness plate

Where:

$$k_1 = \min \left(2.8 \frac{e_2}{d_0} - 1.7 ; 2.5 \right) = \min \left(2.8 \cdot \frac{37.5}{17} - 1.7 = 4.48 ; 2.5 \right) = 2.5 \quad (4.19)$$

$$\alpha_b = \min \left(\frac{e_1}{3d_0} ; \frac{f_{ub}}{f_u} ; 1.0 \right) = \min \left(\frac{55}{3 \cdot 17} = 1.08 ; \frac{800}{275} = 2.91 ; 1.0 \right) = 1.0 \quad (4.20)$$

With:

- d_0 : diameter bolt hole
 f_{ub} : tensile strength bolt material
 e_1 : edge distance bolt hole parallel with loading direction (55 mm)
 e_2 : edge distance bolt hole perpendicular to loading direction (37.5 mm)

The shear resistance of the bolt can be divided into a shear area in the unthreaded and threaded shaft. Since the bolts are equipped with a 2 mm hole for the strain gauge, the section will be reduced. The shear resistance of the unthreaded shaft $F_{v,Rd,d}$ and threaded shaft $F_{v,Rd,t}$ are equal to:

$$F_{v,Rd,d} = \frac{\alpha_v f_{ub} A_d}{\gamma_{M2}} \rightarrow F_{v,Rd,d} = \frac{0.6 \cdot 800 \cdot (201 - \pi \cdot 1^2)}{1.0} \triangleq 95.0 \text{ kN} \quad (4.21)$$

$$F_{v,Rd,t} = \frac{\alpha_v f_{ub} A_t}{\gamma_{M2}} \rightarrow F_{v,Rd,t} = \frac{0.5 \cdot 800 \cdot 157}{1.0} \triangleq 62.8 \text{ kN} \quad (4.22)$$

With:

A_d : nominal cross section unthreaded part

A_t : reduced-shank cross section

Since a double shear joint is considered, 2 shear planes are present. The cumulative shear resistance is derived by considering the weakest possible shear resistance:

$$F_{v,Rd} = 2 \cdot F_{v,Rd,t} = 2 \cdot 62.8 = 125.6 \text{ kN} \quad (4.23)$$

Shear failure of the bolt appears to be dominant in this sample. Depending on the deformation capacity of the bolt, a sudden failure of the bolt can be expected.

The theoretical slip resistance is determined with the formula adopted in NEN-EN-1999-1-1:

$$F_{slip,Rd} = \frac{n\mu}{\gamma_{Ms}} P_0 \quad (4.24)$$

With:

P_0 : design preloading force

$F_{slip,Rd}$: design slip resistance

n : number of friction surfaces

γ_{Ms} : partial safety factor for a slip resistant bolt

μ : slip factor

According to NEN-EN-1999-1-1, a friction coefficient $\mu = 0.40$ can be applied if the plates are grit-blasted and $\sum t \geq 30$ mm. The partial safety factor γ_{Ms} is equal to 1.1 or 1.25, depending if slip is allowed in the Serviceability Limit State (SLS) or Ultimate Limit State (ULS). As mentioned before, the initial preload force P_0 at the start of the tensile test is identical to the preload level noticed at the end of relaxation experiment 3, 4 and 5. The theoretical remote stress at slip corresponding to the slip load found in equation 4.24 is equal to:

$$\sigma_{//,s} = \frac{F_{slip}}{A_g} = \frac{F_{slip}}{75 \cdot 20} \quad (4.25)$$

With:

$\sigma_{//,s}$: remote stress at slip

It should be noted that equations 4.24 and 4.25 do not consider the decreasing preload force as a result of poisson's effect. However, the theoretical slip factor μ is a safe approximation of the real friction coefficient. Underestimating the slip factor will therefore counterbalance the overestimated slip load, leading to a safe approximation of the slip load and remote stresses at slip.

4.8.1 Tensile test M16x75 monitored with Load Cell

After concluding relaxation experiment 3, sample 3 and 4 (monitored with Load Cell 3 and 4) are subjected to a tensile force as demonstrated in figure 4.8.1. The preload level after relaxation is defined as P_0 and is equal to 34 kN and 30 kN ($\approx 0.32F_p$). The preload behaviour of sample 3 and 4 is presented in figure 4.8.2. The tensile load and accompanying remote stress in the sample is determined at the gross cross section of the center plate ($A = 1500 \text{ mm}^2$) and normalized with respect to the proof stress of the plate. Using the Poisson model created in 3.8, theoretical preload behaviour is added by using $\mu = 0.4$ (friction coefficient described in NEN-EN-1999-1-1). Table 4.8.1 presents the theoretical slip load, remote stress at slip and normalized remote stress at slip, determined using an average initial preload force of 32 kN, slip factor $\mu = 0.4$ and nominal proof stress $f_{0.2} = 125 \text{ N/mm}^2$.

Slip loads and (normalized) remote stresses				
		$\gamma = 1.0$	$\gamma = 1.1$ (SLS)	$\gamma = 1.25$ (ULS)
$F_{\text{slip,Rd}}$	[kN]	25.6	23.3	20.5
$\sigma_{//,s}$	[N/mm ²]	17.1	15.5	13.7
$\sigma_{//,s} / f_{0.2}$	[-]	0.137	0.124	0.109

Table 4.8.1: Slip load and (normalized) remote stresses with $P_0 = 32 \text{ kN}$

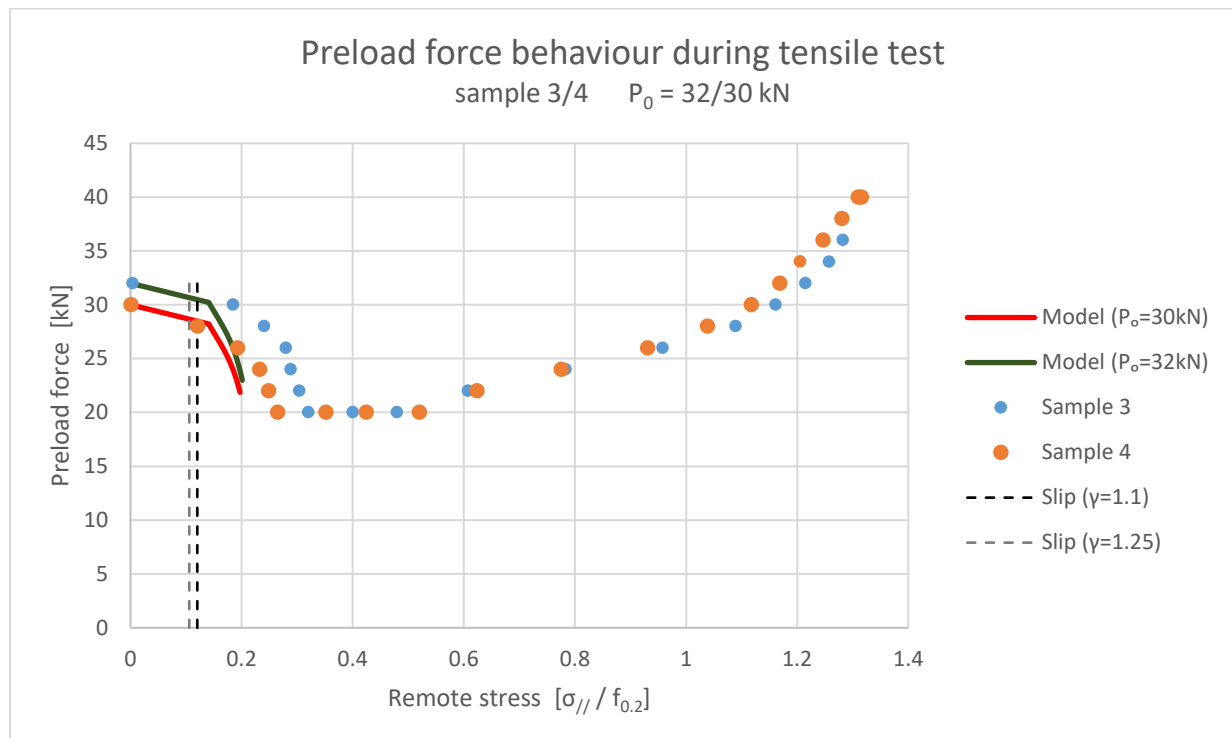


Figure 4.8.2: Experimental preload behaviour sample 3 / 4 versus output model

During the analysis of section 3.8.3, the poisson model was able to fit the experimental data if low remote stresses were considered. The theoretical preload behaviour matches the experimental data well at the low stress regime. Adopting a slip factor of 0.4 will lead to conservative results. As expected, the slip factor $\mu = 0.4$ recommended by NEN-EN-1999-1-1 is a safe approximation of the real friction coefficient. Respecting the design slip resistance in SLS ($\gamma = 1.1$) and ULS ($\gamma = 1.25$) described in NEN-EN-1999-1-1 will prevent the occurrence of slip as can be observed in figure 4.8.2.

4.8.2 Tensile test M16x110 monitored with Load Cell

After concluding relaxation experiment 4, sample 1 and 2 are subjected to a tensile force. An additional ‘sample 0’ was added with an initial preload force $P_0 = 82 \text{ kN}$ ($0.87F_p$) monitored by Load Cell 3. The results of testing sample 0 (LC3), sample 1 (LC1) and sample 2 (LC2) are presented in figure 4.8.3. Using the Poisson model created in 3.8, theoretical preload behaviour is added by using $\mu = 0.4$. Table 4.8.2 presents the theoretical slip load, remote stress at slip and normalized remote stress at slip, determined using an average initial preload force of 79.3 kN , slip factor $\mu = 0.4$ and nominal proof stress $f_{0.2} = 125 \text{ N/mm}^2$.

		$\gamma = 1.0$	$\gamma = 1.1$ (SLS)	$\gamma = 1.25$ (ULS)
$F_{\text{slip,Rd}}$	[kN]	63.5	57.7	50.8
$\sigma_{//,s}$	[N/mm ²]	42.3	38.5	33.8
$\sigma_{//,s} / f_{0.2}$	[-]	0.338	0.308	0.271

Table 4.8.2: Slip load and (normalized) remote stresses with $P_0 = 79.3 \text{ kN}$

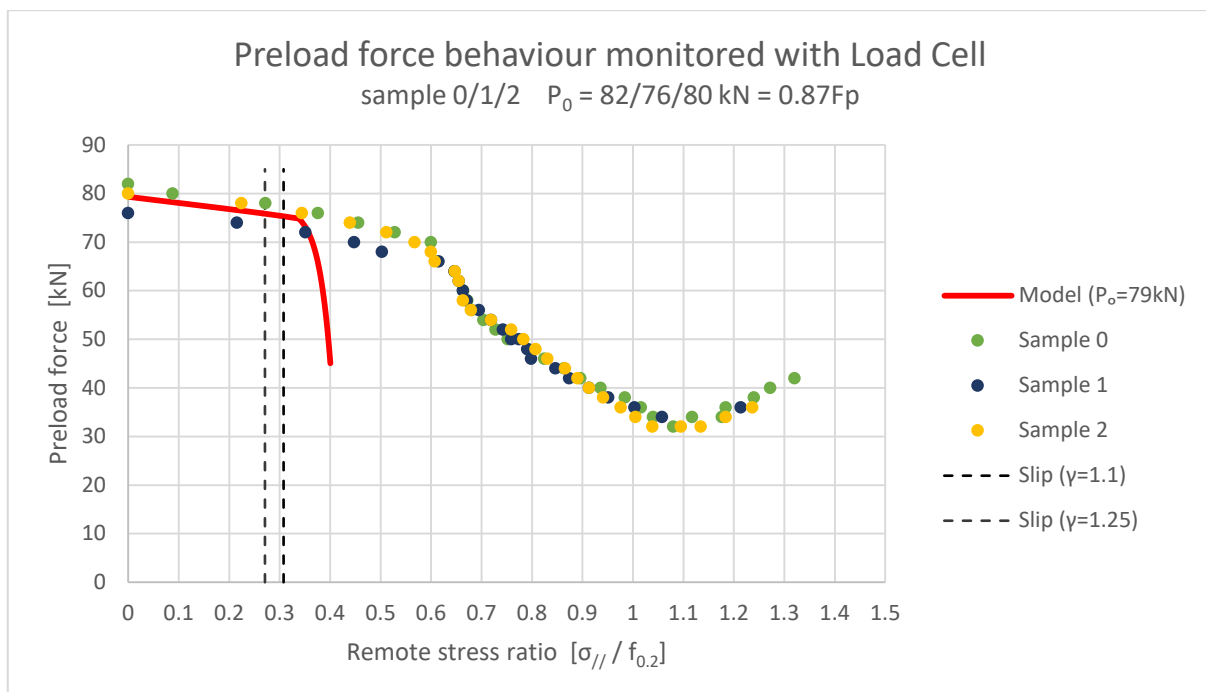


Figure 4.8.3: Experimental preload behaviour sample 0, 1 and 2 versus output model

Again, the theoretical preload behaviour fits the experimental data well at the low stress regime. Adopting a slip factor of 0.4 will lead to conservative results. Furthermore, the design slip resistance is able to give a safe approximation of the slip load. Bolt bending and prying introduce an ascending effect with remote stress ratios exceeding 1.1. Comparable with the results of sample 3 and 4, the shape of the preload behaviour curve deviates from the behaviour found by Chakherlou.

A possible explanation for the deviating behaviour is the relatively low proof stress of 50830 leading to earlier local yielding as compared to 2024T3. Possibly, bolt bending and prying dominated over local yielding in Chakherlou’s experiments due to the low initial preload force, resulting in an ascending preload force behaviour. Furthermore, Chakherlou used a bolt hole almost identical to the bolt diameter (clearance 0.1 mm), affecting the amount of slip that could occur.

4.8.3 Tensile test M16x75 monitored with Strain Gauge

The strain gauges installed in the bolts of sample 3 and 5 are used to continuously monitor the preload behaviour. The bolts corresponding to sample 3 are 1 bolt M16x110 (1L) and 1 bolt M16x75 (1S). Sample 5 contains 2 bolts M16x75 (3S + 4S). As mentioned previously, the strain gauge of the instrumented M16x75 bolts is located within a shear plane. The validity of the strain gauges can only be guaranteed if the load is transferred via friction of the plates instead of bearing via the bolt. The analysis will therefore include a tensile force – deformation graph obtained from the LVDT sensors to identify the occurrence of slip and accompanying transition of friction to bearing. Since the preload behaviour is presented with a remote stress – proof stress ratio, the tensile force is defined as remote stress at the gross cross section of the center plate ($A = 1500 \text{ mm}^2$) and normalized with respect to the proof stress of the plate. The average preload level of bolts 1S, 3S and 4S after relaxation is equal to $P_0 = 32.5 \text{ kN}$ ($\approx 0.35F_p$). Table 4.8.3 presents the theoretical slip load and (normalized) remote stress at slip, determined using an initial preload force of 32.5 kN , $\mu = 0.4$ and $f_{0.2} = 125 \text{ N/mm}^2$.

		Slip loads and (normalized) remote stresses		
		$\gamma = 1.0$	$\gamma = 1.1$ (SLS)	$\gamma = 1.25$ (ULS)
$F_{\text{slip,Rd}}$	[kN]	26.0	23.6	20.8
$\sigma_{//,s}$	[N/mm ²]	17.3	15.8	13.9
$\sigma_{//,s} / f_{0.2}$	[-]	0.139	0.126	0.111

Table 4.8.3: Slip load and (normalized) remote stresses with $P_0 = 32.5 \text{ kN}$

The total slip behaviour of bolts 1S, 3S and 4S is presented in figure 4.8.4. Detailed slip behaviour of the first phase is presented in figure 4.8.5. The slip loads corresponding to SLS and ULS are added to indicate theoretical slip. According to figure 4.8.5, substantial slip occurs at a remote stress ratio of 0.22 - 0.25 which corresponds to a tensile force of approximately 44 kN . After slip has occurred, the deformation increases gradually and bearing of the plate becomes dominant until shear failure of the bolt introduces failure of the joint.

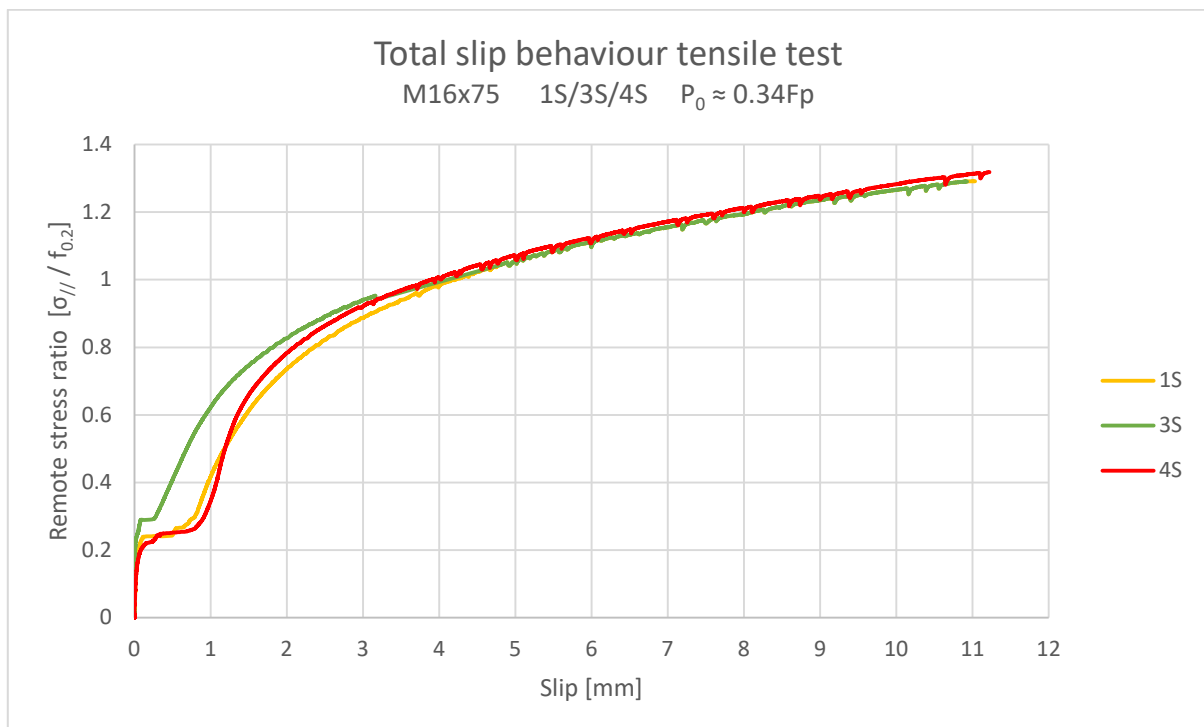


Figure 4.8.4: Total slip behaviour tensile test with bolts 1S, 3S, 4S; $P_0 = 32.5 \text{ kN} \approx 0.34F_p$

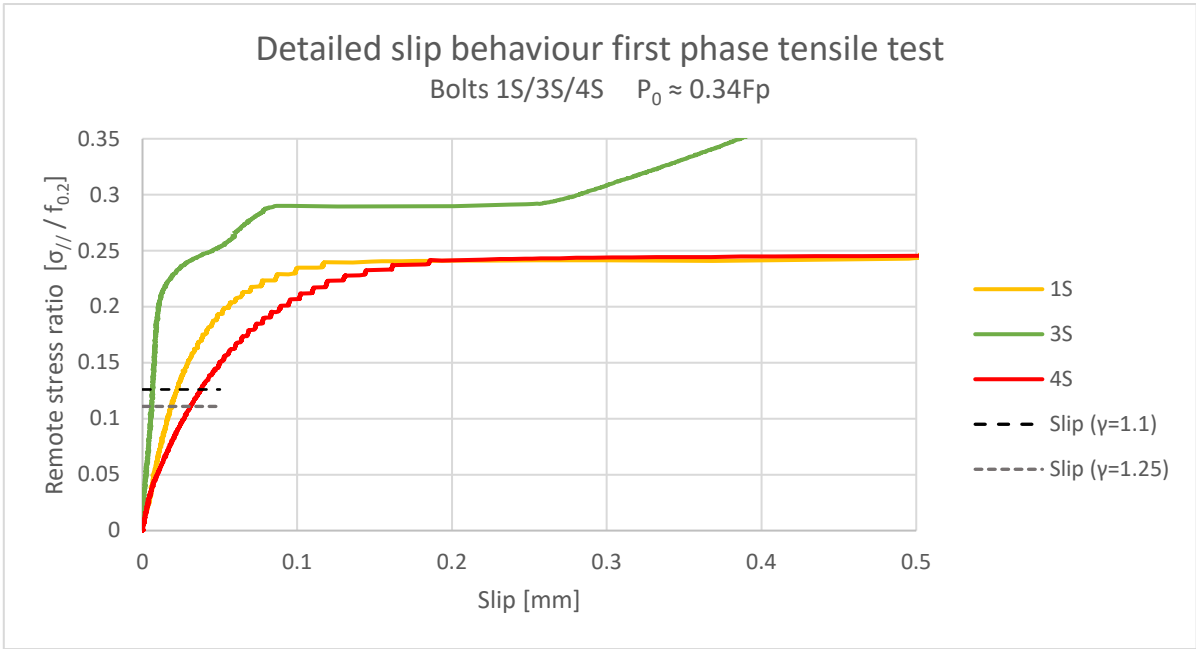


Figure 4.8.5: Detailed slip behaviour first phase tensile test with bolts 1S, 3S, 4S; $P_0 = 32.5 \text{ kN} \approx 0.34F_p$

The output from the strain gauge and accompanying preload behaviour up to a remote stress ratio of 0.4 is presented in figure 4.8.6. Theoretical preload behaviour is added by using $\mu = 0.4$.

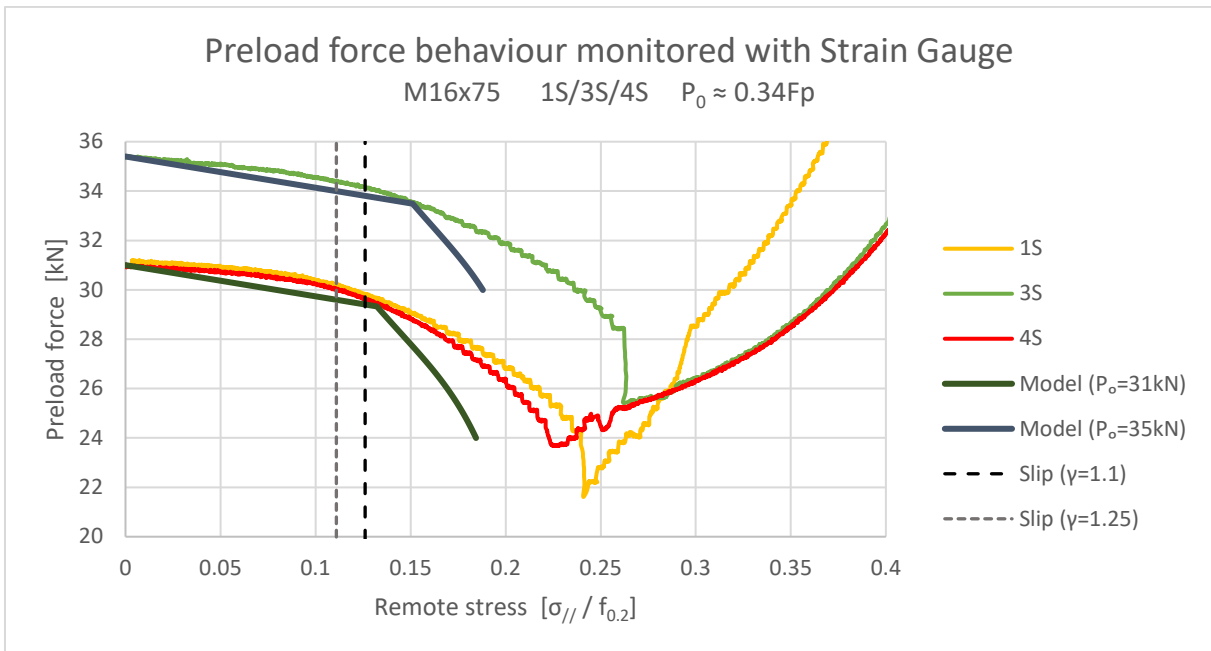


Figure 4.8.6: Experimental preload behaviour bolts 1S, 3S and 4S versus output model

Comparable with the results found with the Load Cells, the preload force of the instrumented M16x75 bolts follow a descending behaviour with increasing remote stresses until bolt bending and prying does occur. The model seems valid up to a remote stress ratio of 0.125. The model does give a conservative output if $\mu = 0.4$ is used. Furthermore, the design slip resistance determined with NEN-EN-1999-1-1 gives a safe approximation of the slip load.

4.8.4 Tensile test M16x110 monitored with Strain Gauge

Bolt 1L has an original length of 110 mm and is applied in sample 3. Bolt 1L is monitored with a Load Cell and a strain gauge providing the possibility to compare the results. The required extra length for installation of the Load Cell gives the possibility to locate the strain gauge outside the shear area as indicated in figure 4.8.10. Therefore, the strain gauge should not be influenced by bearing after slip has occurred extending the range of validity. Since the bolt is calibrated up to 75 kN, the preload levels exceeding 75 kN are disregarded. The total slip behaviour of bolt 1L and a detailed slip behaviour of the first phase are presented in figure 4.8.7 and 4.8.8. Substantial slip occurs at a remote stress ratio 0.27 which corresponds to a tensile force of 51 kN. The average preload level of bolt 1L after relaxation is equal to $P_0 = 30.4 \text{ kN}$ ($\approx 0.32F_p$). Table 4.8.4 presents the theoretical slip load and (normalized) remote stress at slip, determined using an initial preload force of 30.4 kN, $\mu = 0.4$ and $f_{0.2} = 125 \text{ N/mm}^2$.

		Slip loads and (normalized) remote stresses		
		$\gamma = 1.0$	$\gamma = 1.1$ (SLS)	$\gamma = 1.25$ (ULS)
$F_{\text{slip,Rd}}$	[kN]	24.3	22.1	19.5
$\sigma_{//,s}$	[N/mm ²]	16.2	14.7	13.0
$\sigma_{//,s} / f_{0.2}$	[-]	0.130	0.118	0.104

Table 4.8.4: Slip load and (normalized) remote stresses with $P_0 = 30.4 \text{ kN}$

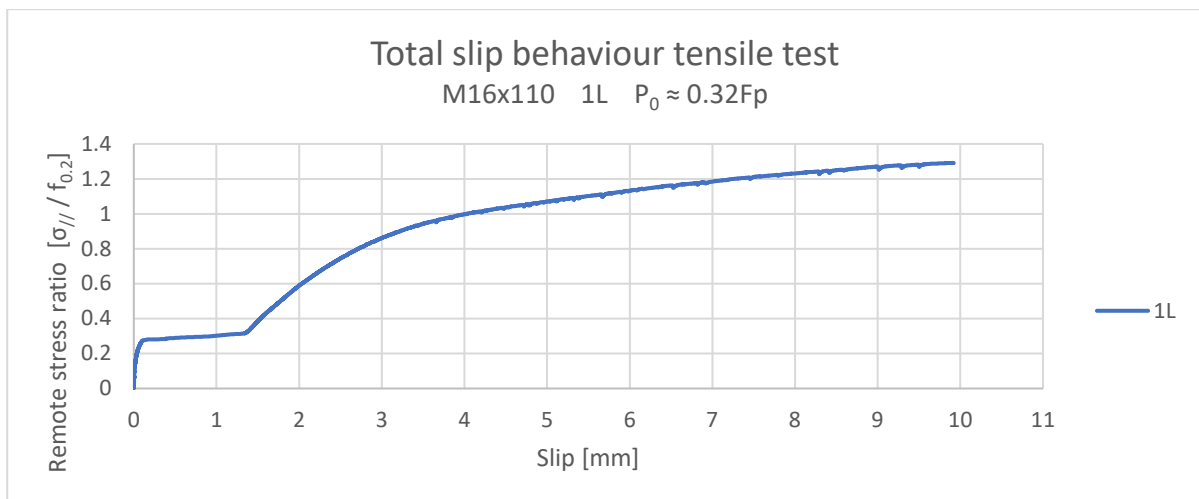


Figure 4.8.7: Total slip behaviour tensile test bolt 1L; $P_0 = 30.4 \text{ kN} \approx 0.32F_p$

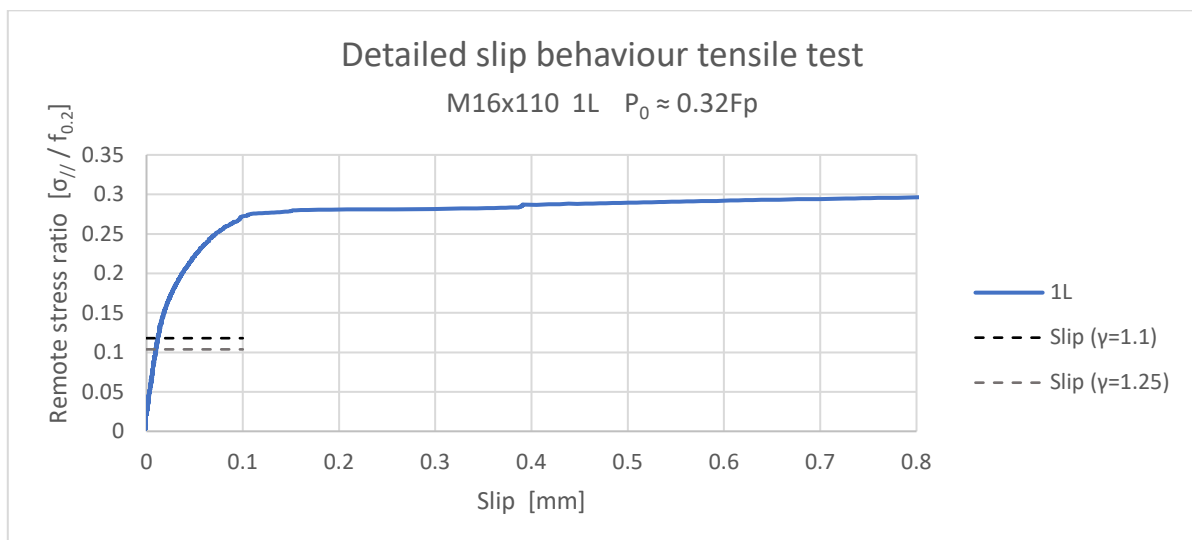


Figure 4.8.8: Detailed slip behaviour tensile test bolt 1L; $P_0 = 30.4 \text{ kN} \approx 0.32F_p$

The output from the strain gauge and accompanying preload behaviour is presented in figure 4.8.9 and figure 4.8.10. Theoretical preload behaviour is added by using $\mu = 0.4$.

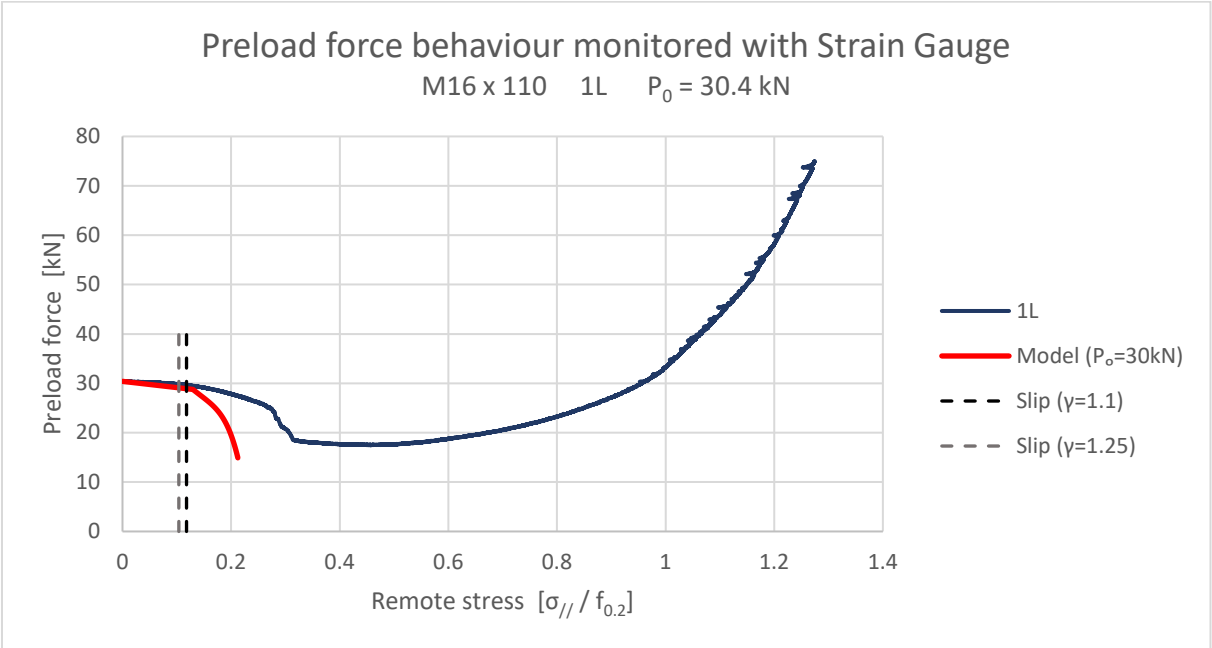


Figure 4.8.9: Experimental preload behaviour bolt 1L versus output model

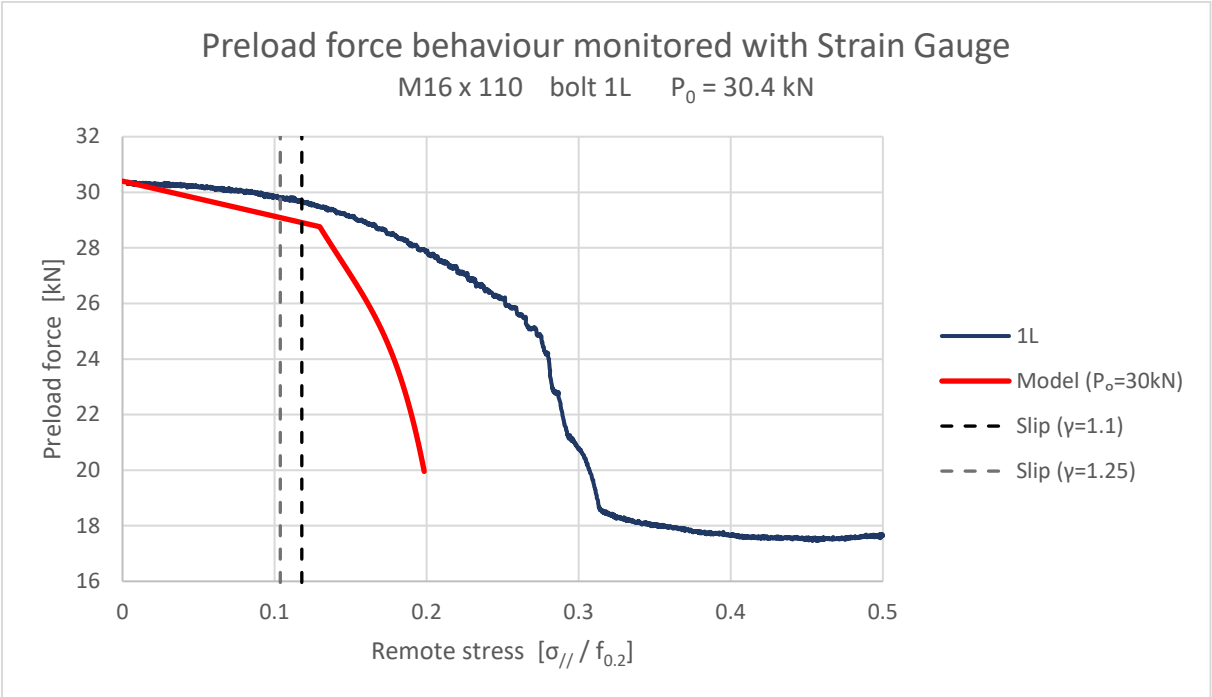


Figure 4.8.10: Detailed experimental preload behaviour bolt 1L versus output model

The addition of the load cell and increased length of the bolt seems to influence the amount of preload losses since the preload behaviour of bolt 1L prior to slip behaves more stiff compared to bolts 1S, 3S and 4S. The preload level of bolt 1L stabilizes after a remote stress ratio of 0.35 is reached. The theoretical model output gives a conservative prediction of the experimental behaviour of all 4 considered bolts and can therefore be considered to give a safe approximation of the preload level.

As mentioned before, bolt 1L is monitored with a Load Cell and a strain gauge providing the possibility to compare the results. The output of Load Cell 3 derived in section 4.8.1 and the preload behaviour monitored with the strain gauge are compared in figure 4.8.11.

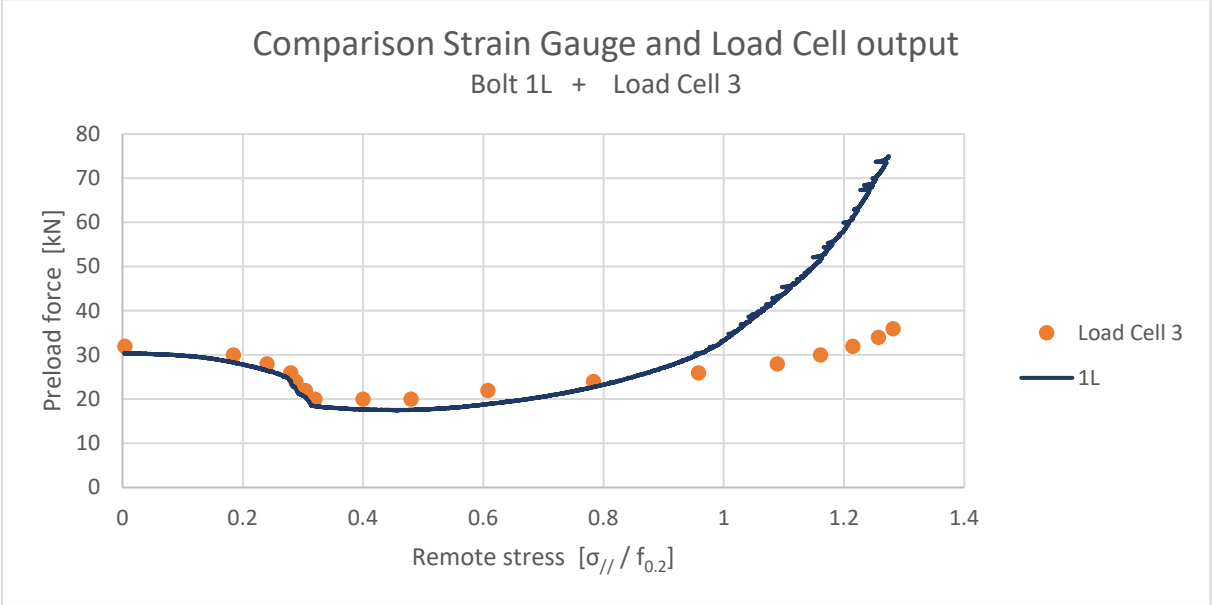


Figure 4.8.11: Comparison between output Strain Gauge Method and Load Cell Method

The output from the Strain Gauge and Load Cell compare well up to a remote stress ratio of 0.8. The deviations at a relative stress level exceeding 0.9 is attributed to bonding of the bolt. The discrepancies can also indicate that either the strain gauge is not perfectly centered in the bolt shaft resulting in deviations once the bolt has bended or that the Load Cell is not able to measure the preload force accurately if the bolt has bended.

4.9 Summary and conclusions experimental verification

The torque method can be applied once a relationship has been discovered between applied torque and preload force. Within the relationship, a coefficient of friction relates the bolt diameter and applied torque to the preload force. Testing of A4 80 M16x110 and M20x100 bolts with various lubrication types give comparable results with respect to the coefficient of friction. Application of lubrication will reduce the coefficient of friction and will therefore reduce the amount of torque for the required preload level.

The model output is validated during relaxation experiments with A4 80 M16x110 and M16x75 bolts combined with 5083 O/H111 plates with as-delivered and grit-blasted surfaces. Various joint types and initial preload levels are regarded to be able to compare the model in practical situations. The tests are performed in a conditioned lab with a constant temperature of 20°C (and a constant relative humidity of 60%) to exclude the impact of thermal variations. The preload force is monitored by either a Load Cell or a Strain Gauge installed in the shank of the bolt or a combination of both load measuring systems. Since the Load Cell can only be read out manually, continuous monitoring is not possible. The strain gauges, however, are able to monitor the preload force continuously. It is observed that the output from the relaxation model has a high sensitivity with respect to the assumed starting point (t_{assembly} or initial time) of the theoretical preload loss behaviour. An initial curve fit was generated by excluding the first 3 seconds after tightening ($t_{\text{assembly}} = 3\text{s}$). With addition of embedment creep, a conservative model output is observed. An accurate or less conservative output is generated if $t_{\text{assembly}} = 10\text{s}$ and $\Delta P_{\text{em}} = 3.5\text{ kN}$ is used. Application of grit-blasting does not have a negative impact on the preload loss behaviour due to relaxation. Furthermore, the applied lubrication type does not influence the preload loss behaviour. A combination of both the Load Cell Method and the Strain Gauge method exhibit comparable preload loss behaviour indicating that both methods can be applied to monitor preload forces.

During the creation of the model regarding plate creep, the creep behaviour of 5454O and 5083O is assumed to be identical. Compressive tests with a duration of 6-22 hours are performed on both grit-blasted and as-delivered plates. The majority of the creep occurs within the first 2 hours after applying the compressive force and increases gradually over time. Blasted surfaces deform more during loading due to settling compared to an as-delivered surface. On the other hand, the total amount of creep and amount of strain needed to reach a compressive stress of 241 MPa is less in the case of blasted surfaces than of as-delivered surfaces. A possible explanation for this phenomenon is that grit-blasting has a hardening effect on the physical properties. The model based on creep data of 5454O predicts the creep behaviour of 5083O/H111 relatively well, indicating that a comparison regarding creep behaviour of 5454O and 5083O/H111 is valid.

A double lap joint is used in a tensile test to identify the preload behaviour with respect to the poisson's effect. Two preload levels are regarded and monitored by either a Load Cell or a Strain Gauge installed in the shank of the bolt or a combination of both load measuring systems. The experimentally derived preload behaviour does not match the behaviour described in literature. A possible explanation for the deviating behaviour is the relatively soft material behaviour of 5083O, introducing larger perpendicular contraction compared to 2024T3. A combination of both the Load Cell Method and the Strain Gauge method exhibit comparable preload loss behaviour up to a remote stress ratio of 0.8. Bolt bending could have an influence on the output of both methods explaining the occurring deviations with higher remote stress ratios. The output from the model matches the real preload behaviour well up to slip, but does overestimate the preload losses after slip since bolt bending and prying are not taken into account.

5 Conclusions and Recommendations

5.1 Major conclusions

This master thesis focused on the determination of the qualitative and quantitative consequences of the time-dependent and time-independent effects on the preload force in a bolted assembly. The major topics are considered with a combination of research conducted in the past, calculations, and/or experiments. The preload variation calculations are performed by implementing deformations introduced by time-dependent and time-independent effects into an analytical spring model.

Creep effects are present in all bolted assemblies if preload forces are applied. According to literature, carbon steel bolted assemblies show minimal creep effects, while aluminium joints combined with stainless steel fasteners are susceptible to creep/relaxation behaviour. Distinctions can be made regarding the proof stress of aluminium alloys. At a given absolute stress, alloys with high proof stresses are less susceptible to creep compared to alloys with lower proof stresses for a given stress. Stainless steel exhibits increasing stress relaxation behaviour with increasing preload forces.

The model output exhibits a high sensitivity with respect to the assumed time of assembly. Taking into account the recommended values for embedment creep, the relaxation and plate creep model with $t_{\text{assembly}} = 3\text{s}$ does overestimate the preload losses in all cases. With modified parameters including an initial time of the relaxation behaviour $t_{\text{assembly}} = 10\text{s}$ and an approximate amount of embedment creep $\Delta P_{\text{em}} = 3.5\text{ kN}$, the spring model is able to give an accurate or conservative prediction of the relaxation behaviour. The discrepancies can be explained with overestimation of the expected amount of embedment deformation and inaccuracies of the model regarding the defined creep strain rate – stress relationship of aluminium and stainless steel, the assumed time of assembly and definition of the stressed areas within the bolted assembly.

Temperature variation will lead to preload variations if a bolted joint is composed of a hybrid material combination with deviating coefficients of linear expansion. Aluminium plates in combination with (stainless) steel fasteners are more susceptible to temperature variations compared to a combination of steel plates and (stainless) steel fasteners. A high initial preload force in the bolt is required to minimize the impact of temperature fluctuations.

Increasing a tensile load in a bolted shear joint will introduce contraction in the plates due to perpendicular strain introduced by Poisson's effect. The deformations around a bolt hole are amplified due to stress concentrations and the load transfer between bolt and plate. Slip and local yielding should be avoided to minimize the preload losses. Therefore, a high initial preload force should be applied. Preload losses due to Poisson's effect are higher in the case of aluminium than in the case of steel due to the lower Young's modulus and (in some alloys) lower proof strength. The spring model matches well with experimental preload behaviour prior to slip. Deviations exist after slip, since bolt bending and prying are not taken into account in the model.

Reviewing the impact of the initial preload force, it can be concluded that a high initial preload force is required to minimize embedment creep and thermal effects effectively. Furthermore, application of a high preload force will increase the slip-resistance of a joint, therefore decreasing the impact of Poisson's effect. A high initial preload force will introduce significant bolt relaxation and plate creep, but the relative preload losses of these effects are minor compared to the extreme relative losses of embedment creep and thermal variations if a low preload force is applied. Increasing the minimum total plate thickness – bolt diameter ratio ($\sum t/d$) will lead to decreasing preload losses in most of the considered aspects.

Application of a preload force equal to the nominal preload force P_{nom} , the maximum relative preload losses in a preloaded bolted joint with a total thickness – bolt diameter ratio of 3-4 ($3 < \sum t/d < 4$) are found to be equal to:

- Embedment creep: 15%
- Combined bolt relaxation and plate creep (50 years): 16%
- Thermal variations ($\Delta T = 45^\circ\text{C}$): 12%
- Poisson's effect (at slip): 19%

5.2 Design and service recommendations

To be able to guarantee the service life of a preloaded bolted connection, design and service recommendations are formulated. Already discussed in section 5.1, the application of a high initial preload force and respecting a minimum total thickness – bolt diameter ratio of 3 ($\sum t/d > 3$) will have a major impact on the preload level during service life. It is therefore recommended to consider both aspects early during the design phase. Furthermore, if shear joints are considered, it is recommended to satisfy the slip resistance in the Ultimate Limit State or Serviceability Limit State to minimize the impact of Poisson's effect. Slip-resistance can be assured by application of a high initial preload force (e.g. large bolt diameter while keeping $\sum t/d$ constant), roughening of the surface (e.g. grit-blasting) and increasing the amount of friction surfaces. The strength properties of the selected alloy type have a significant impact on the preload level. Sufficient strength properties are required to minimize local yielding around the bolt hole and to minimize plate creep. Selection of 6082T6 over 5083O is therefore recommended.

According to literature, retightening has minimal impact on the preload losses due to relaxation of stainless steel. However, retightening procedures are used to neutralize the preload losses introduced by elastic interactions. Retightening can also be applied to minimize the effects of embedment creep, thermal variations and Poisson's effect, if performed at appropriate stages during construction:

- Embedment creep can be neutralized by retightening due to leveling of the imperfections. It is recommended to apply retightening after a minimum of 3 days after tightening
- Preload losses due to thermal variations in the case that aluminium plates are applied (in combination with (stainless) steel fasteners) can be minimized when retightening occurs at the lowest temperature experienced during service life
- The preload losses due to Poisson's effect can be minimized if retightening is applied after the introduction of the (permanent) load

Concluding the recommendations, the preload losses due to relaxation and plate creep should be taken into account during the design phase to guarantee safe preload levels during service life. Assuming retightening occurs at appropriate stages during construction, the relative preload losses during service life of stainless bolts combined with aluminium plates are equal to 15.7%. Reviewing the definition of the nominal preload force in NEN-EN-1999-1-1, it is recommended to consider:

$$P_{nom} = 0.7(1 - 0.16) f_{ub} A_t = 0.59 f_{ub} A_t \quad (5.1)$$

With:

- A_t : reduced-shank cross section
- P_{nom} : nominal minimum preload force
- f_{ub} : tensile strength bolt

5.3 Future research recommendations

Concluding this master thesis, recommendations are given regarding the unknown and uncompleted areas that remain after this research. The model includes a spring model with linear behaviour. A more elaborate (FEM) model should be constructed to account for non-linear effects including material behaviour, parabolic stress distribution within the joint and stress concentrations around the bolt hole.

The creep behaviour of stainless steel fasteners and aluminium alloys should be determined for lower stress levels to verify the assumed creep parameter functions. Future research could also focus on the impact of grit-blasting on the material behaviour and amount of embedment creep.

The impact of poisson's effect should be further explored including surface finishing (as-delivered vs. grit-blasted surfaces), impact of the initial preload force, alloy choice (soft vs. stiff behaviour) and high levels of remote stresses to discover the impact of prying.

Adhesive bonded joints are known to have a more uniform stress and strain distribution as compared to bolted joints without preload force. Therefore, adhesive bonding could be included to analyze the applicability of (preloaded bolted-)adhesive bonded joints.

Finally, a Load Cell should be developed with a high accuracy and ability to monitor the preload force continuously. Ideally, the Load Cell should be able to identify the impact of bolt bending and prying to have insight in the validity of the output of the Load Cell.

6 Bibliography

- Afzali, Nariman, Johan Pilhagen, Erik Schedin, and Natalie Stranghöner. 2017. "Preload Losses in Stainless Steel Bolting Assemblies."
- Ahmad, M.I.M., J.L. Curiel Sosa, and J.A. Rongong. 2017. "Characterisation of Creep Behaviour Using the Power Law Model in Copper Alloy."
- Alkelani, Ali A., Basil A. Housari, and Sayed A. Nassar. 2008. "A Proposed Model for Creep Relaxation of Soft Gaskets in Bolted Joints at Room Temperature."
- Atlas Specialty Metals. 2006. "Atlas 316-316L."
- Blatt. 2003. "Ingenieure Vdi 2230."
- Bossard. 2005. "Bossard - Technical Information."
- Brien, MJO. 2009. "High Strength Engineering Fasteners : Design for Fatigue Resistance."
- Brown, Kevin H., Charles Morrow, Samuel Durbin, and Allen Baca. 2008. "Guideline for Bolted Joint Design and Analysis."
- Chakherlou, T. N., M. J. Razavi, and A. B. Aghdam. 2012. "On the Variation of Clamping Force in Bolted Double Lap Joints Subjected to Longitudinal Loading: A Numerical and Experimental Investigation."
- Chesson, E. 1964. "Studies of the Behavior of High-Strength Bolts and Bolted Joints."
- Deibler, Lisa A. 2014. "Room Temperature Creep in Metals and Alloys."
- Elgin Fastener Group. 2019. "Carbon Steel Grade 1541."
<https://elginfasteners.com/resources/materials/material-specifications/carbon-steel-grade-1541/>.
- Euro Inox. 2014. "Roughness Measurements of Stainless Steel Surfaces."
- Fastenal. 2017. "Metric , Flat Washers , A4 Stainless Steel Specification Requirements :"
- Gerard, George, and Sorrel Wildhorn. 1952. "A STUDY OF POISSON'S RATIO IN THE YIELD REGION."
- Hradil, Petr. 2017. "Numerical Modelling of Stainless Steel Preloaded Bolted Connections."
<http://doi.wiley.com/10.1002/stco.201710039>.
- J.G. Kaufmann. 1999. "Properties of Aluminium Alloys."
- Jaglinski, T., A. Nimityongskul, R. Schmitz, and R. S. Lakes. 2007. "Study of Bolt Load Loss in Bolted Aluminum Joints."
- Kassner, M.E., K. Smith, and C.S. Campbell. 2015. "Low-Temperature Creep in Pure Metals and Alloys."
- Kossakowski, P.G. 2012. "Influence of Initial Porosity on Strength Properties of S235JR Steel at Low Stress Triaxiality."
- Krapf, Carlyn N. 2010. "Stress Relaxation of Post-Tensioned Stainless Steel Rods for Bridge Pier Cap Shear Strengthening."
https://smartech.gatech.edu/bitstream/handle/1853/33859/krapf_carlyn_n_201005_mast.pdf;jsessionid=108F15D11D6BC5CD0CD08D34456F58A8.smart1?sequence=1.

- Maljaars, Johan, Davide Leonetti, and Carlo Maas. 2019. "Fatigue Life Prediction of Hot Riveted Double Covered Butt Joints."
https://www.sciencedirect.com/science/article/pii/S0142112319300702?dgcid=raven_sd_aip_email.
- Matsunaga, Tetsuya, and Eiichi Sato. 2014. "Creep Mechanism in Several Grades of Aluminum at Low Temperatures."
<http://jlc.jst.go.jp/DN/JST.JSTAGE/jilm/64.42?lang=en&from=CrossRef&type=abstract>.
- McGinty, B. 2010. "Stress Concentrations at Holes."
- Metallurgica Veneta. 1980. "DIN 17350: 1980."
- Moeller, Samuel Augustus. 2016. "Relaxation in Bolted Assemblies By."
- NASA Scientific and Technical Information Facility. 1965. "A Reproduced Copy of: Description of Stress-Strain Curves By Three Parameters."
- NEN-EN 1090-2. 2018. "NEN-EN 1090-2."
- NEN-EN 1993-1-1. 2010. "NEN-EN 1993-1-1."
- NEN-EN 1999-1-1. 2013. "NEN-EN 1999-1-1."
- Nijgh, Martin Paul. 2016. "Loss of Preload in Pretensioned Bolts."
- Outokumpu. 2013. "Handbook of Stainless Steel."
- Pilkey, Walter D., and Deborah F. Pilkey. 2008. "Peterson's Stress Concentration Factors."
- Rieth, M. et al. 2004. "Creep of the Austenitic Steel AISI 316 L (N) – Experiments and Models."
https://inis.iaea.org/search/search.aspx?orig_q=RN:36021021.
- SSINA. 2000. "Designer Handbook Stainless Steel Fasteners."
- Staab, George. "Joint Stiffness."
- Steel Industry. 2010. "Preloaded Bolt Assemblies Further Sources of Information."
- TelmaStainless BV. "17-PH Precipitation Hardening Stainless Steel."
- Tylek, Izabela, and Kuchta Krzysztof. 2014. "Mechanical Properties of Structural Stainless Steel."
- Wang, Y. Q. et al. 2017. "Analysis of Elastic Interaction Stiffness and Its Effect on Bolt Preloading."
- Ydstebø, Kristian. 2017. "Capacity of Bolted T-Stub Connections Between Different Materials Subjected to Tension and Thermal Load Credits."

Annex A.1 Literature review gasket creep

In the piping industry many joints are equipped with gaskets. The gasket is designed to seal the imperfections between two flanges to prevent leakage. As mentioned earlier, surfaces are hardly ever perfectly flat and smooth and therefore a seal or gasket is used when no leakage is wanted or allowed. Gaskets are made of a softer material than the adjacent surfaces and therefore the deformation in a gasket is relatively higher than the adjacent materials. Next to that, gasket materials tend to creep resulting in a loss of preload in the bolts. A similar behavior can be found in pressure-resistant isolation used in between aluminium and steel joint members to avoid galvanic corrosion. Gasket creep of styrene butadiene rubber at room temperature has been successfully modelled and tested (Alkelani, Housari, and Nassar 2008). Alkelani suggests a spring-model as shown in figure A.1.1. A spring representing the bolt is placed parallel with springs representing the flanges and springs/dampers representing the gasket.

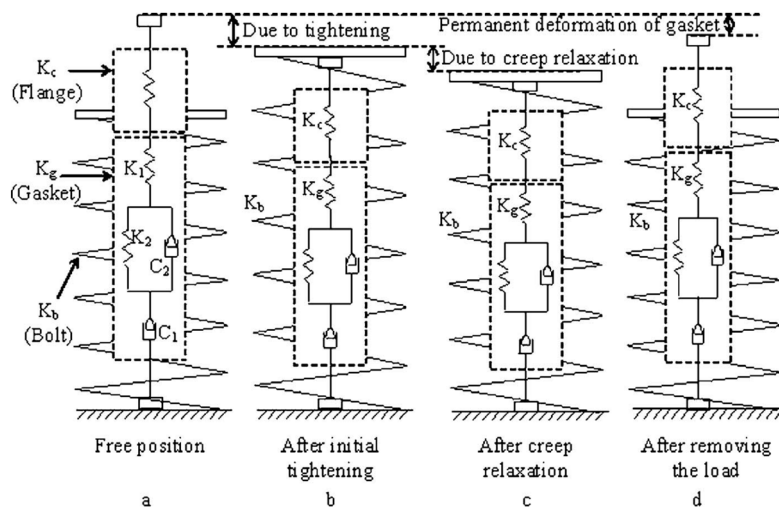


Figure A.1.1: mechanical model of single-bolt gasketed joint (Alkelani, Housari, and Nassar 2008)

The behaviour of the gasket can be mechanically described with four constants: K_1 , K_2 , C_1 and C_2 . These constants represent the elastic spring stiffness and damping rates and have to be determined experimentally using a creep test. The mechanical model of the gasket is shown in figure A.1.2.

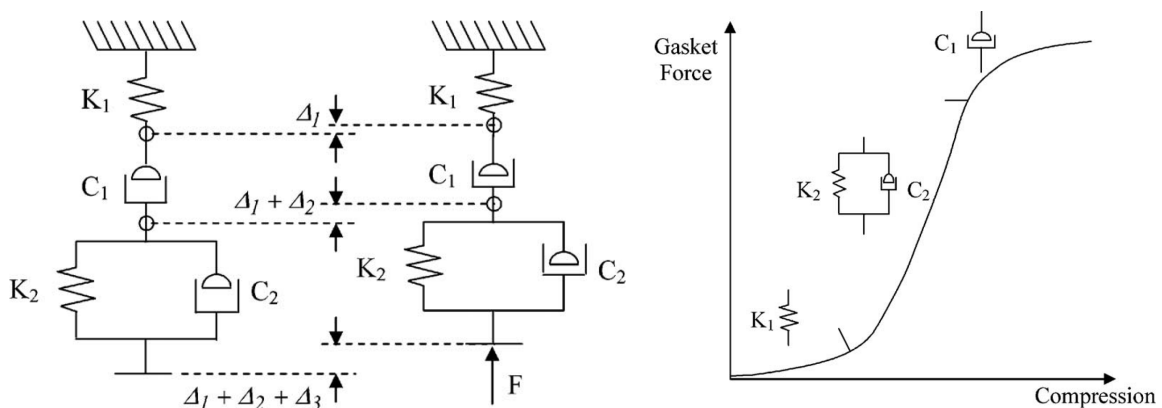


Figure A.1.2: mechanical model of a typical gasket (left); gasket force compression (right) (Alkelani, Housari, and Nassar 2008)

During experimental verification it is discovered that the stress level or preloading level does not affect the gasket constants. The gasket thickness has a significant effect on the gasket constants. However, no clear relationship was found between the constants and the gasket thickness.

The model was validated in 9 different tests containing 3 different gasket thicknesses and 3 different preloading levels. The results and validation of the test containing a gasket with 3/16" thickness are shown in figure A.1.3. The difference of 5% between the model results and experimental data can be caused by normal variation in the gasket mechanical properties. Therefore, the model predicts the creep behaviour of gasketed joints accurately.

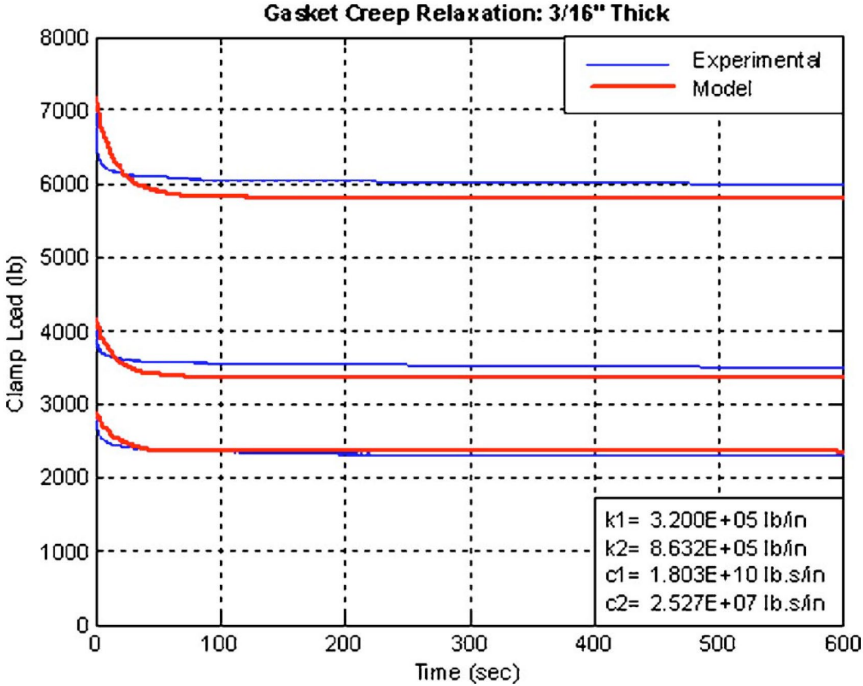





Figure A.1.3: experimental and analytical creep relaxation results for 3/16" thick gasket (Alkelani, Housari, and Nassar 2008)

Annex B.1 Specifications BoltSafe Load Cell

BoltSafe Sensor CMS

BoltSafe Sensor CMS (Continuous Monitoring System) is a specially designed sensor to monitor the residual bolt load in bolted joints. In this way the uncertainty in achieving the desired residual bolt load can be removed. This will result in enhanced safety, dependable joints, better control and improved cost benefit both during installation and throughout the joint's service life.



The BoltSafe Sensor should always be placed directly under a nut to obtain the best possible accuracy of the residual bolt load.

The sensor
BoltSafe Sensor CMS is shaped as a regular washer, used as a washer, and is available in standard sizes to fit both metrical and imperial bolts in sizes from M20 to M64 (corresponding 7/8" to 2 1/2"). The design is rugged and able to withstand through environments.

BoltSafe Sensor CMS employs an ASIC (Application Specific Integrated Circuit) in each unit, which performs all the signal conditioning, digital network connection and a selective identification number for each unit. This means that each BoltSafe Sensor will have its unique serial number for identification and traceability. The calibration of the sensors is done once, and there is no need for re-calibration throughout the lifetime of the sensor when used within the specification.

The BoltSafe Sensor CMS can be read one by one using the handheld instrument SM-200 BoltSafe Reader, or directly from a PC through the CM-1000 Network Adapter, or directly from a PDI-NT. The PDI-NT provides different output signals.

Cable lengths
BoltSafe Sensors CMS have a cable installed for the purpose of interconnecting several sensors into a network and hence monitor the residual bolt load in a continuous manner from one connecting point. CMS washers are delivered with 1m cable as standard. Optional delivered with 3m, 5m, or 10m, always to be specified in the order.

General specification	
Sizes:	To fit bolt sizes from M20 to M64 (Correspondingly 7/8" to 2 1/2") See enclosed table of dimensions
Full Scale Load (FS):	From 286 kN to 1794 kN dependent on Sensor size. (See table of dimensions)
Maximum Load at ambient temperature:	FS range x 1.3 (Load without affecting the validity of the calibration)
Temperature range:	-40°C to 80°C
Storage Temperature:	-40°C to 80°C
Total accuracy at ambient temperature (rms):	< 5 % FS (machined parallel surfaces in bolt-nut assembly)
Linearity:	< 1.5 % FS
Hysteresis:	< 0.9 % FS
Creep:	< 0.1 % FS
Repeatability:	< 0.5 % FS
Typical Temperature effects:	< ± 0.08 % FS/°C
Sealing:	IP66
Material:	Stainless Steel 17-4 PH, Condition H1025
Classification:	10.9
Sensor Output:	Serial digital signal
Power Supply:	Powered through electronic interface
Electrical Connection:	Connector or Flying leads (three wire)
Intrinsic Safe Code:	II 2 G, EEx ib IIC T4 (upon special request)

Remarks:
Note that imperfections in the joining surfaces may lead to degraded accuracy in the reading of residual bolt load.

If the user, due to mechanical constraints, needs to use BoltSafe Sensors in other ways, there is a risk that the calibration will not be valid and that the accuracy cannot be maintained. Please contact your local distributor in each case.

Figure B.1.1: Specifications BoltSafe Load Cell

Annex B.2 Table of dimensions BoltSafe Load Cell



Table of dimensions

See the enclosed table for physical dimensions and corresponding max load.

BoltSafe Sensor CMS Imperial Sizes

Size	Normal Bolt Size (mm)	Clearance Hole (mm)	Outside Diameter (mm)	Overall Thickness (mm)	Steel Wight (gr)	Clamping Load Class 10.9 (kN)
7/8"	22,2	22,6	47	14	133	214
1"	25,4	25,8	52	14	160	280
1 1/8"	28,6	29	57,1	14	191	354
1 1/4"	31,8	32,3	63	17	286	437
1 3/8"	34,9	35,5	69	17	343	529
1 1/2"	38,1	38,7	74	17	391	629
1 5/8"	41,3	41,9	80	17	543	739
1 3/4"	44,5	45,1	85	20	608	857
1 7/8"	47,6	48,2	91	20	698	983
2"	50,8	51,4	98	20	816	1119
2 1/4"	57,2	57,8	108,8	23	1156	1416
2 1/2"	63,5	64,3	116,6	23	1289	1748

BoltSafe Sensor CMS Metric Sizes

Size	Normal Bolt Size (mm)	Clearance Hole (mm)	Outside Diameter (mm)	Overall Thickness (mm)	Steel Wight (gr)	Clamping Load Class 10.9 (kN)
M20	20	20,4	37	14	73	166
M22	22	22,4	40	14	85	208
M24	24	24,4	44	14	104	239
M27	27	27,4	50	14	137	315
M30	30	30,6	56	17	214	385
M33	33	33,6	58	17	218	480
M36	36	36,6	66	17	295	560
M39	39	39,6	68	17	300	670
M42	42	42,6	75	20	445	772
M45	45	45,6	80	20	506	905
M48	48	48,6	86	20	591	1018
M52	52	52,6	92	20	669	1221
M56	56	56,6	100	20	798	1408
M60	60	60,8	108	23	1083	1647
M64	64	64,8	114	23	1196	1794

Figure B.2.1: Table of dimensions BoltSafe Load Cell